A Classical Investigation of the Dynamics of MgO Grain Boundaries and an *Ab Initio* Study of Oxygen Vacancies in Amorphous SiO_2

Natalie Natasha Caday Moore

Department of Physics and Astronomy

University College London

A thesis submitted in partial fulfillment for the degree of

Doctor of Engineering

in

Molecular Modelling and Materials Simulation

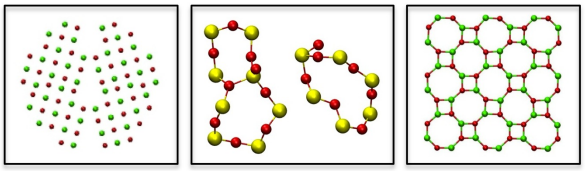

UCL

2012

I, Natalie Natasha Caday Moore confirm that the work presented in this thesis is my own. Where information has been derived from other sources, I confirm that this has been indicated in the thesis.

Natalie Natasha Caday Moore

20th February 2012

Abstract

The arrangement of atoms in most ceramic materials is not perfect and point defects such as vacancies and interstitials, as well as extended defects like grain boundaries exist. In general these defects dominate the properties and processes that are important for the applications of the material. The capture and emission of charge at point defects can affect the stability of dielectrics such as those used in MOS devices. The presence of grain boundaries is also known to lower both the electric and thermal conductivity of a material. Collectively the diffusion of point defects at grain boundaries play a role in mechanisms such as creep and have also been suggested to be involved in the corrosion of metals. In this thesis simulation techniques were used to investigate properties of defects in amorphous silica and near grain boundaries in MgO.

Atomistic methods were used to determine the migration barriers of defects at MgO grain boundaries, the effect of electric field on the stability of the defects, and also the effect of temperature on the structure and stability of the grain boundaries. The nudged elastic band method was used to determine the activation energy for vacancy and interstitial migration at the $\Sigma 17$ {410}/[001] tilt and the $\Sigma 5$ twist grain boundaries. At the tilt and the twist grain boundaries it was found that the activation energies for vacancy migration were up to 1.31 eV and 1.41 eV lower than those in bulk MgO respectively. A finite MgO film model was produced to investigate the effect of electric field on point defects at the tilt grain boundary. The electric field was added to the system by sandwiching the MgO between two layers of point charges. It was found that the field anisotropically lowers the activation energies for vacancy migration by up to 0.37 eV with respect to those determined in the absence of the field. Molecular dynamics simulations were used to investigate the effect of temperature on the stability of the tilt grain boundary and two of its metastable structures and also on the twist grain boundary. The twist grain boundary was found to have the highest entropy in the temperature range 300 - 3000 K which suggests that it may be the most commonly occurring grain boundary in MgO.

An *ab initio* study was also carried out on the structure and electronic structure of the neutral oxygen vacancy in amorphous silica in order to investigate mechanisms associated with dielectric

breakdown such as negative bias temperature instability. Contrary to published suggestions the positively charged and neutral vacancy defects studied were found to have one electron energy levels below the Si valence band which suggests that these defects do not contribute to threshold voltage shifts.

Dedicated to my parents, Lloyd and Numeriana Moore.

"Energy and persistence conquer all things"

- Benjamin Franklin

Acknowledgements

This research was carried out under the supervision of Dr Dorothy Duffy, Dr Keith McKenna and Professor Alexander Shluger to whom I wish to express my sincere gratitude for their guidance and support. I wish to recognise the assistance and kindness I received from members of Professor Shluger's research group, especially Dr Anna Kimmel, Dr David Muñoz Ramo and Dr Tom Trevethan. I would also like to convey my appreciation to Andrew Gormanly, Kyle Rogers and Fabrizio Sidoli for IT support, and to the administration staff from the London Centre for Nanotechnology and the Department of Physics and Astronomy at UCL. I also wish to thank my colleagues and friends from office A25 for physics related and non-physics related discussion, and for each contributing to such a warm and positive working environment. I would like to acknowledge the funding received from the EPSRC and from SEMATECH Incorporated, as well as use of the UCL Legion High Performance Computing Facility, and associated support services, in the completion of this work. Finally, I am indebted to my wonderful family and friends for their unconditional support, encouragement and enthusiasm.

Presentations

"The Effect of Electric Field on Defects at the Grain Boundary of MgO", Thomas Young Centre Student Day, King's College London, 13th December 2010

"The Effect of Temperature on the Stability of MgO Grain Boundaries", Thermodynamics and Kinetics of Surfaces and Interfaces from Simulations: A Thomas Young Centre Workshop, University College London, 23rd June 2011

Contents

List of Figures

List of Tables

Part I

Technological Context and Motivation

Chapter 1

Introduction and Motivation

1.1 The Context of this Thesis

Ceramic materials have traditionally been used in civilisation as pottery formed from clay. However technology has evolved enabling the fabrication of modern ceramics tailored to a wide array of applications. These include bricks and cement for the purpose of construction, refractory materials such furnace linings and fireproof board, white wear such as porcelain and bone china, and nuclear fuel and thermal barrier coatings which are classified as technological applications. Ceramic materials contain defects which can dominate the properties and processes that are important for their applications. In some cases defects facilitate the function of the application. For example, in a solid oxide fuel cell large concentrations of oxygen vacancies provide fast conduction pathways for ions [1], diffusion of impurities at grain boundaries have also been found to extend the lifetime of thermal barrier coatings [2], and in the case of nuclear fuel encapsulation grain boundaries have been suggested to increase radiation resistance by acting as a sink for point defects [3–5]. However defects can also affect the reliability of some applications. In thyristors the presence of dislocations affects the performance of the device [6] and in metal-oxide-semiconductor (MOS) devices diffusion of point defects at grain boundaries and the exchange of charge can lead to the failure of the device. Developing an understanding of the underlying mechanisms behind these phenomena is key in improving the reliability of some applications has been the motivation behind the work in this thesis.

Magnesium oxide (MgO) and amorphous silica (SiO_2) are two common ceramic oxide materials that have been studied extensively and as a result, are often used as models when investigating phenomena in more complex oxides. This thesis presents the results obtained from a classical

investigation into the diffusion of vacancies and interstitials at magnesium oxide grain boundaries and an *ab initio* study of oxygen vacancies in amorphous silica. This was carried out using computer simulation in order to determine:

- the energetics and mechanisms behind the diffusion of vacancies and interstitials at MgO grain boundaries and how they are affected by an applied electric field
- the effect of temperature on the stability of MgO grain boundaries
- the local geometry and electronic structure of neutral and positively charged oxygen vacancies in amorphous SiO_2.

Chapter 2

Background Information

2.1 Ceramic Materials

Ceramic materials are inorganic, non-metallic [7] compounds containing alloys of at least two elements, one of which being a non-metal [8] or a semi-metal [9]. They are formed by the application of heat and sometimes pressure in order to produce a solid. Applications of ceramics in civilization date back thousands of years with one of the earliest uses being clay based pottery. *Traditional* ceramics require minimal processing and the raw materials are silicates of which kaolinite is common. However the fabrication of *modern* ceramics often includes the modification, refinement and even the synthesis of new compounds [10].

A majority of ceramics are oxides and can be of binary form such as alumina (Al_2O_3), magnesia (MgO) and zirconia (ZrO_2), ternary such as the magnesium aluminium spinel ($MgAl_2O_4$), as well as complex like the $NaNdTiO_4$ and $Ba_2EuHfO_{5.5}$ perovskites. However non-oxide ceramics include carbides, nitrides, borides and silicides such as silicon carbide (SiC), silicon nitride (Si_3N_4), titanium boride (TiB) and molybdenum silicide ($MoSi_2$) respectively. Amorphous materials were initially excluded from the ceramic class, however since they are formed using methods common to ceramic processing and exhibit similar properties to ceramics they are sub-classed as "glass ceramics" [8].

In general ceramic materials are solid, strong and wear resistant but, are brittle and susceptible to thermal shock. They are chemically stable, resistant to high temperatures and are thermally and

electrically insulative when undoped. As a result there exists a wide array of ceramic applications, some of which are described in Table 2.1.

Material	Application	Property
ZrO_2	insulation of furnace linings	insulating
		temperature resistant
$MoSi_2$	heating elements for furnaces	conductive
Al_2O_3	insulators in spark plugs	insulating
	catalyst in sulfur refineries	catalytic
SnO_2	gas sensors	gas sensitive conduct
HfO_2	high-$\varkappa$ dielectric	insulating
CaF_2	infrared laser windows	IR transparent
UO_2	nuclear fuel	fission
Si_3N_4	cutting tools	hardness
		temperature resistant
	bearings	wear resistant
Al_4C_3	wear parts in medical engineering	wear resistant
ZrO_2	fuel cell membrane	diffusivity
CeO_2	fuel cell electrolyte	electrolytic

Table 2.1: A selection of ceramic materials, examples of their applications and the properties utilised by the application.

A particular example application to which future chapters will refer is the metal-oxide-semiconductor field-effect transistor (MOSFET) which is an important device in the microelectronics industry, acting as an electronic signal switch. A silicon substrate typically forms the basis of the device and contains doped regions of charge carriers forming the source and the drain. When a voltage is applied across their terminals a current can flow from the source to the drain forming a channel. An insulator and an electrode are layered on the substrate above the channel forming the gate. The application of a voltage across the gate controls the number of charges in the channel. A schematic of a MOSFET is shown in Figure 2.1.

The insulating layer has traditionally been formed of amorphous silica (SiO_2) however due to the scaling down of device dimensions, in keeping with Moore's Law, the thickness of this layer has also decreased in order to maintain a high gate capacitance required to drive current. This has led to leakage currents due to tunnelling effects, resulting in a high power consumption. A solution to this problem has been to replace the silica layer with a layer of material possessing a higher dielectric constant, $\varkappa$, such as hafnia (HfO_2). This type of insulator is known as a high-$\varkappa$ dielectric and permits a higher gate capacitance eradicating some of the leakage issues. However some tunnelling effects still remain which can lead to reliability issues. It has been suggested that the diffusion of point defects at grain boundaries in the insulating layer and the transfer of charge between this

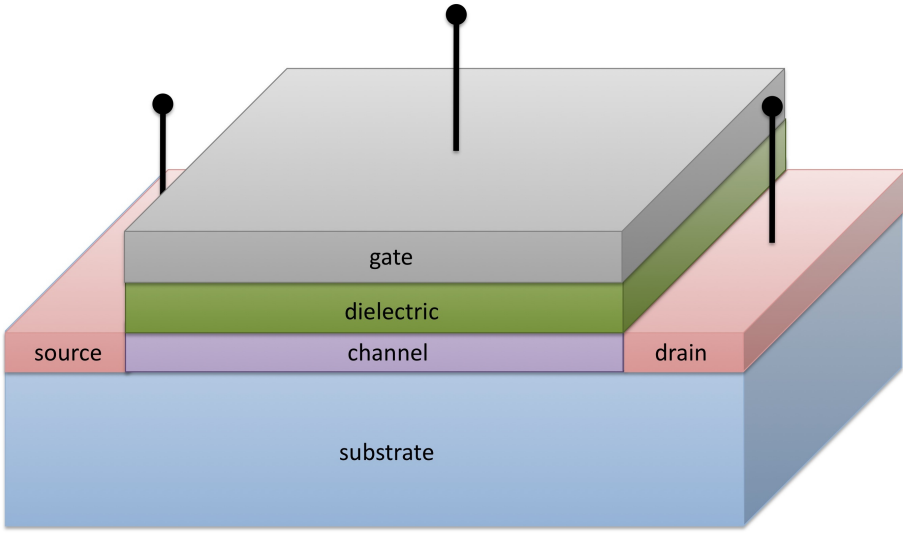

Figure 2.1: A schematic of a metal-oxide-semiconductor field-effect transistor (MOSFET). The source and the drain are doped regions on the substrate containing charge carriers. When a voltage is applied across their terminals current can flow from the source to the drain creating a channel. The applied voltage across the gate determines how much charge flows through the channel.

layer and the channel may establish an electron percolation path leading to the breakdown of the device. Understanding this phenomena is important when considering oxides such as hafnium as the basis of high-$\varkappa$ dielectrics and oxides with simpler crystallographic structure such as MgO and SiO_2 can be used as model materials.

Magnesium Oxide

Magnesium oxide (MgO) is a white, odorless solid alkaline earth oxide. In its cubic form it exists naturally as the mineral periclase however in order to obtain large quantities of the material for use in industry it is usually produced by processing magnesite, magnesium chloride rich brine and sea water. Crystallographically MgO has a rock salt structure as shown in Figure 2.2, and contains doubly ionised ions that undergo ionic bonding. The material has a melting point of 3250 K [11], a boiling point of 3873 K and a bandgap of 7.8 eV [12,13]. Due to its high melting temperature MgO is most commonly used in industry as a refractory material [14], however it also has applications as backfill in nuclear waste repositories [15], a protective coating on plasma display screens [16,17], in superconductors [18,19] and as an electrical insulator [20].

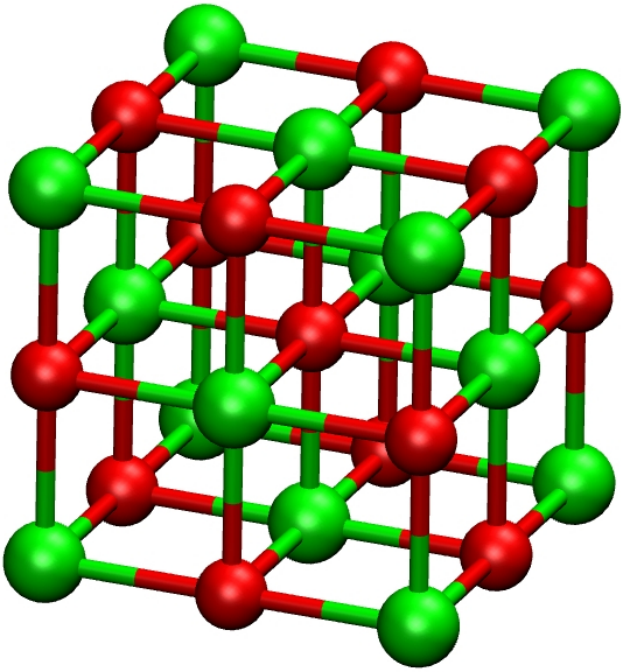

Figure 2.2: The rock salt structure of MgO. Here, and throughout this thesis, the green spheres represent Mg ions and the red spheres represent O ions.

Silica

Silica (SiO_2) is a hard material found naturally as sand (quartz). Crystallographically SiO_2 is composed of tetrahedral structural units of the form SiO_4. A network is formed whereby each Si atom is coordinated to four O atoms and each O atom is coordinated to two Si atoms. SiO_2 exists in several crystalline polymorphs such as α-quartz, β-quartz, α-tridymite, β-tridymite, α-cristobalite, β-cristobalite, faujasite, melanoplogite, keatite, mognite, coesite, stishovite, fibrous and seafertite, of which α-quartz is the most stable. These polymorphs [21–34], shown in Figure 2.3, can be distinguished by their Si-O lengths and Si-O-Si angles. For example the Si-O-Si angles for α-quartz and β-quartz are 144° and 155° respectively. The formation of a polymorph depends on the environment in which it is fabricated with some polymorphs only occurring at high temperatures or pressures. If molten SiO_2 is cooled rapidly then amorphous silica is formed in which the random disorder of the melt is vitrified forming a solid with long-range disorder. Here the Si-O-Si angles range from 120° to 180° with a peak at 145°.

Aside from MOS devices, amorphous silica also has uses in optical fibres [35] as well as photo masks and reflective mirrors for laser optics [36].

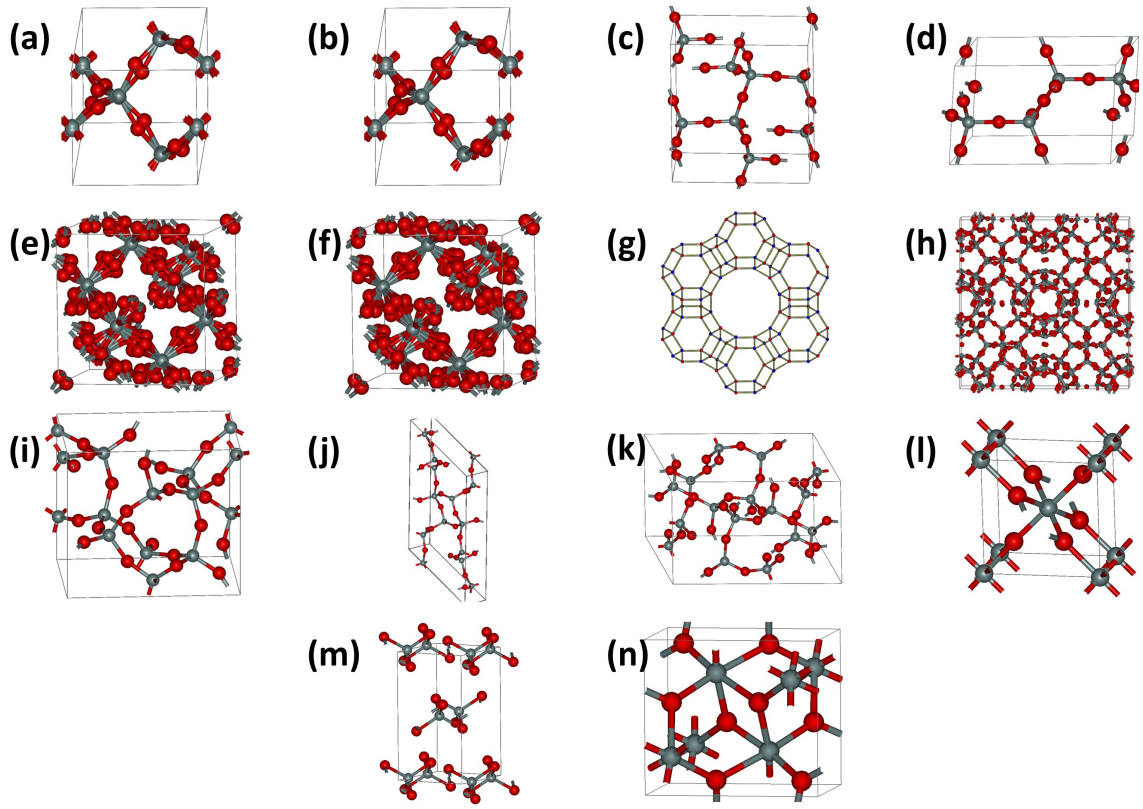

Figure 2.3: Some polymorphs of SiO_2. (a) α-quartz [21], (b) β-quartz [22], (c) α-tridymite [23], (d) β-tridymite [24], (e) α-cristobalite [25], (f) β-cristobalite [26], (g) faujasite [27], (h) melanophlogite [28], (i) keatite [29], (j) mognite [30], (k) coesite [31], (l) stishovite [32], (m) fibrous [33] and (n) seifertite [34]. The red spheres represent O atoms and the grey spheres depict Si atoms.

2.2 Defects in Ceramic Materials

Defects can occur occur naturally in ceramic materials however they can also be introduced to a lattice during fabrication processes such as annealing, ion bombardment and ion implantation. Point defects include vacancies, interstitials, substitutionals, Schottky defects and Frenkel pairs which are shown in Figure 2.4. A vacancy is the absence of an atom from the lattice. An interstitial occurs when an atom occupies a site in the structure that is not a lattice site. A substitutional is an atom on a lattice site that is of a different species to the lattice atoms. A Schottky defect is composed of a set of one or more positively charged vacancies and one or more negatively charged vacancies which form a charge neutral defect such that the stochiometry of the lattice is preserved. A Frenkel defect occurs when an atom moves from its lattice site to an interstitial site creating a vacancy-interstitial pair.

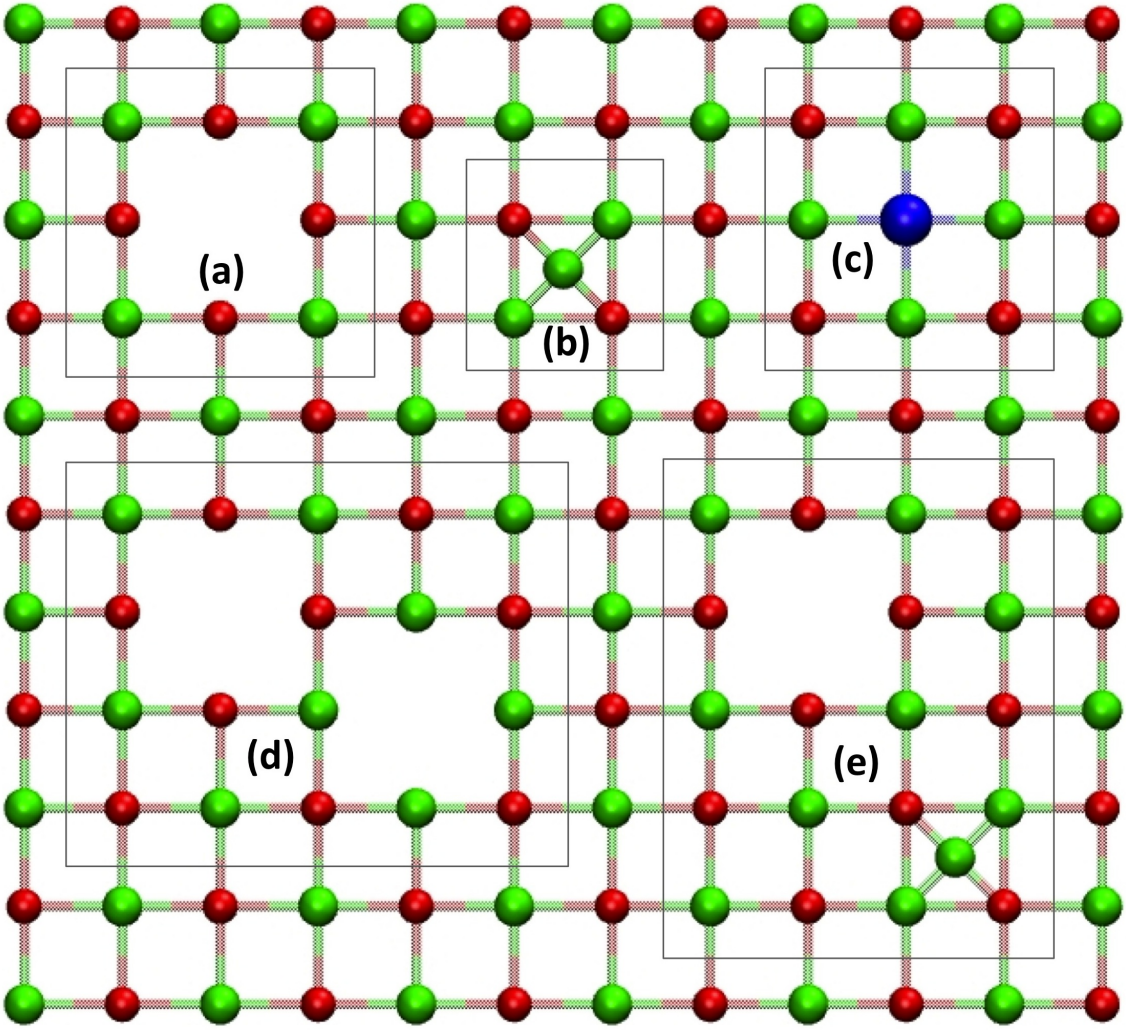

Figure 2.4: Examples of point defects in ceramic materials. (a) a vacancy, (b) an interstitial, (c) a substitutional, (d) a Schottky defect and (e) a Frenkel pair.

Dislocations and grain boundaries are types of defects in which an irregularity extends through the lattice. Two common types of dislocation are the edge and the screw dislocation. In the edge dislocation a plane of ions is abruptly terminated and the remaining planes of the lattice relax towards the space as shown in Figure 2.5 (a). A screw dislocation can be conceptualised as a crystal in which a slit is cut between two planes of ions. One of the edges adjacent to the cut is then displaced parallel to the plane of the cut with respect to the other edge by half a lattice constant as shown in Figure 2.5 (b). Dislocations can also exist which exhibit both edge and screw dislocation properties, these are known as mixed edge screw dislocations.

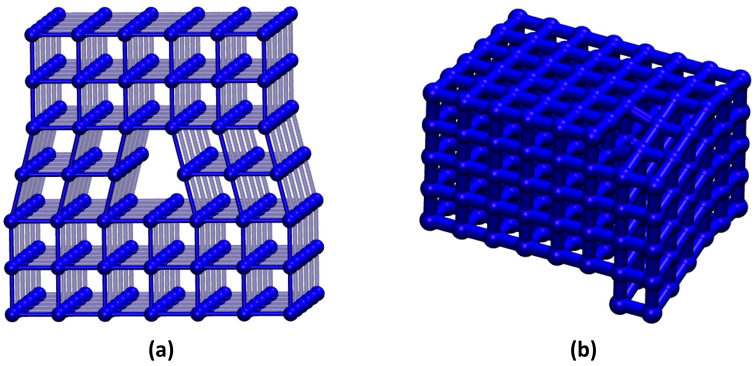

Figure 2.5: Dislocations in a simple cubic lattice. (a) the edge dislocation and (b) the screw dislocation.

Grain boundaries are interfaces that occur in polycrystalline materials between two crystallites. They can be classified as low angle and high angle depending on the angle of misorientation between the crystallites. The low angle types usually include grain boundaries with misorientation angles less than 11°, whereas high angle types have larger misorientation angles. Special high angle grain boundaries exist in which the interfacial energy is low in comparison to most general high angle grain boundaries. These can exist as tilt or twist grain boundaries depending on the axis at which the misorientation occurs. At the tilt grain boundary one crystallite is rotated with respect to the other about an axis parallel to the boundary plane as shown in Figure 2.6 (a). Whereas at the twist grain boundary one crystallite is rotated with respect to the other about an axis that is perpendicular to the grain boundary plane as shown in Figure 2.6 (b).

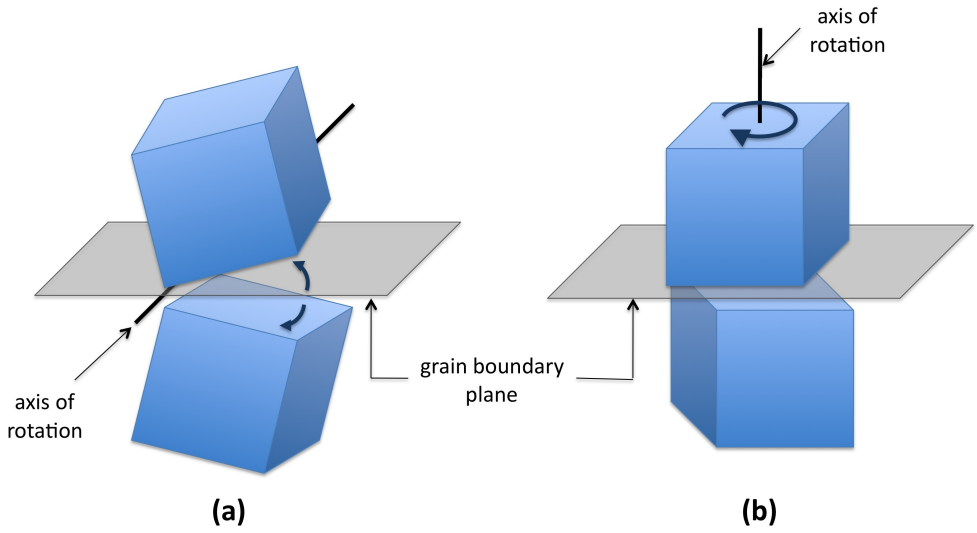

Figure 2.6: The formation of grain boundary units for (a) the tilt grain boundary and (b) the twist grain boundary.

Grain boundaries can be classified by the extent of misorientation of the coincident site lattice

formed by the two grains. Conceptually if the two grains are incident in the same space, then a coincident lattice is formed when one grain is rotated with respect to the other according to the grain boundary type as shown in Figure 2.7. The degree of fit, Σ, is then taken as the inverse of the ratio of coincident sites to the total number of lattice sites.

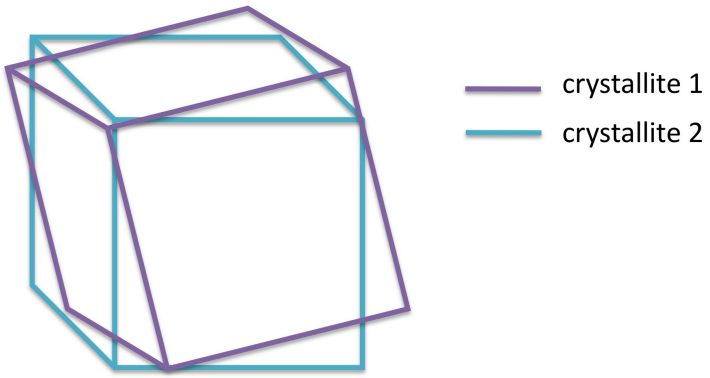

Figure 2.7: The coincident site lattice.

A grain boundary can also be described using Miller indices in terms of the plane of the crystallite adjacent to the boundary plane and the direction of the axis of rotation. This is shown in Figure 2.8 for the Σ17 {410}/[001] tilt grain boundary.

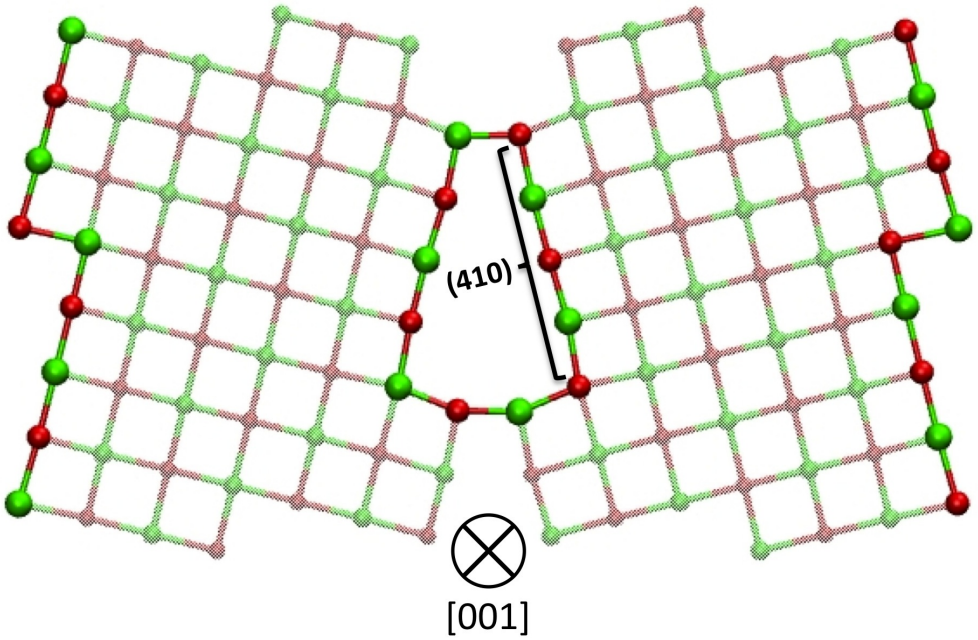

Figure 2.8: Notation used to describe the Σ17 {410}/[001] tilt grain boundary. The solid spheres represent the ions at the grain boundary and the translucent spheres represent the rest of the lattice.

Chapter 3

Literature Review

3.1 Introduction

This literature review provides an overview of the relevant progress of knowledge established prior to the conduction the research presented in this thesis and puts into context the novelty of the work. For MgO some technological applications are mentioned along with the material properties utilised. The effect of grain boundaries in MgO has also been discussed followed by the techniques used to image the defect. Finally a comparison is made of the activation energies obtained experimentally and those determined using computational methods. For silica the E-prime (E') centres are discussed along with the advancement of the models proposed for this family of defects which has been influenced by the computational techniques available. In the final part of the review some MOS device reliability issues are described along with models suggested for their underlying mechanisms.

3.2 Point Defects and Grain Boundaries in MgO

MgO is a polycrystalline ceramic material of significant practical importance due to its numerous and versatile range of applications. In electronics MgO is used as an insulating barrier in tunnelling magnetoresistive junctions [37]. It is also used in plasma display panels as a secondary electron emitter [38] which utilises its high negative electron affinity. Due to its high melting temperature of 2852 °C [8] it is used as a fire proofing material in construction and as a refractory material in the manufacture of steel [10]. MgO exists in the solid mantle of the Earth as the mineral periclase and it has been suggested that grain boundaries provide fast diffusion pathways for carbon to migrate

from the metallic core of the Earth [39]. Its simple rock salt structure also makes MgO ideal as a model for more complex oxides such as HfO_2 [40] and SiO_2, both of which have applications in metal-oxide-semiconductor (MOS) devices, and also for oxides proposed for the encapsulation of spent nuclear fuel [3, 4].

The presence of grain boundaries due to polycrystallinity has been found to affect electrical properties [41] as well as strength, toughness and deformation. Diffusion of point defects at these boundaries have also been found to dominate atomic transport and is a rate determining factor in processes such as creep, annealing of radiation damage, sintering, and in the corrosion of oxide coatings. Grain boundary diffusion is utilised in applications such as magnetoresistive junctions and carbon transfer within the Earth [39]. However for applications such as MOS devices and plasma display screens diffusion of defects at grain boundaries can have a detrimental effect. Therefore studies on diffusion pathways and energetics is key not only towards understanding the rheology of polycrystalline materials but also for the optimisation of applications.

Electron microscopy techniques have commonly been used to image tilt [42, 43] and twist [44–46] grain boundaries in MgO. By analysing Auger electron spectra it was found that that impurities segregate to MgO grain boundaries [47–49]. Experimental studies of MgO using tracer diffusion have shown that impurities such as carbon [39], chromium-51 [50], nickel [51], calcium, silicon and scandium [52], segregate to grain boundaries. In principle this method involves diffusion of tracer impurities into the polycrystalline MgO host, which is driven by heat. Slices of the host are then analysed using spectroscopic techniques such as auger electron spectroscopy [49] and x-ray absorption [51], or, in the case of a radioactive tracer a crystal scintillation counter [50] can be used to determine the concentration of the impurities. Results show an increased concentration of impurities at the grain boundary [49] as well as a diffusion coefficient higher than that of bulk MgO [39,50,51]. Diffusion was found to be anisotropic and occurs most favourably along the grain boundary [50]. Diffusion has also been found to increase with temperature and pressure [39,53,54].

Experimental work carried out using radioactive tracer diffusion on polycrystalline NiO, a material isostructural to MgO, determined a higher grain boundary diffusion coefficient [55] in comparison to that of bulk single crystal NiO. The {310}/[001] tilt grain boundary in NiO has been verified experimentally using high-resolution electron microscopy [43]. The activation energy for ^{63}Ni diffusion in polycrystalline NiO has also been measured as 1.78 eV [55], which is low in comparison to the activation energy in bulk NiO which was determined as 2.5 eV [56]. The structure has been calculated with classical pair potentials. Using static minimisation techniques the activation energy for cation vacancy migration down the boundary was determined as 1.86 eV [57], which is

significantly lower than 2.40 eV which was determined for cation vacancy migration in bulk NiO. The drawbacks of static minimisation are that a number of possible pathways must be considered and it can be difficult to locate the saddle point. Therefore an attempt was made to determine the activation energy of cation and anion vacancies in the {410}/[001] MgO tilt grain boundary using molecular dynamics simulations [58]. Using the pair potentials of Lewis and Catlow [59] and the rigid ion model, the most favourable pathway for diffusion was found to occur down the grain boundary. Here the activation energy for cation and anion vacancies were determined as 1.05 eV and 1.01 eV respectively. Again these are lower than the bulk activation energies which were determined as 1.94 eV and 2.12 eV for cation and vacancy migrations respectively. Further studies on the same MgO grain boundary have shown that pressure increases the vacancy migration energies and causes the vacancy to become more bound to the grain boundary than to the bulk [53].

First principles calculations have also been carried out on the MgO {310}/[001] grain boundary to investigate the notion that defects may exist at grain boundaries with different charged states [60]. Calculations were carried out using the embedded cluster method with the B3LYP hybrid density functional, and also using a periodic model with density functional theory, which allowed the electronic structure of oxygen vacancies and proton impurities to be determined. The results support previous computational and experimental work showing the segregation of defects to the grain boundary. It was found that the most stable vacancies occur at the closely packed region of the grain boundary structural unit and that depending on the placement of the Fermi energy the neutral state can have a formation energy that is lower than that of the F^{+1} and F^{+2} vacancy defects. The proton impurity was found to be most stable when it is located at a site near the close packed region of the structural unit and it was found to have a lower formation energy when it is neutral, corresponding to a proton with a trapped electron (a hydrogen atom), in comparison to its positively charged state.

Transmission electron microscopy has been used to show the existence of the $\Sigma 5$ 36.9° [001] twist grain boundary in NiO [44–46]. Initial computational calculations found this grain boundary to be unstable [61] [62] and that dissociation into two free surfaces was preferable. From further work on NiO using classical techniques it was determined that stable twist grain boundaries can occur by introducing vacancies to the interface and optimising the structure [57, 63, 64]. In this method two crystals are brought together and, in the case of the $\Sigma 5$ 36.9° [001] twist grain boundary, one crystal is rotated 36.9° with respect to the other about the [001] axis. This produces an anti coincident lattice in which there are a number of anti coincident pairs of like atoms that are adjacent across the boundary, and are unstable due to Coulomb repulsion. By removing from one side of the

interface one ion from these anti coincident pairs and permitting relaxation the grain boundary plane restructures to one that is an intermediate of the original adjacent planes above and below the interface. The restructured interfacial plane forms a lattice composed of squares surrounded by octagons, the centres of which coincide with the added vacancy sites. The interfacial energy [56] for this relaxed reconstructed twist grain boundary was determined as 2.2 $J \cdot m^{-2}$ which is lower than the 2.7 $J \cdot m^{-2}$ determined for the unrelaxed structure [64]. This grain boundary has also been investigated using density functional theory with the local density approximation and periodic boundary conditions [65]. Using this method it was found that upon the addition of the Schottky defects the grain boundary plane relaxes to the same arrangement of squares and octagons as was found in classical studies. The calculated density of states show that the added vacancies do not introduce any active states in the band gap and that they are therefore a part of the grain boundary structure. This restructuring method has also been used to produce stable twist grain boundaries using other misorientation angles [63].

3.3 Oxygen Vacancies in Silica

3.3.1 Introduction to Oxygen Vacancies in SiO_2

The reliability of metal-oxide-semiconductor (MOS) devices is governed by issues such as 1/f noise [66], negative bias temperature instability (NBTI) [67] and leakage current [68]. These issues are believed to be caused by the capture and emission of charge carriers by point defects in the SiO_2 dielectric near the interface of the gate and the substrate (see Figure 2.1 in Chapter 2), and are of particular relevance in the development of gate stacks containing high dielectric constant (high-$\varkappa$) oxide films. Much work has focused on studying oxygen deficient centers in crystalline and amorphous silica in various charged states which has led to microscopic models of the defects and the mechanisms for electron capture and hole trapping.

In 1956 electron paramagnetic resonance (EPR) was used to study paramagnetic defects in irradiated crystalline and amorphous silica [69]. Distinct resonances were detected which were correlated to optical absorption spectra [70] and attributed to defects in the oxide. These defects, named after their EPR signal, are known as "E-prime centers" and have the notation E'_n. Here the prime denotes to the number of electrons responsible for the resonance and the subscript, n, corresponds to the local structure of the defect and can be an integer value (e.g. 1, 2, 3) or a Greek character (e.g. α, β, γ), depending on whether the signal is characterising a crystalline or amorphous structure respectively. By determining the hyperfine structure and the g-tensor of the E'_1 and

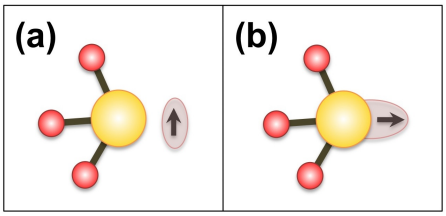

Figure 3.1: Two of the previous models proposed for the E-prime (E') center in α-quartz. (a) E'$_1$ was attributed to an electron trapped on a O vacancy [70] whereas (b) the E'$_2$ centre was attributed to an electron trapped on a Si atom [70] [71]. In this figure and throughout this thesis, the yellow spheres represent Si atoms and the red spheres represent O atoms.

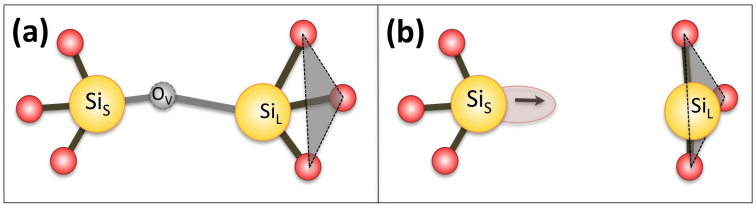

Figure 3.2: The asymmetric relaxation observed in a Si_2O_6 cluster of α-quartz [73]. The initial configuration of the cluster is shown in (a). The grey atom, O_V, represents the vacancy site and the light grey bonds represent bonding of the oxygen lattice atom before the vacancy is added to the system. The grey triangle shows the plane formed by the three oxygen atoms neighbouring Si_L. (b) shows the asymmetric configuration in which Si_Lhas relaxed through the triangular plane [72].

E'$_2$ centers in α-quartz [71] initial suggestions for the defects were an electron trapped on an O ion vacancy and an unpaired electron trapped on a Si atom [69–71] respectively. Both of these models are shown in Figure 3.1. However the long standing model was that of a positively charged oxygen vacancy characterised by a neighbouring pair of asymmetrically relaxed three coordinated Si atoms [72, 73]. This model is shown in Figure 3.2 (b). It can be seen that the long bonded Si atom, Si_L, relaxes through the plane formed by the three O atoms to which it is coordinated, and the unpaired electron is localised on the short bonded, Si_S, atom, which is consistent with EPR data [71].

The configuration behind the E'$_1$ centre has since developed due to advancements in computational resources and computational methods. This has also led to models predicting oxygen vacancy configurations in amorphous silica in various charge states. This section describes the developments in these methods leading to the proposed model for the E'$_1$ configuration that stands today. Models predicting the configuration of oxygen vacancies in amorphous silica will also be discussed. Finally, an overview of the microscopic models predicting the underlying mechanisms behind reliability issues in MOS devices will be presented.

3.3.2 Previous Computational Work on SiO_2 Oxygen Vacancies

3.3.2.1 Small Cluster and Periodic Models

Computational techniques have been used to investigate neutral and positively charged oxygen vacancies in α-quartz and amorphous silica. These techniques include the molecular cluster method, periodic density functional theory and the embedded cluster method. Initial studies focussed on the positively charged oxygen vacancy in α-quartz clusters following on from experimental work suggesting that it is responsible for the E'$_1$ signal, but also because the regular structure of quartz was easier to study in comparison to the disorder of amorphous silica. Using a linear combination of localised orbitals and a finite Si_2O_6 cluster of α-quartz [73] the asymmetric relaxation shown in Figure 3.2 was observed. Here Si_L relaxes into the plane formed by its three nearest oxygen atom neighbours. It was suggested that this non-uniform relaxation removes the degeneracies of the non-bonding orbitals pointing towards the vacancy, allowing the unpaired electron to become localised on Si_S, supporting the model proposed from EPR data [72].

It was recognised that the bridging nature of the oxygen atom in the Si-O-Si unit and the flexibility of the bonds are likely to produce long-range relaxation [74]. Therefore larger clusters composed of 30-40 atoms, with dangling bonds terminated by H atoms, were studied using the modified intermediate neglect of differential overlap (MINDO/3) method with its open shell adaptation (MOPN). Upon adding a positively charged oxygen vacancy to the cluster it was found that the long bonded silicon atom, Si_L, not only relaxes through the plane formed by its three neighbouring oxygen atoms but that it also stabilises by bonding with a back oxygen atom, O_B, as shown in Figure 3.3. This stabilisation could not occur in the smaller clusters, and this local geometry has become known as the puckered configuration.

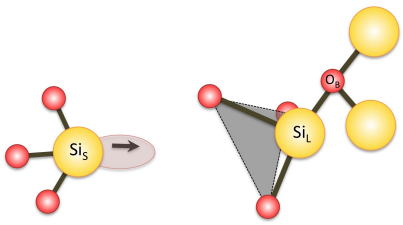

Figure 3.3: The puckered configuration observed in large α-quartz clusters.

Periodic density functional theory was used to study the positively charged oxygen vacancy in α-quartz and found it to be a bistable defect. As well the stable puckered configuration it was found that the defect can occur in a metastable dimer configuration. Here the two Si atoms neighbouring

the vacancy relax towards each other and form a weak bond where the unpaired electron is localised on both Si atoms. This is shown in Figure 3.4.

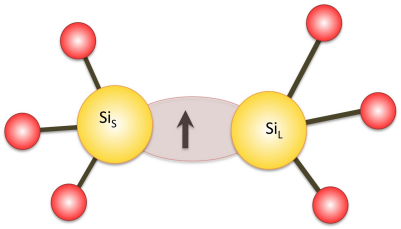

Figure 3.4: The dimer configuration in which the unpaired electron is localised on both Si_S and Si_L.

With the reliability of SiO_2 based electric devices becoming a more prominent issue, focus turned towards modelling oxygen vacancies in amorphous silica. EPR signals analogous to those of the E'$_1$ centre in α-quartz have been detected in amorphous silica, however it was found that the random network made computational work more difficult [75]. The first obstacle was establishing a realistic model exhibiting the vitreous nature of the amorphous structure. Once this was produced it became apparent that there is a wide distribution of topographies at the oxygen vacancy sites due to the random disorder of the lattice. It was observed that not all oxygen sites in amorphous silica will exhibit the same bistable configurations that were found in α-quartz. For example, the puckered configuration will only occur in α-quartz if there is a back oxygen atom, O_B, available for the long bonded Si_L atom to bond with.

Molecular dynamics simulation was used to generate an amorphous unit cell and oxygen sites with local geometry similar to that in α-quartz were carefully selected in order to study the positively charged oxygen vacancy in amorphous silica [75]. It was found that analogous to the E'$_1$ centre this vacancy is bistable and exists in the stable puckered configuration, E'$_\gamma$, as well as in the metastable dimer configuration, E'$_\delta$. It was suggested that in the absence of a back oxygen atom, O_B, other stable configurations may occur. In order to establish criteria for determining and predicting the occurrence of these configurations a statistical study was required to identify the distribution of defect states within the varying local structure of the amorphous network.

Periodic density functional theory was used to study the distribution of E'$_\delta$ and E'$_\gamma$ centers and their neutral oxygen vacancy precursors in amorphous silica [76]. In this study 60 oxygen sites from four generated amorphous supercells were considered. It was observed that all neutral oxygen vacancies exist in the stable dimer configuration. With 90% of these sites also exhibiting the dimer configuration when positively charged. Of the remaining sites 5% assume the conventional, 4-fold, puckered configuration in their positively charged state. The remaining 5% undergo 5-fold

puckering in which the long bonded Si_L atom not only relaxes through the plane of its three neighbouring O atoms and bonds with a back oxygen, O_B, atom, but also bonds with one of the Si atoms coordinated to O_B. This is shown in Figure 3.5 (b).

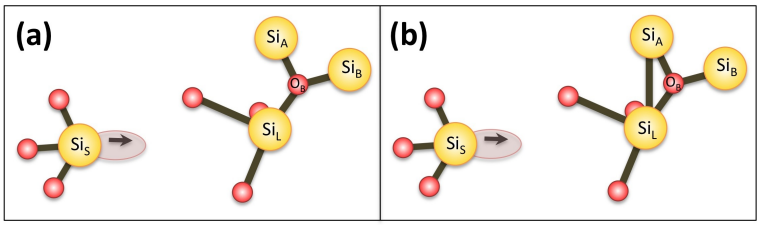

Figure 3.5: (a) Four-fold (conventional) puckering and (b) five-fold puckering.

The same method was used to investigate a 1 million atom supercell [77]. The criteria shown in Figure 3.6 were proposed for predicting oxygen vacancy sites that are likely to pucker.

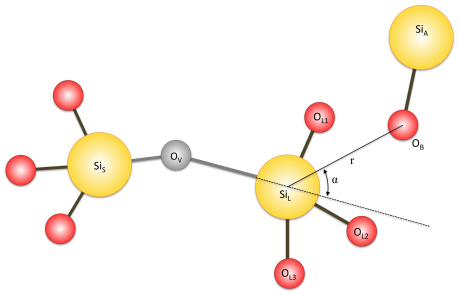

Figure 3.6: Criteria for predicting four fold and five fold puckering [77].

It was suggested that the following conditions be observed in order for four-fold puckering to occur:

$$3.2\,\mathring{A} < r < 3.8\,\mathring{A}$$

$$\alpha < 30^{\circ}$$

$$Si_L - O_{L1}\,,\; Si_L - O_{L2}\,,\; Si_L - O_{L3} > 3.8\,\mathring{A}$$

Whereas the conditions for five-fold puckering are:

$$2.5\,\mathring{A} < r < 3.2\,\mathring{A}$$

$$\alpha < 15^{\circ}$$

For the neutral oxygen vacancy the dimer configuration was again observed to be a stable state. It was found that 80% of the sites do not exhibit bi-stability and that the dimer configuration is the only stable state for both the neutral and positively charged oxygen vacancy. 12 % of the sites were found to undergo 4-fold puckering when hosting a positively charged oxygen vacancy, whereas for the same vacancy 8% of the sites were observed to exhibit 5-fold puckering.

The molecular cluster and periodic methods described predict the geometry of the E'$_1$ and E'$_\gamma$ centres to good qualitative agreement, however quantitatively they fail to predict the properties of oxygen vacancies universally. The molecular cluster method has been found to predict optical properties to good agreement with experimental results, however it fails to produce EPR data comparable to experiment because the long range polarisation is excluded [78]. First principles methods also have their inconsistencies whereby the electronic structure produced by HF differs from that of DFT [79]. Using DFT the band gap is found to be narrow in comparison to experimental findings and this method also fails to predict optical absorption spectra and luminescence energies [79]. Both computational methods fail to include the long range lattice distortion that occurs when a vacancy is present [80].

In the molecular cluster method a finite cluster is used to represent the average local structure of the system. In this case the lattice relaxation beyond the volume of the cluster is not accounted for and the Madelung potential of the infinite lattice is ignored. In the periodic method the distorted structure of the defect is included explicitly within a small cell, which is then translated allowing the periodicity to be forced upon the initial amorphous structure. In this case the lattice distortion is limited by the size of the cell.

3.3.2.2 The Embedded Cluster Method

The embedded cluster method was formulated as an improvement on the molecular cluster method as it includes the distortion of the lattice beyond the cluster. This method employs a hybrid technique in which a quantum mechanical cluster is embedded in a classical representation of the surrounding lattice [80]. This method is described in detail in Chapter 4, Section 4.10. After testing [78] and calibration [81] using α-quartz clusters this method was used to perform a statistical analysis on oxygen sites in amorphous silica [82]. In this study the unrestricted Hartree Fock Hamiltonian was used to investigate a 648 atom amorphous structure that was generated using

a molecular dynamics simulation. The average Si-O distances from the non-defective amorphous structure were correlated to calculated hyperfine constants of positively charged oxygen vacancies. From these results two regimes were observed pertaining to dimer and dangling bond configurations. It was found that upon hosting a positively charged oxygen vacancy 25% of the sites will exist in the dimer configuration and the remaining 75% of the sites were classified as having dangling bond configurations. A dangling bond configuration is one in which the unpaired electron resides on only one of the Si atoms neighbouring the vacancy. The puckered configuration is one such example of a dangling bond configuration that was observed. Another dangling bond configuration is the back projected configuration in which one of the Si atoms neighbouring the vacancy relaxes backwards through the plane formed by the three oxygen atoms to which it is coordinated, much like the puckered configuration. However, unlike the puckered configuration the unpaired electron resides on the asymmetrically relaxed Si atom. This configuration was originally suggested from a study in which the super hyperfine constants were correlated to the local geometry of amorphous silica [83].

In total it was found that 10% of the oxygen sites produce the puckered configuration which is in good agreement with the results observed using periodic DFT [77]. However, in contrast to this work it was found that overall more dangling bond configurations were predicted in comparison to dimer configurations. This occurs because density functional theory favours delocalised states [84]. Some criteria were proposed for predicting the oxygen sites from an amorphous silica structure that are likely to produce the back projected configuration upon hosting a positively charged oxygen vacancy [83, 85]. These criteria are shown in Figure 3.7. It can be seen that the formation of the configuration depends on the three Si_x-O-Si angles, ϑ_1, ϑ_2 and ϑ_3 which are suggested to be in the range 170° - 180°. Here Si_x can be either the long bonded or short bonded Si atom neighbouring the vacancy.

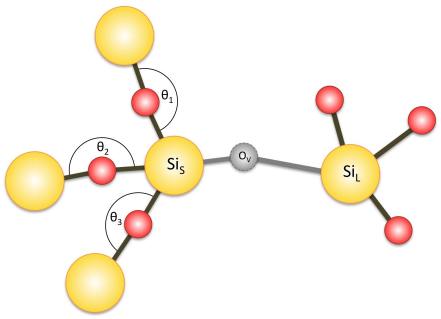

Figure 3.7: Initial criteria for obtaining back projected configurations [85].

An alternative criterion was proposed by investigating the geometry of a 648 atom amorphous

silica supercell [85]. It was considered that in the back projected configuration one of the Si atoms neighbouring the vacancy relaxes beyond the plane formed by its three oxygen nearest neighbours to point P which is shown in Figure 3.8 (a) and (b). The free space around this point was taken as a measure of the distance from P to its nearest lattice ion neighbour with the exception of the three oxygen atoms neighbouring the back projected Si atom. For the puckered configuration this nearest neighbour will be the oxygen atom, O_B. A distribution of P-O_B distances was found which ranged from 1.8 Å to 3.7 Å with a peak at 2.8 Å. It was found that the shortest P-O_B distance required to produce stable back projected configurations is 2.6 Å and that 65% of the oxygen sites have a Si_L-O_B distance greater than 2.6 Å. It was suggested that if O_B is part of a Si_A-O_B-Si_B unit that points towards the Si_L at point P then the puckered configuration will occur if the following criteria are satisfied:

$$d < 2.6\,\mathring{A}$$
$$h < 0.6\,\mathring{A}$$

as shown in Figure 3.8 (c). Here d is the distance between Si_L and O_B and h is the distance from Si_L to the perpendicular bisector of Si_A and Si_B.

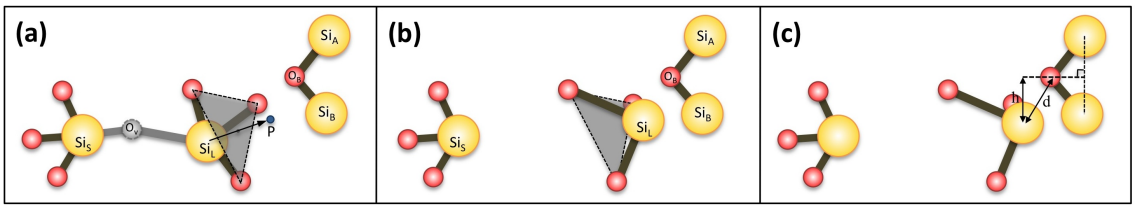

Figure 3.8: Alternative back projected configuration criteria [85]. (a) shows the plane formed by the three O atoms neighbouring Si_L. In (b) it is considered that Si_L relaxes through the plane to point P. (c) shows the geometric parameters that need to be satisfied by the criteria in order for puckering to occur.

EPR was used on irradiated amorphous silica in order to study the previously characterised [86] E'$_\alpha$ centre [87]. It was suggested that this signal could be attributed to a positively charged oxygen vacancy with an unpaired electron in an sp^3 orbital pointing away from the vacancy and localised on the back projected Si atom. The embedded cluster method was used to investigate the properties of oxygen vacancies in amorphous silica in different charged states [88]. Two types of doubly positively charged oxygen vacancy configurations were observed which were named α and $\varkappa$. In the α configuration both of the Si atoms neighbouring the vacancy relax through the

plane formed by their nearest O atom neighbours and bond with a back oxygen atom. In the ϰ configuration one of the Si atoms relaxes through the plane formed by its three nearest O atom neighbours and bonds with a back oxygen atom, whereas the other Si is projected towards the vacancy site and bonds with one of the O atoms to which the other Si is coordinated. The α and ϰ configurations are shown in Figure 3.9 and are referred to as $V^{+2}{}_{\alpha}$ and $V^{+2}{}_{\varkappa}$ respectively, whereby V indicates that the defect is a vacancy, +2 is the charge of the defect and the configuration is denoted by α or ϰ.

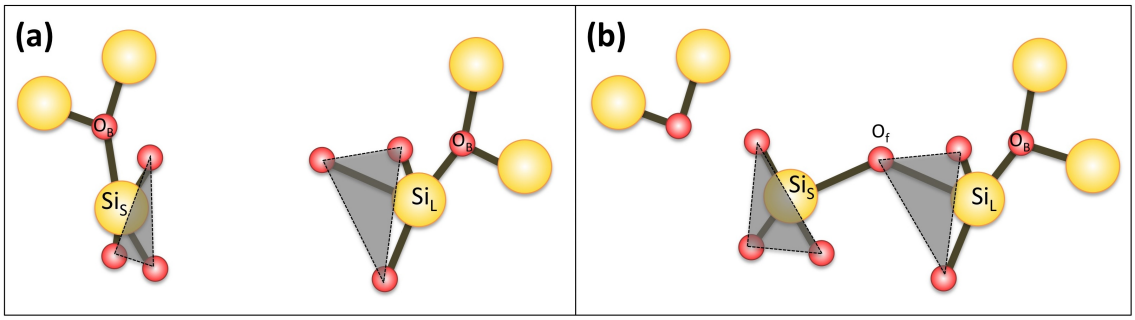

Figure 3.9: The (a) $V^{+2}{}_{\alpha}$ and (b) $V^{+2}{}_{\varkappa}$ configurations for the doubly positively charged oxygen vacancy.

When an electron was added to the doubly positively charged oxygen vacancies the local geometries of the vacancies formed were variations of the α and ϰ configurations. For the $V^{+1}{}_{\alpha}$ the bond between one of the Si atoms and the back oxygen atom is broken. This Si atom remains in its puckered position and hosts the unpaired electron. For the $V^{+1}{}_{\varkappa}$ configuration the bond between the puckered Si atom and the back oxygen is broken, however it maintains its puckered position. The forward projected Si also remains coordinated to four O atoms. However the unpaired electron is localised on the three coordinated Si atom. These configurations are shown in Figure 3.10. It was suggested that adding an additional electron to these V^{+1} configurations may produce more stable neutral oxygen vacancy configurations [88].

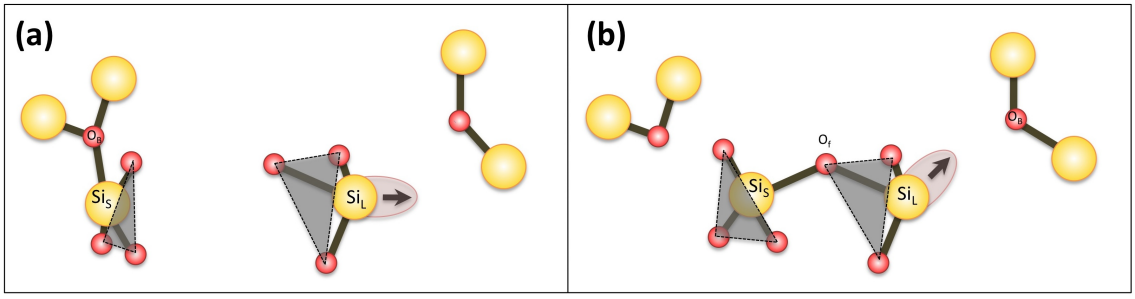

Figure 3.10: The $V^{+1}{}_{\alpha}$ and $V^{+1}{}_{\varkappa}$ configurations for the positively charged oxygen vacancy.

3.3.3 Models Proposed from Experimental Findings for the Reversibility of Charge Traps

3.3.3.1 Negative Bias Reverse Annealing

Metal-oxide-semiconductor (MOS) devices can be exposed to radiation or high electric field stress during fabrication or during the operation of the device. More recently radiation induced defects have been linked to the reliability of these devices. Experimental work has determined that the irradiation of MOS devices using x-rays results in a build up of trapped positive charge in the oxide, close to its interface with the Si substrate [89]. It has been suggested that the radiation induces the formation of electron-hole pairs. These holes compensate or become temporarily trapped at pre-existing neutral oxygen vacancy hole traps located in the oxide close to the Si-SiO_2 interface forming positively charged vacancies. These positive charges have been determined as E' centres [90] and have been attributed to a weakly bonded Si atom pair where each Si atom is coordinated to three oxygen atoms [72].

Reliability issues in MOSFETs often manifest as variations in the threshold voltage shift. It was found that applying a positive bias to an irradiated MOSFET causes the threshold voltage shift to increase. If the bias is subsequently reversed the voltage shift restores towards its original value [91]. It was found that this cycle could be repeated. The Harry Diamond Laboratory (HDL) model was proposed to explain these findings and is shown in Figure 3.11. In this model the irradiation of the MOSFET causes a hole to become trapped on a neutral oxygen vacancy within the oxide, resulting in a positively charged oxygen vacancy. In this configuration it is suggested that one of the Si atoms relaxes into the plane formed by its three oxygen neighbours with the other Si atom hosting the unpaired electron. This is similar to the geometry of the puckered E'_γ configuration without the bonding of the asymmetrically relaxed Si atom to a back oxygen atom. Upon the application of a positive bias an electron is trapped by the defect forming a neutral oxygen vacancy in which both electrons are localised on a single Si atom. Over time this defect can reform the original neutral vacancy configuration in which the electron pair is shared by both Si atoms. However when the bias is reversed an electron tunnels back to the Si substrate and the positively charged oxygen vacancy is reformed.

Following on from this, negative and positive bias annealing of irradiated MOS devices has been investigated as a function of temperature [92] in order to determine the energy level of the positively charged oxygen vacancy charge trap. It was found that below 398.15 K there is a slight increase in the response to the positive bias which was attributed to the tunnelling of an electron to a

band gap state below that of the Si valence band. However for temperatures above 398.15 K a larger response to the bias was observed, suggesting the existence of a low temperature and high temperature regime. Two mechanisms were suggested for the high temperature regime, tunnelling of an electron to an excited state above the Si conduction band, and thermal detrapping of a hole to the oxide valence band [92]. The first mechanism corresponds with other experimental work [93] [94] and it has been suggested that the charge trap can exist in two states, an excited state adjacent to the Si conduction band and a ground state below the Si valence band. E' centres have since been correlated to leakage currents [68]. From this work it was proposed that leakage currents are caused by the inelastic tunnelling of electrons from the Si conduction band to a band gap state in the oxide. Previous work suggests that this state is the E' centre ground state configuration.

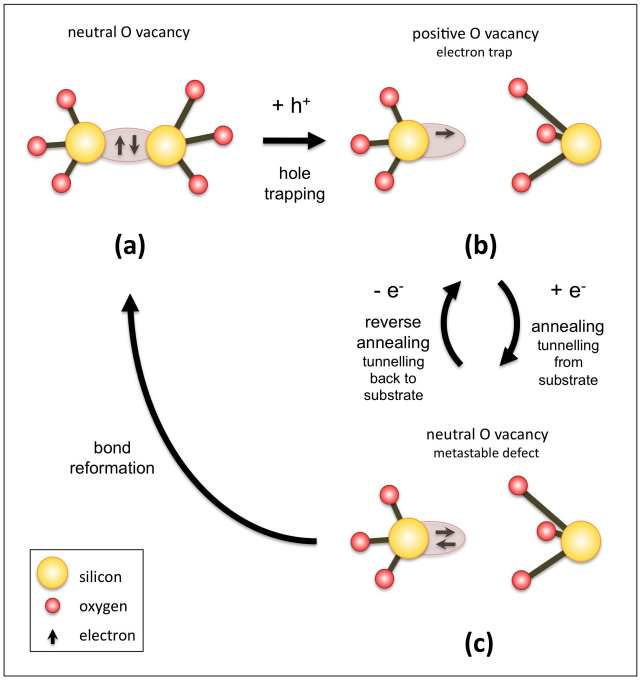

Figure 3.11: The Harry Diamond Laboratory (HDL) model [92] showing the cyclability of charge trapping at oxygen vacancies in silica. Hole trapping can occur from (a) to (b). Annealing can occur from (b) to (c) in which the positively charged defect captures an electron. Conversely reverse annealing can occur from (c) to (b) in which the neutral defect captures a hole due to the tunnelling of an electron back to the substrate. The dipolar defect at (c) can also undergo reformation to the defect structure at (a).

3.3.3.2 Generation of Neutral Electron Traps

As well as naturally occurring neutral oxygen vacancy hole traps, the existence of the radiation induced neutral electron trap has also been identified in the SiO_2 gate insulator using experimental techniques [95–100]. These electron traps were studied further using optically assisted electron

injection on x-ray irradiated insulated gate field effect transistors [101]. The I-V characteristics of the devices were measured after each injection of electrons in order to determine the threshold voltage shifts. It was found that there was a build up of fixed positive charge and neutral electron traps which was dependent on the gate bias. It was therefore suggested that there is a link between the formation of neutral electron traps and the compensation of fixed positive charges. By combining these results with the HDL model [91, 92] a model was proposed for the generation of neutral electron traps, which is shown in Figure 3.12. The model suggests that the first set of injected electrons are captured by the radiation induced positively charged oxygen vacancies near the Si-SiO_2 interface forming neutral vacancies. Upon further electron injection these neutral vacancies trap electrons generating negatively charged defects.

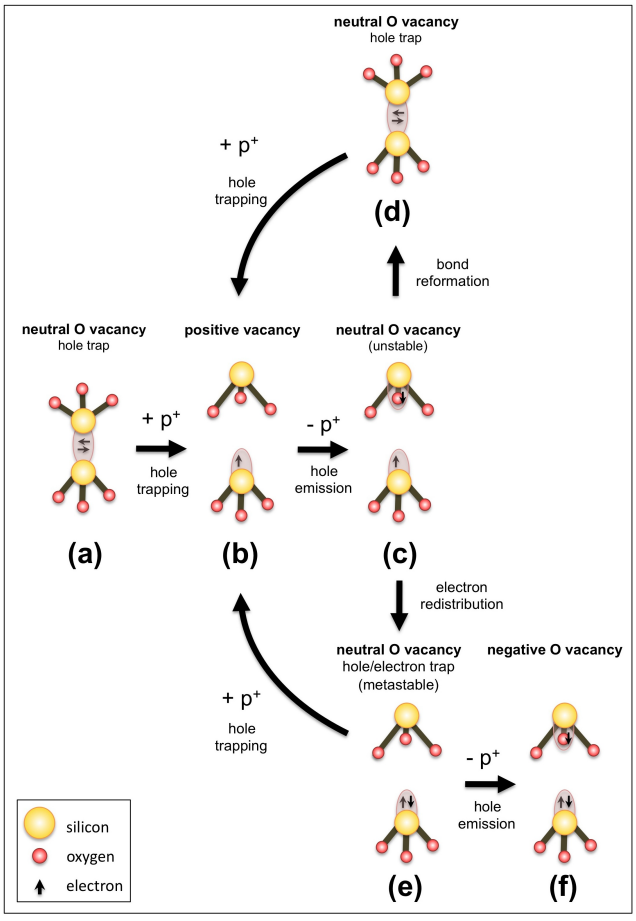

Figure 3.12: The neutral electron trap model [101] in a SiO_2 gate oxide. Positive charge is generated at (b) by radiation induced hole trapping at (a). The positive charge is then compensated by an electron and can either reform (d) the initial neutral structure or form a dipolar structure (e). This neutral dipolar structure can then trap an additional electron via electron injection forming a fixed negative charge.

3.3.3.3 1/f Noise

1/f noise manifests itself as a signal where the power spectral density (the energy or power per unit of frequency), s, is inversely proportional to frequency, f:

$$s(f) \propto \frac{1}{f}$$

It is a phenomena that occurs regularly in nature such as in electromagnetic radiation of astronomical bodies, heart beat rhythms, the long term memory effect in finance and as flicker noise in electronic devices. In electronic devices flicker noise has been suggested to originate from fluctuations in defect configurations and fluctuating occupancies of charge traps. In a study combining capture cross section data and molecular defect models obtained using DFT it was suggested that 1/f noise in MOS devices is caused by fluctuations in the number of charge carriers from which charge carrier mobility fluctuates accordingly [66]. 1/f noise was found to correlate strongly to the density of oxygen vacancies in SiO_2. It was suggested that for an nMOS device 1/f noise increases with an increase in oxygen vacancies during irradiation and decreases with decreasing numbers of oxygen vacancies during post irradiation annealing. Whereas for a pMOS device 1/f noise increases during irradiation and can increase or decrease during post irradiation annealing. In order to resolve differences between optical and thermal energies for trapped hole annealing it was suggested that charge capture and emission may be accompanied by relaxation of the atoms surrounding the oxygen vacancy. Using oxygen vacancy models derived using density functional theory one model was proposed for 1/f noise in pMOS devices and three models were suggested for 1/f noise in nMOS devices. These are shown in Figure 3.13.

For pMOS devices 1/f noise is suggested to arise from the capture and emission of a hole from an E'_{δ} centre. The first mechanism for 1/f noise in nMOS devices involves the capture and emission of an electron by an $E'_{\gamma 4}$ centre. In the second method phonons cause the back oxygen atom and one of its Si nearest neighbours to relax towards the long bonded Si atom. An electron is then emitted and the long bonded Si atom forms an additional bond with a back Si atom and becomes five coordinated. This mechanism is reversible and phonons may cause the back Si and O unit to relax away from the long bonded Si atom enabling the defect to capture an electron. In the third nMOS model lattice relaxation may cause a strained E'_{δ} centre to relax such that the distance between the long and short bonded Si atoms is reduced and an electron may be captured.

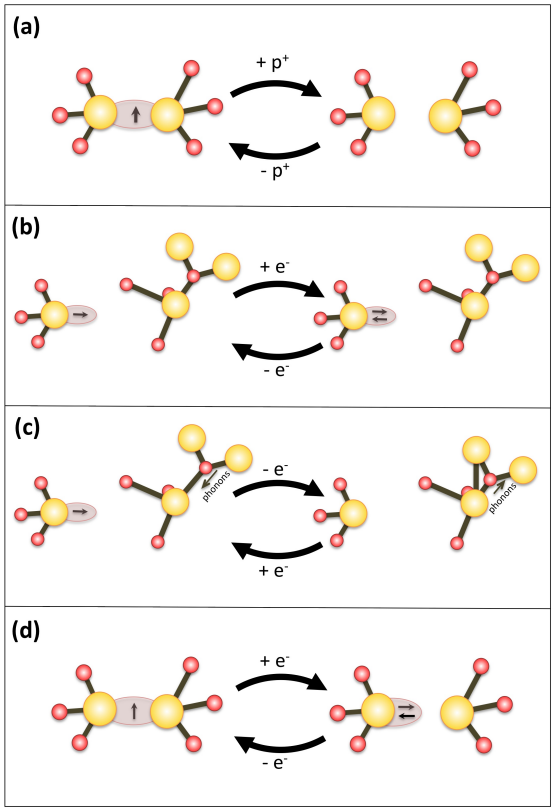

Figure 3.13: Models proposed for the underlying molecular mechanisms involved in 1/f noise for (a) pMOS devices and (b)-(d) nMOS devices. (a) depicts the cyclability between the positively charged defect and the neutral defect via the capture or emission of a hole. In (b) the defect can cycle between the positively charged and neutral dipolar structures. In (c) phonons can change the local geometry of the defect permitting the breaking/formation of a bond between a Si atom and a back oxygen atom. (d) shows the cyclability between a positively charged defect and a neutral dipolar defect via the capture and emission of an electron. [66].

3.3.3.4 Negative Bias Temperature Instability

Negative bias temperature instability (NBTI) is a reliability issue affecting MOSFETs manifesting itself as an increase in threshold voltage and results in a decrease in drain current. NBTI involves two types of defect, the E'$_\gamma$ centre which is a positively charged asymmetrically relaxed oxygen vacancy, and the P_b centre, which is a Si dangling bond. The general consensus is that NBTI is composed of two regimes, a non-permanent recoverable regime and a permanent regime. The non-permanent regime involves the generation of an E' centre followed by capture and emission of a hole. The permanent regime involves the generation of the dangling bond. From experimental studies characterising pMOSFETs [67] a model was derived dispelling the notion that NBTI is composed of two independent components. This model is shown in Figure 3.14. The electronic energy levels for this model correspond well to those required by the HDL [91, 92] model.

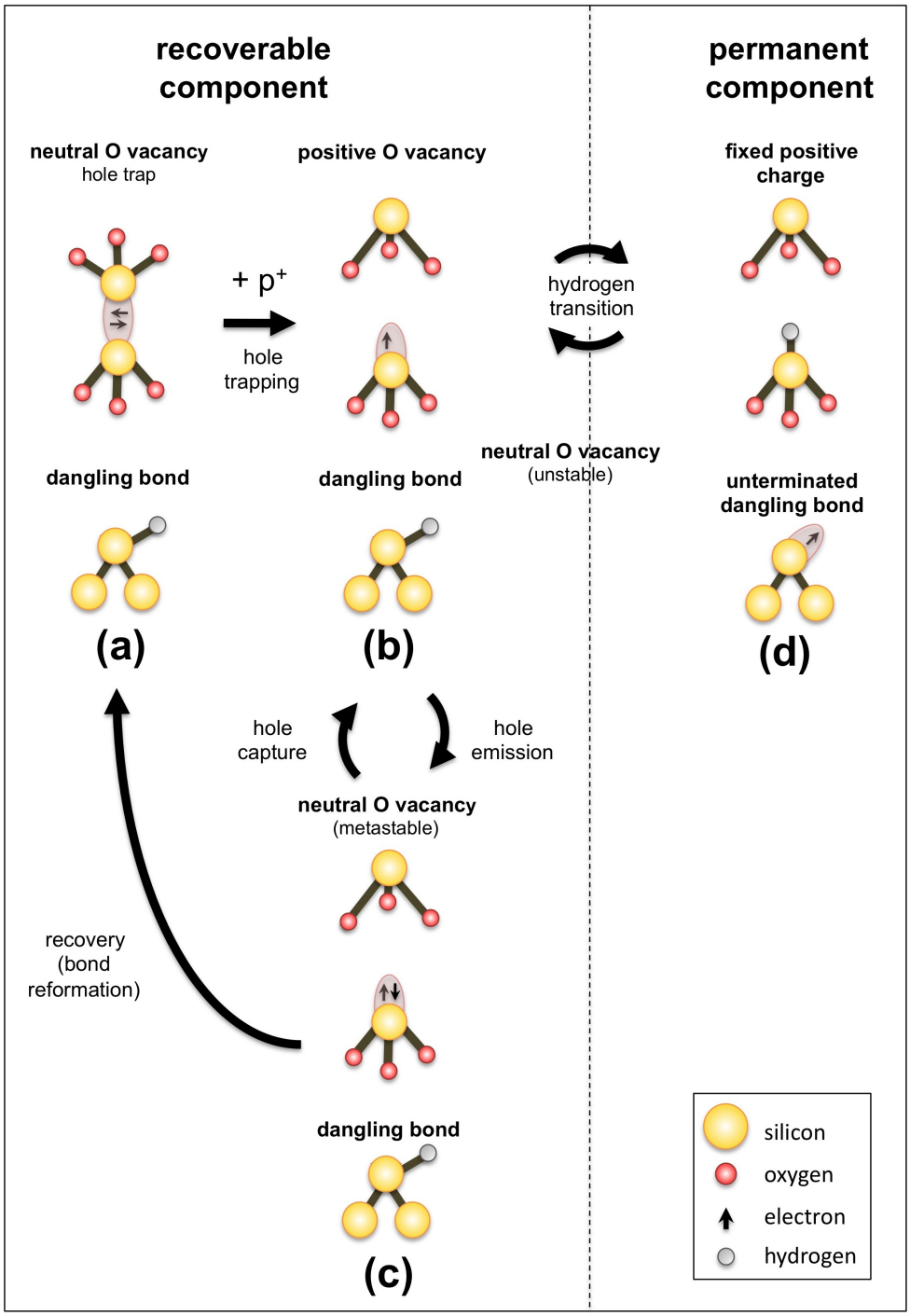

Figure 3.14: The two-stage negative bias temperature instability model (NBTI) [67]. In the recoverable component a hole can be trapped by the neutral precursor defect at (a) forming the positively charged defect at (b). Cyclability can occur between this positively charged defect and a dipolar neutral defect at (c) via the capture or emission of a hole. The dipolar neutral defect can then relax to the initial neutral structure at (a). In the permanent component the hydrogen from the passivated Si dangling bond at (b) can become trapped at the positively charged defect forming the fixed positive charge at (d).

Part II

Computation

Chapter 4

Computational Methods and Software

4.1 Introduction

Computer simulation has developed greatly since the 1940s in line with the evolution of modern day computers and the results obtained from this method are now as significant to scientific research as those obtained from theoretical and experimental methods. It has become common practice, and oftentimes complementary, to combine the results from more than one of these research methods in order to gain a better insight into a research problem. Computer simulation has proved particularly valuable for studying systems undergoing extreme conditions such as high temperature or pressure that may be difficult to achieve in a laboratory. It can also be used to determine the underlying mechanisms behind properties measured in an experiment. Computer simulation is also a useful method for investigating systems that are too complex for an analytical solution to be obtained.

Before a simulation can take place a model is generated which is an approximation of a real life system. The properties of the model are then determined from the interactions of its components. Simulations can be atomistic or from first principles, depending on the fundamental level at which the system is considered. In an atomistic simulation the system is considered at the atomic scale where classical laws of physics are valid. Whereas in a first principles simulation the electronic structure of the atoms is taken into account and therefore the properties of the system are determined by solving quantum mechanical equations. In both cases the properties determined will be

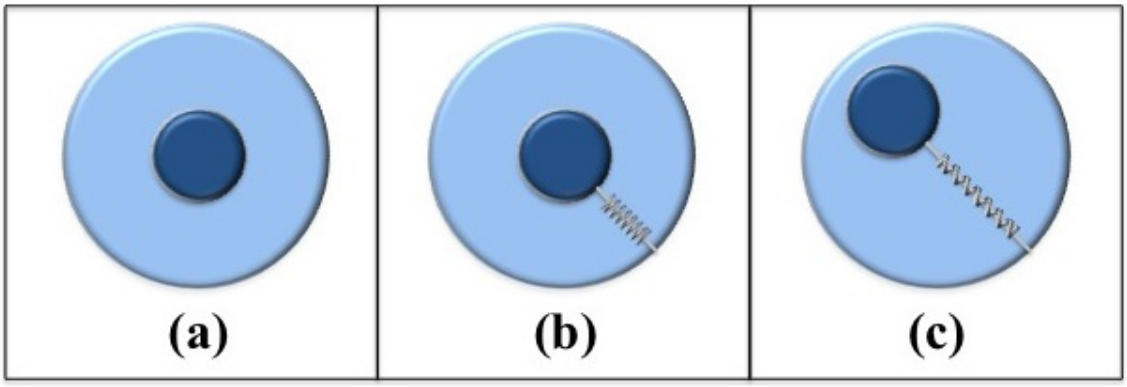

Figure 4.1: (a) The rigid ion model, (b) the shell model in the absence of polarisation and (c) a polarised shell model ion.

precise for the model, however the validity of the results with respect to the real life system depends on the number of interactions that are included in the model. For example, the internal energy of a system can be taken as a summation of individual interactions such as the self interaction, the two-body interaction, the three-body interaction, etc. The precision of this property increases with the number of higher order terms included in the summation. However the contribution of the terms to the internal energy decreases with order and therefore the summation can be truncated. In this chapter the main computational methods and models used to obtain the results in Part III of this thesis are described along with a summary of the software in which they are implemented.

4.2 The Rigid Ion Model and the Shell Model

One way in which polarisability can be included in a computational model is to represent a single ion as a core and a shell. The core represents the nucleus and inner electrons of the ion and contains all its mass, whereas the shell is massless and corresponds to the valence electrons. If the shell is centred on the core and its position does not move relative to the core then this is known as the rigid ion model. However to take into account the polarisation of the ion due to the presence of an external electric field, the core and the shell may be coupled by a harmonic spring force with a spring constant, k_{spring}. The shell can then respond to the field by displacing with respect to the core and the ion becomes polarised. The polarisability of the ion is:

$$\alpha = \frac{q_{shell}^2}{k_{spring}}$$

where q_{shell} is the charge of a shell. This is known as the shell model [102].

4.3 The Coulomb Interaction

The Coulomb interaction is the term with the longest range and has the form

$$U_{coulomb}\left(r_{ij}\right) = \frac{q_i q_j}{4\pi\epsilon_0 r_{ij}}$$

where q_i and q_j are the charges of atom i and atom j respectively, r_{ij} is the distance between the two ions and ϵ_0 is the permittivity of free space. The Coulomb interaction between ions decreases with distance however the number of interacting ions increases with the surface area of a sphere. This interaction therefore does not converge and is ill-defined. One way of treating this is using the Ewald method. Here the conditions of charge neutrality and zero dipole moment are imposed on the system and the Coulomb interaction undergoes a Laplace transformation. The result can be separated into two components, a short-range component that is convergent in real space and a long-range imaginary component that converges rapidly in imaginary space. The cut-offs can be specified and the Coulomb interaction becomes the sum of the real part, the imaginary part and the self interaction.

4.4 The Dispersion Interaction and Pauli Repulsion

The dispersion interaction is a weak intermolecular force however its long-range nature is second only to that of the Coulomb interaction. It is a summation of terms involving inverse even powers of interatomic distance. In the calculations used for this thesis only the first, most dominant, term of the summation is included which takes into account the attractive force between instantaneous dipole - instantaneous dipole moments which occur as the electron cloud of atoms respond to the polarisation of those of adjacent atoms. The dispersion interaction is of the form:

$$U_{dispersion}(r_{ij}) = -\frac{C_6}{r_{ij}^6}$$

When atoms are in close enough proximity such that electron clouds overlap then Pauli repulsion occurs whereby the energy state of electrons increases to obey the Pauli Exclusion Principle. Throughout this study the Pauli repulsion term is represented in Born-Mayer [103] form:

$$U_{Pauli-Repulsion}(r_{ij}) = A\,\exp\left(\frac{-r_{ij}}{\rho}\right)$$

When the dispersion and Pauli repulsion interactions are combined then they are known as the Buckingham pair potential:

$$U_{Buckingham}(r_{ij}) = A \exp\left(\frac{-r_{ij}}{\rho}\right) - \frac{C_6}{r_{ij}^6}$$

Here r_{ij} is the distance between atom i and atom j and the parameters A, ρ and C_6 are constants that can be fit to experimental data or properties determined from first principles calculations. This type of potential is known as an empirical pair potential. In order to fit the potential to an experimentally observed property an initial guess is made of the pair potential parameters and the potential is used to calculate the property. The observed and calculated properties are then compared and the potential parameters are adjusted. This step is repeated until the difference between the two values is minimised.

4.5 Structural Optimisation

The structure of a system can be optimised using energy minimisation whereby the minima of the potential energy surface is determined. There are different schemes for determining energy minima depending on the system. These include the method of steepest descents, the conjugate gradients method and the Broyden Fletcher Goldfarb Shanno (BFGS) method. The internal energy of the system can be expanded in a Taylor series as follows:

$$U(x + \delta x) = U(x) + \frac{\partial U}{\partial x}\delta x + \frac{1}{2!}\frac{\partial^2 U}{\partial x^2}(\delta x)^2 + \dots$$

The series can be truncated after the first few terms because the closer the energy is to a minimum the more harmonic its behavior. The first derivative is the gradient, g, and the the second derivative is known as the Hessian, H. In the method of steepest descents only the internal energy and its first derivative are determined and a line search is used to determine the configuration coordinates of the next step of the calculation. Information determined about the energy surface is not used in subsequent steps therefore this method is considered to be inefficient. In the conjugate gradients method the displacement vector of subsequent steps are orthogonal to those used in the previous step. However this method involves the determination of the inverse Hessian matrix at each step of the calculation. For systems with large degrees of freedom this requires much computational effort and in most cases the Hessian matrix does not vary greatly from step to step. Therefore for really large systems this method is not efficient. The BFGS method is a minimisation technique

which employs an updating scheme. The Hessian is determined in the first step and instead of being calculated again in subsequent steps it is updated. The updated Hessian is as follows [104]:

$$H_{i+1}^{BFGS} = H_i^{BFGS} + \frac{\Delta x \otimes \Delta x}{\Delta x \cdot \Delta g} - \frac{\left(H_i^{BFGS} \cdot \Delta g\right) \otimes \left(H_i^{BFGS} \cdot \Delta g\right)}{\Delta g \cdot H_i^{BFGS} \cdot \Delta g} + \left(\Delta g \cdot H_i^{BFGS} \cdot \Delta g\right) v \otimes v$$

where

$$v = \frac{\Delta x}{\Delta x.\Delta g} - \frac{H_i^{BFGS} \cdot \Delta g}{\Delta g \cdot H_i^{BFGS} \Delta g}$$

Here, H_i^{BFGS} is the Hessian from the previous step, x represents the configuration coordinates and g is the gradient of the internal energy. In the case when the number of degrees of freedom impacts the performance of the computer then a limited memory version of the BFGS method, known as LBFGS, can be used. This method is less exhaustive as only data from a specified number of iterations is stored and used to update the Hessian.

4.6 The Mott-Littleton Method for Defect Calculations

The effect of defects such as vacancies, interstitials and impurities propagate so far into the surrounding crystal that computational resources would be exhausted before convergence of the calculation can be achieved. In the method of Mott and Littleton [105] an infinite crystal can be modelled with reasonable computational effort by imposing approximations on some of the surrounding crystal. Here the defect centre is taken as the centre of the crystal if there is only a single defect in the system, or it can be taken as the mid point of a group of defects. The crystal surrounding the defect centre is then split into three concentric spherical regions, centred on the defect centre, which are specified by their radii. These three regions in order of the radial distance to their boundary with respect to the defect centre are labelled Region 1, Region 2a and Region 2b respectively and are shown in Figure 4.2.

The atoms in Region 1 undergo explicit relaxation with respect to the defect centre, whereas the atoms in Regions 2a and 2b interact weakly with the defect and therefore approximations are made on these regions. The ions in Region 2a respond harmonically to the presence of the defect centre, and the atoms in Region 2b undergo implicit relaxation where the sub lattice as a whole is polarised with respect to the defect.

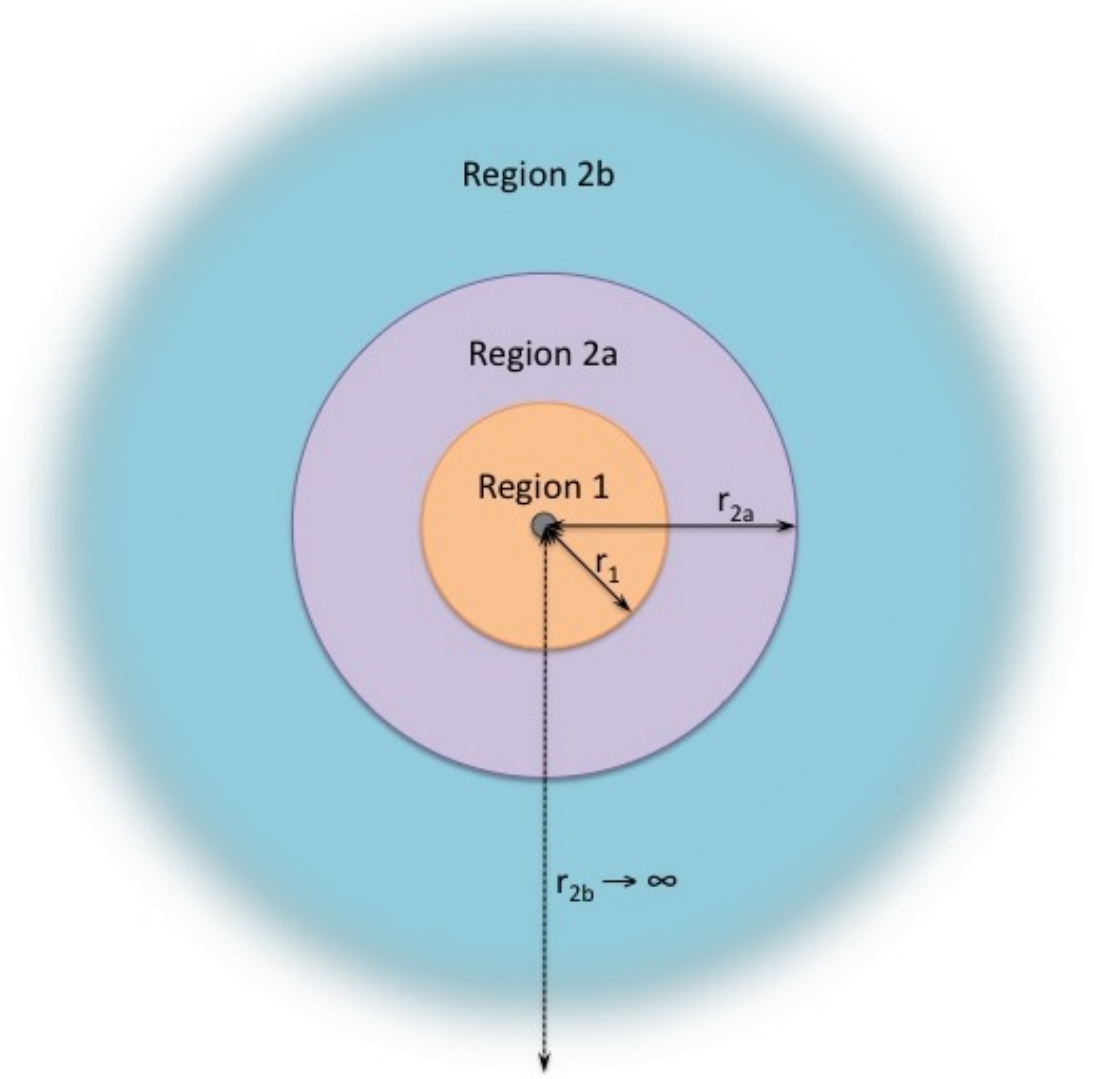

Figure 4.2: A schematic diagram showing the defect centre and the three surrounding spherical regions for the Mott Littleton Method. The defect is depicted by the grey sphere at the centre and is surrounded by the concentric spheres of Region 1 and Region 2. In Region 1 ions undergo explicit relaxation with respect to the defect. The ions in Region 2a relax harmonically with respect to the defect. Region 2b extends to infinity and represents implicit relaxation in which the whole sublattice is polarised with respect to the defect.

If , for now, Regions 2a and 2b are indistinguishable and they are subsumed as Region 2 then the total energy of the defective system is as follows:

$$U_{def}(x,\xi) = U_{11}(x) + U_{12}(x,\xi) + U_{22}(\xi)$$

where U_{11} and U_{22} are the self interaction of Region 1 and Region 2 respectively, U_{12} is the interaction between Region 1 and Region 2, x is the position of the atoms in Region 1 and ξ is the displacement of the atoms in Region 2. It can be assumed that the self interaction energy of

Region 2 is a quadratic function of displacements:

$$U_{22}(\xi) = \frac{1}{2}\xi H_{22}\xi$$

where H_{22} is the Hessian matrix of Region 2. The displacements in Region 2 are in equilibrium when:

$$\frac{\partial U_{def}(x,\xi)}{\partial \xi} = 0$$

Therefore,

$$\frac{\partial U_{def}(x,\xi)}{\partial \xi} = \frac{\partial U_{12}(x,\xi)}{\partial \xi} + H_{22}\xi = 0$$

and:

$$H_{22}\xi = -\frac{\partial U_{12}(x,\xi)}{\partial \xi}$$

The expression for the total energy of the defective lattice can then be re-written as

$$U_{def}(x,\xi) = U_{11}(x) + U_{12}(x,\xi) - \frac{1}{2}\left(\frac{\partial U_{12}(x,\xi)}{\partial \xi}\right)$$

which eliminates the need to evaluate the self energy interaction of Region 2.

If the radius of Region 1 is sufficiently large then the displacements of the ions in Region 2a become small and it is valid to approximate their response to the force of the defect centre as harmonic. Subsequently if the radius of Region 2a is large enough then it can be approximated that the ions in Region 2b only interact by polarising in accordance to the electric field of the total defect in Region 1. For a cubic crystal the energy of Region 2b can be taken as follows:

$$U_{2b} = -\frac{1}{2}Q^2\left(\sum_{i\,\epsilon\,2b}\frac{m_i}{r_{id}^4}\right) \tag{4.1}$$

where Q is the net charge of the defect, m_i is the average of the diagonal elements of the onsite polarisability matrix $M_i^{\alpha\beta}$ and r_{id} is the distance between the i^{th} atom in Region 2b to the defect centre. The on-site polarisability matrix is:

$$M_i^{\alpha\beta} = \sum_{\gamma} \left[\left(D^{-1} \right)^{\alpha\beta} q \right]_i \left(\varepsilon^{-1} \right)^{\alpha\beta}$$

where D^{-1} is the on-diagonal block of the modified second derivative matrix which assumes that that polarisation is divided equally between cation and anion sub lattices and ε is the static dielectric constant tensor. The interaction between Region 2b and the net charge of the defect centre is long range and therefore the distance term in equation 4.1 can be rewritten as

$$r_{id}^4 = \frac{r^\alpha r^\beta}{r^6} = \frac{1}{8} \left[\frac{\partial^2 \left(\frac{1}{r^4} \right)}{\partial r^\alpha \, \partial r^\beta} \right] + \frac{\delta_{\alpha\beta}}{4} \left(\frac{1}{r^4} \right)$$

and a lattice summation technique is used. This technique is the equivalent of the Ewald summation for the inverse fourth power distance and the second derivative with respect to the cartesian displacements.

4.7 The Nudged Elastic Band Method

The nudged elastic band method [106, 107] is a chain of states technique that can be used to determine the minimum energy path of a system undergoing a transition when the initial and final states are known. An initial guess is made of the reaction path or chain which is usually a linear interpolation between the initial and final configurations of the transition. Each point in the interpolation is known as an image and represents a configuration of the system at a particular point of the energy profile. Images are coupled in series by a harmonic spring force, with force constant k, to ensure that equal spacing between the images in the reaction path is maintained throughout the relaxation. Relaxation of each image to the minimum energy path occurs via a force projection scheme. The nudged elastic band force, $\mathbf{F}_i^{NEB}$ acting on image i is the sum of a perpendicular potential force, $\mathbf{F}_i^{\perp}$, and the spring force acting along the band, $\mathbf{F}_i^{spr}$:

$$\mathbf{F}_i^{NEB} = \mathbf{F}_i^{\perp} + \mathbf{F}_i^{spr}$$

where

$$\mathbf{F}_i^{\perp} = -\nabla(\mathbf{R}_i) + \nabla(\mathbf{R}_i) \cdot \hat{\tau}_i \hat{\tau}_i$$

and

$$\mathbf{F}_i^{spr} = k\left(|\mathbf{R}_{i+1} - \mathbf{R}_i| - |\mathbf{R}_i - \mathbf{R}_{i-1}|\right)\hat{\tau}_i$$

Here $\mathbf{R}_i$ is the position of the i^{th} image and its tangent, $\hat{\tau}_i$, is taken as the unit vector between the image and its higher energy neighbour. A schematic of the nudged elastic band method is shown in Figure 4.3.

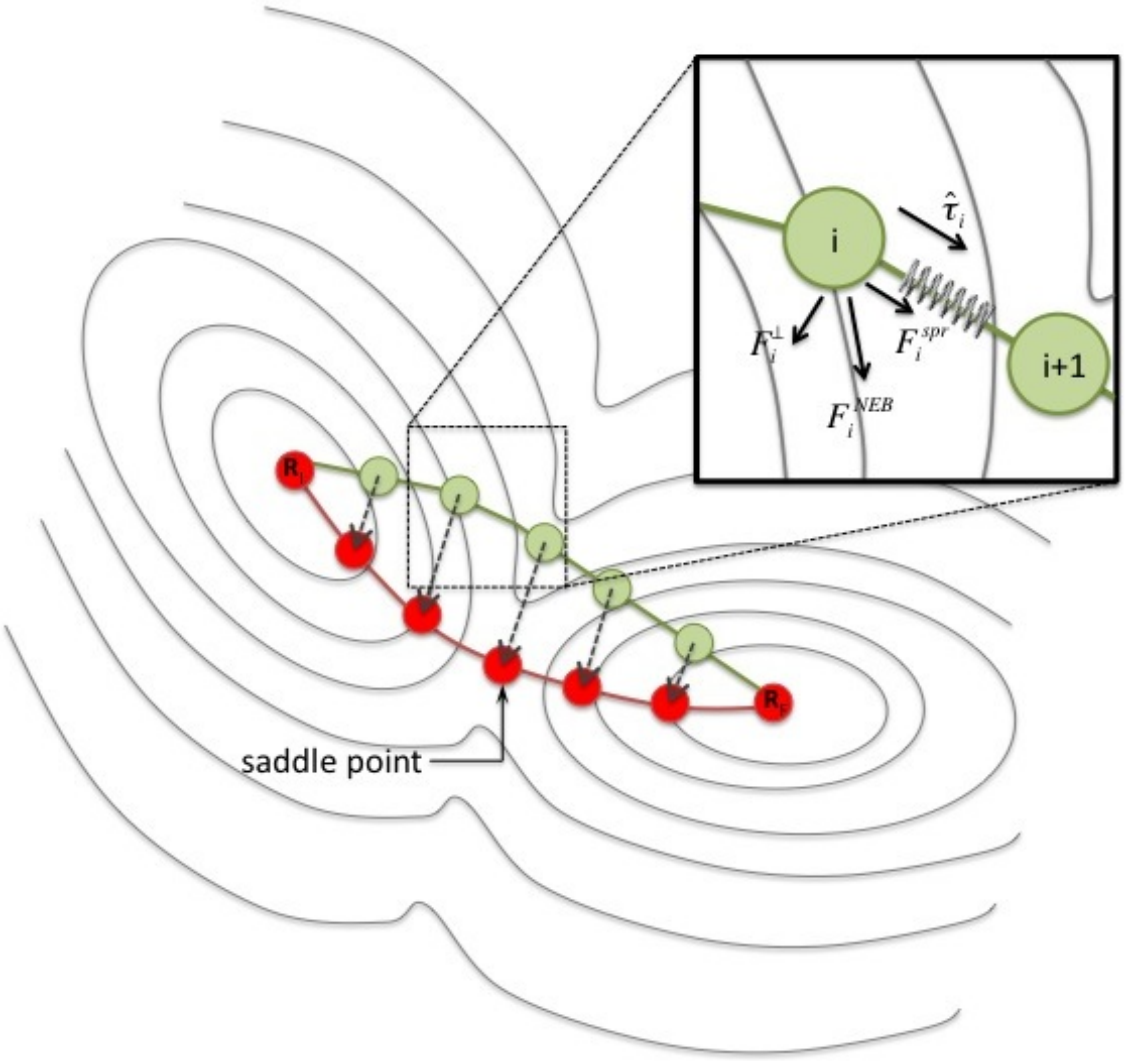

Figure 4.3: A schematic diagram of the nudged elastic band method [107]. The green spheres represent the images in the initial chain whereas the red spheres depict the configurations which occur in the minimum energy path. The grey lines represent the contours of the potential energy surface. The forces acting on an NEB image are shown inset.

The activation energy, E_A, can then be determined as the difference in energy between the saddle point, E_{saddle}, and the energy of the initial or final state of the chain, E_I or E_F respectively:

$$E_A = E_{saddle} - E_F$$

4.8 Molecular Dynamics Simulations

Molecular dynamics simulations can be used to determine microscopic properties of the system such as atomic displacement and diffusion coefficient as well as its thermodynamic properties which include internal energy and enthalpy. In this method the effect of temperature is accounted for by explicit inclusion of kinetic energy. Therefore dynamics of atoms within a system far from its equilibrium state can be investigated. In this study the system is modelled using periodic boundary conditions and the atomic forces and interactions between atoms were determined from empirical pair potentials, as described in Section 4.4. During a simulation the forces are used to produce numerical solutions to the equations of motion:

$$\mathbf{v} = \mathbf{v}_i + \mathbf{a}\,\Delta t$$

$$\mathbf{r} = \mathbf{r}_i + \mathbf{v}\,\Delta t$$

where, $\mathbf{a}$ is acceleration, $\mathbf{v}$ is velocity and $\mathbf{r}$ is position. The subscript i represents the initial value of the property. These equations satisfy Newton's second law of motion, which equates force, $\mathbf{f}$, as follows:

$$\mathbf{f} = m\mathbf{a}$$

where, m is mass.

At the start of the simulation the atom velocities are set such that they follow the Boltzmann distribution and the simulation proceeds with an equilibration period in which the fluctuations in temperature are settled by adjusting the velocities of the atoms. The simulation then continues without velocity rescaling for a specified number of timesteps. In this study a Nosé-Hoover [108,109] thermostat and barostat was used to ensure that the average temperature and pressure of the system do not deviate greatly from those specified. This is done by introducing to the system a friction coefficient, χ which alters the equations of motion as follows:

$$\frac{d\mathbf{r}(t)}{dt} = \mathbf{v}(t) + \eta[\mathbf{r}(t) - \mathbf{R}_0]$$

$$\frac{d\mathbf{v}(t)}{dt} = \frac{\mathbf{f}(t)}{m} - [\chi(\mathrm{t}) + \eta(\mathrm{t})]\,\mathbf{v}(t)$$

$$\frac{d\chi(\mathrm{t})}{dt} = \frac{N_f k_B}{Q}\left[T(t) - T_{req}\right] + \frac{1}{Q}\left[W\eta(\mathrm{t})^2 - k_B T_{req}\right]$$

$$\frac{d\eta(\mathrm{t})}{dt} = \frac{3}{W}V(t)\left[P(t) - P_{req}\right] - \chi(\mathrm{t})\eta(\mathrm{t})$$

$$\frac{dV(t)}{dt} = 3\eta(\mathrm{t})\ \mathrm{V(t)}$$

where $\mathbf{R}_0$ is the centre of mass of the system, η is the friction coefficient of the barostat and N_f is the number of degrees of freedom. T and P are the instantaneous temperature and instantaneous pressure of the system respectively and the subscript req pertains to the required temperature or required pressure of the system. V is the volume of the system and k_B is the Boltzmann constant. Q is the effective mass of the thermostat:

$$Q = N_f k_B T_{req} \tau_T^2$$

where τ_T is a specified time constant for temperature. W is the effective mass of the barostat:

$$W = N_f k_B T_{req} \tau_P^2$$

where τ_P is a specified pressure constant for temperature.

The trajectory of the system is generated using the Verlet leapfrog algorithm in which the velocity of the atoms in one timestep are used to calculate the position of the atoms in the next half a timestep, hence the name leapfrog. The algorithm is as follows:

$$\chi\left(t+\frac{\Delta t}{2}\right) \leftarrow \chi\left(t-\frac{\Delta t}{2}\right)+\frac{\Delta t\, N_f k_B}{Q}\left[T(t)-T_{req}\right]+\frac{\Delta t}{Q}\left[W\eta(\mathrm{t})\text{-}\mathrm{k}_B T_{req}\right]$$

$$\chi(\mathrm{t}) \leftarrow \frac{1}{2}\left[\chi\left(t-\frac{\Delta t}{2}\right)+\chi\left(t+\frac{\Delta t}{2}\right)\right]$$

$$\eta\left(t+\frac{\Delta t}{2}\right) \leftarrow \eta\left(t-\frac{\Delta t}{2}\right)+\Delta t\left(\frac{3V(t)}{W}\left[P(t)-P_{req}\right]-\chi(\mathrm{t})\,\eta(\mathrm{t})\right)$$

$$\eta(t) \leftarrow \frac{1}{2}\left[\eta\left(t-\frac{\Delta t}{2}\right)+\eta\left(t+\frac{\Delta t}{2}\right)\right]$$

$$\mathbf{v}\left(t+\frac{\Delta t}{2}\right) \leftarrow \mathbf{v}(\left(t-\frac{\Delta t}{2}\right)+\Delta t\left[\frac{\mathbf{f}(t)}{m}-\left[\chi(\mathrm{t})+\eta(\mathrm{t})\right]\mathbf{v}(t)\right]$$

$$\mathbf{v}(t) \leftarrow \frac{1}{2}\left[\mathbf{v}\left(t-\frac{\Delta t}{2}\right)+\mathbf{v}\left(t+\frac{\Delta t}{2}\right)\right]$$

$$\mathbf{r}\left(t+\frac{\Delta t}{2}\right) \leftarrow \mathbf{r}(t)+\Delta t\left\{\mathbf{v}\left(t+\frac{\Delta t}{w}\right)+\eta\left(t+\frac{\Delta t}{2}\right)\left[\mathbf{r}\left(t+\frac{\Delta t}{2}\right)-\mathbf{R}_0\right]\right\}$$

$$\mathbf{r}(t) \leftarrow \frac{1}{2}\left[\mathbf{r}\left(t-\frac{\Delta t}{2}\right)+\mathbf{r}\left(t+\frac{\Delta t}{2}\right)\right]$$

The instantaneous position or velocity can then be determined by taking the average of the previous and subsequent half timestep, whereas the instantaneous temperature, T, is determined from the atomic velocities as follows:

$$T=\frac{1}{k_B f}\sum_{i=1}^{N} m_i v_i^2(t)$$

where f is the number of degrees of freedom of the system.

In a real-life experiment the system is usually a macroscopic sample containing a large number

of atoms and a vast amount of conformations whereas the system simulated contains just a few atoms in comparison. In an experimental situation the sample can also be exposed to external pressures and exchange heat with the environment. Therefore to relate the microscopic system of the simulation to a real-life macroscopic system a statistical ensemble should be used which is an infinite collection of system replicas spanning all possible states of the system. Where one replica represents a possible state of the system. The replicas have the same microscopic state, however their thermodynamic properties may differ. For this research the isobaric-isothermal NPT and NST ensembles were used as shown in Figure 4.4. In these ensembles the number of atoms in the system, N, is the same for all replicas, however the volume of the replicas can differ in order to maintain a constant pressure, P, or constant stress, S. This ensemble was chosen because in the temperature range studied MgO remains cubic. In order to calculate a particular experimental observable the ensemble average over all possible values of momentum and position is required. This would entail the determination of all possible states of the system of which there is an infinite number. This is omitted by presuming the ergodic hypothesis which states that the ensemble averaged observable is equal to the time averaged value:

$$\langle A \rangle_{ensemble} = \langle A \rangle_{time}$$

where A is the observable.

The isothermal-isobaric ensemble can be visualised as a system surrounded by a reservoir which maintains the temperature. Pistons are used to change the system volume in order to keep the pressure constant. In the NPT ensemble pressure is applied to the system isotropically, whereas in the NST ensemble only opposite facing pistons are coupled allowing the pressure to vary anisotropically permitting the system to change shape.

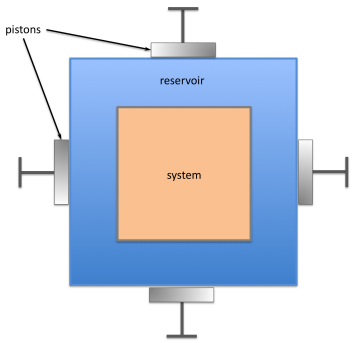

Figure 4.4: A schematic of the NPT ensemble. The system can be conceptualised as being surrounded by a reservoir. The pistons are used to change the volume of the system in order to preserve a constant pressure.

4.9 Density Functional Theory

Density functional theory is a computational technique used to investigate the electronic structure of quantum mechanical many-body systems by determining an approximate solution to the Schrödinger equation using electron density functionals. Analogous to Newton's equations of motion for classical systems, the Schrödinger equation describes the evolution of a quantum mechanical system with respect to time. The time independent Schrödinger equation is

$$\hat{H}\Psi = E\Psi$$

where $\hat{H}$is known as the Hamiltonian or energy operator, E is the total energy of the system, and Ψ is the wave function. The wave function is a probability amplitude which describes the quantum state a particles and their behaviour. In order for Ψ to represent a physically observable system it must be a solution of the Schrödinger equation. The Hamiltonian is comprised of kinetic and potential energy components with kinetic, $\hat{T}$, and potential, $\hat{V}$, energy operators respectively and using atomic units the full molecular Hamiltonian can be expanded as follows:

$$\hat{H} = \underbrace{-\frac{1}{2}\sum_{A=1}^{N}\frac{1}{M_A}\nabla_A^2}_{\hat{T}_{pp}} \underbrace{-\frac{1}{2}\sum_{i=1}^{n}\nabla_i^2}_{\hat{T}_{ee}} + \underbrace{\sum_{A<B}^{N}\frac{Z_A Z_B}{R_{AB}}}_{\hat{V}_{pp}} + \underbrace{\sum_{i<j}^{r}\frac{1}{r_{ij}}}_{\hat{V}_{ee}} \underbrace{-\sum_{A=1}^{N}\sum_{i=1}^{n}\frac{Z_A}{r_{iA}}}_{\hat{V}_{pe}}$$

where M is the ratio of the mass of a nucleus to that of an electron, R is the inter-nuclei distance, r is the inter-electron distance, Z is the atomic number of the nucleus, A and B are indices for the nuclei, i and j are indices for the electrons, N is the total number of nuclei in the system and n is the total number of electrons. Of the terms of the Hamiltonian, $\hat{T}_{pp}$ is the kinetic energy operator of the nuclei, $\hat{T}_{ee}$ is the kinetic energy operator of the electrons, $\hat{V}_{pp}$ is the potential energy operator due to repulsion between nuclei, $\hat{V}_{ee}$ is the potential energy operator for inter-electron repulsion and $\hat{V}_{pe}$ is the operator for the Coulomb interaction between electrons and nuclei.

The Schrödinger equation becomes impossible to solve beyond the scope of a simple system such as the hydrogen atom and as a result, many theories have been proposed for determining approximate solutions. Two such examples are Hartree-Fock theory and density functional theory. In both methods the Born-Oppenheimer approximation is made which is based on the principle that nuclei are significantly heavier than electrons and as a result the electrons are considered to respond instantaneously to changes in the configuration of the nuclei. The nuclei are therefore considered as being fixed in a molecular configuration with zero kinetic energy and a constant potential energy

in which the electrons move. Hartree-Fock theory still involves finding a solution to a many-body problem. Here a further approximation is made that considers a single electron to move in the effective potential of the other electrons in the system. It is assumed that each energy wave function can be described by a single Slater determinant, which is an asymmetric product of 1-electron wave functions. An approximate solution to the Schrödinger equation for an n electron system can then be determined by solving n 1-electron wave functions. The down side to Hartree Fock theory is that electron correlation is not taken to account and all possible electron configurations are equally probable despite the unphysical occurrence of electrons in close proximity. In contrast electron correlation effects are included in density functional theory and the many-body problem with $3n$ variables is reduced to a problem with just 3 spatial variables.

Density functional theory is based on two theorems proposed by Hohenburg and Kohn. The first theorem states that for a normalised wave function in which

$$\langle \Psi | \Psi \rangle = n \int d^3\mathbf{r_1} \int d^3\mathbf{r_2} \ldots \int d^3\mathbf{r_n}\, \Psi^*(\mathbf{r_1}, \mathbf{r_2}, \ldots, \mathbf{r_n})\, \Psi(\mathbf{r_1}, \mathbf{r_2}, \ldots, \mathbf{r_n}) = 1$$

the Hamiltonian can be described in terms of the electron density, ρ, which can be written as follows:

$$\rho(\mathbf{r}) = n \int d^3\mathbf{r_2} \int d^3\mathbf{r_3} \ldots \int d^3\mathbf{r_n}\, \Psi^*(\mathbf{r_1}, \mathbf{r_2}, \ldots, \mathbf{r_n})\, \Psi(\mathbf{r_1}, \mathbf{r_2}, \ldots, \mathbf{r_n})$$

This equation can be rearranged in order to determine the wave function in terms of the density. For the ground state wave function, Ψ_0, and electron density, ρ_0, this is as follows:

$$\Psi_0 = \Psi[\rho_0]$$

which shows that the ground state wave function is a function of the ground state electron density function, i.e. Ψ_0 is a functional. As a result the expectation value of a ground state observable, O_0, is also a functional of the ground state electron density

$$O_0 = O[\rho_0] = \left\langle \Psi[\rho_0] \,\middle|\, \hat{O} \,\middle|\, \Psi[\rho_0] \right\rangle$$

where $\hat{O}$ is the Hamiltonian for the observable. In particular the ground state energy can be described as

$$E_0 = E[\rho_0] = \left\langle \Psi[\rho_0] \,\middle|\, \hat{H} \,\middle|\, \Psi[\rho_0] \right\rangle = \left\langle \Psi[\rho_0] \,\middle|\, \hat{T} + \hat{V} \,\middle|\, \Psi[\rho_0] \right\rangle$$

The second Hohenberg-Kohn theorem states that the energy functional is variational and therefore the expectation value of the energy is never less than that of the ground state:

$$E[\Psi] = \left\langle \Psi[\rho] \,\middle|\, \hat{H} \,\middle|\, \Psi[\rho] \right\rangle \geq \left\langle \Psi[\rho_0] \,\middle|\, \hat{H} \,\middle|\, \Psi[\rho_0] \right\rangle = E_0$$

The energy can therefore be minimised in order to determine an approximation to the ground state energy using the Lagrangian method of undetermined multipliers. If the system is modelled such that the potential energy component of the Hamiltonian is solely due to the effective external potential, $\hat{V}_{eff}$, in which the electrons move then the system becomes non-interacting and therefore can be represented using Kohn-Sham equations:

$$\left[-\frac{1}{2}\nabla^2 + V_{eff}(\mathbf{r})\right] \phi_i(\mathbf{r}) = \epsilon_i \phi_i(\mathbf{r}) \tag{4.2}$$

where ϵ_i is the energy eigenvalue and ϕ_i is the 1-electron eigenvector or orbital which can be used to determine the effective electron density, ρ_{eff}, of the system as follows:

$$\rho_{eff}(\mathbf{r}) = \sum_i^n |\phi_i(\mathbf{r})|^2$$

The effective potential from Equation 4.2 can be written as:

$$V_{eff}(\mathbf{r}) = V(\mathbf{r}) + \int \frac{e^2 n_{eff}(r')}{r - r'} d^3r' + V_{XC}\left[\rho_{eff}(\mathbf{r})\right]$$

where the first term is the potential energy of the system, the second term is the electron-electron Coulomb potential and the third term is the exchange-correlation potential functional.

The exchange-correlation potential can only be determined for a free electron gas therefore an approximation is required. Two such examples are the local density approximation (LDA) and the generalised gradient approximation (GGA). Using the local density approximation the functional is only dependent on the density at the coordinate where it is being evaluated:

$$V_{XC}^{LDA}[\rho] = \int \epsilon_{XC}(\rho)\, \rho(\mathbf{r})\, d^3\mathbf{r}$$

The general gradient approximation also depends on the density at the coordinate but also takes into account the gradient of the density:

$$V_{XC}^{GGA}[\rho_\uparrow, \rho_\downarrow] = \int \epsilon_{XC}(\rho_\uparrow, \rho_\downarrow, \nabla\rho_\uparrow, \nabla\rho_\downarrow)\, \rho(\mathbf{r})\, d^2\mathbf{r}$$

As well as these functionals which are determined solely from *ab initio* methods hybrid exchange-correlation functionals exist which combine *ab initio* exchange and correlation with a proportion of exact exchange from Hartree-Fock theory. One such example is the B3LYP functional which is of the form

$$V_{XC}^{B3LYP} = V_{XC}^{LDA} + a_0 \left(V_X^{HF} - V_X^{LDA}\right) + a_X \left(V_X^{GGA} - V_X^{LDA}\right) + a_c \left(V_C^{GGA} - V_C^{LDA}\right)$$

where the coefficients $a_0 = 0.20$, $a_X = 0.72$, and $a_C = 0.81$ are empirical parameters determined by fitting the functional to atomisation energies, ionisation potentials, proton affinities and total atomic energies.

In density functional theory the exchange-correlation potential depends on the electron density, which depends on the one-electron orbitals from the Kohn-Sham equations, which in turn depend on the effective potential of the system. The Kohn-Sham equations are therefore solved self consistently. By making an initial guess of the electron density the following procedure can be repeated until convergence occurs:

$$\rho \rightarrow V_{XC} \rightarrow V_{eff} \rightarrow \phi \rightarrow \rho$$

4.10 The Embedded Cluster Method

The embedded cluster method implemented in the GUESS [110] computer code can be used to determine the properties of an infinite system containing a single point defect. It was found that models used previously for defect calculations such as the molecular clusters and periodic models, are limited in that the full extent of long range lattice perturbations is not accounted for. The embedded cluster method was specifically developed to include full lattice relaxation. Results obtained using this technique have shown that a more complete inclusion of this perturbation has an effect on calculated properties such as luminescence energy [80]. The embedded cluster method is a hybrid technique in which an infinite system is divided into three regions. Region I is composed

of a quantum mechanical cluster containing a single point defect and is surrounded by a classical domain. The remaining atoms in the lattice are also treated classically and are divided into Region II which surrounds Region I and Region III which is approximated as an infinite continuum and encloses Region II. A schematic diagram of the embedded cluster method is shown in Figure 4.5. The stoichiometry of the atoms in the the system is preserved from region to region and the quantum mechanical cluster is specifically terminated by silicon atoms which form an interfacial region between the quantum and classical domains.

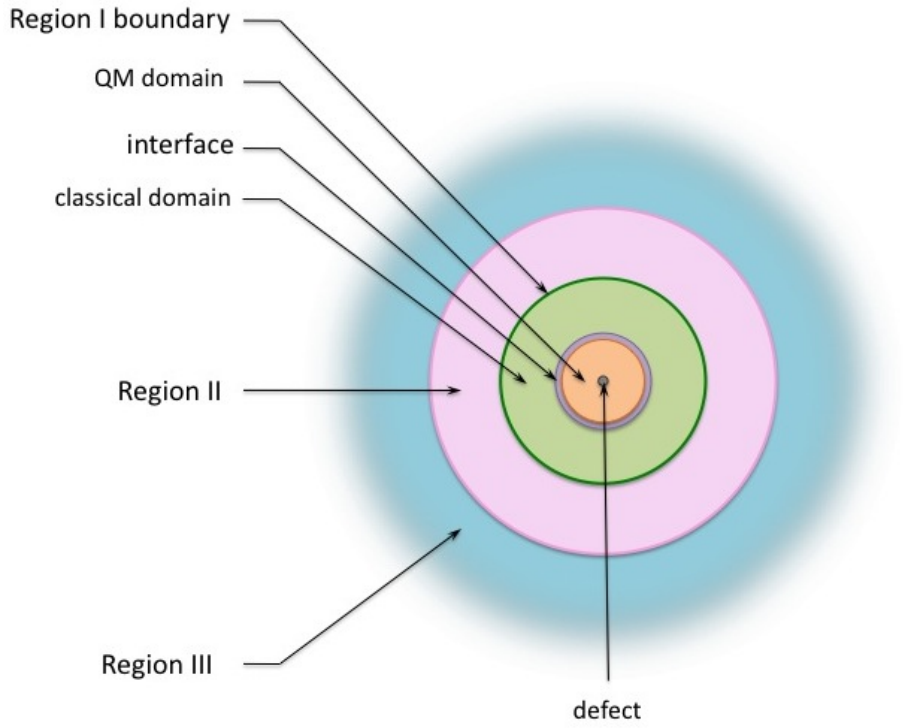

Figure 4.5: The embedded cluster method. The defect is represented by the sphere at the centre of the system. It is surrounded by five concentric spherical regions. The atoms immediately surrounding the defect are in the quantum mechanical domain and respond to the defect via quantum laws of physics. Surrounding this is a layer interfacing the quantum and classical regions of the system. The green region is the classical domain in which the atoms respond via classical laws of physics. The atoms in Region II are treated classically and are fixed in their ideal lattice positions. Region III is approximated as an infinite continuum.

For SiO_2 the energy of the quantum mechanical domain in Region I is determined using density functional theory with the hybrid B3LYP-x functional which is a modification of the B3LYP functional of Becke [111], Lee, Yang and Par [112]. In this modified functional x is the percentage of exact Hartree Fock electron exchange and $x = 32.5\%$. The wave functions of the Si and O atoms in this region are represented by the Gaussian 6-31G all electron basis set. In the classical domain of Region I the atoms are represented by the shell model as described in Section 4.2. The classical atoms in Region II are fixed in the ideal lattice positions of the bulk system in the

absence of the defect. This region exists to provide the atoms in Region I with the correct electric potential variation. The infinite polarisable continuum of Region III enables the determination of the polarisation energy of the infinite lattice due to the defect in Region I and, accounts for the consequent effect of this polarisation on the defect. It is treated the same way as the infinite region in the Mott-Littleton method as described in Section 4.6. The interactions between the classical atoms and the quantum-classical atomic interactions are modelled using a modified form of the Buckingham potential known as the BKS interatomic potential [113]. Using this potential the interaction energy between two atoms i and j is as follows:

$$U_{BKS}(r_{ij}) = \frac{q_i q_j}{r_{ij}} + A_{ij}\exp(-\beta_{ij} r_{ij}) - \frac{C_{ij}}{r_{ij}^6}$$

where q_i and q_j are the charges of atom i and j respectively and r_{ij} is the interatomic distance. A_{ij}, β_{ij} and C_{ij} are tunable parameters and the potential was fit to the fractional ionic charges of a silicon and oxygen ion, where $q^{Si} = 2.4\,e$ and $q^{O} = -1.2\,e$ respectively. These charges were determined from *ab initio* calculations of small SiO_2 clusters using the 6-31G* basis set. Therefore the effective charges of the atoms in Regions I and II depend on the parameters of the interatomic potential.

The atoms in the interfacial region are known as pseudo silicon atoms. The purpose of a pseudo-atom is to interact with both the quantum mechanical and classical regions of the system. The electronic structure of a regular Si atom is:

$$1s\,(\uparrow\downarrow)\ 2s\,(\uparrow\downarrow)\ 2p\,(\uparrow\downarrow)\,(\uparrow\downarrow)\,(\uparrow\downarrow)\ 3s\,(\uparrow\downarrow)\ 3p\,(\uparrow\,)\,(\uparrow\,)\,(\ \ )$$

In SiO_2 the Si atom undergoes hybridisation in which there is a mixing of the s and p orbitals. The electronic structure thus becomes:

$$1s\,(\uparrow\downarrow)\ 2s\,(\uparrow\downarrow)\ 2p\,(\uparrow\downarrow)\,(\uparrow\downarrow)\,(\uparrow\downarrow)\ 3s\,(\uparrow\,)\ 3p\,(\uparrow\,)\,(\uparrow\,)\,(\uparrow\,)$$

and there are four unpaired electrons available for bonding, each possessing a *sp* orbital. A single pseudo silicon atom, Si^* is coordinated to four oxygen atoms, one belonging to the quantum mechanical cluster and three from the surrounding classical lattice as a result Si* can be considered as $1/4$ quantum mechanical and $3/4$ classical as shown in Figure 4.6. Therefore to the quantum mechanical domain Si^* is essentially a one electron atom with a *sp* orbital and an effective charge $q^{Si^*} = +2.4\ |e|$ which is equal to the charge of a regular Si atom. However this charge exhibits a large un-natural attractive force towards the electrons in the cluster and as a result an effective

repulsive electrostatic potential is added to mimic the screening of the Si core potential by the valence electrons. This has the form:

$$U_{repulsive} = A \exp(-Bv)$$

The parameters of the potential are determined by applying the following three conditions to the system. In the first, the charge of the electrons is distributed evenly within the quantum mechanical cluster. In the second the Si^* do not contribute states in the band gap. The third condition is that the short range interaction between Si^* and its next nearest oxygen atom in the quantum mechanical cluster is modelled using a Morse potential which has the form:

$$U_{Morse}(r) = A([1 - \exp[-\alpha(r - r_0)]]^2 - 1)$$

Si^* interacts with the classical domain via the Coulomb and short range potential. The interaction between the Si^* electron and the classical cores and shells is included in the Fock matrix. The interactions between atoms in the interface is also modelled by the BKS potential.

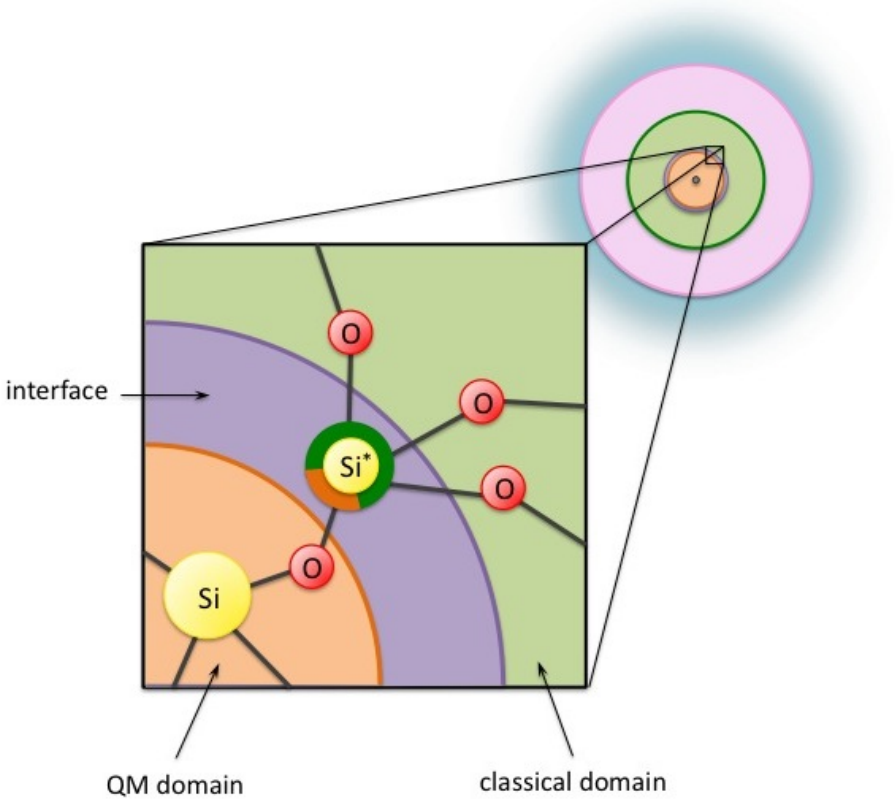

Figure 4.6: The Si^* pseudo-atom in the embedded cluster method.

4.11 Description of the Software Used in this Study

METADISE (Minimum Energy Techniques Applied to Dislocations, Interface and Surface Energies)

A code for the energy minimisation of 1D and 2D defects such as dislocations, surfaces and interfaces using classical methods.

MIDAS (Minimisation for Interfacial Defects and Surfaces)

A code developed for computer simulation of planar defects in ionic crystals. Using classical laws of physics the energy of planar defects with 2D periodicity can be determined.

GULP (General Utility Lattice Programme) Version 3.4

A materials simulation code using classical lattice dynamics to determine analytical solutions to 0D, 1D, 2D and 3D models. The capabilities of the code include energy minimisation, the determination of crystal and defect properties as well as transition states using the nudged elastic band method.

Gaussian 98

A code used to model the electronic structure of molecules and reactions using quantum mechanical laws of physics. It can be used to predict energy, structure and vibrational frequencies.

GUESS (Gaussians Used for Embedded System Studies)

This code enables embedded cluster calculations of point defects in ionic crystals. It provides an interface between quantum mechanical and atomistic simulation which are coupled using an embedding potential.

DL_POLY_2

A parallel molecular dynamics simulation package for the study of macromolecules, polymers and ionic systems of up to 30,000 atoms. The code utilises classical forcefields and periodic boundary conditions.

Part III

Presentation of Research

Chapter 5

Point Defects Near MgO Grain Boundaries

5.1 Introduction

Magnesium oxide has applications as a secondary electron emitter in plasma displays, as an insulator in magnetic tunnelling junctions and it is considered as a host for nuclear and transuranic waste. The presence of grain boundaries in this material is known to affect several material properties such as creep, and both thermal and electrical conductivity. Using tracer diffusion it has been found that the diffusion coefficient of impurities at grain boundaries is increased in comparison to that in bulk diffusion. Spectroscopic techniques have also shown increased impurity concentrations at grain boundaries in comparison to the bulk. Computer simulations have found that the activation energy for vacancy migration at MgO grain boundaries is lower than in the bulk material. In order to describe the macroscopic effects of grain boundaries it is important to understand the microscopic mechanisms involving grain boundaries.

An initial investigation was carried out to determine the best empirical pair potential to use for the study of bulk MgO. Atomistic simulation using static minimisation was then used to investigate the properties of point defects in MgO. For the purpose of calibration initial calculations were carried out to determine formation and activation energies for vacancies and interstitials in bulk MgO and for vacancies at the $\Sigma 17$ $\{410\}/[001]$ tilt grain boundary as these values can be compared to published experimental and theoretical work. The novelty of this work is the

calculation of formation energies for interstitials at the tilt grain boundary and for vacancies and interstitials at the Σ5 twist grain boundary. The corresponding configurations were used to determine the minimum energy paths and activation energies for vacancy and interstitial migrations using nudged elastic band calculations. Being an ionic solid, space charge theory applies to MgO grain boundaries. Since grain boundaries act as sinks for point defects the defect type with the lowest formation energy tends to migrate from the bulk and accumulate at the boundary. This forms a modified region of charge, known as the space charge layer, in the vicinity of the grain boundary which is of opposite charge to that accumulated. The concentration of defects at the grain boundary and its vicinity is dependent on the difference in formation energy of the defect at the grain boundary and that of the defect in the bulk. If for example, the anion (O^{-2}) vacancy has the lowest formation energy at the grain boundary then an accumulation of anion vacancies will exist at the grain boundary resulting in a space charge region of negative charge adjacent to the boundary. A potential difference will arise between the charges in the space charge layer and those at the grain boundary which opposes the migration of further anion vacancies to the grain boundary. This potential however facilitates the migration of cation vacancies to the grain boundary resulting in charge neutrality at the bulk in thermal equilibrium. The study of neutral defects such as Schottky and Frenkel defects is therefore of great importance.

5.2 Methods

5.2.1 Justification of the Pair Potential

From published literature it is apparent that a number of empirical pair potentials have been derived for MgO. These have been fit to different combinations of experimental observables and typically the highest quality potentials are those fit to the most observables. There is however no known literature indicating the optimum pair potential. In this study seven pair potentials, were investigated using the Mott-Littleton method, described in Chapter 4 Section 4.6, to determine properties of bulk MgO. These pair potentials are of Buckingham form:

$$U_{Buckingham}(r_{ij}) = A \exp\left(\frac{-r_{ij}}{\rho}\right) - \frac{C_6}{r_{ij}^6}$$

and permit polarisation via the shell model. The pair potentials were taken from the publications of Baram and Parker 1996 [114], Binks 1994 [115], Bush et al 1994 [116], Catlow 1988 [117,118], Lewis and Catlow A and B [59] and Sangster and Stoneham 1981 [119]. Their parameters are shown in

Table 5.1 along with the observable properties to which they were fit. The properties determined are lattice parameter, cohesive energy, elastic constants, bulk modulus, activation energy, longitudinal optical frequency and phonon dispersion curves. These values are given in Table 5.2 and Figure 5.1 shows the dispersion relations. A comparison is made to both experimental and other theoretical results.

It can be seen that all pair potentials reproduce the lattice parameter, cohesive energy and migration barrier reasonably well as these properties were used as fitting parameters. However the values for elastic constants, bulk modulus and longitudinal optical frequency deviate greatly from the published experimental values. The Lewis and Catlow B [59] and the Catlow [117, 118] potentials produced values for elastic constant and bulk modulus which have the best agreement with experiment. It is not surprising that the longitudinal optical frequency does not compare well to experiment since none of the pair potentials were fit to this property. However optical frequencies obtained using the Sangster and Stoneham [119] and Lewis and Catlow A [59] potential deviate the least from the experimental results and these two potentials were also found to produce dispersion relations with the least deviation to experiment. This investigation suggests that the Catlow [117, 118], Lewis and Catlow A [59], Lewis and Catlow B [59] and the Sangster and Stoneham [119] pair potentials are optimum pair potentials for calculating a range of MgO properties comparable to experiment.

5.2.2 Computational Methods and Properties Calculated

The empirical pair potential of Sangster and Stoneham [119] was used throughout this study along with the rigid ion model. The $\Sigma 17$ $\{410\}/[001]$ tilt grain boundary was generated using the METADISE [149] computer code. In forming this boundary two crystalline grains are misorientated with respect to each other by an angle of 28.1° about an axis parallel to the grain boundary. The tilt grain boundary structure was used to form a supercell containing 1344 ions with dimensions of 29.5 Å × 17.0 Å × 10.5 Å. Here the grain boundary plane is perpendicular to the x and y axes. The twist grain boundary was generated using the MIDAS code [150]. Here one crystalline grain was misorientated with respect to the other by an angle of 36.9° about an axis perpendicular to the grain boundary. At the twist grain boundary plane it was found [63] that a number of ions of the same species coincide forming anti coincident pairs resulting in a boundary with a high interfacial energy. In order to stabilise the twist boundary Schottky defects were added to the boundary plane removing the anti coincident pairs. By further optimising structure it was found that the ions at the grain boundary plane restructure forming a lattice of octagons and

Pair Potential	Mg $_{\text{core}}$- O$_{\text{shell}}$		O $_{\text{shell}}$- O$_{\text{shell}}$			Mg			O			Fit To (empirical properties)
	A	ρ	A	ρ	C	q_{core}	q_{shell}	k_{spring}	q_{core}	q_{shell}	k_{spring}	
	$[eV]$	$[\AA]$	$[eV]$	$[\AA]$	$[eV\,\AA^6]$	$[e]$	$[e]$	$[eV\,\AA^{-2}]$	$[e]$	$[e]$	$[eV\,\AA^{-2}]$	
Baram and Parker [114]	1428.5	0.2945	22764.0	0.149	27.88	2.0			0.869	-2.869	74.92	lattice parameter
Binks [115]	1284.38	0.2997	9547.96	0.2192	32.0	2.0			0.04	-2.04	6.3	lattice parameter
Bush [116]	2457.243	0.261	25.4	0.6937	32.32	1.58	0.42	349.95	0.513	-2.513	20.53	crystal structure relative permitivities elastic constants
Catlow [117, 118]	946.627	0.3181	22764.0	0.149	27.879	2.0			0.869	-2.869	74.92	-
Lewis and Catlow A [59]	1428.5	0.2945	22764.3	0.149	20.37	0.415	1.585	361.6	1.0	-3.0	54.76	elastic constant dielectric constant cohesive energy
Lewis and Catlow B [59]	821.6	0.3242	22764.3	0.149	20.37	2.0				-2.0	15.74	elastic constant dielectric constant cohesive energy
Sangster and Stoneham [119]	1275.2	0.3012	22764.3	0.149	20.37	2.0			0.8107	-2.8107	46.7725	dielectric constant

Table 5.1: The parameters of the empirical pair potentials of *Baram* [114], *Binks* [115], *Bush* [116], *Catlow* [117, 118], *Lewis and Catlow A* [59], *Lewis and Catlow B* [59] and *Sangster and Stoneham* [119].

Pair Potential	Lattice Parameter [Å]	Cohesive Energy [eV]	Elastic Constants [GPa]			Bulk Modulus [GPa]	Migration Barrier [eV]		LO Frequency [cm^{-1}]		
			C_{11}	C_{12}	C_{44}		Mg	O	(0.4 0.0 0.0)	(1.0 1.0 0.0)	(0.1 0.1 0.1)
Baram and Parker [114]	**4.199**	-41.31	392.91	164.19	164.19	240.43	2.15	2.15	723.15	416.05	810.18
Binks [115]	**4.212**	-41.16	373.94	171.47	171.47	238.96	2.09	2.14	644.85	292.82	406.02
Bush [116]	**4.20**	-41.00	**334.89**	**202.55**	**202.55**	246.66	1.9	1.89	639.69	344.55	576.10
Catlow [117,118]	4.242	-40.43	311.25	160.63	160.63	210.83	1.78	1.78	700.93	344.18	791.20
Lewis and Catlow A [59]	4.206	**-41.23**	**386.76**	**165.49**	**165.49**	239.25	2.10	2.14	695.26	410.23	739.43
Lewis and Catlow B [59]	4.219	**-40.47**	**291.19**	**167.41**	**167.41**	208.67	1.66	1.64	642.26	285.92	571.95
Sangster and Stoneham [119]	4.227	-40.91	361.27	163.03	163.03	229.11	2.02	2.04	682.50	390.74	717.73
Computational	4.195 [120]*	-41.0 [119]†	374.0 [119] †	157.0 [119]†	157.0 [119]†	146.0 [121]*	2.07 [122]†	2.11 [122]†	570.39 [59]†	360.25 [59]†	569.73 [59]†
			291.0 [123]*	91.0 [123]*	139.0 [123]*	161.6 [124]†	2.2 [125]†	2.1 [125]†	659.79 [59]†	455.98 [59]†	718.83 [59]†
							1.8 [125]†	1.3 [125]†			
							1.9 [125]†	2.0 [125]†			
							2.1 [126]†	2.4 [126]†			
							2.39 [127]*	2.48 [127]*			
Experiment	4.2 [128]	-40.4 [129]	289.0 [130]	88.0 [130]	155.0 [130]	162.6 [131]	2.76 [132]	2.71 [133]	661.12 [134]	443.31 [134]	724.83 [134]
	4.215 [120]	-40.8 [129]	348.0 [135]	85.7 [135]	167.8 [135]	161.6 [136]	1.56 [137]	2.61 [138]			
	4.19 [131]	-40.06 [139]	322.7 [140]	108.0 [140]	163.8 [140]		2.28 [141]	2.42 [142]			
			318.8 [143]	100.0 [143]	162.4 [143]			1.95 [144]			
			296.8 [145]	95.3 [145]	155.8 [145]			2.03 [146]			
			299.0 [147]	96.4 [147]	157.1 [147]						

Table 5.2: Properties determined using the *Baram* [114], *Binks* [115], *Bush* [116], *Catlow* [117,118], *Lewis and Catlow A* [59], *Lewis and Catlow B* [59] and *Sangster and Stoneham* [119] pair potentials. The values in bold text show the properties to which the potential was fit. Of the published computational results those labelled with * were obtained using *ab initio* methods whereas those labelled with † were produced using classical methods.

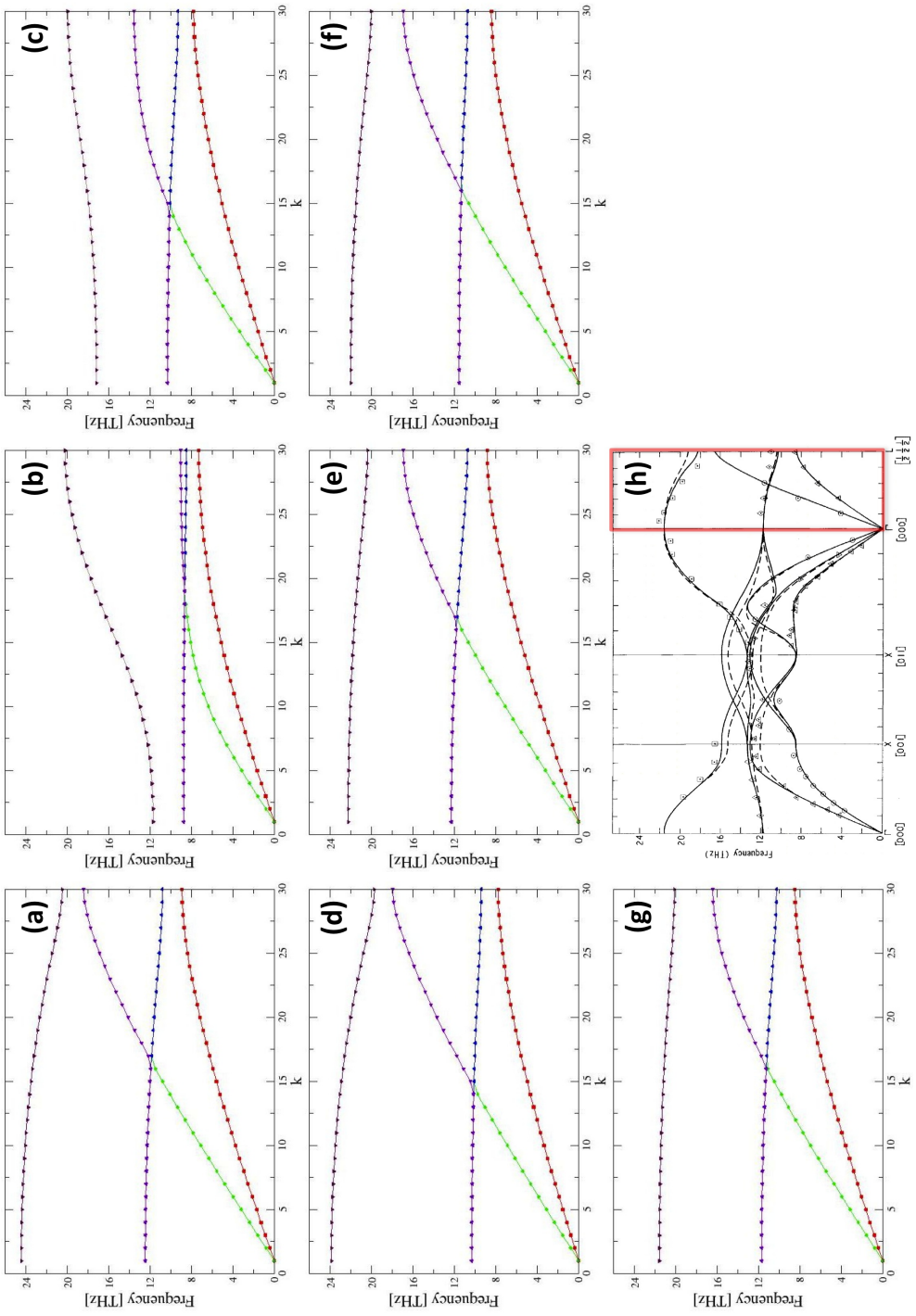

Figure 5.1: The dispersion relation (angular frequency as a function of wavenumber), in the range from the Γ point to the L point, calculated for bulk MgO using the interatomic pair potentials of (a) *Baram* [114], (b) *Binks* [115], (c) *Catlow* [117, 118], (d) *Lewis and Catlow A* [59], (e) *Lewis and Catlow B* [59] and (f) *Sangster and Stoneham* [119]. Subfigure (g) shows a published dispersion relation [134] obtained computationally using classical methods (solid and dashed lines) as well as from experiment [148] (symbols). The red box indicates the range $k = \Gamma$ to $k = L$.

squares. This structure was used to form a supercell comprising of 1584 ions with dimensions of 25.3 Å × 18.0 Å × 18.0 Å such that grain boundary planes are separated by 12 bulk-like planes. Both grain boundary supercells were relaxed using the constant temperature-constant stress, NST ensemble with Hoover thermostat and barostat relaxation times of 0.1 ps and 1.0 ps respectively. A simulation time of 100 ps was used with an equilibration time of 0.2 ps where one timestep equates to 0.001 ps. The interfacial energies were determined as 1.88 Jm^{-2} and 1.89 Jm^{-2} for the tilt and twist grain boundaries respectively. The tilt grain boundary interfacial energy compares well to the published value of 1.89 Jm^{-2} [64] determined for a {410}/[001] tilt grain boundary in NiO, which is isostructural to MgO. Whereas the twist grain boundary interfacial energy compares reasonably to the published value for the Σ5 twist grain boundary in NiO which was determined as 2.2 Jm^{-2} [64]. The difference in the values is due to the differences in the materials and the pair potentials used. Optimisation was carried out using the conjugate gradients optimiser, first using energy convergence with a tolerance of 2.5×10^{-4} eV followed by force convergence to within a tolerance of 1.66×10^{-13} N. This was done for the non-defective grain boundaries as well as for defective systems in which the grain boundary contained either a single vacancy or a single interstitial. The formation energy, E_f, was determined as the difference in energy between the defective system, E_{def}, and non defective system, E_{perf}:

$$E_f = E_{def} - E_{perf}$$

The nudged elastic band method implemented in DL_POLY_2 [151] was used to determine the minimum energy paths for vacancy and interstitial migration. A description of this method can be found in Chapter 4 Section 4.7. In these calculations the reaction path contains 13 images and a nudged elastic band spring force constant, $\mathbf{F}^{spr}$ of 5×10^{10} eV A^{-2} was used to couple adjacent images. The force of the images is optimised to within a tolerance of 1.66×10^{-13} N.

For the purpose of comparison an alternative method was used to determine the average activation energy, E_a, for a diffusing interstitial through the tilt grain boundary using the Arrhenius equation for diffusion:

$$D = D_0 \exp\left(\frac{-E_a}{k_B T}\right) \tag{5.1}$$

Here D is the diffusion coefficient, D_0 is the maximum diffusion coefficient at infinite temperature, k_B is the Boltzmann constant and T is temperature. This equation is often used to predict the dependance of the diffusion coefficient on temperature. By taking the natural logarithm of both

sides of the equation the following linear relationship is obtained:

$$\ln D = -\frac{E_A}{k_B}\frac{1}{T} + \ln D_0$$

Therefore if the diffusion coefficient is known then the activation energy can be determined from the gradient of the plot of $\ln D$ as a function $\frac{1}{T}$.

The diffusion coefficient can determined using the following Einstein relationship for the mean square displacement:

$$< r^2(t) >= 2dDt \tag{5.2}$$

here d is the spatial dimension and t is the time interval for the diffusion. The mean square displacement for the interstitial can be determined from the trajectory of an atom as follows:

$$< r_i^2(t) >=< |r_i(t) - r_i(0)|^2 > \tag{5.3}$$

where $r_i(t) - r_i(0)$ is a vector distance travelled by the atom in the time interval t. D is therefore determined from the gradient from the plot of $< r_i^2(t) >$.

The formation energy, minimum energy path and activation energy were also determined for vacancies and interstitials in bulk MgO, in order to make comparisons between the grain boundaries and the bulk. The bulk MgO supercell contains 1728 ions and has dimensions of 23.17 Å × 23.17 Å × 23.17 Å. The relative formation energy was determined as the difference in formation energy of the defect at the grain boundary, E_{f_GB}, and that of the defect in bulk MgO, E_{f_Bulk}:

$$E_{f\_Rel} = E_{f\_GB} - E_{f\_Bulk}$$

Vacancy formation energies were also used to determine the Schottky defect formation energy, $E_{Schottky}$. This is taken as the sum of the Mg vacancy formation energy, E_{vac_Mg}, and the O vacancy formation energy, E_{vac_O}, reduced by the cohesive energy, E_{coh}, of the non-defective system:

$$E_{Schottky} = E_{vac\_Mg} + E_{vac\_O} - E_{coh}$$

Here the cohesive energy is the energy of a single Mg-O unit in the system as follows:

$$E_{coh} = \frac{E_{total}}{n}$$

where E_{total} is the total energy of the non-defective system and n is the number of Mg-O units in the simulation cell. The Frenkel defect formation energy, $E_{Frenkel}$, is determined as the sum of the energy required to remove an ion from the lattice to infinity and generate a vacancy, E_{vac}, and the energy required to add an interstitial to the system from infinity, E_{int}:

$$E_{Frenkel} = E_{vac} + E_{int}$$

The bulk, tilt grain boundary and twist grain boundary supercells are shown in Figure 5.2, Figure 5.4 and Figure 5.4 respectively.

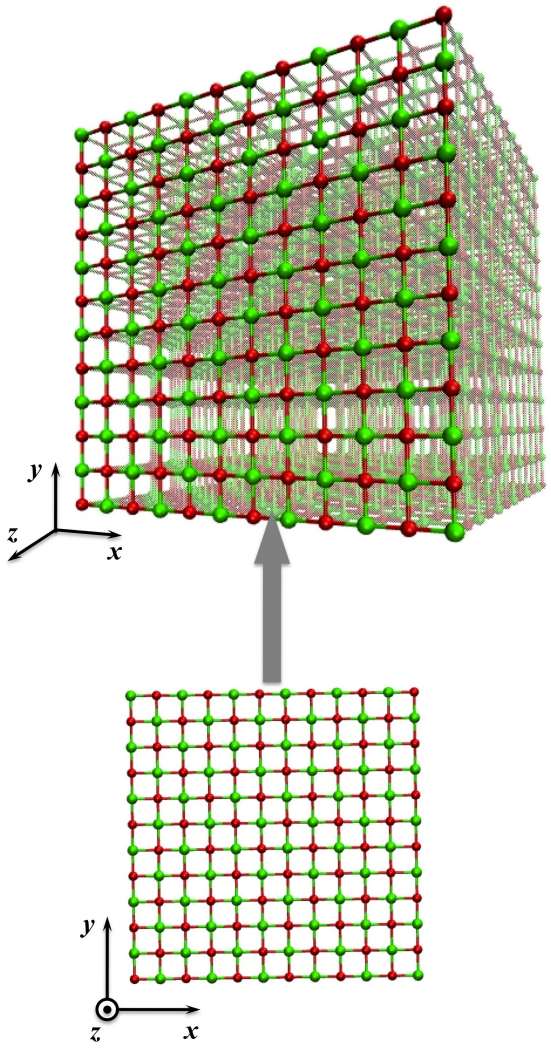

Figure 5.2: The bulk MgO supercell.

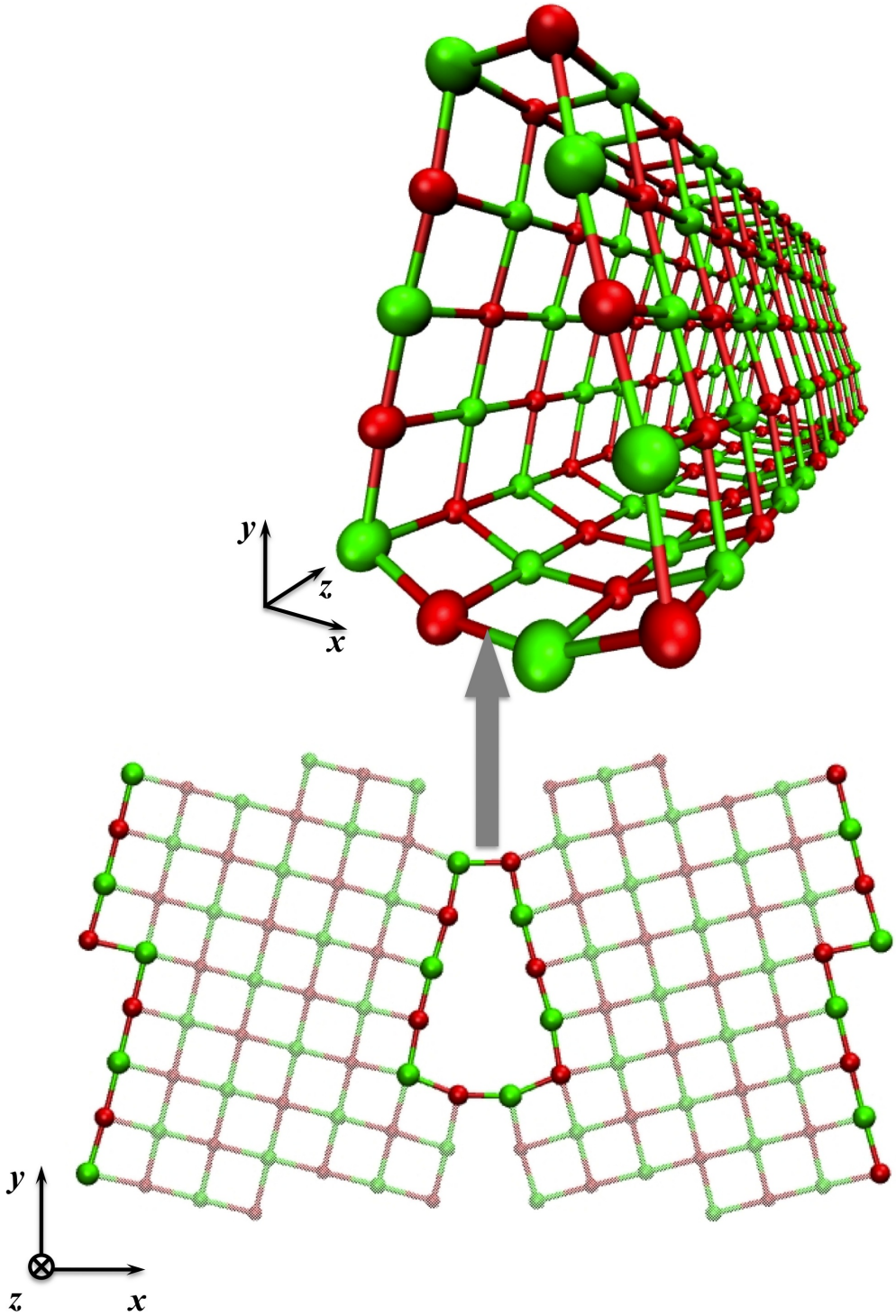

Figure 5.3: The tilt grain boundary supercell. For clarity the bulk-like ions and the outer grain boundary ions are not included in the upper image. The solid spheres represent the ions at the grain boundary whereas the translucent spheres represent the remaining lattice ions.

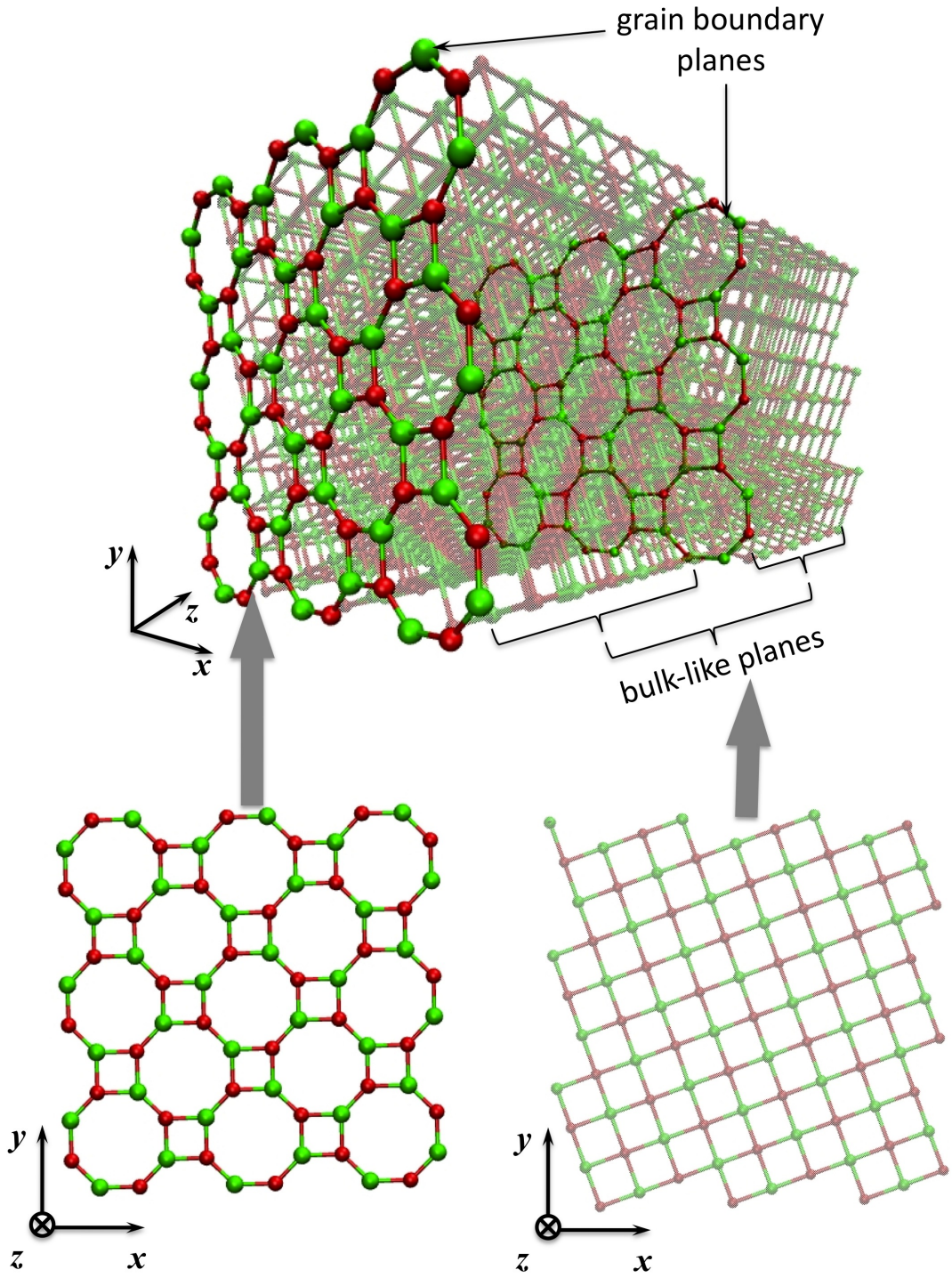

Figure 5.4: The twist grain boundary supercell. The solid spheres represent the ions at the grain boundary plane whereas the translucent spheres represent the remaining lattice ions.

5.3 Results and Discussion

5.3.1 Vacancies in Bulk MgO

The formation energy, E_f, of Mg and O vacancies in bulk MgO were determined as 23.89 eV and 24.41 eV respectively for the sites shown in Figure 5.5. Due to the periodicity of the model all vacancies of the same species are equivalent. It can be seen that the formation energies compare reasonably to published results [122] where the formation energies were determined as 24.0 eV and 24.7 eV for Mg and O vacancies respectively. The values differ due to the differences in the computational methods employed. Although the published result was also obtained using the Sangster and Stoneham pair potential, the shell model was used with the Mott-Littleton method whereas periodic boundary conditions are used with the rigid ion model in this study. When a vacancy is added to the bulk its nearest neighbour ions displace away from the vacancy site whereas the next nearest ions displace towards the vacancy. This is shown in Figure 5.6 for a Mg vacancy. Using the vacancy formation energies the Schottky defect formation energy was calculated as 7.39 eV. The minimum energy paths for vacancy migration and corresponding energy profiles are shown in Figures 5.7 and 5.8 for Mg and O vacancy migration respectively.

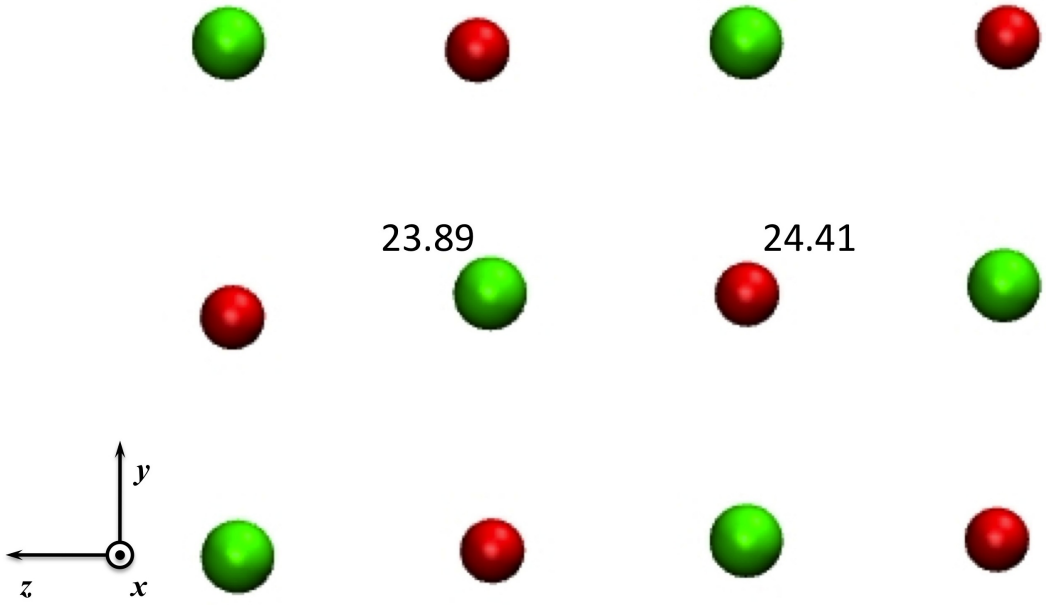

Figure 5.5: Mg (green spheres) and O (red spheres) vacancy sites in bulk MgO. The vacancy formation energies are given in units of eV. Due to the periodicity of the supercell all sites of the same species are equivalent.

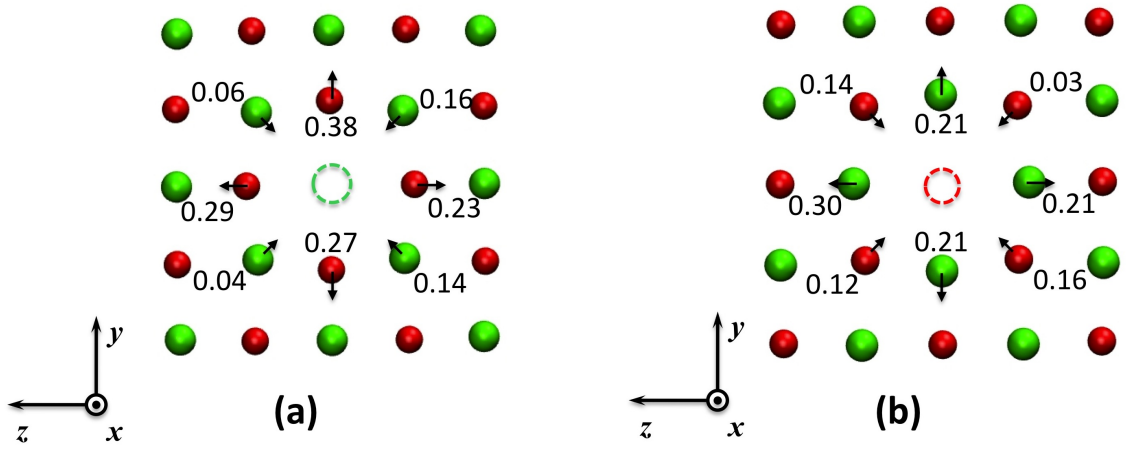

Figure 5.6: The relaxed (a) Mg and (b) O vacancy in bulk MgO. The dashed green and red circular outlines represent the Mg and O vacancy respectively. Upon relaxation the nearest ion neighbours exhibit the most displacement, directed away from the vacancy. The next nearest ions displace slightly towards the vacancy. The magnitude of the displacements are given in units of Å and the direction of the displacement is shown by the arrows.

It can be seen that since migration is between two equivalent sites the minimum energy path is a straight line and the energy profile is symmetric. The activation energies were determined as 2.08 eV and 2.05 eV for Mg and O vacancies respectively. These values compare reasonably to published results [122] of 2.07 eV and 2.11 eV for Mg and O vacancies respectively, which were determined using the same pair potential as this study, however the Mott-Littleton and shell model were used which can account for the difference in the values.

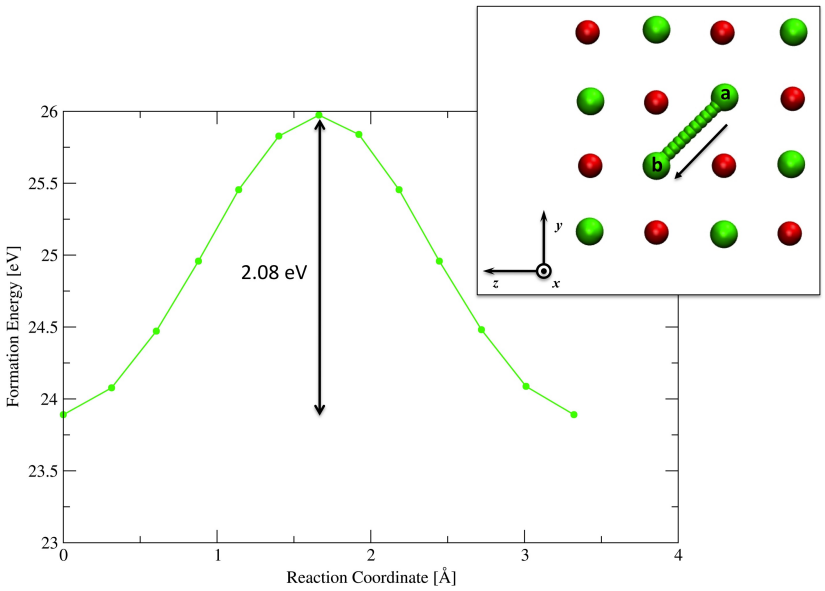

Figure 5.7: The energy profile, activation energy and inset the minimum energy path for a Mg vacancy migration from Site *a* to Site *b* in bulk MgO. The vacancy starts at Site *a*. The ion at *b* migrates towards the vacancy, as indicated by the arrow, and a vacancy is generated at Site *b*.

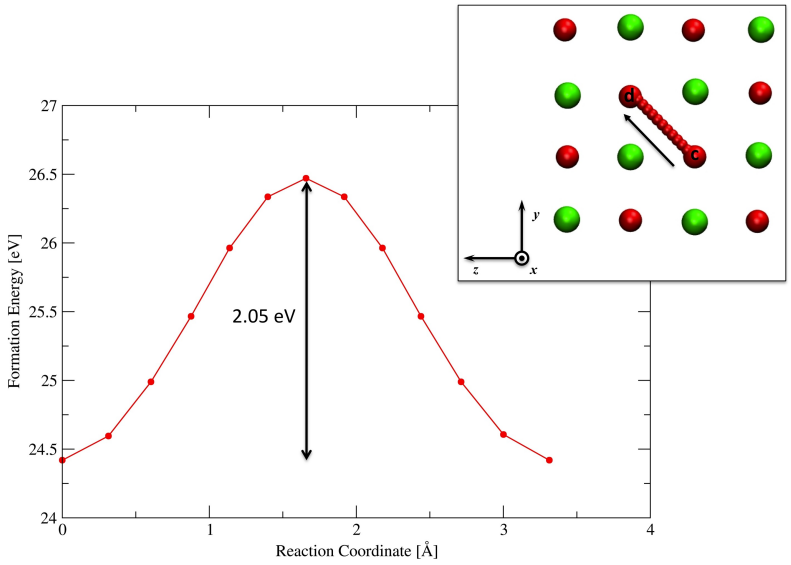

Figure 5.8: The energy profile, activation energy and inset the minimum energy path for O vacancy migration from Site *c* to Site *d* in bulk MgO. The vacancy starts at Site *c*. The ion at *d* migrates towards the vacancy, as indicated by the arrow, and a vacancy is generated at Site *d*.

5.3.2 Vacancies at the Tilt Grain Boundary

The formation energies were determined for vacancies at the tilt grain boundary and are shown in Figure 5.9. Due to the periodicity of the model all structural units are equivalent and have equivalent vacancy sites. Relative formation energies were determined for the vacancies as the difference in formation energy between the vacancy at the grain boundary and the vacancy in bulk MgO. For example, the Mg vacancy at Site *a* of the grain boundary has a formation energy of 23.32 eV which corresponds to a relative formation energy of -0.57 eV, since the formation energy of a Mg vacancy in bulk MgO is 23.89 eV. The vacancy sites at the tilt grain boundary are shown in Figure 5.9 along with their relative formation energies. It can be seen that Mg and O vacancies at Site *a* have the lowest formation energies, followed by Site *d*. Using the lowest vacancy formation energies the Schottky defect formation energy was determined as 5.82 eV which is lower than its analogue in bulk MgO by 0.95 eV. A qualitative comparison can be made to partial Schottky energies determined for the {410}/[001] tilt grain boundary by Harris et al [58]. Here the Sangster and Stoneham pair potential was also used with the rigid ion model and periodic boundary conditions. The findings in this work support the published results whereby vacancies at Site *a* have the lowest energies followed by vacancies at Site *d*.

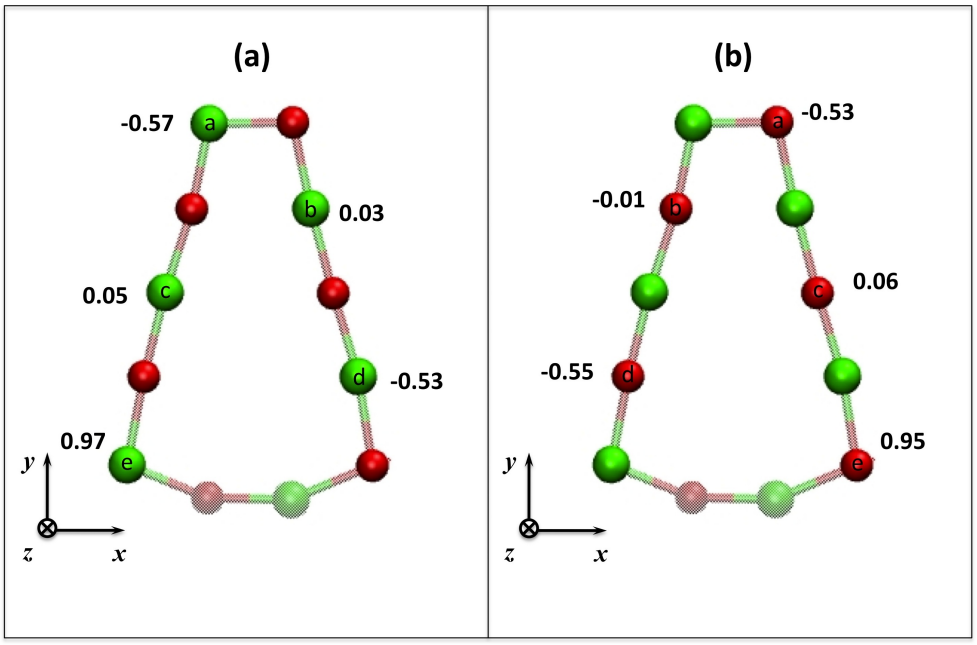

Figure 5.9: Relative formation energies, in units of eV, for (a) Mg and (b) O vacancies at the central *x*-*y* plane of the tilt grain boundary supercell.

The minimum energy paths for vacancy migration between two planes is shown in Figure 5.10 along with corresponding activation energies. It can be seen that the activation energy for both Mg and

O vacancy migration is lowest for migration from Site c to Site d. Here the activation energies were determined as 0.77 eV and 0.78 eV for an Mg and O vacancy respectively. These values compare well to the published results of Harris et al [58] who used molecular dynamics simulation with the addition of a small driving force on an ion adjacent to the vacancy. In this publication vacancy migration was also reported to have the lowest activation energy for migration from Site c to Site d with activation energies of 0.78 eV and 0.77 eV for Mg and O vacancy migration respectively. This is also consistent with published results for the position of the lowest activation energy for vacancy migration determined for the the $\{310\}/[001]$ NiO twist grain boundary [57, 152]. However the published activation energy for a Ni vacancy migration was determined as 1.86 eV which is much higher than the activation energy determined in this work for an Mg vacancy. This difference is mainly due to the method used to obtain the activation energy. Constrained minimisation was used for the published result in which the configurational space explored by the minimum energy path is limited. In the case of Mg and O vacancies, migration from Site c to Site d corresponds to diffusion towards one of the most stable vacancy sites. From Site d the vacancy will have the option to migrate back to Site c or to Site e, however these are not favourable as the formation energies at these sites are higher than those of vacancies in bulk MgO. Hence the corresponding activation energies are high and in the case of migration to Site e the activation energy for both Mg and O vacancies is higher than the respective vacancy analogue in bulk MgO. Therefore the vacancy will remain strongly bound to Site d. Vacancies at Site a are very stable and the activation energies for migrations between these sites are 1.32 eV and 1.35 eV for Mg and O vacancies respectively. Due to the equivalence of the sites the forward and backwards barriers are equal. A fast diffusion pathway can be considered to exist if a defect can diffuse in a particular direction via migration between metastable sites whereby the energy of the forward barrier for each migration is the lower than the corresponding reverse barrier. Fast diffusion pathways exist for vacancies at the MgO tilt grain boundary involving migration between equivalent a sites in the close packed region of the boundary.

These results show that the activation energy for vacancy migration can be lower than that in bulk MgO and indicates that the presence of the grain boundary lowers the activation energy for vacancy migration. Despite the nudged elastic band parameters trialled the minimum energy path between sites labelled e and f could not be determined for both Mg and O vacancies due to kinks in the nudged elastic band chain. These occur when the force perpendicular to the chain is larger than the perpendicular restoring force and the chain does not converge to the minimum energy path. This could be due to the instability of Site e where the relative vacancy formation energies were determined as 0.98 eV and 0.95 eV for Mg and O vacancies respectively.

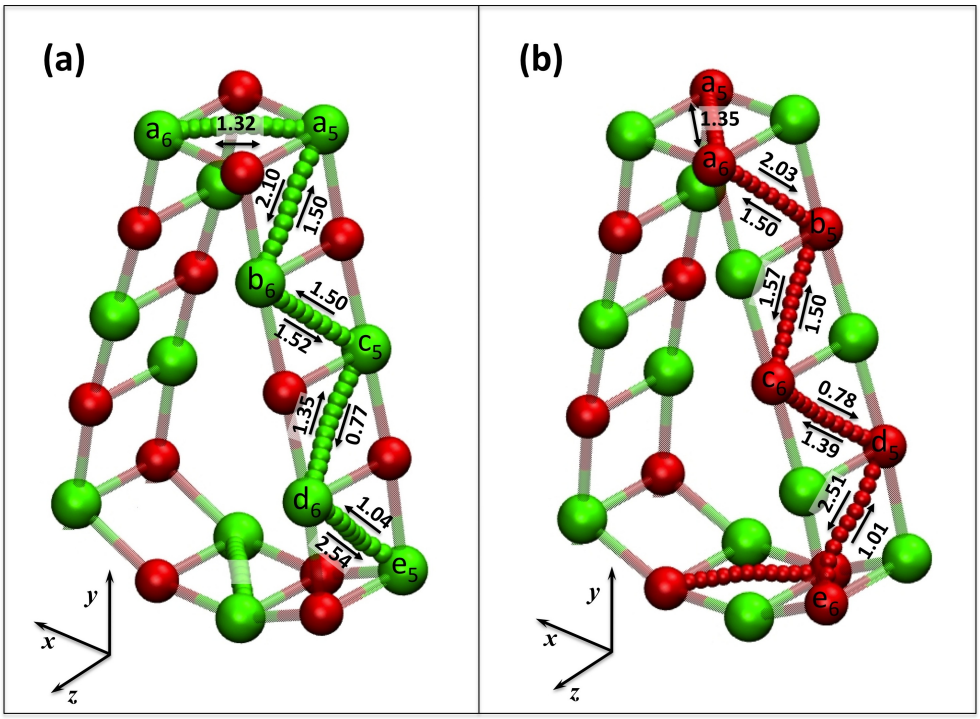

Figure 5.10: Minimum energy paths and activation energies, in units of eV, for (a) Mg and (b) O vacancy migration at the tilt grain boundary. The arrows indicate the direction of the vacancy migration.

From Figure 5.10 it can also be seen that the minimum energy paths are not straight lines and that they tend to curve towards the grain boundary space. The deviation of the path was determined as the distance between the saddle point of the minimum energy path and the mid-point of the straight line connecting the start and end points of the path. These deviations are shown in Table 5.3. In agreement with Harris et al [58] it was found that the minimum energy paths are not straight lines and curve into the grain boundary space. It can be seen that the lowest deviations occur for migrations at the close-packed region of the grain boundary structural unit and were determined as 0.080 Å for Mg vacancy migration from Site *a* to Site *b* and 0.065 for O vacancy migration from Site *b* to Site *c*. The largest deviation occurs for the migration of a vacancy from Site *c* to Site *d* which was determined as 0.238 Å and 0.125 Å for Mg and O vacancies respectively. Mg vacancy migration between two *a* sites was found to have a deviation of 0.104 Å which compares well to the published value [58] of 0.1 Å.

Migration Path	Deviation [Å]	
	Mg Vacancy	O Vacancy
$a \leftrightarrow a$	0.104	0.100
$a \leftrightarrow b$	0.080	0.079
$b \leftrightarrow c$	0.084	0.065
$c \leftrightarrow d$	0.238	0.125
$d \leftrightarrow e$	0.226	0.102

Table 5.3: The deviation of the minimum energy paths for vacancy migration from the mid-point of straight line connecting the start and end points of the path.

5.3.3 Vacancies at the Twist Grain Boundary

Relative formation energies were determined for vacancies at the grain boundary plane and at the adjacent bulk-like planes. These are shown in Figure 5.11. It can be seen that Mg and O vacancies have the lowest formation energy when they are located in the bulk-like plane as opposed to at the grain boundary plane and that these vacancies have lower formation energies than in bulk MgO. This occurs because the bulk-like planes are more dense and resemble the stable structure of bulk MgO and ions from this plane have the ability to relax into the space of the adjacent grain boundary plane. Using the lowest vacancy formation energies the Schottky formation energy was determined as 6.44 eV which is 0.95 eV lower than its bulk MgO analogue.

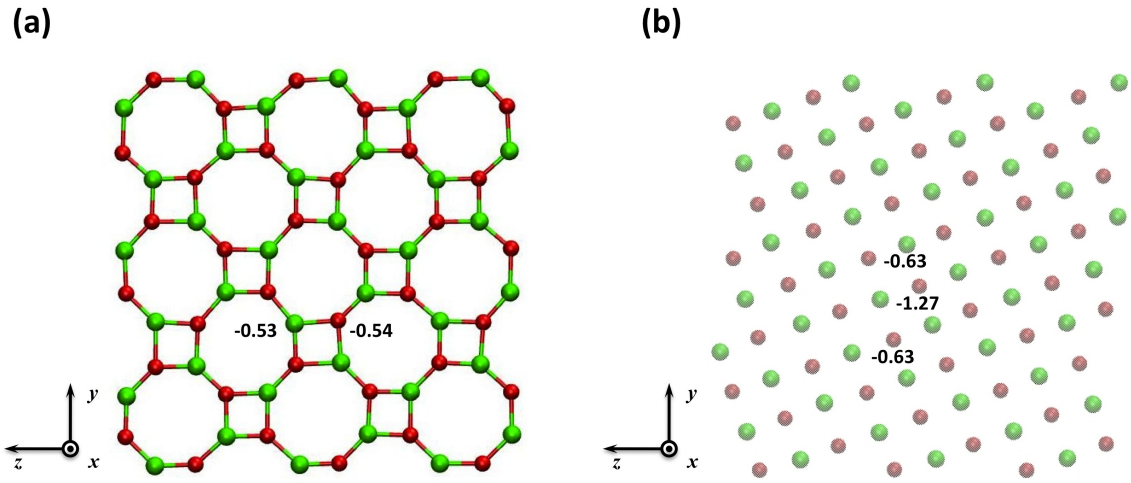

Figure 5.11: Mg and O vacancy sites and corresponding relative vacancy formation energies, in units of eV, at (a) the twist grain boundary (solid spheres) and (b) at one of the adjacent bulk-like planes (transparent spheres).

It was found that migrations only involving sites at the grain boundary plane and migrations only involving sites in the adjacent bulk-like plane have higher activation energies than those in bulk MgO. The lowest activation energies were determined for migrations involving both the grain

boundary plane and bulk-like plane sites, and that these activation energies are lower than their bulk analogues. These activation energies are shown in Figure 5.12 and Figure 5.13. It can be seen that the lowest Mg activation energy was determined as 0.70 eV for a migration from Site b to Site i which is 1.38 eV lower than that in bulk MgO. From Site i the vacancy can then migrate to Site n if the activation energy of 1.13 eV can be overcome. For an O vacancy the lowest activation was determined as 0.72 eV for migration from Site d to Site j. From Site j the activation energy for migration to Site q is 1.05 eV which is still lower than the activation energy for the migration of an O vacancy in bulk MgO. These results suggest that a fast diffusion path can occur at the grain boundary whereby a vacancy can migrate by zig-zagging between the grain boundary plane and an adjacent bulk-like plane.

For these low energy pathways it was found that the paths curve towards the centre of the grain boundary octagon associated with the vacancy sites involved. The deviation of the curves from the straight line connecting the initial and final points of the paths are shown in Table 5.4. It can be seen that these deviations range from 0.118 Å to 0.462 Å and 0.125 Å to 0.464 Å for Mg and O vacancy migrations respectively.

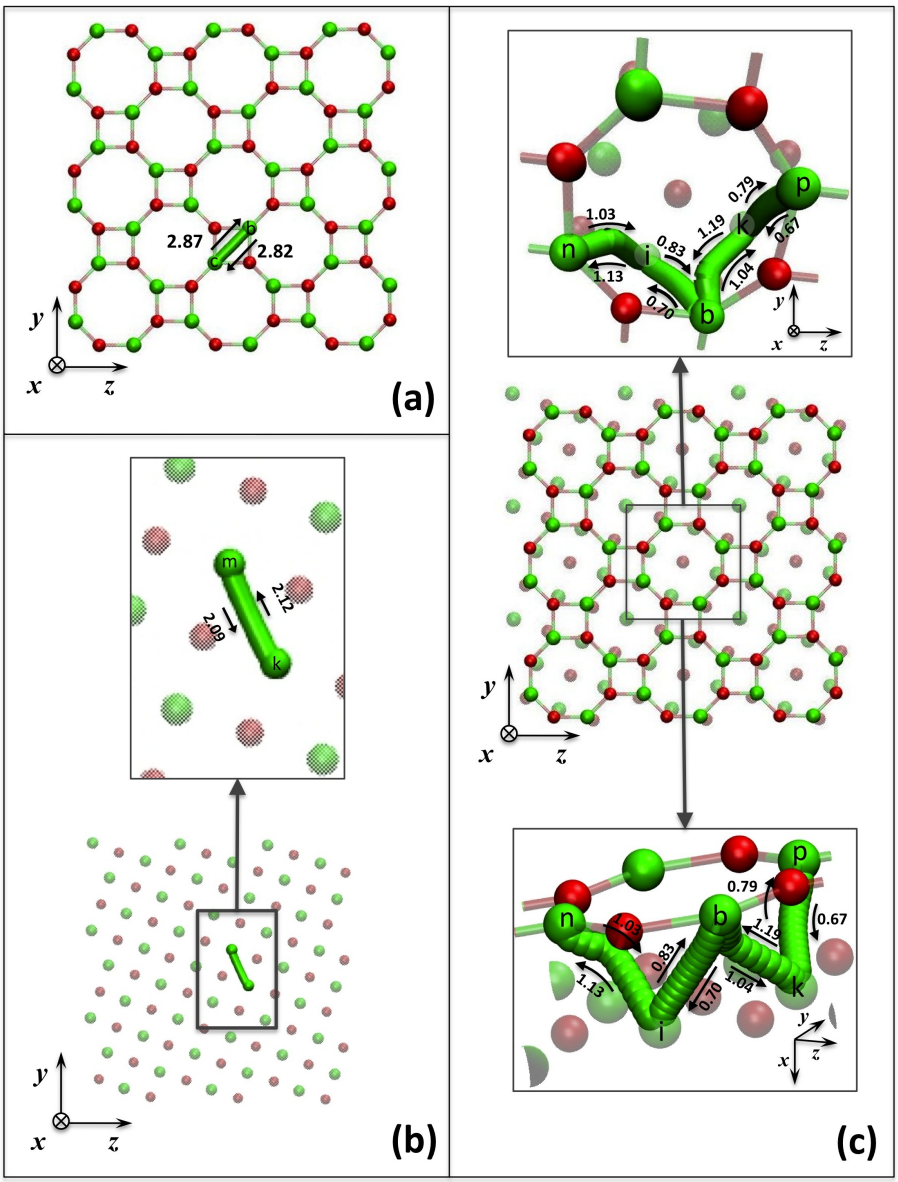

Figure 5.12: The minimum energy paths and activation energies, in units of eV, for Mg vacancy migration in the twist grain boundary. At (a) the grain boundary plane, (b) the bulk-like plane and (c) between the grain boundary and bulk-like plane (inset).

5.3.4 Interstitials in Bulk MgO

Figure 5.14 shows the stable sites and corresponding interstitial formation energies for Mg and O interstitials in the bulk MgO supercell which were determined as -11.70 eV and -12.56 eV respectively. Using these values the corresponding Frenkel defect formation energy is 11.85 eV. The lowest activation energy was found to occur when the interstitial migrates via the interstitialcy mechanism. Here an interstitial moves towards a lattice site whilst the ion at the lattice site

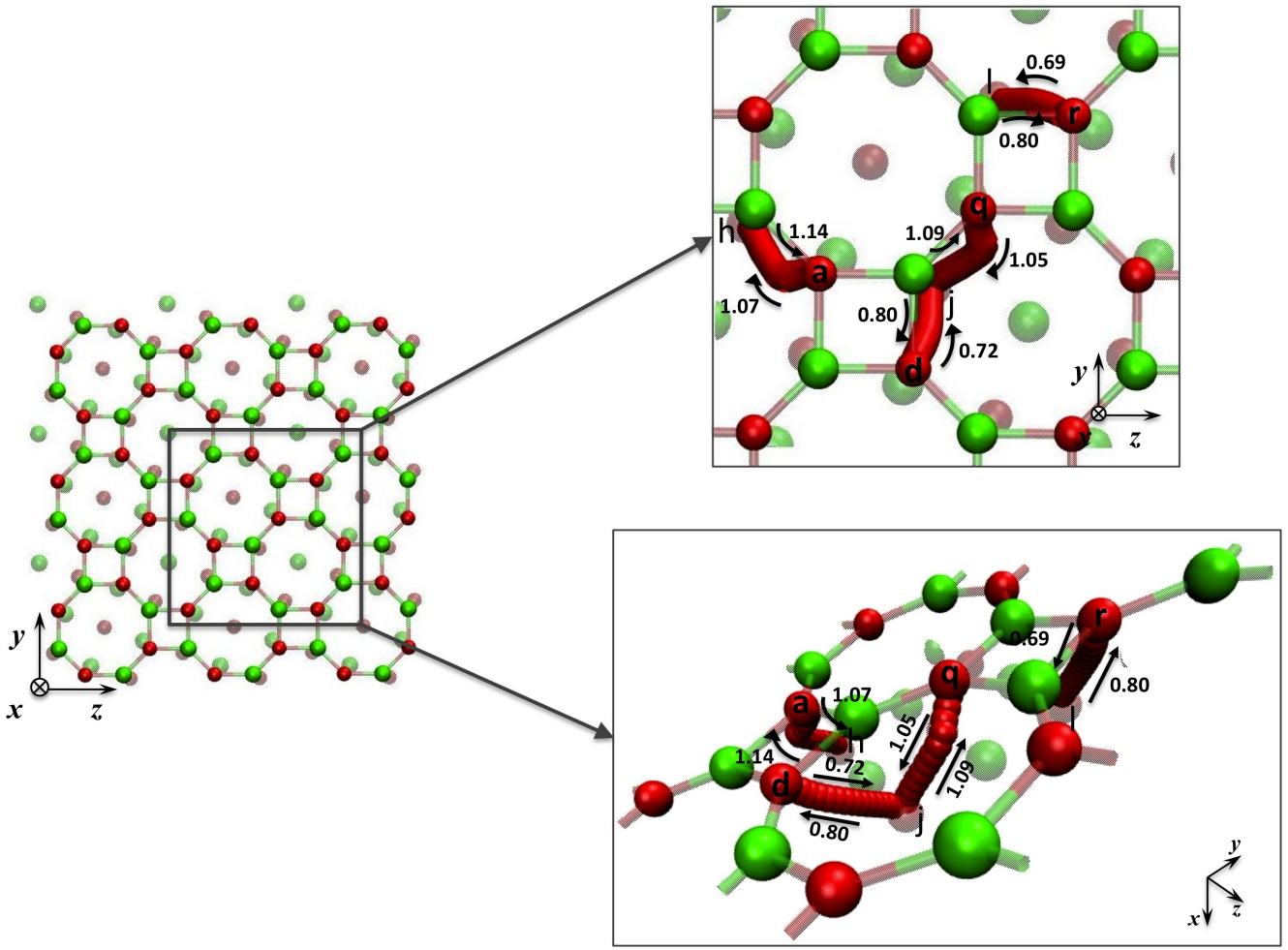

Figure 5.13: The minimum energy paths and activation energies, in units of eV, for O vacancy migration in the twist grain boundary. At (a) the grain boundary plane, (b) the bulk-like plane and (c) between the grain boundary and bulk-like plane (inset).

(a)

Mg Vacancy	
Migration Path	Deviation [Å]
$b \leftrightarrow c$	0.170
$b \leftrightarrow i$	0.122
$k \leftrightarrow m$	0.195
$i \leftrightarrow n$	0.458
$k \leftrightarrow p$	0.118

(b)

O Vacancy	
Migration Path	Deviation [Å]
$a \leftrightarrow h$	0.464
$d \leftrightarrow j$	0.130
$j \leftrightarrow q$	0.461
$l \leftrightarrow r$	0.125

Table 5.4: The deviation of the minimum energy path from the straight line between the initial and final positions of the vacancy for (a) Mg and (b) O vacancy migration in the twist grain boundary.

moves concurrently towards an interstitial site. This mechanism is also shown in Figure 5.14. The activation energies were determined as 0.35 eV and 0.39 eV for Mg and O interstitial migration respectively. These compare well to published values of 0.32 eV and 0.40 eV for Mg and O interstitial migration respectively [153] which were determined using the Mott Littleton method with static minimisation, and 0.54 eV [154] for O interstitial migration [153] which was determined using density functional theory with periodic boundary conditions.

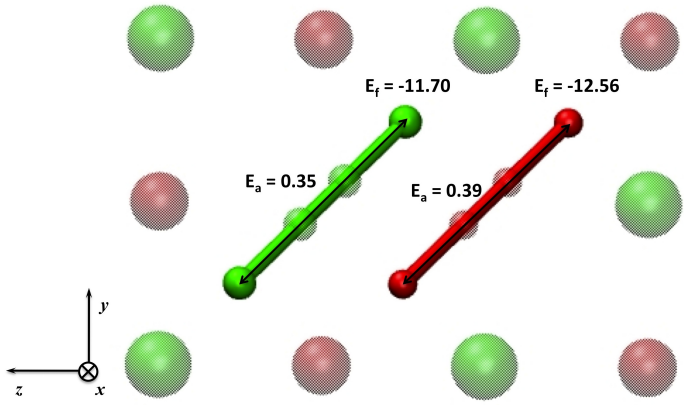

Figure 5.14: Stable Mg and O interstitial sites and their minimum energy paths for migration in bulk MgO. Interstitials migrate via the interstitialcy mechanism. The large translucent red and green spheres represent the bulk MgO lattice and the smaller solid spheres depict the interstitials. The small translucent spheres show the dumbell configurations in the middle of the path. The formation energy, E_f, and activation energy, E_a, are given in units of eV.

5.3.5 Interstitials in the Tilt Grain Boundary

Interstitials were placed at various sites within a grain boundary structural unit and upon structural optimisation it was found that both Mg and O interstitials relax to four distinct metastable sites. These sites will be referred to as *top*, *middle*, *planar* and *bottom* and are shown in Figure 5.15 for different orientations of the grain boundary. The relative interstitial formation energies for Mg and

O interstitials are shown in Figure 5.16. It can be seen that interstitials in the grain boundary are much more stable than their bulk MgO analogues. Mg and O interstitial formation energies are respectively 4.42 eV to 4.76 eV and 3.75 eV to 4.49 eV lower in the grain boundary than in bulk MgO. The *top* interstitial site is the most stable location for both Mg and O interstitials. Using these formation energies the Frenkel defect formation energy is determined as 6.21 eV which is 5.64 eV lower in energy than its bulk MgO analogue.

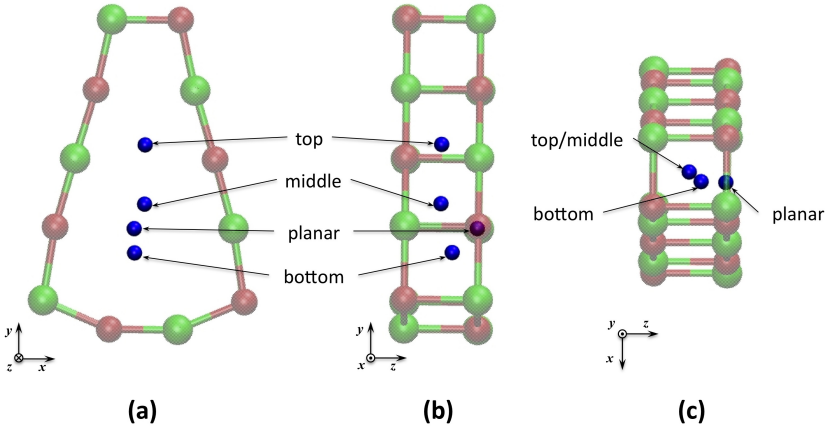

Figure 5.15: Metastable interstitial sites in the tilt grain boundary.

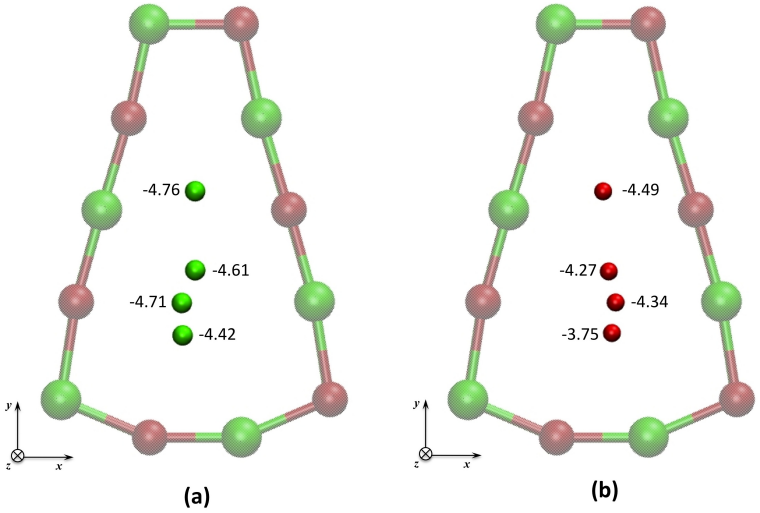

Figure 5.16: Relative formation energies, in units of eV, for (a) Mg and (b) O interstitial sites in the tilt grain boundary.

By determining the minimum energy paths it was found that interstitials can migrate between sites in one region, such as in the *top*, *middle* and bottom regions. It was also found that migrations can occur between sites in different regions, such as from *middle* to *planar*, *top* to *planar* as well as *bottom* to *planar* sites. These are shown in Figure 5.17. For an Mg interstitial the lowest activation energy was determined as 0.54 eV for migration between a *planar* and *bottom* site which

is 0.19 eV higher than Mg interstitial migration in bulk MgO, whereas for the O interstitial the lowest activation was found to be 0.22 eV for migration between two *bottom* sites. Although these interstitial sites are more stable than Mg and O interstitials in bulk MgO the *planar* and *bottom* sites involved in these migrations also have the highest formation energies in comparison to the other metastable interstitial sites determined in the grain boundary. This suggests that a fast diffusion pathway does not exist involving these sites. The low activation energies are due to a flat potential energy landscape arising from the large distance between the interstitial site and its nearest lattice ion neighbours. The interstitial therefore has less interaction with the lattice resulting in a smaller activation energy. A fast diffusion pathway may however occur for Mg and O interstitial migration between two *middle* sites however the activation energy is higher than that in bulk MgO therefore bulk migration is more favourable. Migrations between stable *top* sites were found to have the highest activation energies, these were determined as 1.33 eV and 1.34 eV for Mg and O interstitials respectively. These are higher than Mg and O interstitial migration in bulk MgO. This suggests that interstitials at these sites are so bound to the system that migration is unfavourable.

Determination of the Activation Energy for Interstitial Migration in the Tilt Grain Boundary Using the Arrhenius Equation

An interstitial was placed in the grain boundary and a molecular dynamics simulation was run for 500 ps using the NVT ensemble. This was done for temperatures ranging from 300 - 3000 K. The interstitial diffused randomly through the grain boundary and a Fortran 90 program was used to determine the mean square displacement of the interstitial trajectory in the z- direction, hence for Equation 5.2 d=1. Time intervals in the range 2 - 10 ps were used and the plots of mean square displacement are shown in Figure 5.18 for Mg and O interstitial diffusion.

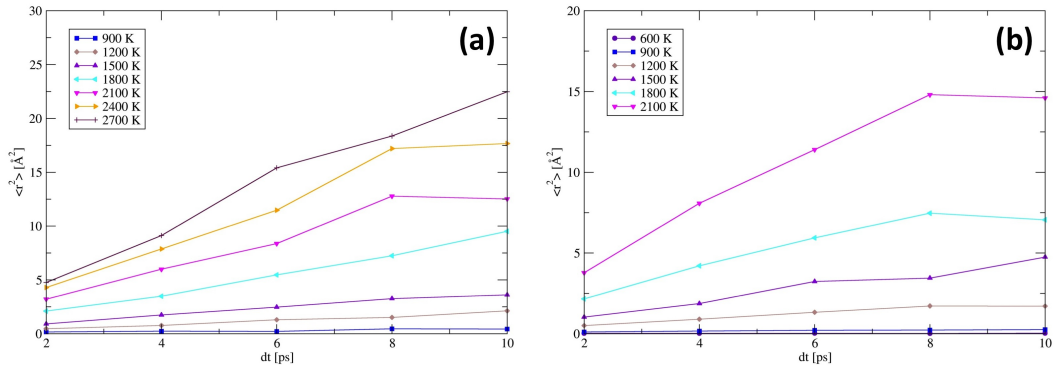

Figure 5.18: The mean square displacement as a function of time interval for (a) Mg and (b) O interstitial migration in the tilt grain boundary.

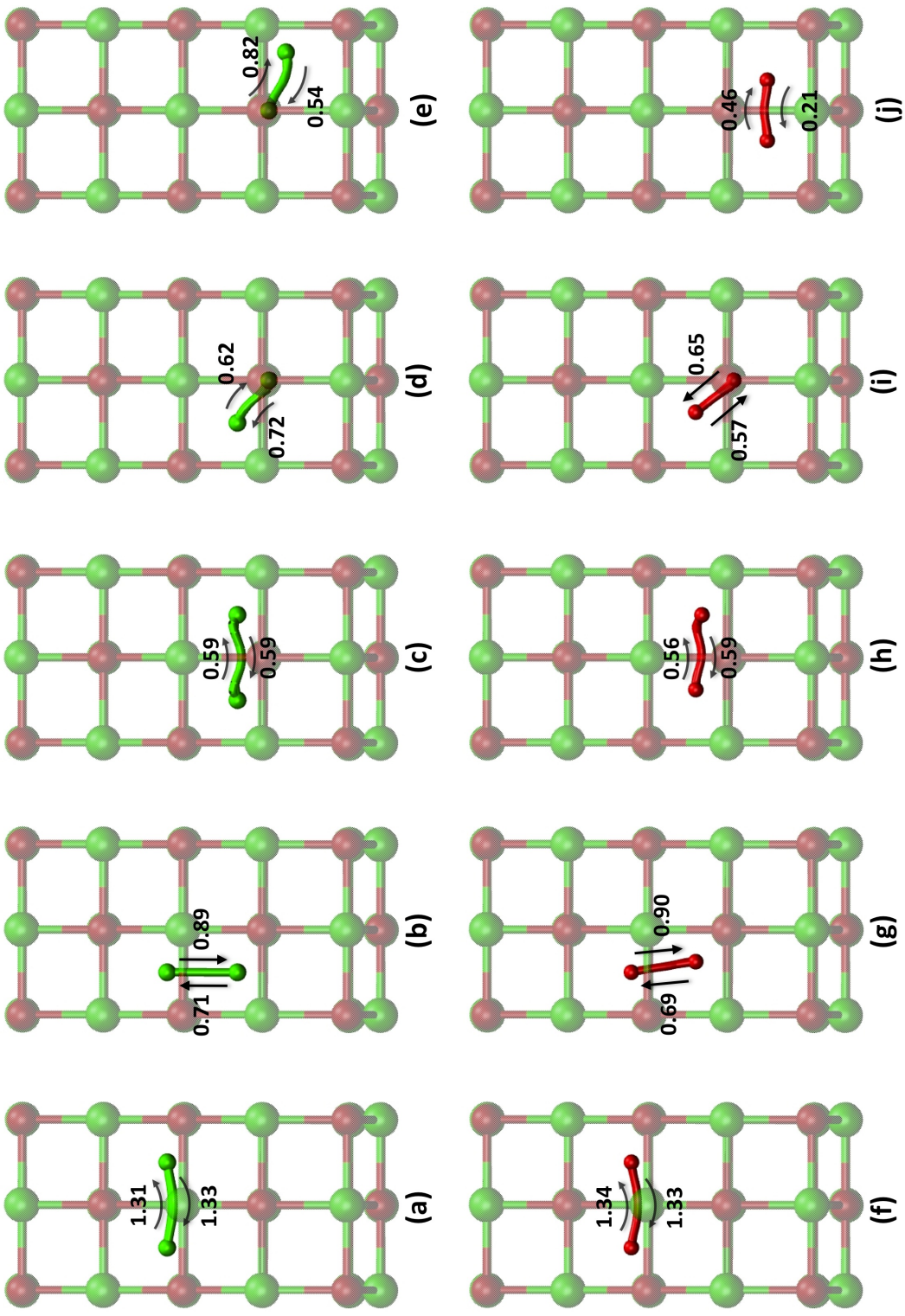

Figure 5.17: The minimum energy paths and activation energies, in units of eV, for interstitial migrations in the tilt grain boundary.

The natural logarithm of the diffusion coefficient was plotted as a function of inverse temperature as shown in Figure 5.19. From the gradients of the linear regression the activation energies were determined as 0.57 eV and 0.63 eV for Mg and O interstitials respectively. These values are within the range of those determined for Mg and O interstitial migration in the grain boundary using the nudged elastic band method which are 0.54 - 1.33 eV and 0.21 - 1.34 eV respectively.

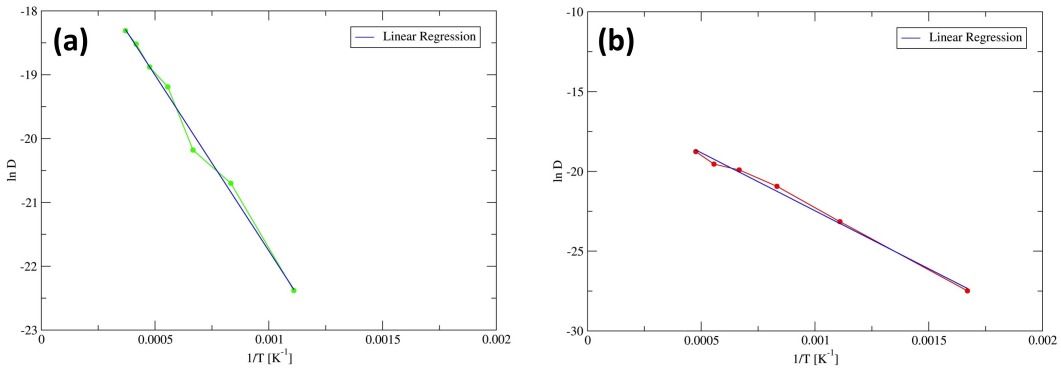

Figure 5.19: The natural logarithm of the diffusion coefficient as a function of inverse temperature for (a) Mg and (b) O interstitial migration in the tilt grain boundary.

5.3.6 Interstitials in the Twist Grain Boundary

The relative formation energies were determined for interstitial sites in the twist grain boundary as shown in Figure 5.20, Figure 5.21 and Figure 5.22. It can be seen that the formation energies are lower for interstitials at the grain boundary than in bulk MgO and that both Mg and O interstitials are most stable when located in the grain boundary plane at the centre of an octagon. A metastable interstitial site can also occur in the dumbell configuration whereby the presence of the interstitial within an octagonal space causes a lattice ion to displace into the space of an adjacent octagon, as shown in Figure 5.22.

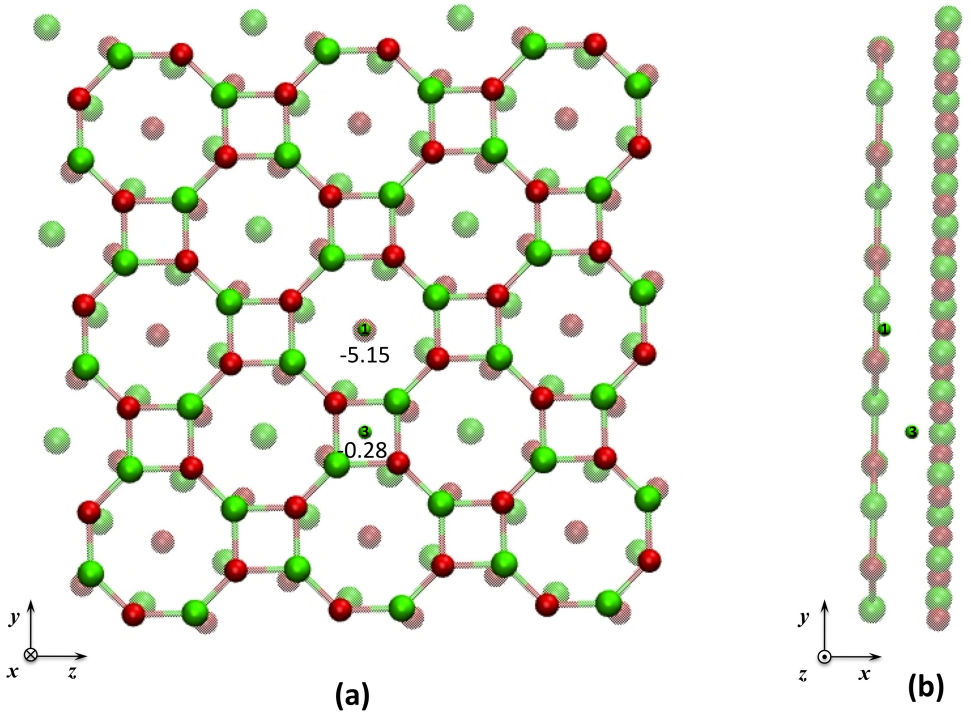

Figure 5.20: Mg interstitial sites in the twist grain boundary as seen from (a) the y-z plane and (b) from the x-y plane. The corresponding relative formation energies are also given, in units of eV, and were determined with respect to the formation energy of the interstitial in bulk MgO.

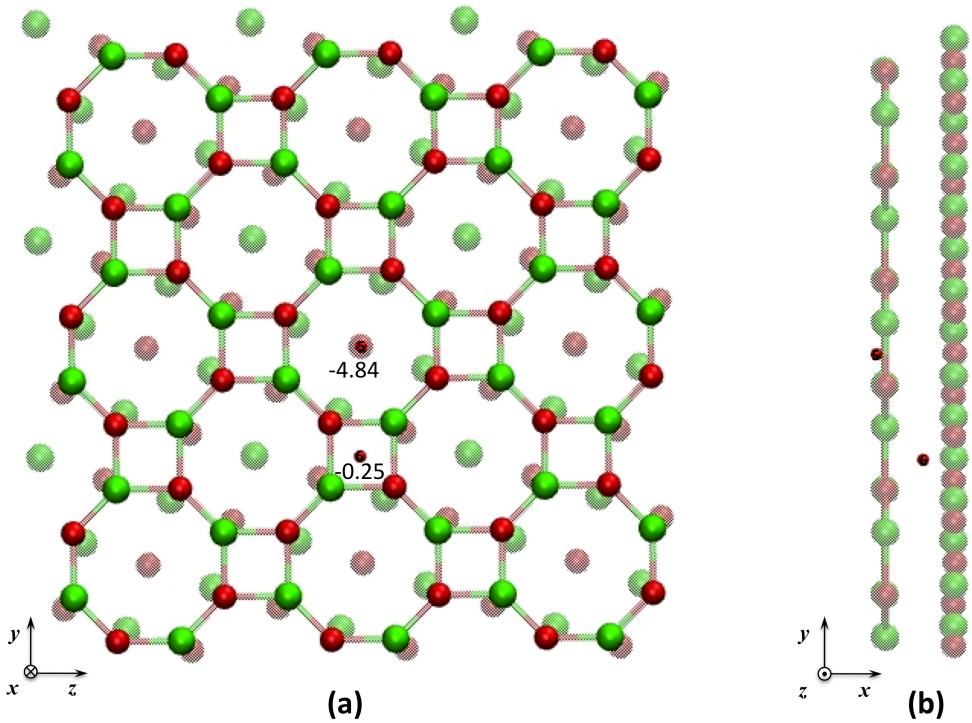

Figure 5.21: O interstitial sites in the twist grain boundary as seen from (a) the y-z plane and (b) from the x-y plane. The corresponding relative formation energies are also given, in units of eV, and were determined with respect to the formation energy of the interstitial in bulk MgO.

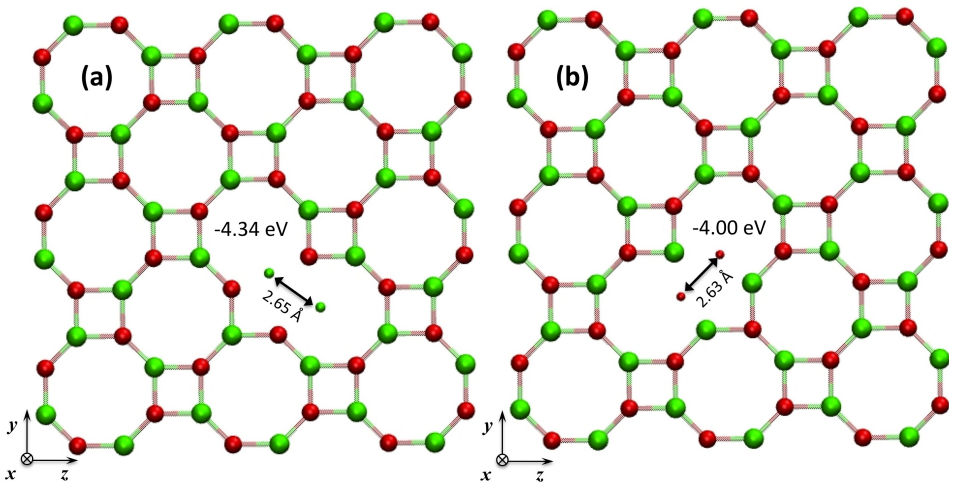

Figure 5.22: Metastable (a) Mg and (b) O interstitial dumbell sites. The dumbell configuration occurs when an interstitial within one of the octagons at the grain boundary plane strongly interacts with a lattice ion causing it to displace into an adjacent octagon. The relative formation energy, in units of eV, and the distance, in Å, between the two ions forming the dumbell are also included.

Minimum energy paths and activation energies were determined for migration between interstitial sites located at the centre of octagons in the grain boundary plane, these are shown in Figure 5.23 and the corresponding energy profile for the Mg interstitial migration is shown in Figure 5.24. It can be seen that migration of the interstitial from the dumbell configuration to a site in the centre of the octagon corresponds to migration towards the most stable interstitial site at the twist grain boundary. The reverse barrier has a higher activation energy than that determined for the interstitialcy mechanism in bulk MgO. This suggests that there is not a fast diffusion pathway for interstitials at the twist grain boundary.

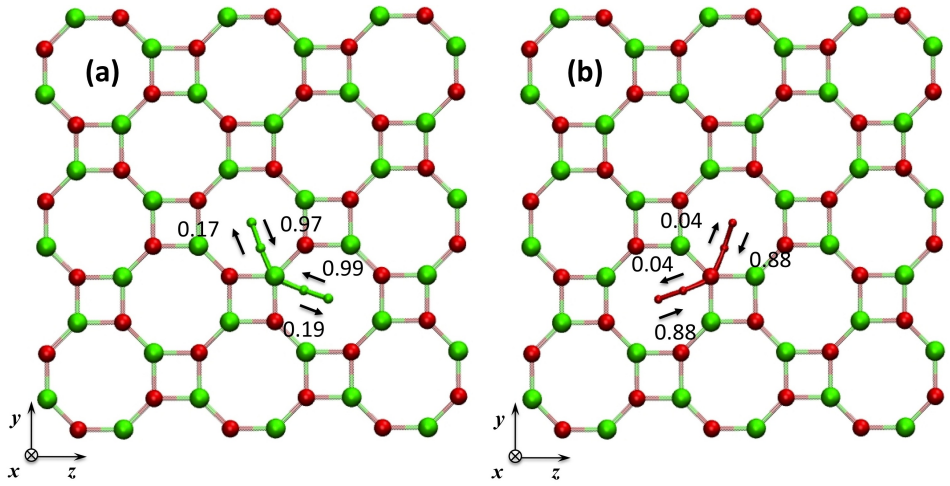

Figure 5.23: Minimum energy paths and corresponding activation energies, in units of eV, for (a) Mg and (b) O interstitial migration. The arrows indicate the the direction in which the migration has the lowest energy.

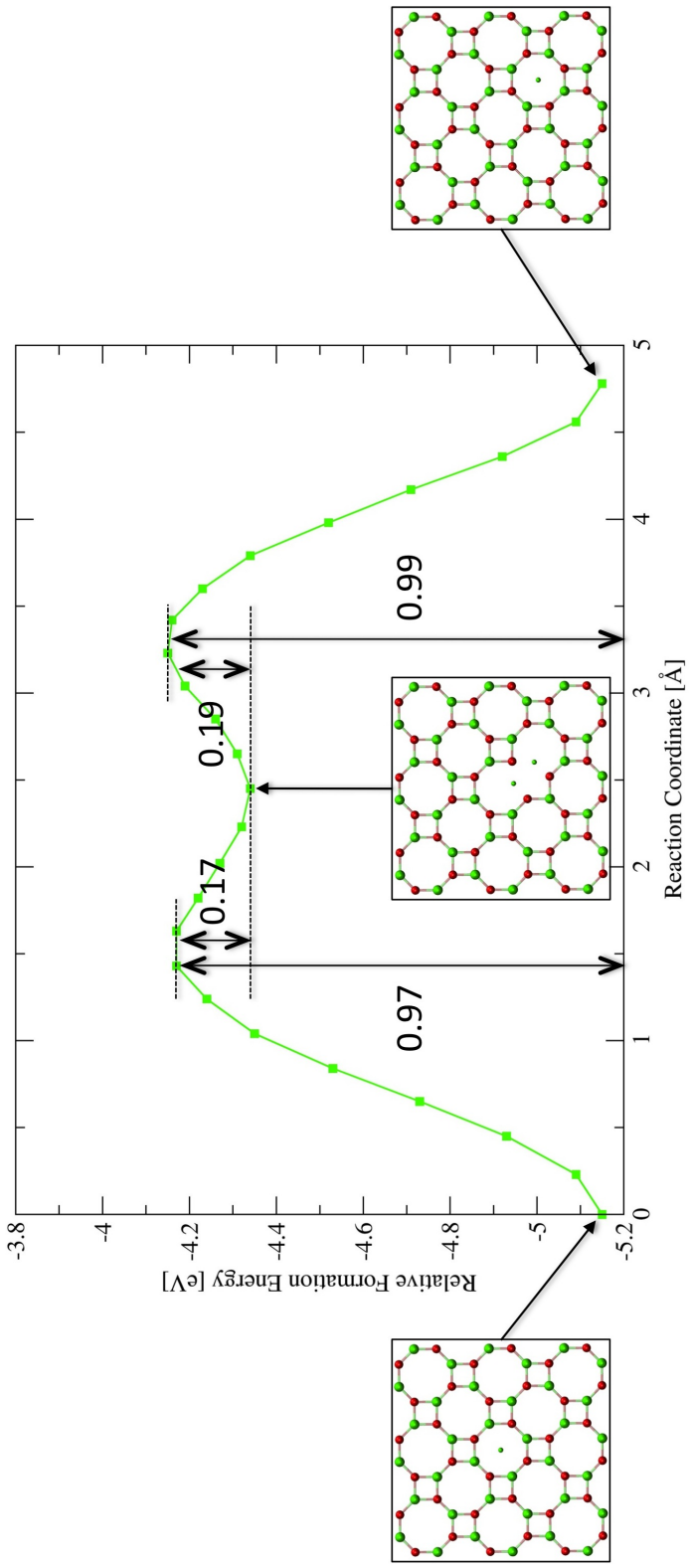

Figure 5.24: Relative formation energy profile for (a) Mg and (b) O interstitial migration at the twist grain boundary. Values are given in units of eV.

5.4 Conclusions

Table 5.5 summarises the lowest formation energies and relative formation energies for vacancies and Schottky defects observed in bulk MgO as well as the tilt and twist grain boundaries. The lowest activation energies for vacancy migration are also included. It can be seen that it is energetically more favourable for a vacancy to reside at a grain boundary in comparison to in bulk MgO which supports the general consensus that grain boundaries act as sinks for these defects. The lowest activation energies occur for migration towards a more stable vacancy site. For the tilt grain boundary vacancy migrations were found to be isotropic and a fast diffusion pathway was determined through the grain boundary structural unit, perpendicular to the grain boundary plane. This pathway involves equivalent vacancy sites in the close packed region of the structural unit. Rapid diffusion is also suggested to occur in the twist grain boundary and it was found that vacancies migrate in a zig-zag motion between sites at the grain boundary plane and the adjacent bulk-like plane.

Table 5.6 summarises the lowest formation energies and relative formation energies for interstitials and Frenkel defects observed in bulk MgO as well as at the tilt and twist grain boundaries. Also included are the lowest activation energies for interstitial migration. The table shows that interstitials are more stable at grain boundaries than in bulk MgO. Lower activation energies were observed for interstitial migration at the grain boundaries in comparison to those determined for vacancy migration. For the tilt grain boundary low activation energies were observed for interstitial migration in the sparsely packed region of the structural unit, however the formation energy of these interstitial sites were the highest in comparison to the other sites observed. This suggests that the potential energy landscape is flat due to the large distance from neighbouring lattice ions. Other activation energies observed for interstitial migration at the tilt grain boundary were found to be higher than in bulk MgO. Therefore no fast diffusion pathways were identified for interstitial migration in this grain boundary. At the twist grain boundary it was found that interstitial migration can occur from a dumbell site to a site at the centre of an octagon however the interstitial becomes strongly bound to the octagonal site. The activation energy for interstitial migration away from the octagonal site is higher than that in bulk MgO. Therefore no fast diffusion pathway can be suggested at the twist grain boundary plane.

	Mg Vacancy			O Vacancy			Schottky Defect	
	Formation		Migration	Formation		Migration	Formation	
	E_f [eV]	E_{f_rel} [eV]	E_a [eV]	E_f [eV]	E_{f_rel} [eV]	E_a [eV]	$E_{Schottky}$ [eV]	$E_{Schottky\_rel}$ [eV]
Bulk	23.89	-	2.08	24.41	-	2.05	7.39	-
Tilt	23.32	-0.57	0.77	23.86	-0.55	0.78	5.82	-1.57
Twist	23.36	-0.53	0.67	23.87	-0.54	0.69	6.44	-0.95

Table 5.5: The lowest formation energies and activation energies determined for Mg and O vacancies in. The Schottky defect formation energy was also calculated for bulk MgO and for the grain boundaries.

	Mg Interstitial			Mg Frenkel Defect		O Interstitial			O Frenkel Defect	
	Formation		Migration	Formation		Formation		Migration	Formation	
	E_f [eV]	E_{f_rel} [eV]	E_a [eV]	$E_{Frenkel}$ [eV]	$E_{Frenkel\_rel}$ [eV]	E_f [eV]	E_{f_rel} [eV]	E_a [eV]	$E_{Frenkel}$ [eV]	$E_{Frenkel\_rel}$ [eV]
Bulk	-11.69	-	0.35	12.20	-	-12.56	-	0.39	11.85	-
Tilt	-16.45	-4.76	0.54	6.87	-5.33	-17.05	-4.49	0.22	6.21	-5.64
Twist	-16.84	-5.15	0.17	6.52	-5.58	-17.40	-4.84	0.04	6.47	-5.38

Table 5.6: The lowest formation energies for Mg and O interstitials at the two grain boundaries. Frenkel defect formation energies were also determined.

Chapter 6

The Effect of an Electric Field on Defects Near an MgO Tilt Grain Boundary

6.1 Introduction

MgO can be used as a model for more complex oxides such as HfO_2 which is used as a dielectric layer in MOSFET devices (refer to Figure 2.1 in Chapter 2). In these applications the oxide film is in the presence of an electric field and it has been suggested that the field may enhance the migration of point defects in grain boundaries within the material leading to the failure of the device. In order to determine methods for prolonging the lifetimes of these devices it is vital to understand the effect of the field on point defects within the oxide. In this study atomistic simulation is used to calculate the formation energies and activation energies of vacancies and interstitials in a $\Sigma 17$ {410}/[001] MgO tilt grain boundary in the presence of a uniform external electric field. A finite grain boundary film model was used in this study as opposed to the periodic model used in Chapter 5 as it allows the oxide to be sandwiched between a pair of oppositely charged sheets of point charges which generate the external electric field.

6.2 Methods

6.2.1 Generating a Bulk MgO Film

The GULP computer programme was used throughout this study along with the shell model and the Lewis and Catlow A [59] pair potential, the parameters of which are given in Table 5.1 of Chapter 5. The selection of this potential is based on the results of the pair potential investigation also carried out in Chapter 5, Subsection 5.2.1. For this study the model required is that of a capacitor in which an MgO thin film dielectric containing a grain boundary is sandwiched in between two conductive plates of opposite charge polarity. The film is to be orientated such that the direction of the grain boundary and the thickness of the film is parallel to the z- axis. When considering the width of the dielectric it was decided that it should be wide enough such that ions at the centre of the film experience minimal effects due to the surfaces and that adequate lattice distortion is permitted when a point defect is present. Bulk MgO films of increasing size were generated and properties such as the electrostatic potential of the ions at the centre of the film along with cohesive energy and vacancy formation energies were calculated in order to determine their convergence. Starting with a $8 \times 8 \times 8$ ion film larger films were produced by increasing the number of ions in the x- and y- direction whilst maintaining $n \times n \times m$ stoichiometry. Here n and m are even integer values whereby $m = 8$ for all films and n is incremented by 2 for each subsequent film. This stoichiometry was chosen such that the system is symmetrical and does not contain a single ion directly in the centre of the film which allows the activation energies and minimum energy paths to be determined for the migration of defects directly at the centre of the film. It is expected that the ions in the top and bottom surfaces of the film will polarise although this will be restricted by the presence of the charged conductive plates. The extent of the interaction between the surfaces and the plates is not known therefore it was decided that the ions at the surfaces should be represented using the rigid ion model.

When investigating convergence the difference in the properties between two sequential film sizes was determined and compared to a tolerance. For electrostatic potential a tolerance of 0.01 V was considered small enough and for energy properties the tolerance was taken as 0.025 eV which corresponds to the thermal energy of a system at room temperature (21 °C = 294.15 K) when the energies of the ions are distributed according to the Boltzmann distribution.

The convergence of the electrostatic potential for both an Mg and an O ion at the centre of the film is shown in Figure 6.1 (a) and (b) respectively. It can be seen that the electrostatic potential of the Mg ion is converged to within 0.01 V when m =18 and for the O ion convergence of the

electrostatic potential occurs when m =10. The graphs differ due to differences in the immediate environment of the Mg and O ions investigated. The O ion is surrounded by six Mg neighbours which undergo less polarisation in comparison to O ions due to the high spring constant acting between the cores and the shells. As a result the O ion is more screened from the rest of the system and the electrostatic potential of the O ion is less than that of the Mg ion. The convergence of the cohesive energy is shown in Figure 6.2. Adequate convergence was considered to occur when m = 18.

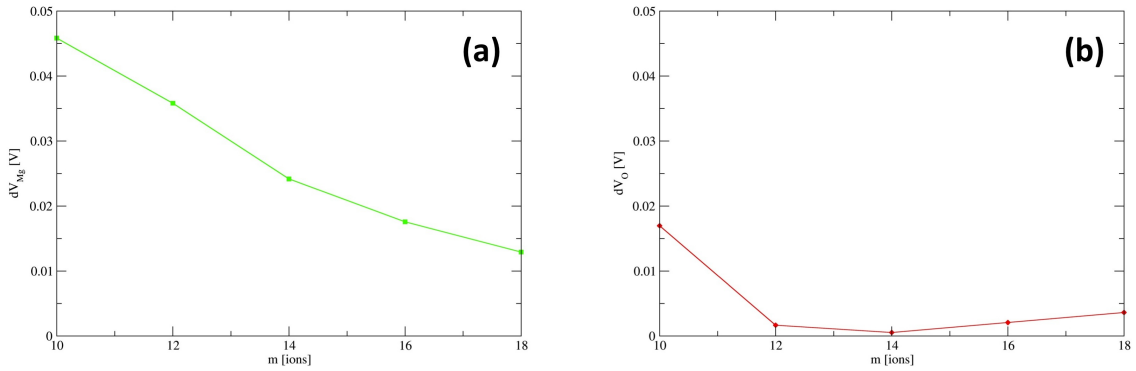

Figure 6.1: The convergence of the electrostatic potential as a function of film width for (a) a Mg ion and (b) an O ion in the centre of a MgO film. dV is the difference between the electrostatic potential for the ion for subsequent values if m.

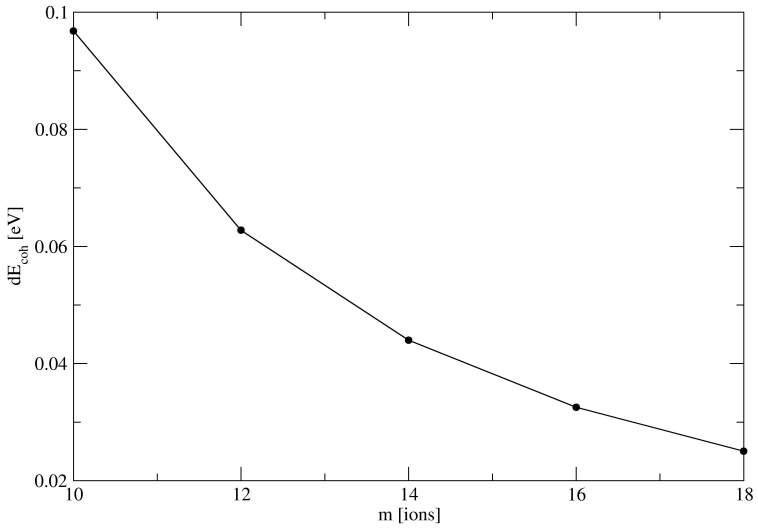

Figure 6.2: The convergence of the cohesive energy of MgO thin films as a function of the film width. dE_{coh} is the difference in the cohesive energy determined for consecutive values of m.

The convergence of the formation energies of an Mg and O vacancy near the centre of the film was also determined. This is shown in Figure 6.3 (a) and (b) respectively. It can be seen that

when m =18 the formation energies for the Mg and O vacancies are only converged to within a tolerance of 0.13 eV and 0.10 eV respectively. This suggests that the lattice distortion due to the presence of the vacancy has a longer range than the dimensions of the MgO film. By plotting the vacancy formation energy as a function of the inverse of m and extrapolating the linear regression, the formation energies for an infinitely large film can be predicted. This is shown in Figure 6.4 where it can be seen that the Mg and O vacancy formation energies should be approximately 24.98 eV and 25.49 eV respectively. These values are 0.96 eV and 0.77 eV higher than those calculated for Mg and O vacancies in bulk MgO which were determined using the Lewis and Catlow A pair potential and the Mott Littleton method. Here the vacancy formation energies were determined as 24.02 eV and 24.72 eV for Mg and O vacancies respectively. The increase in energy in this work is due to the fixed top and bottom surfaces of the model which limits the polarisation of the ions.

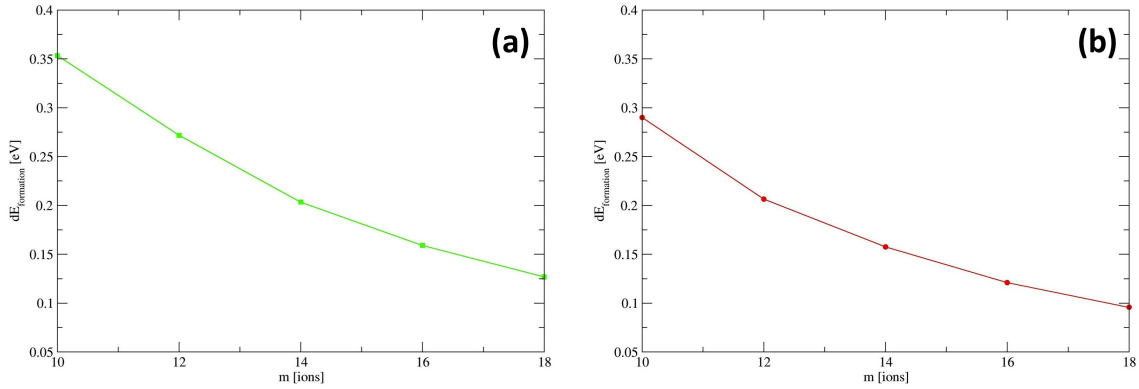

Figure 6.3: The convergence of the formation energy of (a) a Mg and (b) an O vacancy in near the centre of the MgO film as a function of film width. $dE_{formation}$ is the difference in formation energy between two consecutive values of m.

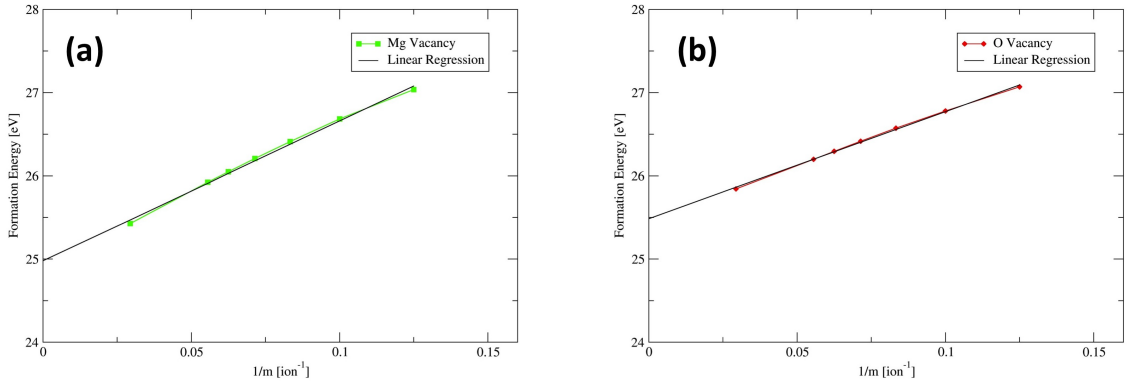

Figure 6.4: Vacancy formation energy as a function of the inverse of m for (a) Mg and (b) O vacancies. The extrapolation of the linear regression is also plotted in order to determine the y-axis intercept and hence approximate the formation energies in an infinitely large MgO film.

A 34 × 34 × 8 ion MgO film was generated and as a compromise between the film size, com-

putational resources and calculation time, the system was optimised using the Limited Memory Broyden-Fletcher-Goldfarb-Shanno (LBFGS) optimiser which limits the components of the Hessian matrix that are stored to memory at each iteration. Approximations were also made by splitting the un-optimised film into three regions similar to those of the Mott-Littleton method described in Chapter 4, Section 4.6. These three regions exclude the fixed top and bottom surfaces of the film. Region I is cylindrical and contains ions whereby the cores and the shells undergo explicit relaxation. Region II is a hollow cylinder concentric with Region I. In this region ions can only undergo polarisation due to the relaxation of the shells. The cores in this region are fixed in their optimised bulk MgO positions. The ions beyond Region II belong to Region III in which the cores and shells of the ions are fixed in the ideal bulk MgO positions. In order to determine the region sizes the ions in the optimised non-defective film and in a defective film containing a Mg vacancy were first investigated. In these models the cores and shells of the top and bottom surfaces were fixed. The displacements of the cores in the defective film with respect to their positions in the non-defective film were determined. Only relaxation in the x- and y- direction were included and the fixed ions in the top and bottom surfaces of the film were excluded. These displacements were plotted as a function of the distance of the core in the defective film from the vacancy site and is shown in Figure 6.5. It can be seen that the presence of the vacancy causes displacements of lattice ions of up to 0.16 Å. The displacements decrease rapidly with distance from the vacancy site and that beyond a distance of 9 Å the displacements are less than 0.001 Å. Therefore a Region I radius of 9 Å is reasonable however in order to take into account the absence of an ion directly in the centre of the film the radius of Region I was set as 11 Å.

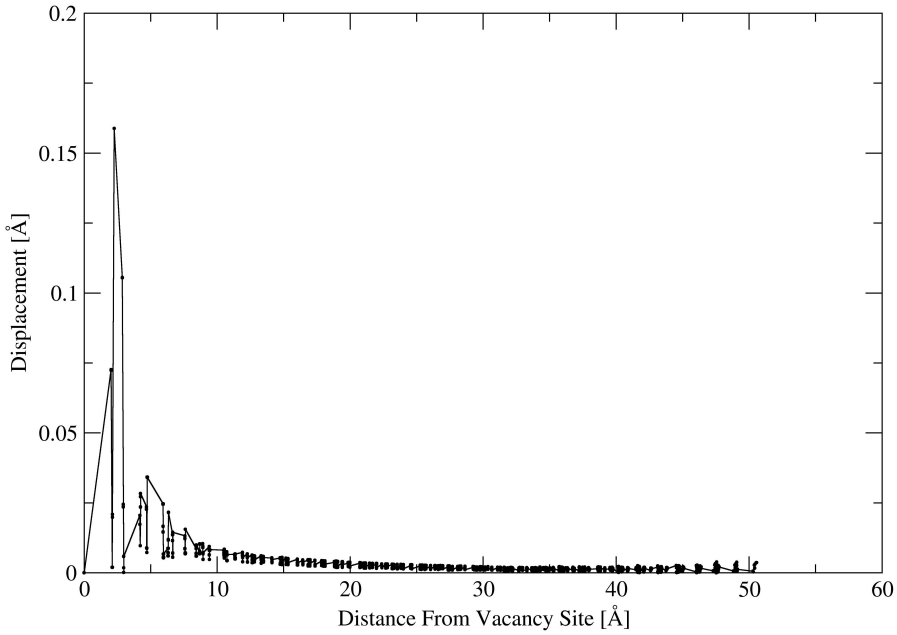

Figure 6.5: Displacement of cores as a function of distance from a Mg vacancy.

The polarisation of the ions was also investigated by determining the separation between cores and their corresponding shells in the defective film. Once again the the fixed top and bottom surfaces were excluded and only the separation in the x- and y- directions were included. Again this was plotted as a function of the distance of the core from the vacancy site and is shown in Figure 6.6. It can be seen that within the range 14 - 31 Å from the vacancy site the core-shell separations are less than 0.005 Å and that the separations are converged to within a tolerance of 0.002 Å. Therefore the radius of Region II was set as 32 Å. Beyond Region II the remaining ions constitute Region III. The graph in Figure 6.6 shows fluctuations in the core-shell separations beyond a distance of 31 Å. These occur due to the edges of the film where rumpling can be observed and this effect is eradicated by fixing the cores and the shells of these ions in their ideal bulk MgO lattice positions.

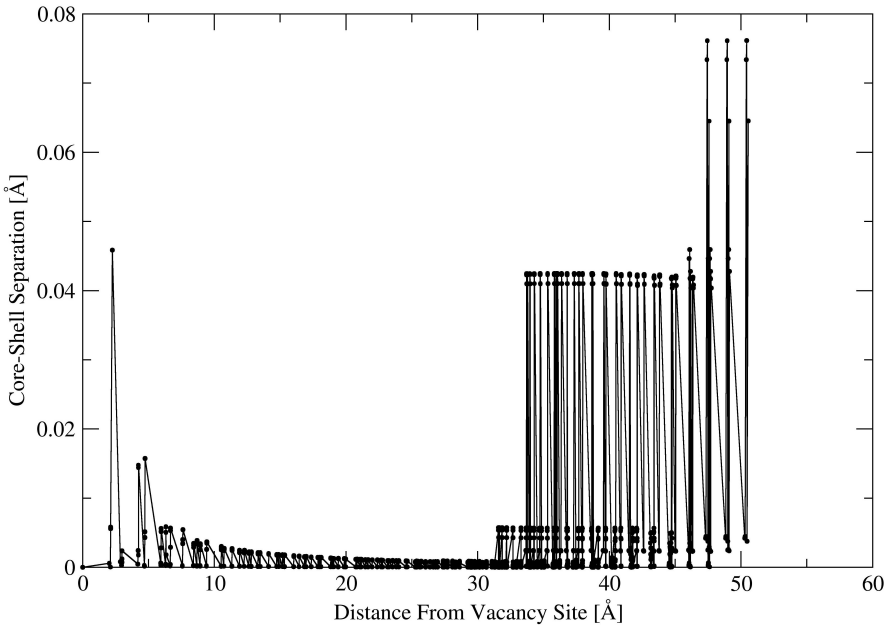

Figure 6.6: Polarisation as a function of distance from a Mg vacancy.

A schematic of the 3 region bulk MgO film is shown in Figure 6.7 and Table 6.1 gives a comparison of this model with that of the standard Mott-Littleton method. The average electrostatic potential and standard deviation of Mg and O ions in each x-y plane of Region I was determined. These were plotted as a function of the average z- position of the ions and are shown in Figure 6.8. The standard deviations were also determined for each plane and can be seen in Figure 6.9. Taking into account the magnitude of the electrostatic potential it can be seen that the ions in the planes closest to the surfaces have the highest electrostatic potential since their relaxation is limited by the fixed surfaces adjacent. Excluding this effect the two x-y planes at the centre of the film have the highest electrostatic potential. Figure 6.9 shows that for these planes the standard deviation is highest for the Mg ions and lowest for the O ions.

	3 Region bulk MgO thin Film	Mott-Littleton Method
Geometry	System is finite.	System is infinite.
	Regions close to the defect are concentric cylinders.	Regions close to the defect are concentric spheres.
Regions	Region I: Cores and shells relax explicitly.	Region 1: Cores and shells relax explicitly.
	Region II: Ions have fixed cores and polarisable shells.	Region 2a: Ions are close to their equilibrium positions and displace harmonically.
	Region III: Ions are rigid.	Region 2b: Ions polarise explicitly due to presence of defect.
Surfaces	Fixed top and bottom surfaces.	Undefined surfaces which relax according to Region 2b.

Table 6.1: A comparison of the regions in the finite bulk MgO film model used in this study and those of the Mott-Littleton approach.

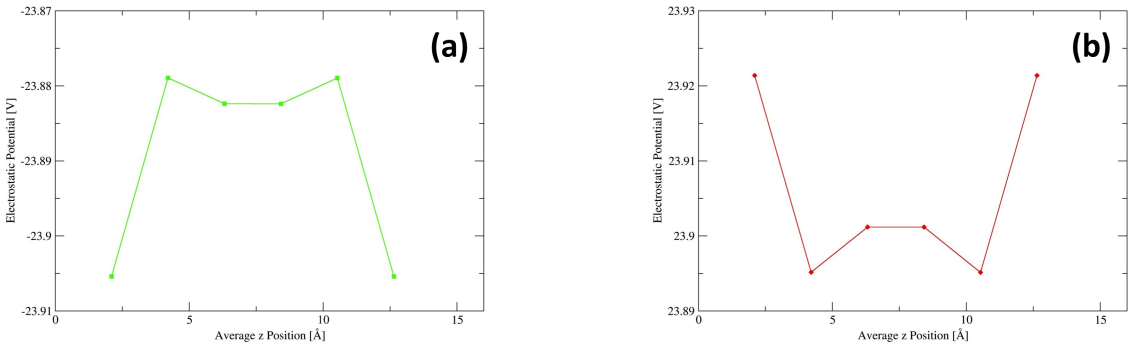

Figure 6.8: The average electrostatic potential as a function of average z- position for (a) Mg and (b) O ions in Region I of the three region bulk MgO film.

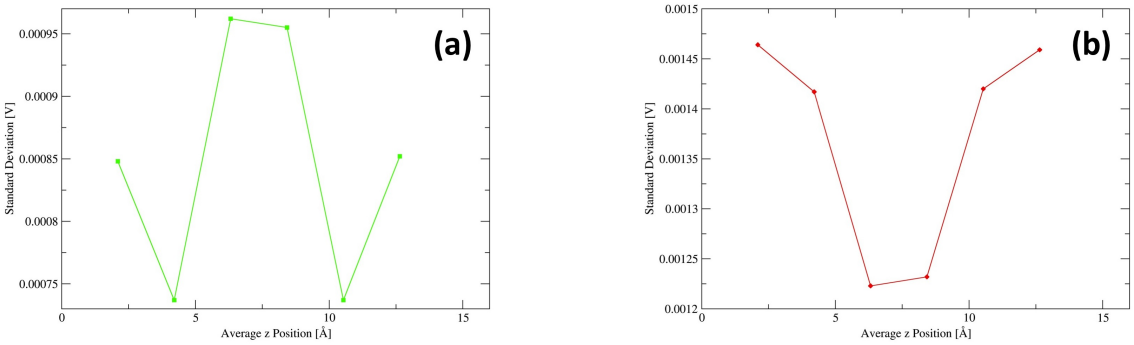

Figure 6.9: The standard deviation of the electrostatic potential plotted as a function of average z- position for (a) Mg and (b) O ions in Region I of the three region bulk MgO film.

The formation energies of an Mg and an O vacancy close to the centre of the film were determined as 25.69 eV and 26.41 eV respectively. This was compared to vacancy formation energies in alternative

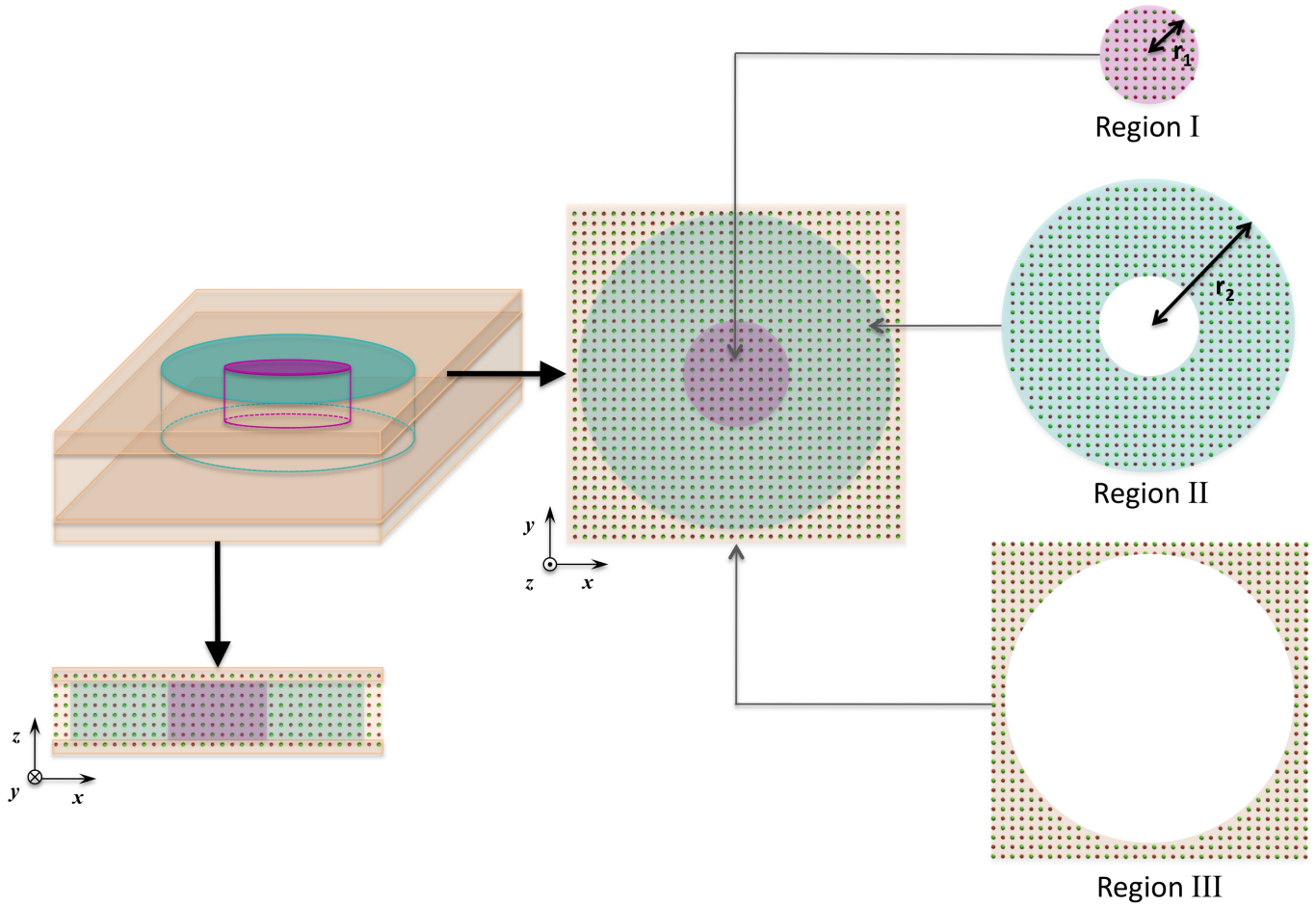

Figure 6.7: The finite bulk MgO film model. Regions subjected to explicit optimisation where both the cores and the shells of the ions can relax are represented by the pink shading. Regions undergoing implicit optimisation where the cores are fixed and the shells are permitted to relax are depicted by the turquoise shading. The orange shading represents regions where the cores and the shells of the ions are fixed, these include all ions beyond Region II and the top and bottom surfaces of the film.

models such as the 34 × 34 × 8 ion film with fixed surfaces but no defined regions, the Mott-Littleton method, a model periodic in 3 dimensions representing bulk MgO, a model periodic in 2 dimensions representing a MgO film and a model periodic in 3 dimensions representing infinite layers of MgO thin films separated by a gap. In the periodic models an 8 × 8 × 8 supercell was used. Three variations of the 2D periodic and the 3D periodic film models were utilised which differ by the way in which the top and bottom surfaces of the supercell were treated. In one variation the cores and the shells of the surfaces were permitted to relax, in another the cores were fixed and the shells underwent relaxation and in the third, both the cores and the shells were free to relax. The comparisons are shown in Table 6.2 which also includes the published results [122] obtained using the Mott-Littleton method and the Sangster and Stoneham pair potential [119]. It can be seen that the implementation of the three regions increases the energy required to add a vacancy to the system and that in general formation energies increase as the number of degrees of freedom of the top and bottom surfaces is reduced. This occurs because the extent of the lattice distortion due to the presence of the defect is limited. However this method was chosen due its efficiency in that it reduces the computation time from 337 minutes to 44 minutes for the non- defective 34 × 34 × 8 ion film. Table 6.2 also suggests that more energy is required to add a vacancy to a film than to bulk MgO. The formation energies of the three region film compare most reasonably to those obtained from the 3D periodic film model.

Model/Method	Formation Energy [eV]	
	Mg Vacancy	O Vacancy
34 × 34 × 8 ion finite film surfaces: fixed core, fixed shell 3 region	25.69	26.41
34 × 34 × 8 ion finite film surfaces: fixed core, fixed shell no regions	25.43	25.84
Standard Mott-Littleton Method $r_1 = 9$ Å $r_{2a} = 12$ Å	24.02	24.72
3D Periodic Bulk 8×8×8 ion supercell	23.51	24.21
2D Periodic Film 8×8×8 ion supercell surfaces: free cores, free shells	25.33	25.39
2D Periodic Film 8×8×8 ion supercell surfaces: fixed cores, free shells	27.10	24.40
2D Periodic Film 8×8×8 ion supercell surfaces: fixed cores, fixed shells	26.26	26.94
3D Periodic Film 8×8×8 ion supercell surfaces: free cores, free shells	26.19	26.39
3D Periodic Film 8×8×8 ion supercell surfaces: fixed cores, fixed shells	27.61	27.92
Extrapolation $E_{formation}$ Vs $\frac{1}{m}$ Finite Films - no regions or fixed surfaces	24.98	25.49
Published Values [122] Mott-Littleton method with the Sangster and Stoneham potential	24.0	24.7

Table 6.2: A comparison of Mg and O vacancy formation energies between the three region MgO film and those generated using the standard Mott-Littleton method, a 34 × 34 × 8 ion finite film with fixed surfaces and no regions, a 3D periodic bulk model, a 2D periodic film model, and a 3D periodic film model. Published values are also included which were produced using the Mott-Littleton method with the Sangster and Stoneham pair potential [119].

6.2.2 Generation of the Electric Field Using Parallel Plates of Point Charges

In order to implement the external electric field the MgO film was sandwiched between a pair of parallel charged plates. The plates were modelled by point charges of opposite polarity represented by the rigid ion model. Due to the three region setup of the MgO film it was important to ensure that the ions in Region I, which undergo explicit polarisation, experience a uniform electric field

with minimal effects due to the edge of the charged parallel plates. Different factors were considered such as whether the plates should be round in keeping with the surfaces of Region I and Region II of the MgO film or square conforming to the surface of the overall film. The dimensions of the charged plates were also considered as an important factor. It was thought that charge plates only covering the ions in Region I would produce a uniform field in Region I however that the edge effects of the field may introduce artificial polarisation in Region II. Other dimensions considered include plates with the same dimensions as the entire surface of the MgO film and plates larger than the film surface. Flex PDE version 5 finite element analysis software was used to investigate the electric field in these three models. In all models the plates were square and placed half an MgO lattice spacing (2.106 Å) away from the surfaces of the MgO film and also such that the centre of the plates is aligned with the centre of the surfaces of the MgO film. The MgO film was modelled without cylindrical regions or fixed surfaces. In the first model the width of the plates is equal to the diameter of Region I. In the second model the width of the plates is equal to the width of the MgO film. Whereas in the third model the width of the plates is 36.502 Å, larger than that of the MgO film and overhangs the perimeter of the film surfaces by 18.251 Å. These models are shown in Figure 6.10.

Using Flex PDE a 3D model was built and split into a number of finite elements. The Poisson equation relating electrostatic potential, $\mathbf{V}$, and charge density, ρ, was then solved:

$$\nabla^2 \mathbf{V} = -\frac{\rho}{\varepsilon_0}$$

where, ε_0, is the permittivity of free space.

The contour maps in Figure 6.11 and Figure 6.12 show the variation in electrostatic potential and electric field for a plane through the models. From Figure 6.11 (a) it can be seen that the electrostatic potential at the centre of the MgO film appears most uniform for Model A, however Figure 6.12 (c) shows that the electric field lines are uniform for Model C.

The charge plate models were investigated further using GULP 3.4. Using the three region MgO film the effect of the field on the electrostatic potential of the ions in Region I and polarisation of ions in Region II were determined. In these models the three region film was implemented along with the charged plates. An electric field corresponding to a potential difference of 1 V was chosen and by solving Gauss' law the relationship between electric field and the charge density of the two plates, σ, was taken as:

Figure 6.10: Models investigated using finite element analysis. The charged plates are shown in grey and the MgO film is depicted in blue. In (a) Model A the width of the charged plates is equal to the diameter of Region I, in (b) Model B the width of the plates equals the width of the MgO film and in (c) Model C the width of the plates is larger than the width of the film.

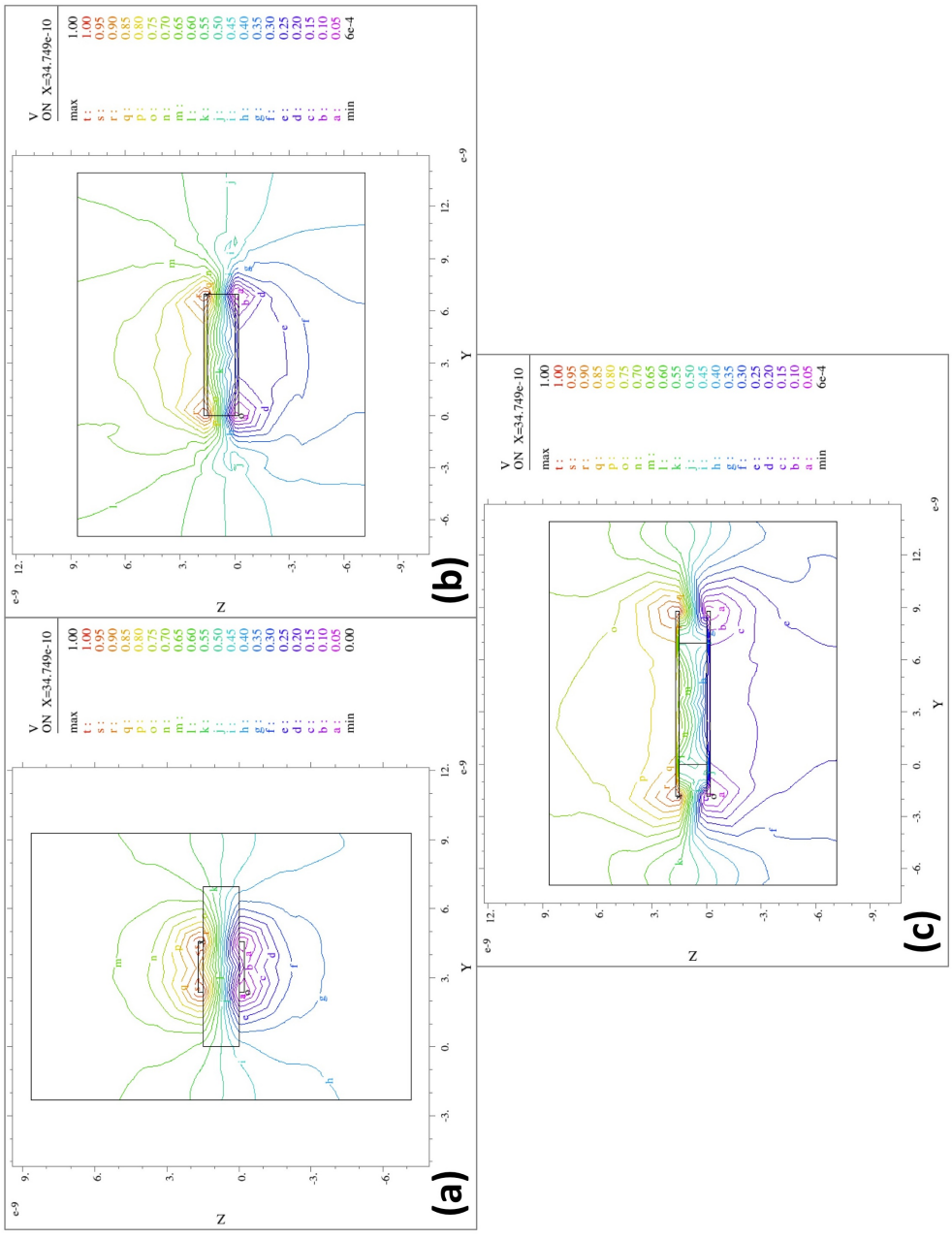

Figure 6.11: Contour maps showing the electrostatic potential in a slice of (a) Model A in which the width of the charged plates is equal to the diameter of Region 1, (b) Model B in where the width of the plates equals the width of the MgO film and (c) Model C in which the width of the plates is larger than the width of the film.

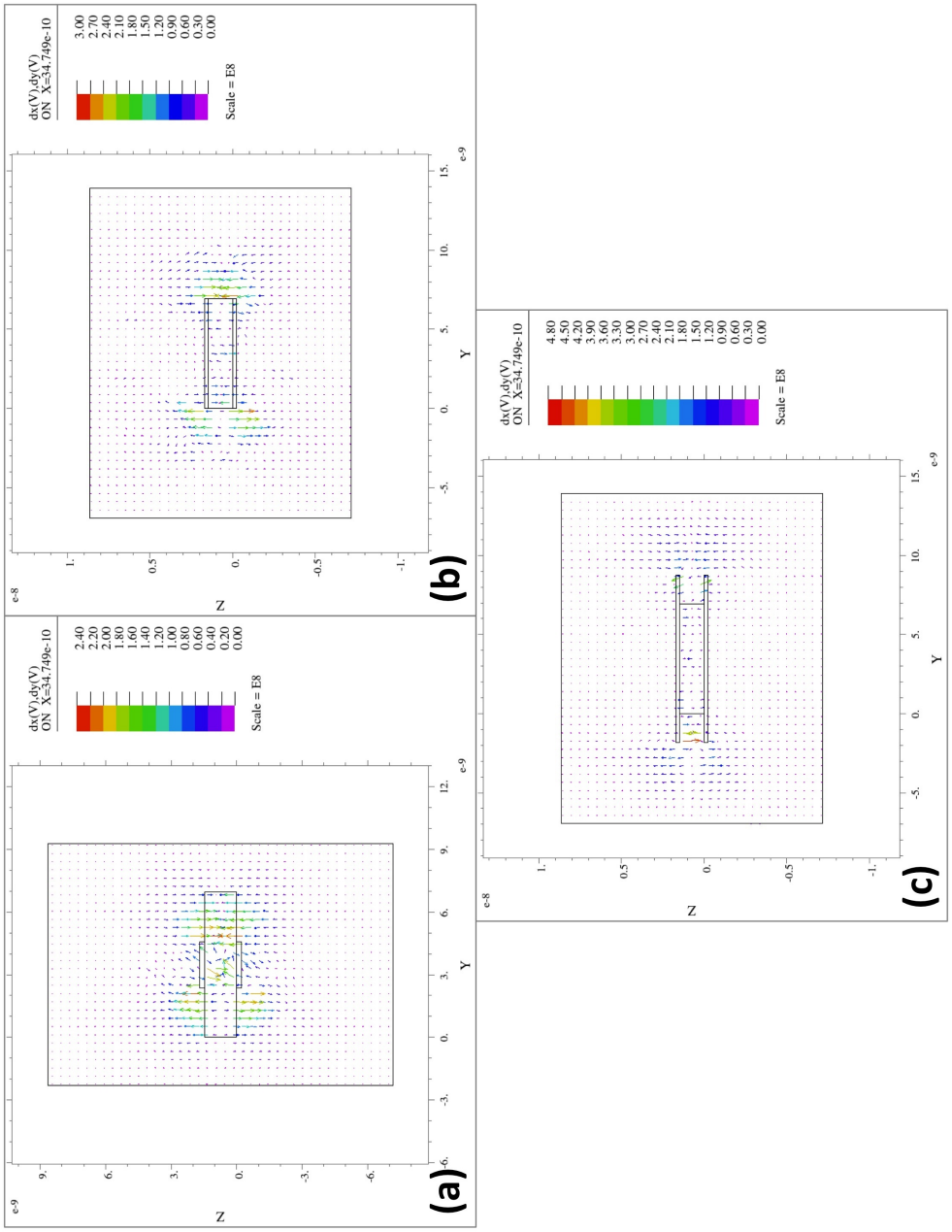

Figure 6.12: Contour maps showing the electric field lines in a slice of (a) Model A in which the width of the charged plates is equal to the diameter of Region 1, (b) Model B in where the width of the plates equals the width of the MgO film and (c) Model C in which the width of the plates is larger than the width of the film.

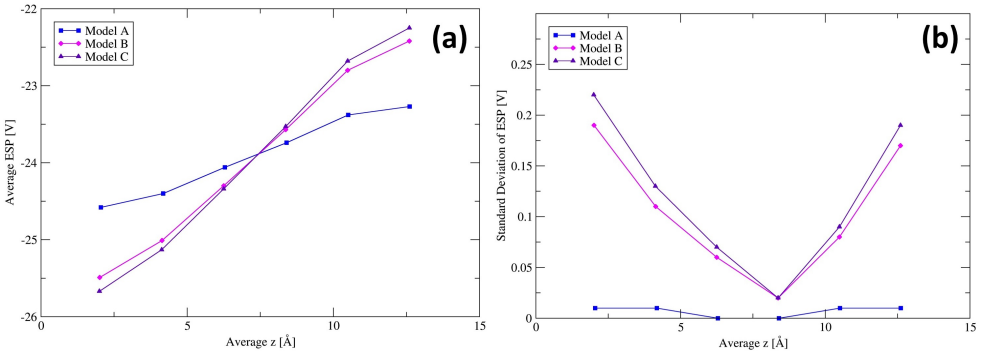

Figure 6.13: The (a) average electrostatic potential and (b) standard deviation of the electrostatic potential as a function of average z position for Mg cores in Region 1 of the MgO film when the applied electric field corresponds to a potential difference of 5 V.

$$\mathbf{E} = \frac{\sigma}{2\varepsilon}$$

where ε is relative permittivity. The electric field can be determined as:

$$\mathbf{E} = \frac{\triangle \mathbf{V}}{\triangle z}$$

Since the number of point charges per plate, N, and the area, A, of the charged plates is known the charge per point, q, can be determined using the relationship:

$$q = \frac{\triangle \mathbf{V}\, 2\, \varepsilon\, A}{N\ \triangle\ z}$$

In Model A and Model B the charged plates contain approximately 3.6 point charges per Å^2 whereas the charged plates in Model C are less dense and contain approximately 2 point charges per Å^2 as a compromise with the computational effort required. The plates were placed adjacent to the top and bottom surfaces of the MgO film such that as many point charges are commensurate with the Mg and O ions of the film as possible in order to maintain the symmetry of the system.

The average electrostatic potential and corresponding standard deviation was plotted as a function of average z- position for Mg and O cores in Region I and are shown in Figure 6.13 and Figure 6.14. It can be seen that the electrostatic potential increases with z- and Figure 6.13 (a) and Figure 6.14 (a) show that for both Mg and O cores the variation in the electrostatic potential is the least for Model A.

An Mg vacancy was placed close to the centre of the MgO film and the polarisation of the ions in Region II were investigated for all three charged plate models. The core-shell separations were

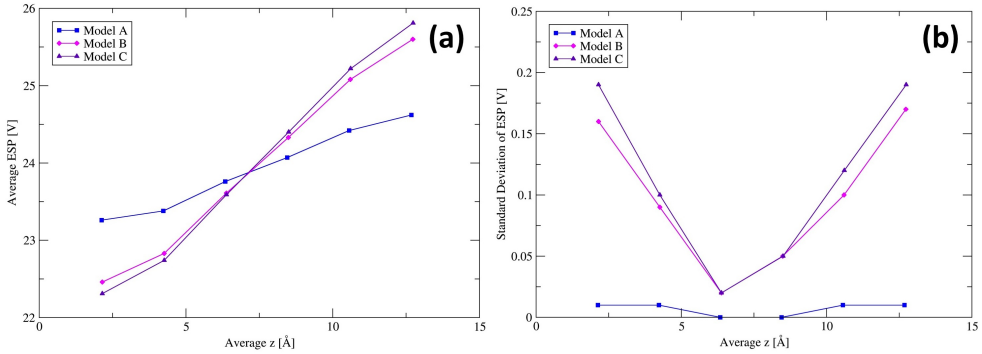

Figure 6.14: The (a) average electrostatic potential and (b) standard deviation of the electrostatic potential as a function of average z position for O cores in Region 1 of the MgO film when the applied electric field corresponds to a potential difference of 5 V.

plotted as a function of the radial distance of the core from the vacancy site. It can be seen from Figure 6.15 that for Models B and C the polarisation increases as a function of radial distance. However for Model A the polarisation decays with distance from the vacancy as would be expected for the ions surrounding a vacancy in bulk MgO in the absence of an electric field. Therefore the charged sheets of Model A were used to apply the external electric field to the system.

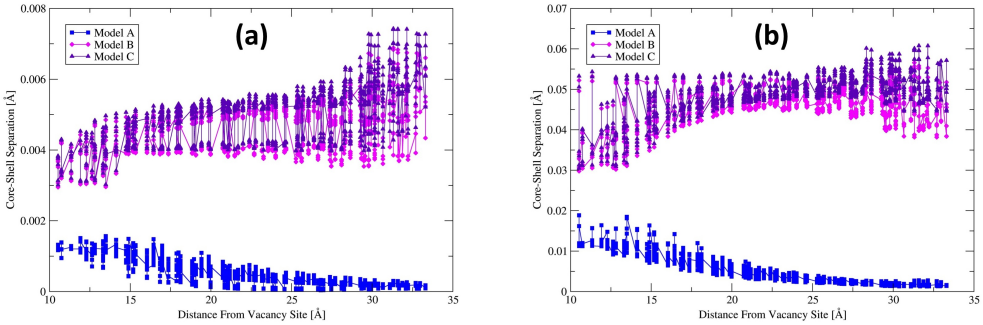

Figure 6.15: The polarisation of the (a) Mg and (b) O ions in Region II as a function of the radial distance from the centre of the film when an external field corresponding to a potential difference of 5 V is applied.

The lower magnitude of the Mg ion polarisations reflects the high spring constant acting between Mg cores and shells in comparison to that of the O ions.

6.2.3 Generating the MgO Grain Boundary Film

The Σ17 {410}/[001] MgO tilt grain boundary was produced using the METADISE code whereby two crystalline grains are misorientated by an angle of 28.1°. A film was generated with dimensions of 72.488 Å × 68.962 Å × 14.742 Å. The film was orientated such that the grain boundary plane is perpendicular to the *z*- axis and was split into three regions with the same dimensions as that

of the bulk MgO film. A schematic diagram of the grain boundary film and the three regions is shown in Figure 6.16.

In order to predict sites within the grain boundary at which interstitials are likely to reside the electrostatic potential was determined for points in the space within a grain boundary structural unit, as shown in Figure 6.17(a) and (b). The contour maps for slices perpendicular to the z- axis are shown in Figure 6.17 (c) to (d). It can be seen that the range of the electrostatic potential for slices in between two x-y planes of lattice ions, such as when $z = 7.37$ Å and $z = 5.28$ Å, is significantly lower than that of slices taken in the same plane as the lattice ions. This occurs because for each point in the plane the lattice ions are further away. In these planes there is a region near the close packed structure of the grain boundary where the electrostatic potential is lowest at around 0.02 V. For slices in the x-y plane of the lattice ions it can be seen that the electrostatic potential is close to zero for a region near the close packed structure of the structural unit but also for a region of the structural unit where the lattice ions are sparse. Again points within the sparse region of structural unit have less interaction with the lattice ions which results in the low electrostatic potential.

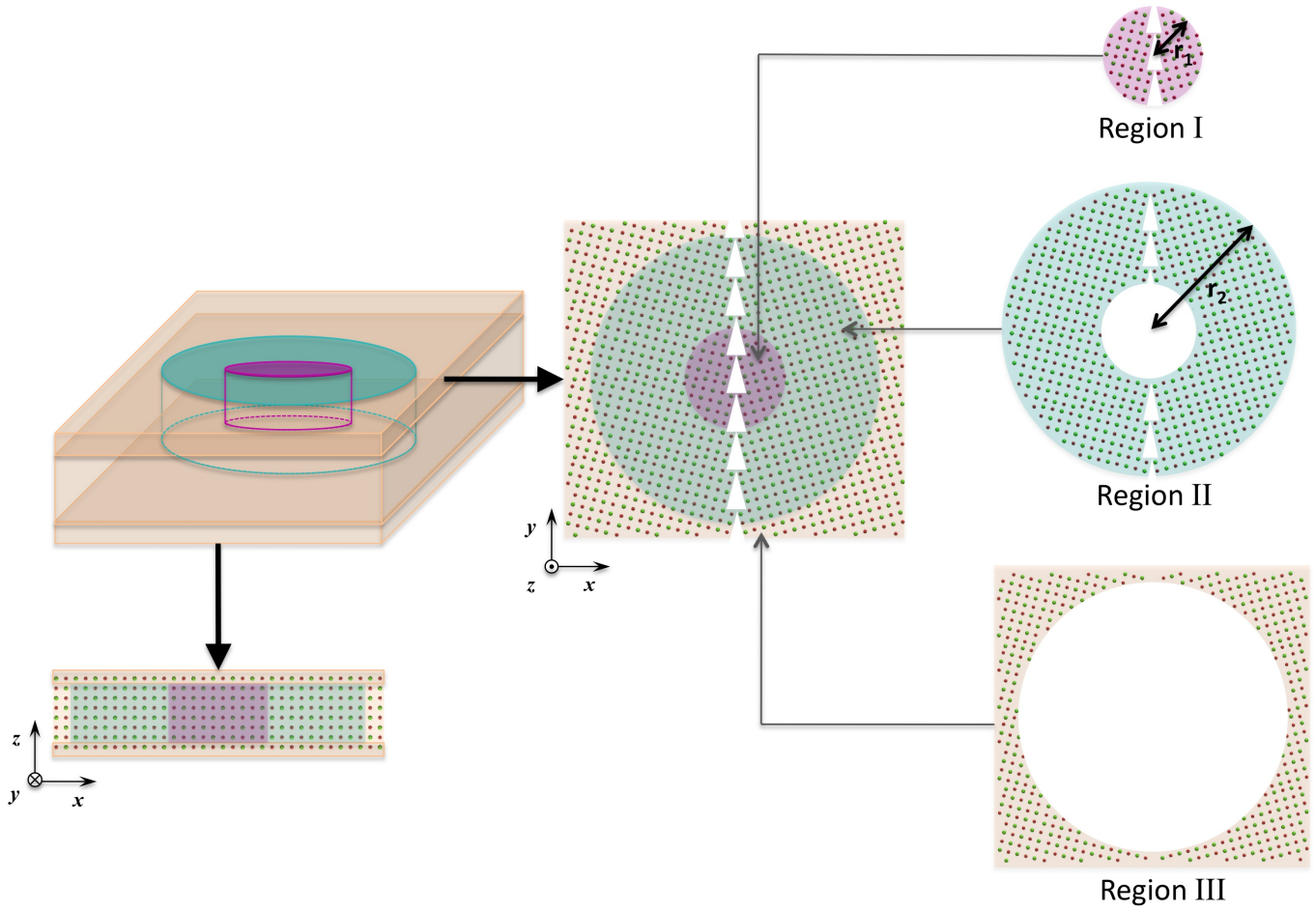

Figure 6.16: The MgO tilt grain boundary film and the three regions. Regions subjected to explicit optimisation where both the cores and the shells of the ions can relax are represented by the pink shading. Regions undergoing implicit optimisation where the cores are fixed and the shells are permitted to relax are depicted by the turquoise shading. The orange shading represents regions where the cores and the shells of the ions are fixed, these include all ions beyond Region II and the top and bottom surfaces of the film.

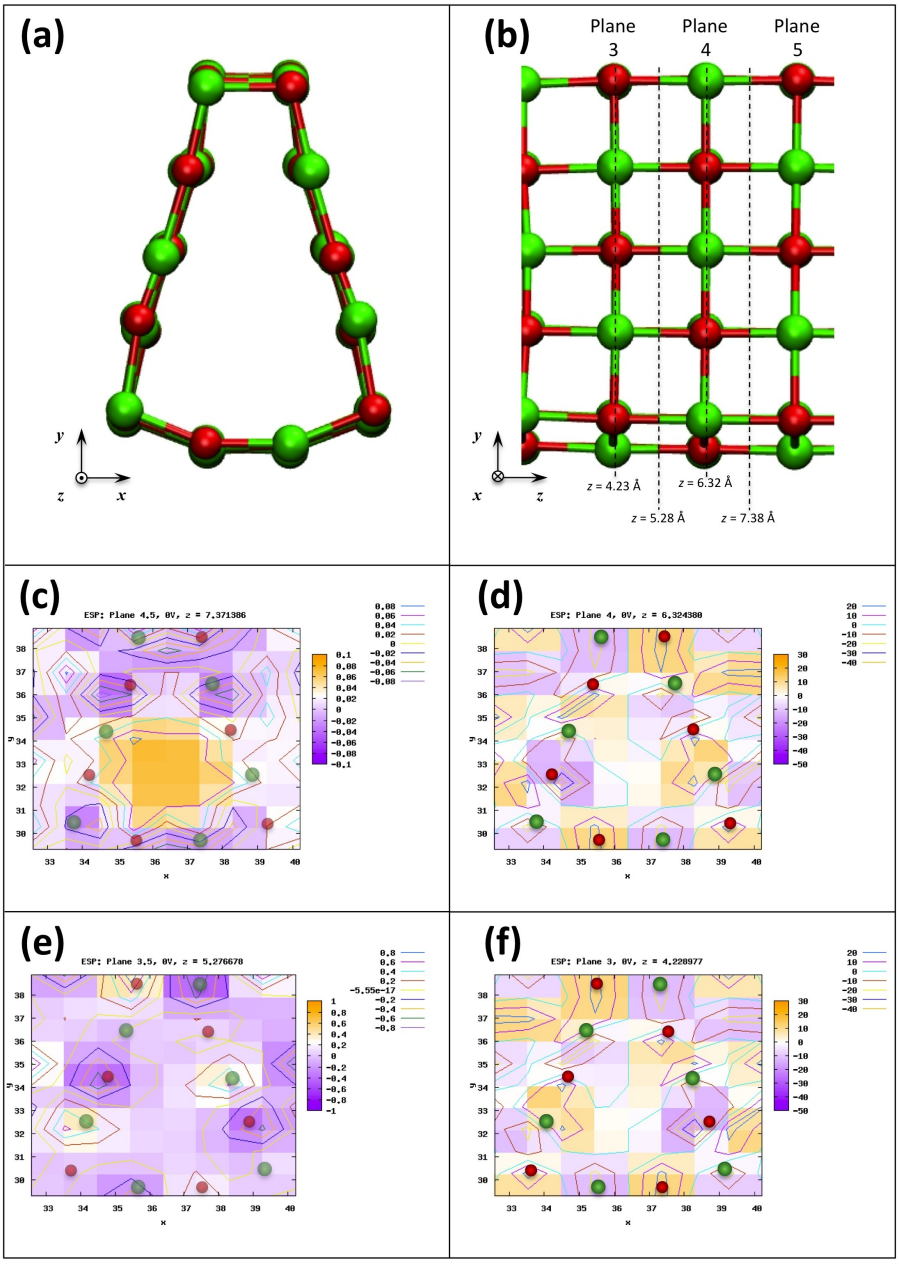

Figure 6.17: The electrostatic potential, in units of V, for slices perpendicular to the z axis within a grain boundary structural unit in the absence of an applied electric field. The structural unit is shown from (a) the x-y plane and (b) the y-z plane. The electrostatic potential is given when (c) z = 7.37 Å, which is directly in the centre of the grain boundary film, (d) z = 6.32 Å, (e) z = 5.28 Å and (f) z = 4.23 Å.

6.2.4 Properties Calculated

Formation and activation energies were first determined for vacancies and interstitials in the bulk-like MgO film and the grain boundary film in the absence of an external electric field. This allowed comparisons to be made to the results obtained using the periodic model in Chapter 5

and also to published experimental and theoretical work and determined the validity of the model. Finally the formation and activation energies were determined for vacancies and interstitials in the bulk-like MgO film and the grain boundary film in the presence of an external electric field corresponding to a potential difference of 5 V. Properties such as the formation energy, relative formation energy, cohesive energy, Schottky defect formation energy, and Frenkel defect formation energy were determined as in Chapter 5, Subsection 5.2.2.

6.3 Results and Discussion

6.3.1 Defect Properties in the Absence of an Electric Field

6.3.1.1 Vacancies in the MgO Bulk-Like Film In the Absence of an Electric Field

The formation energies were determined for the vacancies in one of the central x-z planes of the bulk MgO film in the absence of an external field. Figure 6.18 depicts the vacancy sites, and Figure 6.19 shows a plot of the vacancy formation energy as a function of z- position. Vacancies were not studied in the fixed top and bottom surfaces as they do not have any degrees of freedom available for relaxation. The planes adjacent to these surfaces were also excluded from this study as it was thought that they undergo artificial relaxation due to their close proximity to the fixed surfaces. If an imaginary x-y plane bisecting the film at its centre is considered then it can be seen that there are equivalent sites either side of this plane, as is shown by the symmetry of the graphs in Figure 6.19. Mg and O vacancies have the lowest formation energy when they are located close to the centre of the MgO film and they become less energetically favourable the closer they are to the surfaces. The vacancies closest to the centre of the film are the most comparable to those in bulk MgO since they are furthest from the surfaces and edges of the film. Here the formation energies were determined as 25.69 eV and 26.42 eV for Mg and O vacancies respectively. These values are 1.69 eV and 1.72 eV higher than the published values for vacancies in bulk MgO which were determined as 24.0 eV and 24.7 eV for Mg and O vacancies respectively [122]. These values were obtained using the Sangster and Stoneham pair potential [119] and the Mott-Littleton method. The high values in this study are attributed to the presence of the top and bottom surfaces which limits the relaxation of the MgO lattice in the z- direction.

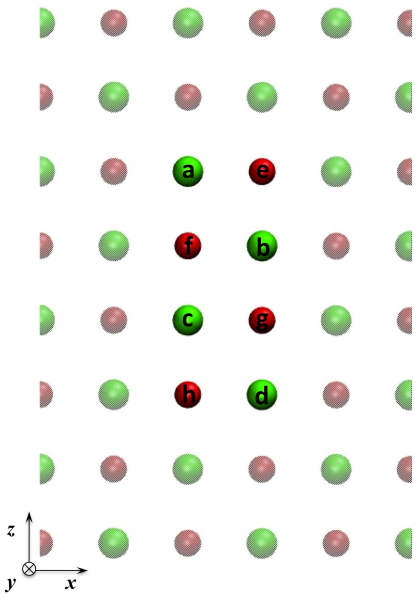

Figure 6.18: Vacancy sites in the bulk MgO film. The green spheres are Mg ions and the red spheres depict O ions.

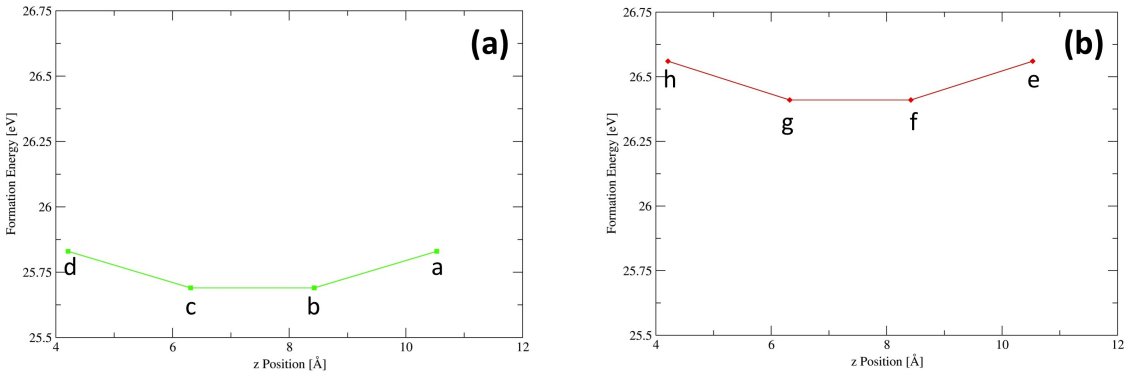

Figure 6.19: Vacancy formation energy as a function of z- position for (a) Mg and (b) O vacancies in the bulk-like MgO film in the absence of an external electric field. The corresponding vacancy sites are also labelled.

Activation energies for the migration of Mg and O vacancies close to the centre of the film were also determined and are shown in Figure 6.20. It was found that for migration across the centre of the film the activation energy is 2.09 eV and 2.10 eV for Mg and O vacancy migrations respectively. These values compare well to the published results [122] of 2.07 eV and 2.11 eV for Mg and O vacancies respectively. These were obtained using the Sangster and Stoneham pair potential with static minimisation. The results also compare well the activation energies for Mg and O vacancy migration in the periodic MgO model in Chapter 5 which were determined as 2.08 eV and 2.05 eV. From Figure 6.20 it can be seen that the activation energies are lower for vacancy migrations towards the more stable vacancy sites in the two central x-y planes.

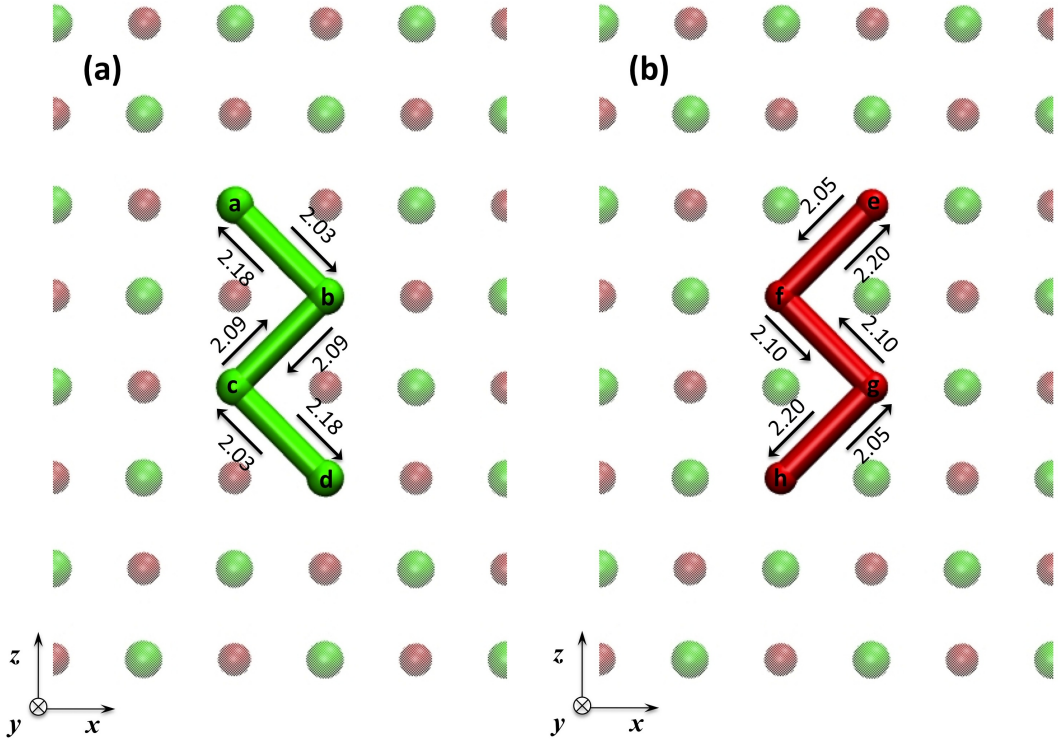

Figure 6.20: Activation energies for (a) Mg and (b) O vacancy migration in the bulk-like MgO film in the absence of an external electric field. Activation energies are given in units of eV.

6.3.1.2 Interstitials in the Bulk-Like MgO Film in the Absence of an External Electric Field

For the bulk-like film stable sites were found to occur when the interstitial is located at the centre of an Mg-O cube belonging to the bulk-like lattice. The formation energies were determined for the interstitial sites shown in Figure 6.21 and were plotted as a function of z- position as shown in Figure 6.22. It can be seen that interstitials are significantly more stable than vacancies. It is most energetically favourable for an interstitial to be located at the centre of the MgO film and it was found that the formation energy increases the closer the interstitial is to the fixed top and bottom surfaces of the film, as shown in Figure 6.22. The lowest formation energies were determined as -10.41 eV and -11.39 eV for Mg and O interstitials respectively.

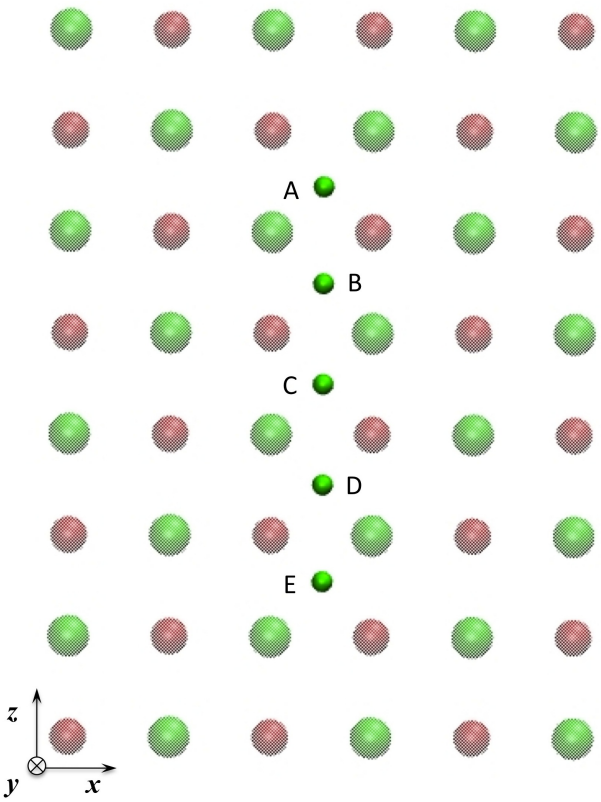

Figure 6.21: Interstitial sites (small solid green spheres) in the bulk-like MgO film.

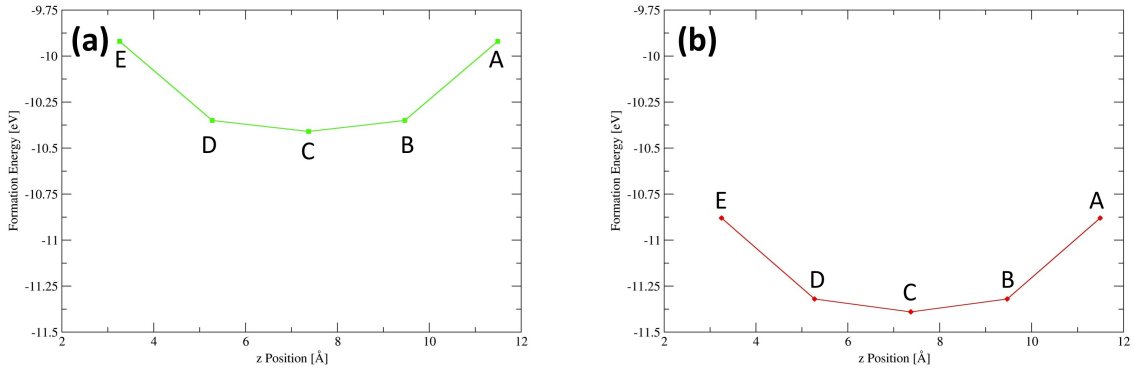

Figure 6.22: Formation energy as a function of z position for an (a) Mg and an (b) O interstitials in the bulk-like MgO film in the absence of an external electric field.

In agreement with published results [153] it was found that the lowest activation energy occurs when the interstitial migrates via the interstitialcy mechanism. Here the interstitial migrates from a stable site towards an adjacent lattice ion site, whilst the lattice ion concurrently moves in the same direction towards the adjacent stable interstitial site opposite. This mechanism can be split into four stages as shown in Figure 6.23.

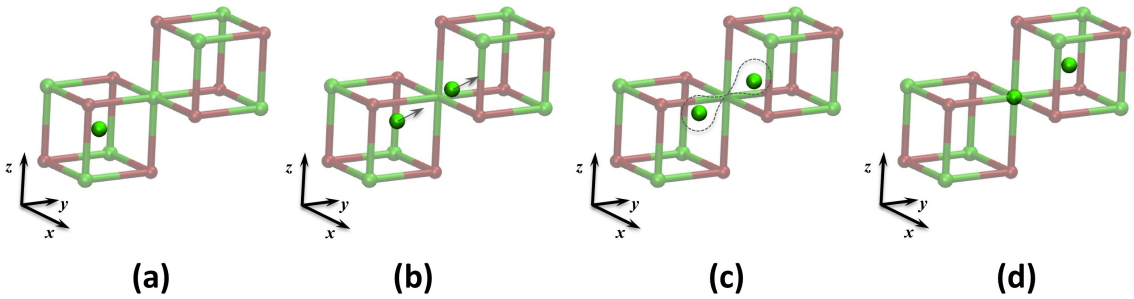

Figure 6.23: The interstitialcy mechanism shown for an Mg interstitial. (a) Stage 1: The initial configuration. The interstitial is located in a stable site at the centre of an MgO cube in the lattice. (b) Stage 2: The interstitial migrates towards an Mg lattice ion and at the same time the lattice ion migrates towards the opposite interstitial site. (c) Stage 3: The dumbell configuration formed at the saddle point of the minimum energy path. (d) Stage 4: The final configuration. The interstitial is now located at the centre of the opposite MgO cube.

Activation energies were determined for interstitial migration in the z- direction as shown in Figure 6.24. It can be seen that the lowest activation energy was determined as 0.14 eV and 0.25 eV for Mg and O migration from the centre of the film to the next nearest interstitial site towards one of the fixed surfaces. These values are lower than those for Mg and O interstitial migration in the periodic bulk model in Chapter 5 which were determined as 0.35 eV and 0.39 eV respectively.

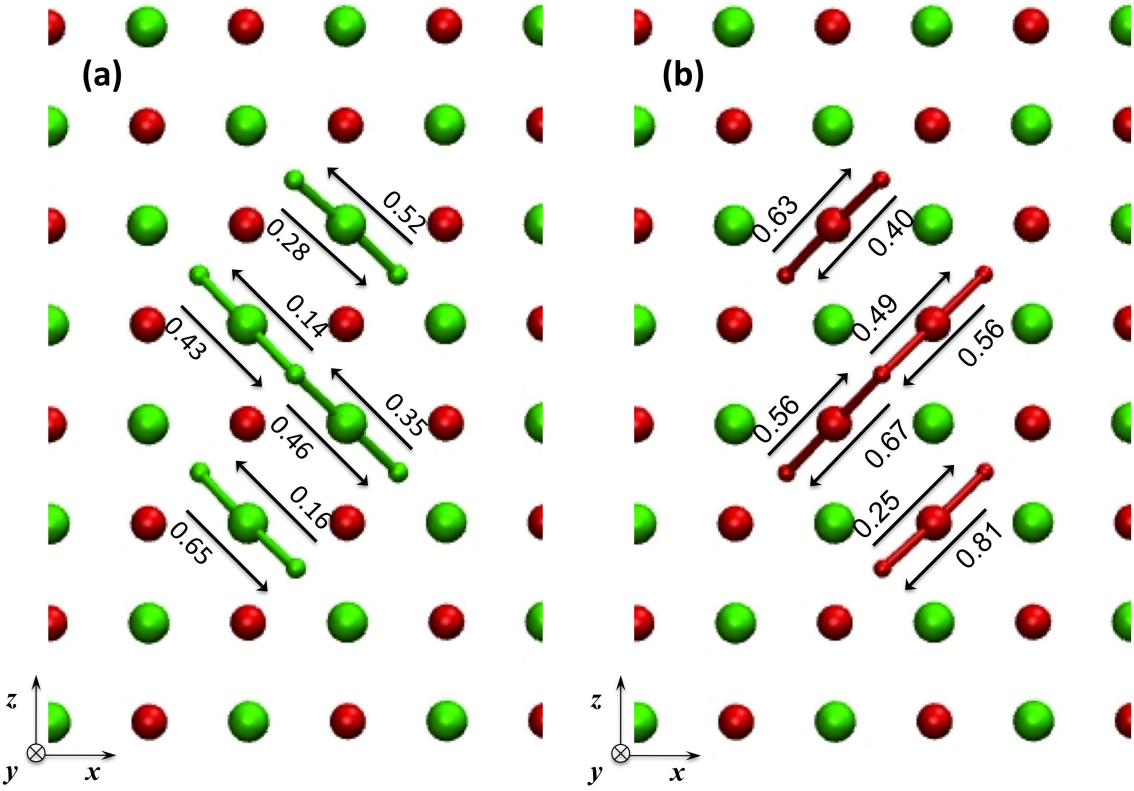

Figure 6.24: Activation energies, in units of eV, for (a) Mg and (b) O interstitial migrations in the bulk MgO film in the absence of an external electric field. The larger spheres represent the ions in the bulk-like lattice whereas the smaller spheres depict metastable interstitial sites.

6.3.1.3 Vacancies in the MgO Grain Boundary Film in the Absence of an External Electric Field

Formation energies were determined in the absence of an external electric field for the vacancy sites at the grain boundary as shown in Figure 6.25. The formation energies were compared to the lowest vacancy formation energy determined in the bulk-like MgO film for the equivalent species. These were determined as 25.69 eV and 26.42 eV for Mg and O vacancies respectively. These relative formation energies were plotted for Mg and O vacancies as a function of the z- position as shown in Figure 6.26. In contrast to the results obtained in Chapter 5 it was found that using a finite grain boundary model causes sites a and f to become inequivalent as the lack of periodicity causes the sites to be affected by the presence of the film edges by different extents. It can be seen that for both Mg and O vacancies the sites labelled a have the lowest formation energy and that these vacancies are the most energetically stable when they are located at the two central x-y planes of the MgO film as they are furthest from the fixed top and bottom surfaces of the film. Here the formation energies were determined as 25.13 eV and 25.75 eV for Mg and O vacancies respectively. When compared to vacancies in the bulk-like MgO film they correspond to relative formation energies of -0.56 eV and -0.67 eV for Mg and O vacancies respectively, and it can be seen that less energy is required to add a vacancy to the grain boundary in comparison to bulk MgO.

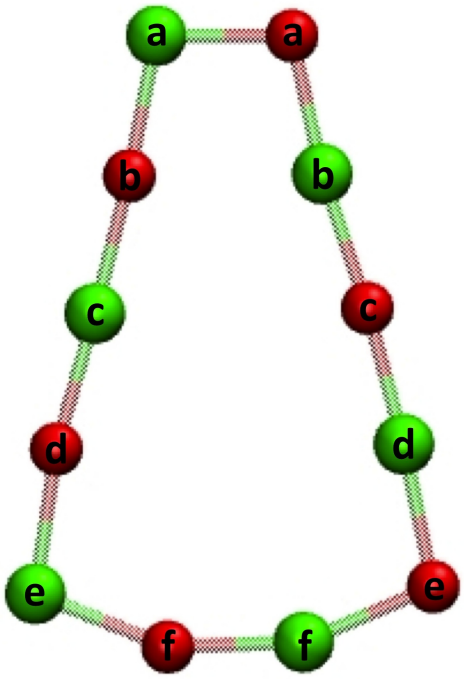

Figure 6.25: Vacancy sites in the grain boundary film.

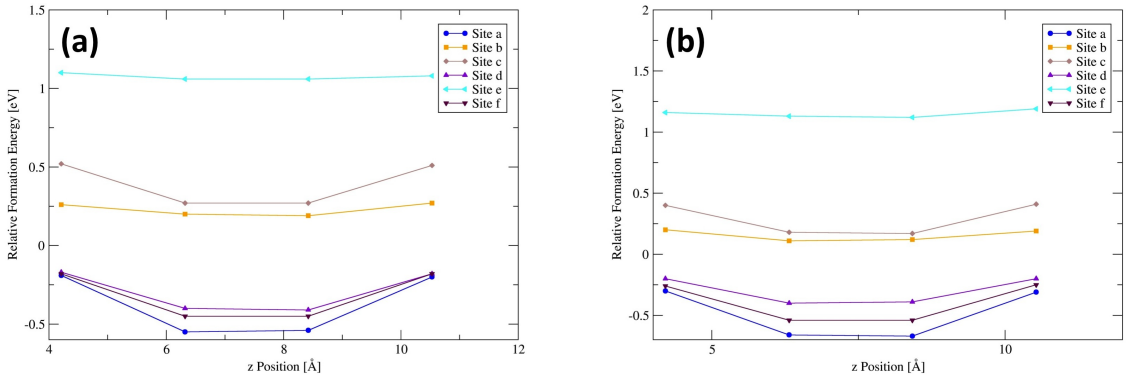

Figure 6.26: Relative formation energy as a function of z- position for (a) Mg and (b) O vacancy sites at the grain boundary in the absence of an external field.

The activation energies were determined for Mg and O vacancy migration at the grain boundary and are shown in Figure 6.27. In order to visualise from the figure the vacancy site with respect to z- position the sites are labelled with the notation h_{ij}. Here h represents the location of the vacancy site with respect to the structural unit (see Figure 6.25), i has the attribute of M or O corresponding to whether the site contains an Mg or O vacancy respectively, and j denotes the x-y plane in which the vacancy is located. It was found that the lowest formation energies occur for migration towards the two central x-y planes which corresponds to migration towards the most stable vacancy sites. For both Mg and O vacancy migrations the lowest activation energies were determined as 0.84 eV and 0.96 eV and were found to occur for migration towards the vacancy site labelled d, which corresponds to a vacancy at the grain boundary where the structure is less dense. This is in agreement with the results presented in Chapter 5.

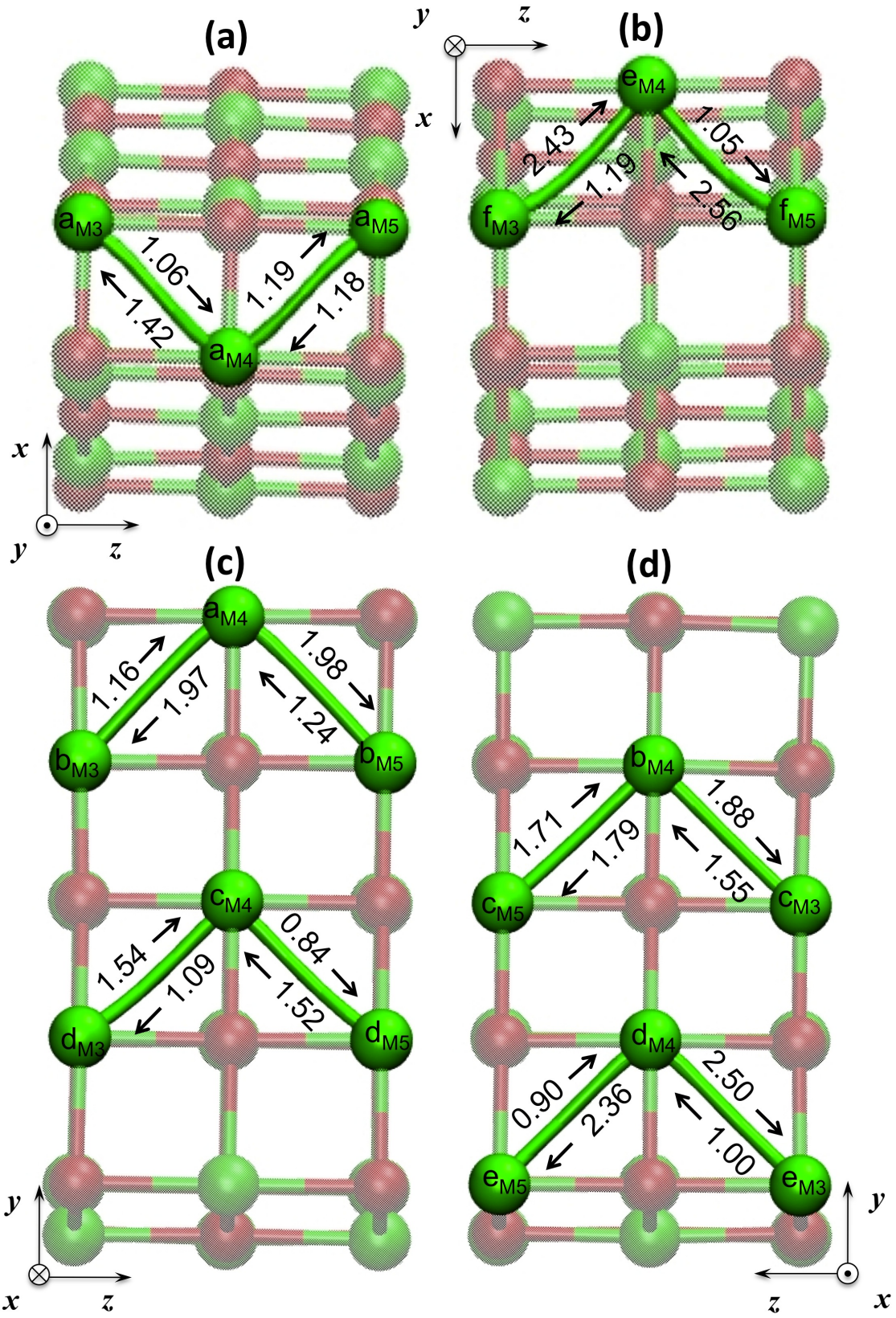

Figure 6.27: Activation energies, in units of eV, for Mg vacancy migration in the grain boundary in the absence of an external electric field.

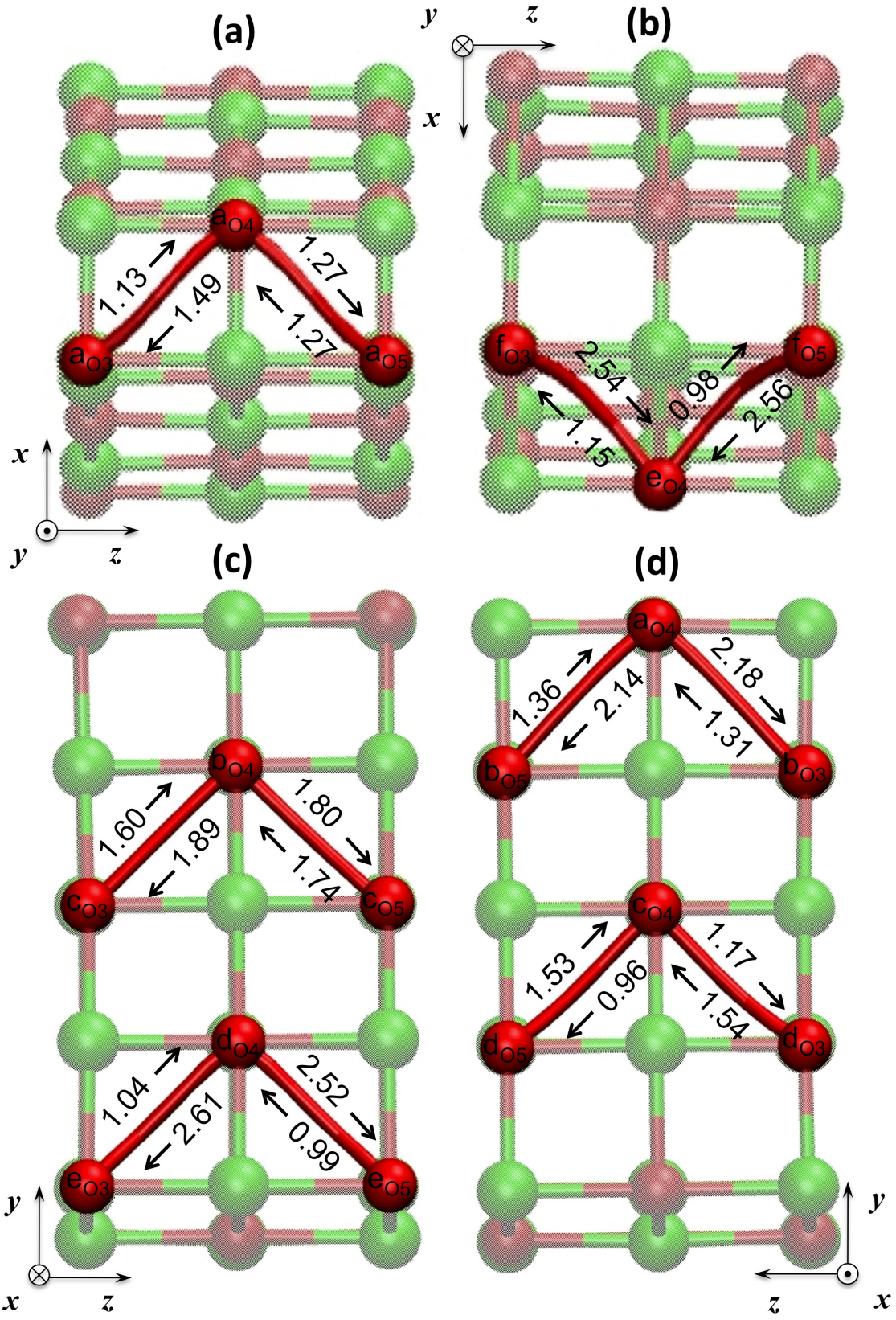

Figure 6.28: Activation energies, in units of eV, for O vacancy migration in the grain boundary in the absence of an external electric field.

(a)

Mg Vacancy	
Migration Path	Deviation [Å]
$a_{M3} \leftrightarrow a_{M4}$	0.20
$a_{M4} \leftrightarrow a_{M5}$	0.20
$b_{M3} \leftrightarrow a_{M4}$	0.09
$a_{M4} \leftrightarrow b_{M5}$	0.09
$c_{M3} \leftrightarrow b_{M4}$	0.06
$b_{M4} \leftrightarrow c_{M5}$	0.12
$d_{M3} \leftrightarrow c_{M4}$	0.17
$c_{M4} \leftrightarrow d_{M5}$	0.16
$e_{M3} \leftrightarrow d_{M4}$	0.22
$d_{M4} \leftrightarrow e_{M5}$	0.21
$f_{M3} \leftrightarrow e_{M4}$	0.32
$e_{M4} \leftrightarrow f_{M5}$	0.36

(b)

O Vacancy	
Migration Path	Deviation [Å]
$a_{O3} \leftrightarrow a_{O4}$	0.25
$a_{O4} \leftrightarrow a_{O5}$	0.25
$b_{O3} \leftrightarrow a_{O4}$	0.10
$a_{O4} \leftrightarrow b_{O5}$	0.11
$c_{O3} \leftrightarrow b_{O4}$	0.02
$b_{O4} \leftrightarrow c_{O5}$	0.12
$d_{O3} \leftrightarrow c_{O4}$	0.26
$c_{O4} \leftrightarrow d_{O5}$	0.19
$e_{O3} \leftrightarrow d_{O4}$	0.32
$d_{O4} \leftrightarrow e_{O5}$	0.30
$f_{O3} \leftrightarrow e_{O4}$	0.45
$e_{O4} \leftrightarrow f_{O5}$	0.51

Table 6.3: Deviation of the minimum energy path from the straight line connecting the initial and final positions for (a) Mg and (b) O vacancy migration at the tilt grain boundary in the absence of an applied electric field.

The deviation of the minimum energy paths from the straight line connecting the initial and final positions of the vacancy are given in Table 6.3. It can be seen that the deviations are greater than those presented in Chapter 5, Table 5.3 for the periodic grain boundary model. This occurs because in the finite model there are less ions surrounding the path of migration therefore the migrating species is less constricted and can take a wider path. In agreement with Chapter 5 it was found that the deviations are largest for migrations in the sparsely packed region of the grain boundary.

6.3.1.4 Interstitials in the MgO Grain Boundary Film in the Absence of an External Electric Field

Interstitials were placed at different sites within the grain boundary structural unit and it was found that they relax to four distinct sites labelled *top*, *middle*, *planar* and *bottom*, as shown in Figure 6.29. This is in good qualitative agreement with the metastable interstitial sites found in Chapter 5 for the same grain boundary modelled using periodic boundary conditions. However, in this study the model is that of a finite film and it was found that the formation energy varies with z- position as shown in Figure 6.30. It can be seen that the interstitial is most energetically stable when it is located close to the centre of film and that the formation energy increases as it moves towards the fixed surfaces. This occurs because lattice relaxation is restricted closer to the

surfaces. In general *planar* sites have lower formation energies, whereas *bottom* sites are the most unstable. This is in contrast to the results obtained using the periodic model in Chapter 5. This suggests that the fixed edges and surfaces affects the formation energies of the interstititals.

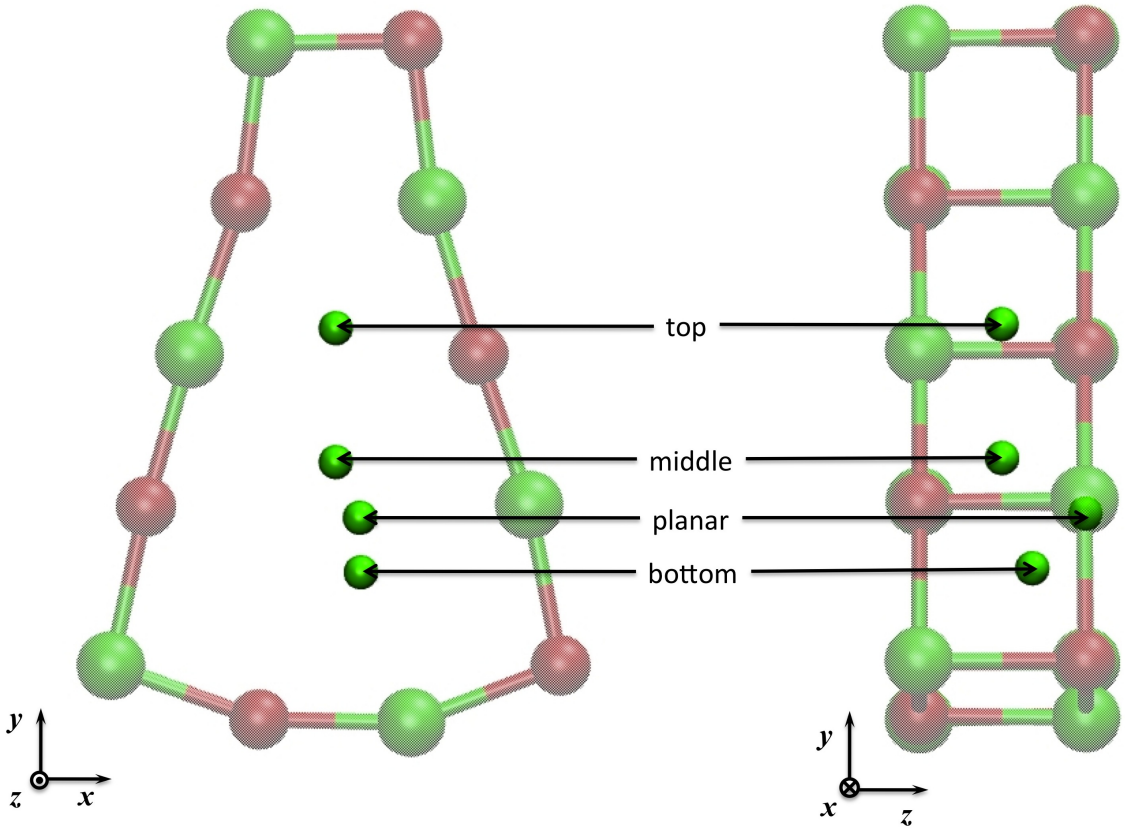

Figure 6.29: Interstitial sites in the grain boundary structural unit.

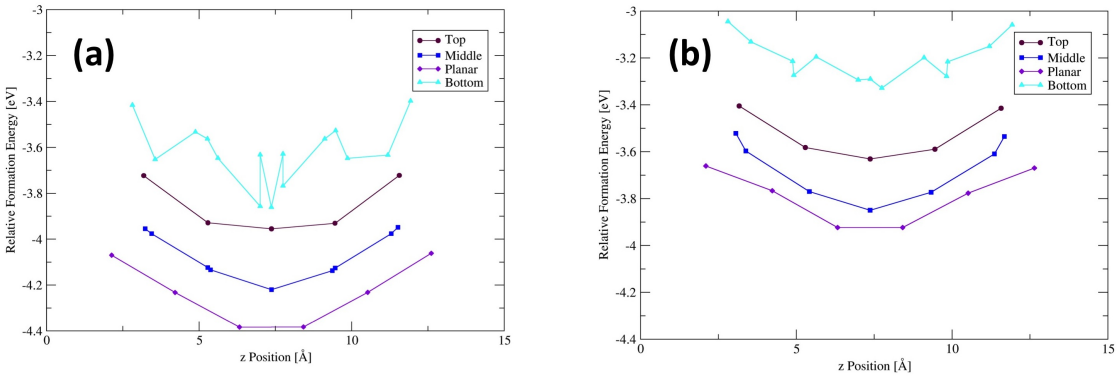

Figure 6.30: Relative formation energy as a function of z- position for (a) Mg and (b) O interstitials in top, middle, planar and bottom sites of the tilt grain boundary in the absence of an external field.

The activation energies for Mg and O interstitial migration were determined and are shown in Figure 6.31 and Figure 6.32. It was found that interstitials migrate between *top* sites, between

middle and *planar* sites and between *planar* and *bottom* sites. The lowest activation energies occur for migrations from *bottom* sites to *planar* sites which corresponds to migration from sites with the highest formation energy to those with the lowest formation energy. Once an interstitial migrates to a *planar* site it becomes strongly bound such that the reverse barrier is significantly high. It can also be seen that in general it is most energetically favourable for interstitials to migrate away from the fixed surfaces towards the centre of the film.

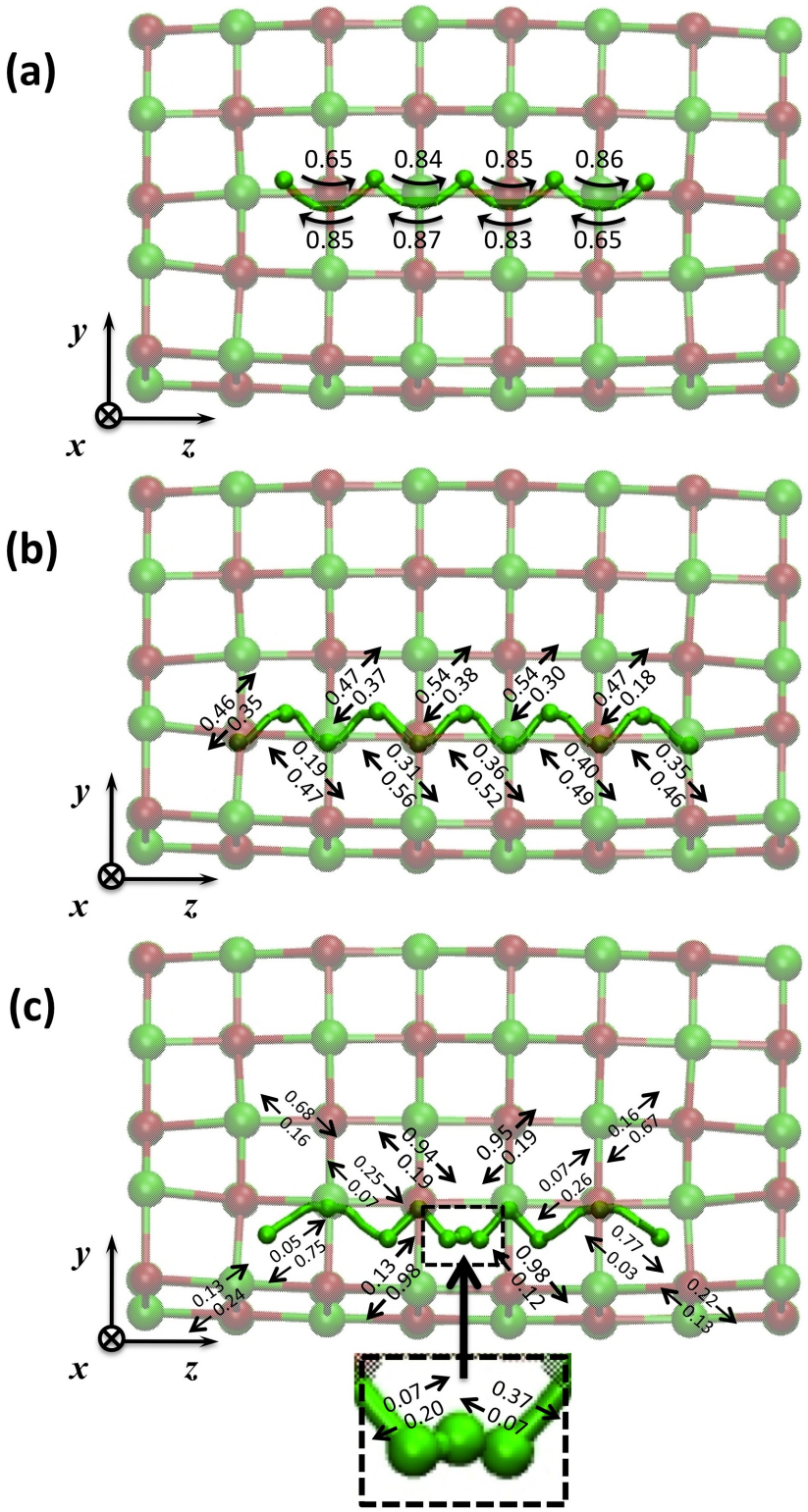

Figure 6.31: Activation energies, in units of eV, for Mg interstitial migration in the grain boundary film in the absence of an external electric field.

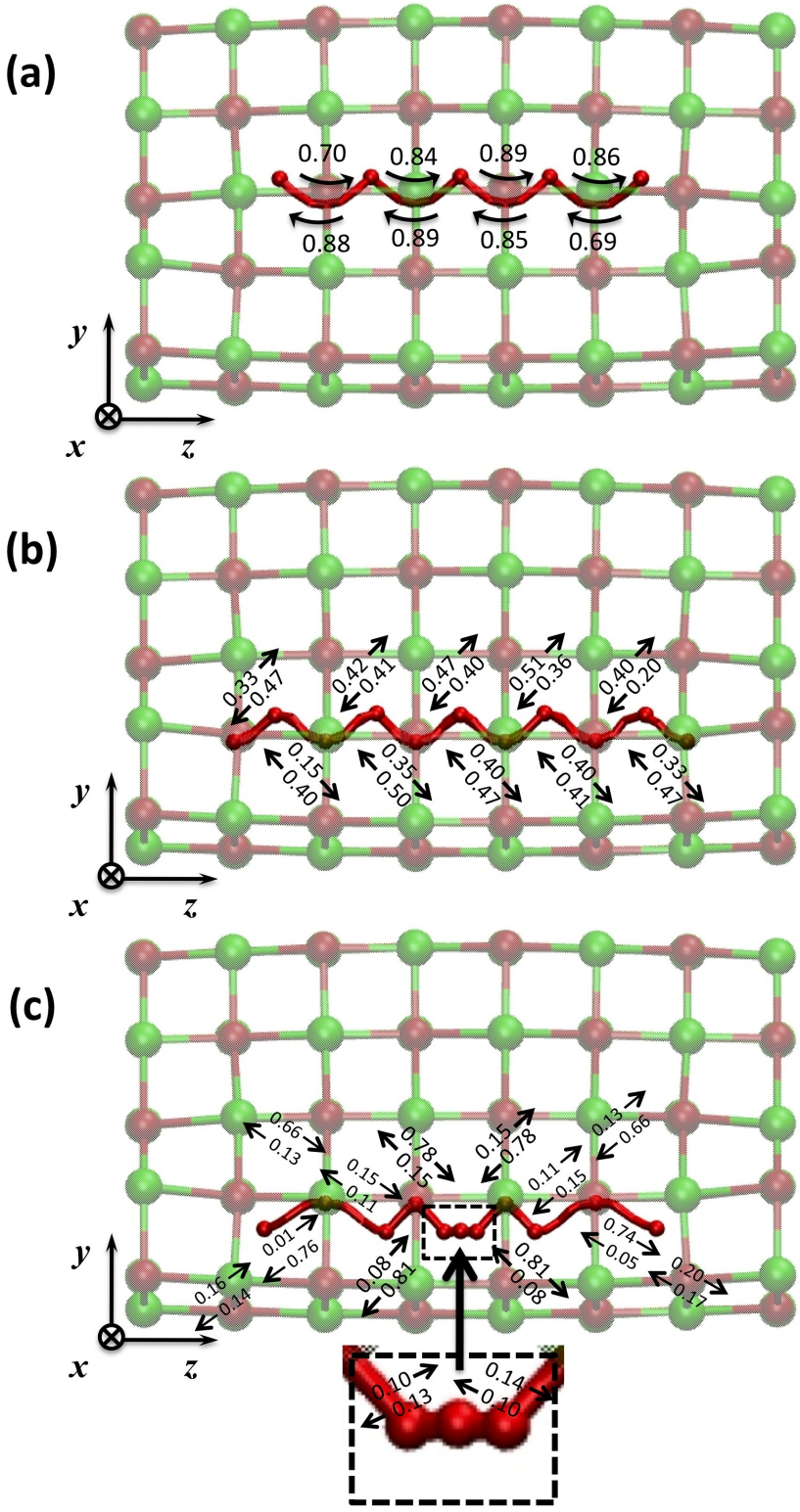

Figure 6.32: Activation energies, in units of eV, for O interstitial migration in the grain boundary film in the absence of an external electric field.

6.3.2 Defect Properties in the Presence of an Electric Field

6.3.2.1 Vacancies in the Bulk-Like MgO Film in the Presence of an External Electric Field

An external electric field corresponding to a potential difference of 5 V was applied to the MgO film using the charged plates of Model A. The formation energy of the vacancy sites were determined and were plotted as a function of z- position as shown in Figure 6.33. It can be seen that the application of the field causes vacancy sites to become inequivalent across the imaginary central x-y plane and the symmetry is lost from the plots of the formation energy. For Mg vacancies the formation energy increases with increasing z- position, however the O vacancy formation energies decrease with increasing z- position. For the Mg vacancy this occurs because the absence of the Mg lattice ion causes the net charge of the film to be negative and localised at the vacancy site. Therefore as the z- position of this negative charge increases and the vacancy approaches the positively charged plate the vacancy site becomes energetically favourable due to electrostatic attraction. With the application of the field the most energetically favourable Mg vacancy identified was found to have a formation energy of 24.77 eV. Conversely, the most energetically favourable O vacancy observed occurred in a plane close to the negatively charged plate. This occurs because the presence of the vacancy results in a positive net film charge localised at the vacancy site which is electrostatically attracted to the negatively charged plate. Here the O vacancy was found to have a formation energy of 25.51 eV.

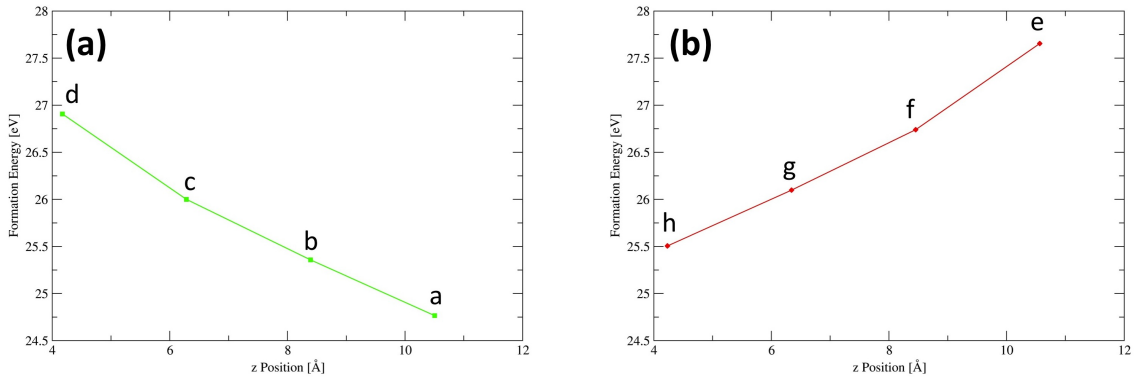

Figure 6.33: Formation energy as a function of z- position for (a) Mg and (b) O vacancies in the presence of an external field corresponding to a potential difference of 5 V.

Activation energies were determined for vacancy migration in the presence of the external electric field. It can be seen that for Mg vacancies a low energy pathway exists involving migrations in the positive z- direction from metastable sites towards lower energy vacancy sites. The activation

energy increases with each migration towards the positively charged plate. Conversely for O vacancies a low energy pathway exists in the negative z- direction towards the negatively charged plate. Again the activation energies increase with each migration.

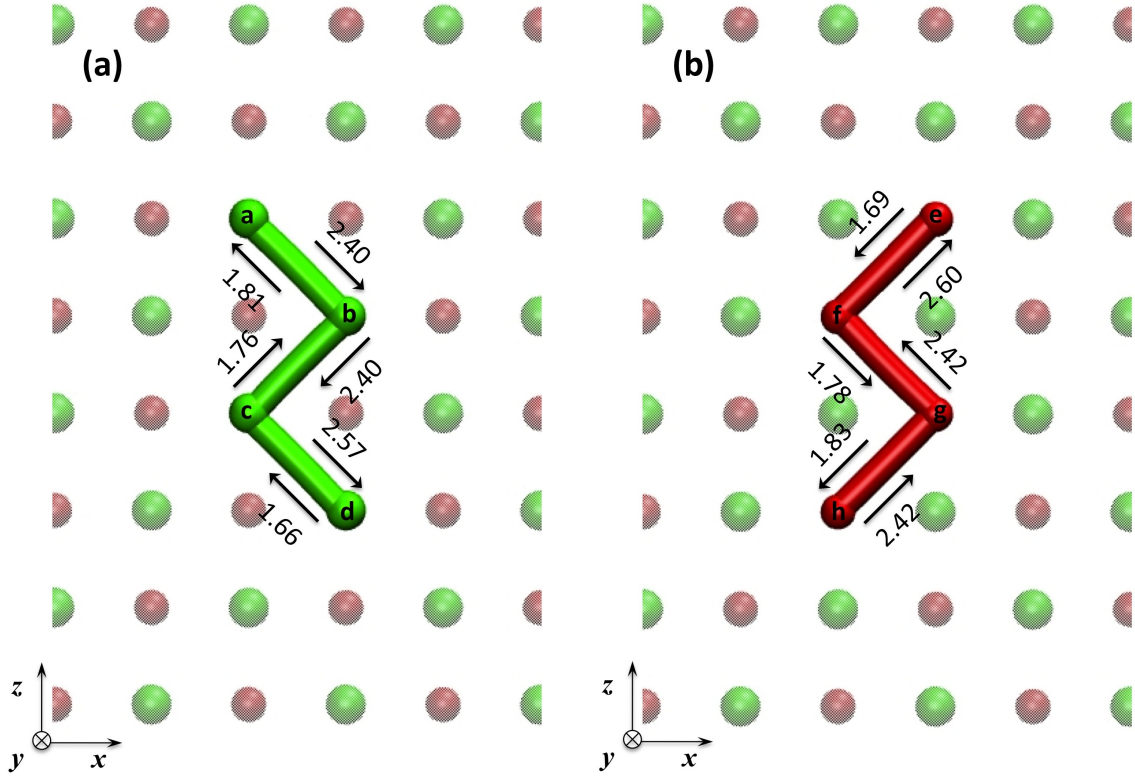

Figure 6.34: Activation energies for (a) Mg and (b) O vacancy migration in the bulk-like MgO film in the presence of an external electric field corresponding to a potential difference of 5 V. Activation energies are given in units of eV.

6.3.2.2 Interstitials in the Bulk-Like MgO Film in the Presence of an External Electric Field

When an external electric field corresponding to a potential difference of 5 V was applied it can be seen from Figure 6.35 that for Mg interstitials the formation energy increases with increasing z-position. It is energetically favorable for the Mg interstitial to be located close to the bottom x-y plane of the film. This occurs because the Mg interstitial is positively charged and therefore due to electrostatics it will be attracted towards the negatively charged plate adjacent to the bottom surface of the film. Conversely the O interstitial is energetically favourable when it is located close to the positively charged plate. The lowest formation energies were determined as -11.29 eV and -12.25 eV for Mg and O interstitials respectively.

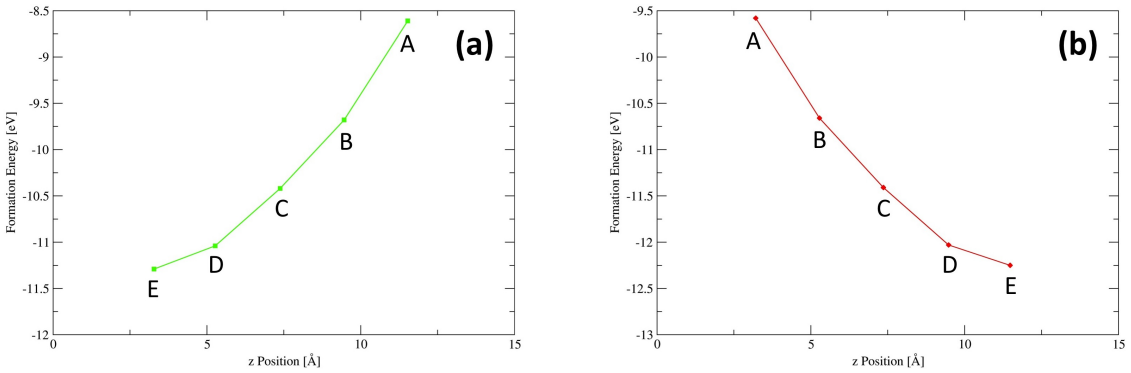

Figure 6.35: Formation energy as a function of z- position for (a) Mg and (b) O interstitials in the bulk-like MgO film in the presence of an external field corresponding to a potential difference of 5 V.

Activation energies were determined for interstitial migrations in the z- direction in the presence of the external electric field. These are shown in Figure 6.36. It can be seen that for Mg interstitials the activation energies for migration in the negative z- direction are lower than the reverse barriers. This corresponds to migration towards the interstitial site with the lowest formation energies. Whereas for O interstitials the lowest activation energies correspond to migrations towards the positively charged plate.

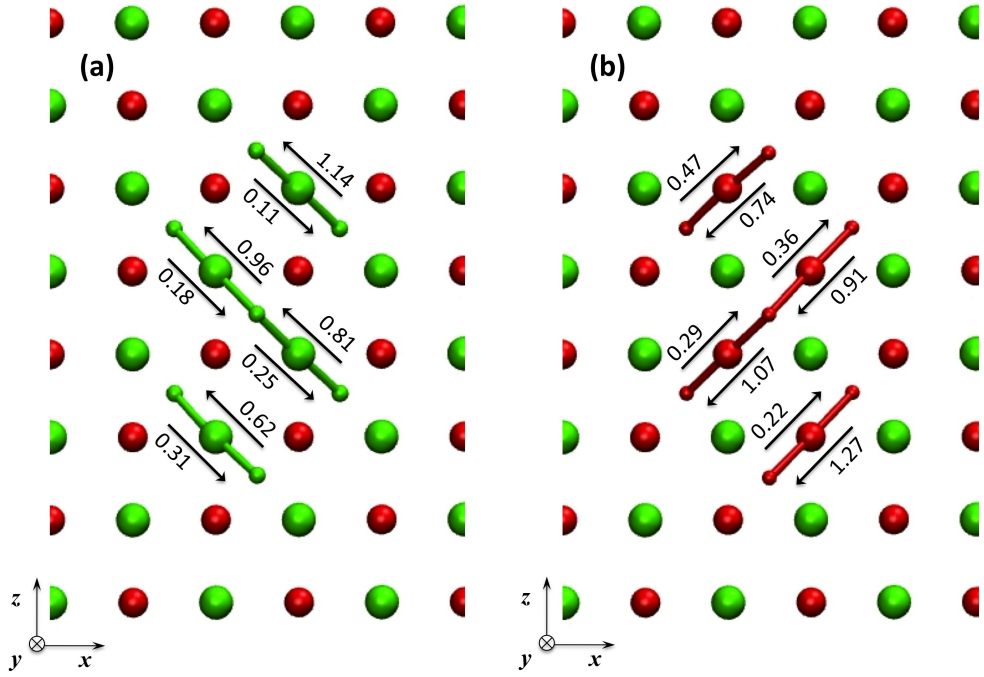

Figure 6.36: Activation energies, in units of eV, for (a) Mg and (b) O interstitial migration in the bulk MgO film in the presence of an external electric field corresponding to a potential difference of 5 V.

6.3.2.3 Vacancies in the MgO Grain Boundary Film in the Presence of an External Field

An external electric field corresponding to a potential difference of 5 V was applied across the grain boundary film and the formation energies were determined for the sites shown in Figure 6.25. The relative formation energies were found by comparing the formation energies to the lowest formation energy determined for the equivalent vacancy species at the two central x-y planes of the MgO film in the presence of the electric field of the same value. In the bulk-like film these formation energies were determined as 25.36 eV and 26.10 eV for Mg and O vacancies respectively. The relative formation energies were plotted as a function of z- position and are shown in Figure 6.37. It can be seen that the electric field reduces the symmetry of the film in the z- direction and that for Mg vacancies the formation energy decreases with increasing z-position, as the vacancy approaches the positively charged plate. For O vacancies the formation energy increases as the vacancy approaches the positively charged plate due to electrostatic repulsion. Again both Mg and O vacancies tend to have lower formation energies when they are located at Site a and the lowest formation energies were determined as 24.25 eV and 25.08 eV for Mg and O vacancies respectively, which correspond to relative formation energies of -0.55 eV and -0.67 eV.

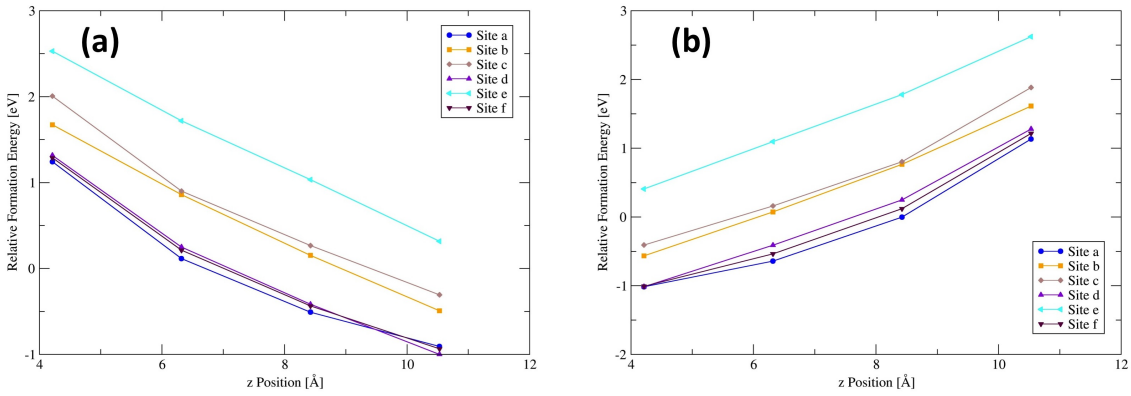

Figure 6.37: Relative formation energy as a function of z position for (a) Mg and (b) O vacancy sites at the grain boundary in the presence of an external electric field corresponding to 5 V.

The activation energies for vacancy migration in the presence of a field are shown in Figure 6.38 and Figure 6.39. For Mg vacancies it can be seen that fast diffusion pathways occur in the z-direction towards the positively charged electrode. These pathways involve migrations between vacancy sites in the close packed region of the grain boundary and between sites b and c. Whereas for O vacancies fast diffusion pathways occur in the negative z- direction for migrations involving vacancy sites c and d where the structure is less dense.

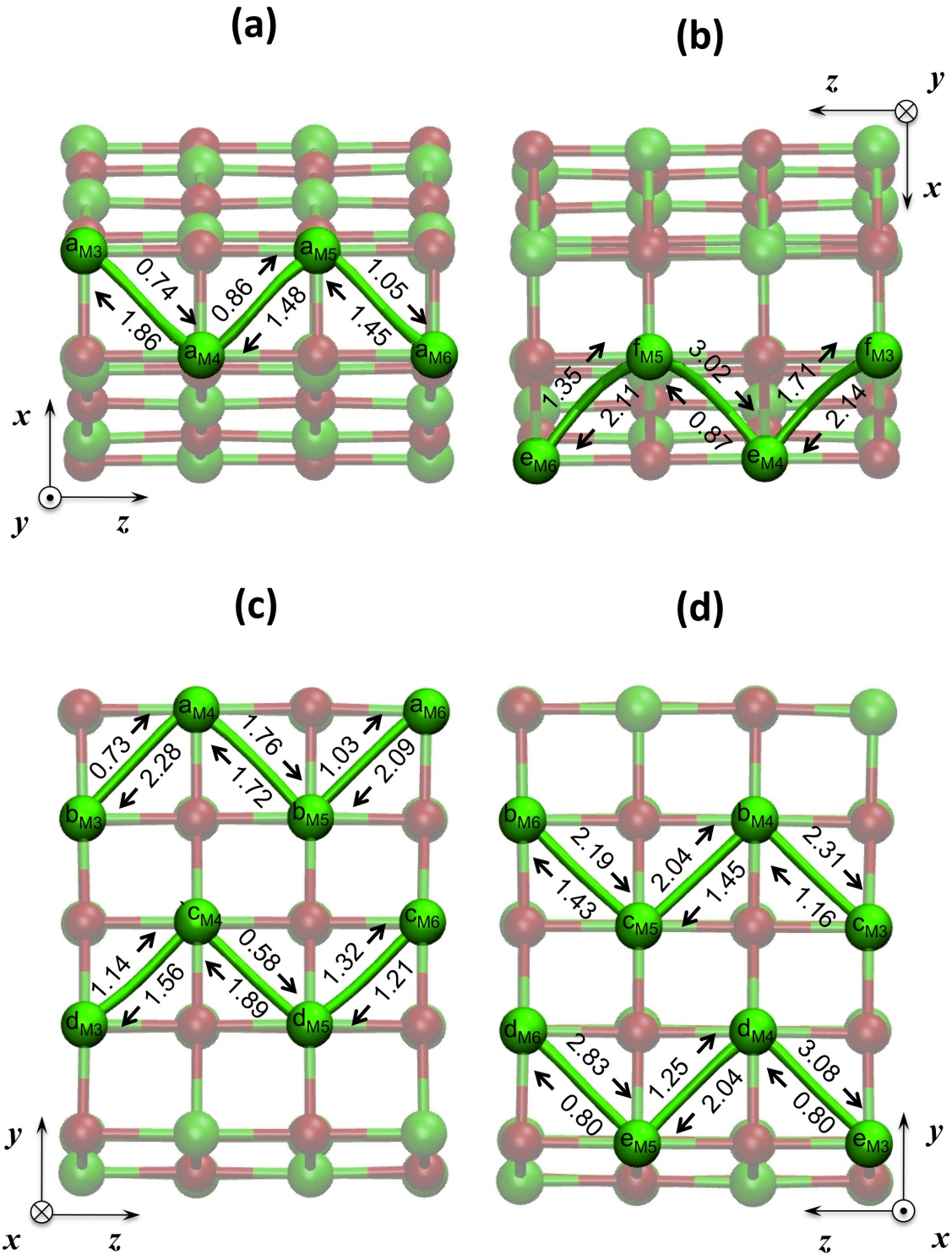

Figure 6.38: Activation energies, in units of eV, for Mg vacancy migration in the grain boundary in the presence of an external electric field corresponding to a potential difference of 5 V.

The deviation of the minimum energy path from the straight line connecting the initial and final positions of the vacancy are given in Table 6.4. It can be seen that the application of the field increases the deviations. However the largest deviations still occur a for migrations at the sparsely

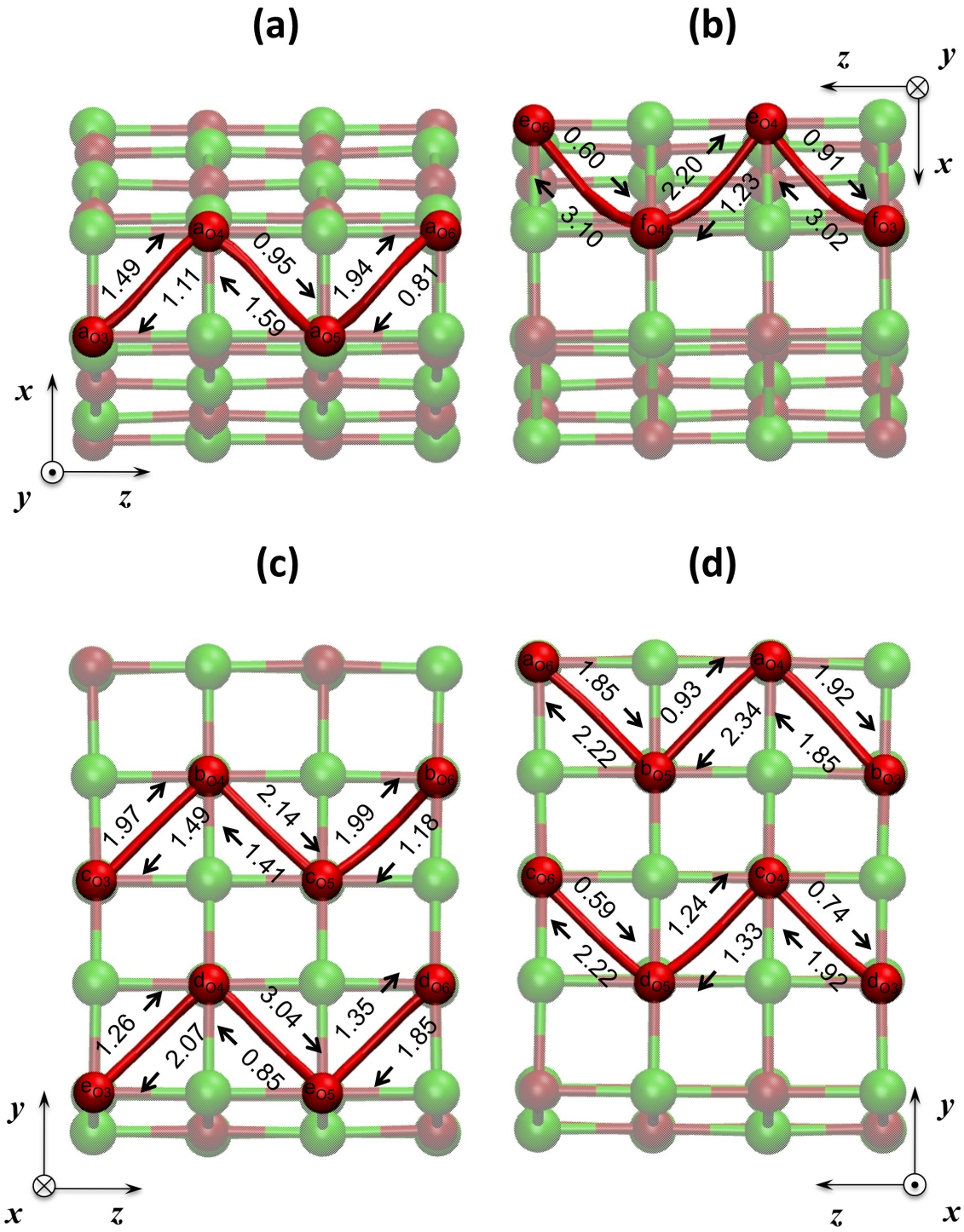

Figure 6.39: Activation energies, in units of eV, for O vacancy migration in the grain boundary in the presence of an external electric field corresponding to a potential difference of 5 V.

(a)

Mg Vacancy	
Migration Path	Deviation [Å]
$a_{M3} \leftrightarrow a_{M4}$	0.42
$a_{M4} \leftrightarrow a_{M5}$	0.20
$a_{M5} \leftrightarrow a_{M6}$	0.21
$b_{M3} \leftrightarrow a_{M4}$	0.41
$a_{M4} \leftrightarrow b_{M5}$	0.11
$b_{M5} \leftrightarrow a_{M6}$	0.12
$c_{M3} \leftrightarrow b_{M4}$	0.05
$b_{M4} \leftrightarrow c_{M5}$	0.15
$c_{M5} \leftrightarrow b_{M6}$	0.13
$d_{M3} \leftrightarrow c_{M4}$	0.18
$c_{M4} \leftrightarrow d_{M5}$	0.42
$d_{M5} \leftrightarrow c_{M6}$	0.16
$e_{M3} \leftrightarrow d_{M4}$	0.51
$d_{M4} \leftrightarrow e_{M5}$	0.22
$e_{M5} \leftrightarrow d_{M6}$	0.48
$f_{M3} \leftrightarrow e_{M4}$	0.33
$e_{M4} \leftrightarrow f_{M5}$	0.58
$f_{M5} \leftrightarrow e_{M6}$	0.43

(b)

O Vacancy	
Migration Path	Deviation [Å]
$a_{O3} \leftrightarrow a_{O4}$	0.30
$a_{O4} \leftrightarrow a_{O5}$	0.22
$a_{O5} \leftrightarrow a_{O6}$	0.42
$b_{O3} \leftrightarrow a_{O4}$	0.11
$a_{O4} \leftrightarrow b_{O5}$	0.11
$b_{O5} \leftrightarrow a_{O6}$	0.18
$c_{O3} \leftrightarrow b_{O4}$	0.04
$b_{O4} \leftrightarrow c_{O5}$	0.07
$c_{O5} \leftrightarrow b_{O6}$	0.62
$d_{O3} \leftrightarrow c_{O4}$	0.45
$c_{O4} \leftrightarrow d_{O5}$	0.20
$d_{O5} \leftrightarrow c_{O6}$	0.43
$e_{O3} \leftrightarrow d_{O4}$	0.40
$d_{O4} \leftrightarrow e_{O5}$	0.53
$e_{O5} \leftrightarrow d_{O6}$	0.34
$f_{O3} \leftrightarrow e_{O4}$	0.66
$e_{O4} \leftrightarrow f_{O5}$	0.52
$f_{O5} \leftrightarrow e_{O6}$	0.74

Table 6.4: Deviation of the minimum energy path from the straight line connecting the initial and final positions for (a) Mg and (b) O vacancy migration at the tilt grain boundary in the presence of an applied electric field corresponding to a potential difference of 5 V.

packed region of the grain boundary.

6.3.2.4 Interstitials in the MgO Grain Boundary Film in the Presence of an External Electric Field

An external field corresponding to a potential difference of 5 V was applied and the interstitial formation energies were plotted as a function of z- position as shown in Figure 6.40. It can be seen that for Mg interstitials the formation energy increases with an increase in z- and that it is energetically most favourable for an interstitial to be located near the bottom x-y plane where it is close to the negatively charged plate. Conversely for O interstitials the formation energy decreases with increasing z- position.

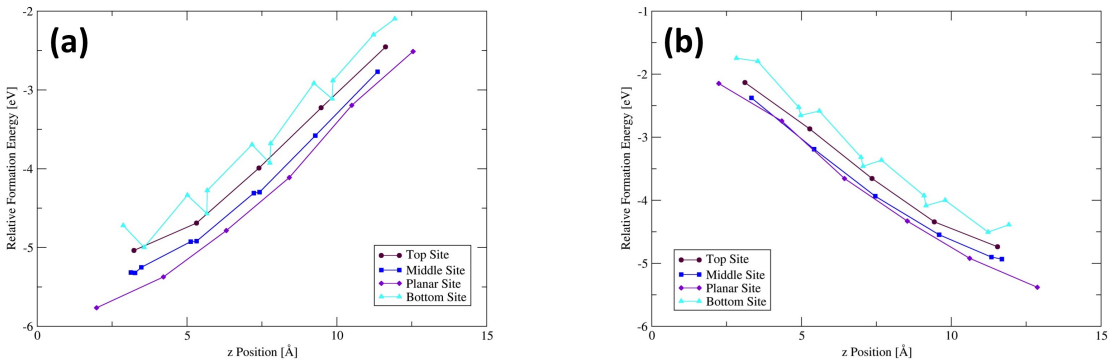

Figure 6.40: Relative formation energy as a function of z- position for (a) Mg and (b) O interstitials in *top*, *middle*, *planar* and *bottom* sites of the tilt grain boundary in the presence of an external field corresponding to a potential difference of 5 V.

The activation energies for Mg and O interstitial migration at the grain boundary in the presence of the field are shown in Figure 6.41 and Figure 6.42 respectively. It can be seen that the presence of the field induces lower energy barriers for Mg migration in the negative z- direction and that fast diffusion pathways exist with mechanisms involving *top* to *top* and *middle* to *planar* sites. For migrations between *planar* and *bottom* sites it can be seen that lower barriers exist for migration towards *planar* sites however the reverse barriers are significantly higher. This suggests that an interstitial can migrate from a *bottom* site to a *planar* site where it will remain or migrate to a *middle* site. The lowest activation energy determined is 0.21 eV for a migration from a *middle* to a *planar* site, which is large in comparison 0.11 eV which was determined for Mg interstitial migration in bulk MgO. For O interstitials it can be seen that lower energy barriers are determined for migration in the positive z- direction and again, fast diffusion pathways exist for *top* to *top* and *middle* to *planar* site migration. The lowest barrier observed for O interstitial migration is 0.20 eV for migration from a *planar* to a *middle* site which is slightly lower than 0.22 eV which was determined for migration in bulk MgO.

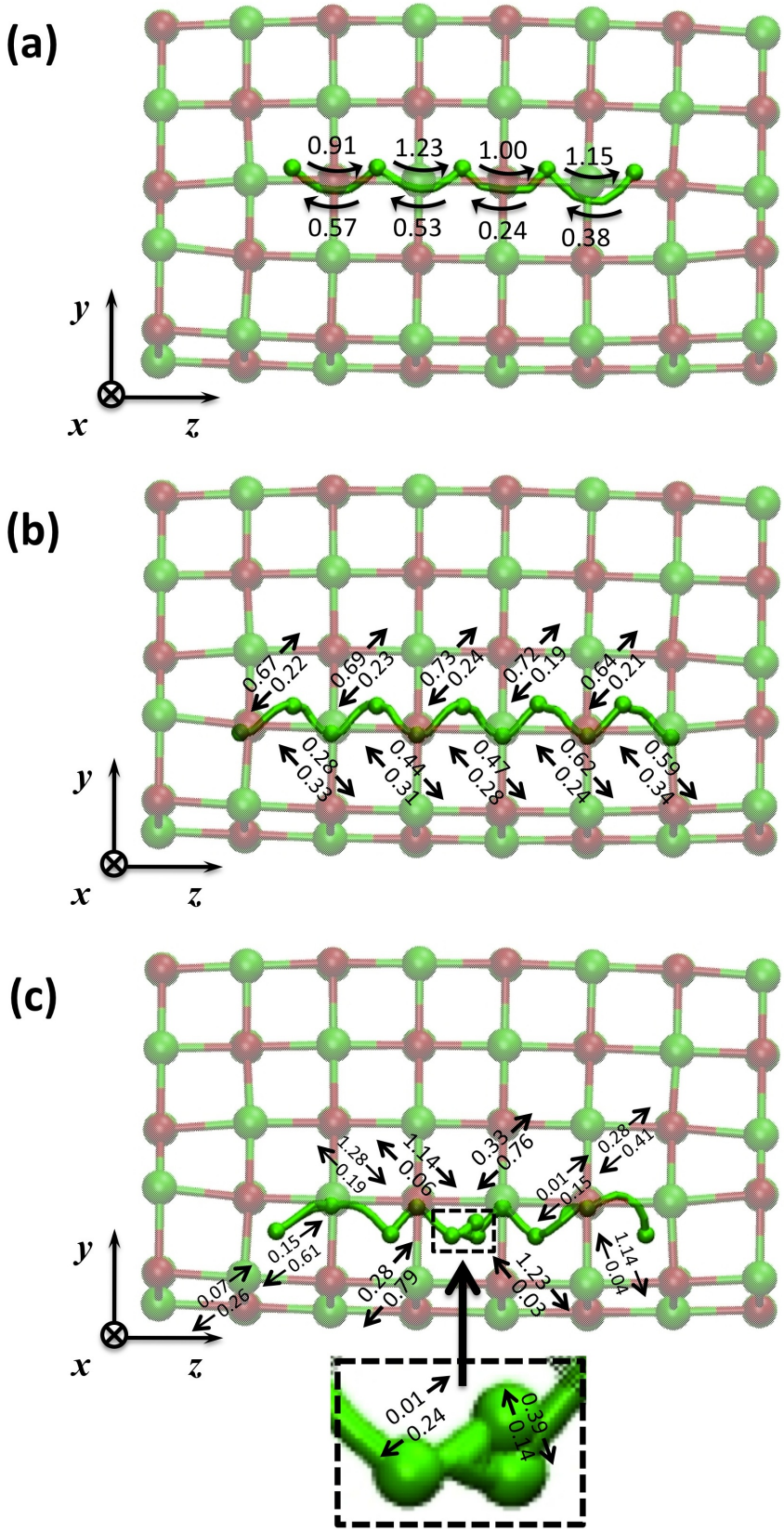

Figure 6.41: Activation energy, in units of eV, for Mg interstitial migration in the grain boundary film in the presence of an external electric field corresponding to 5 V.

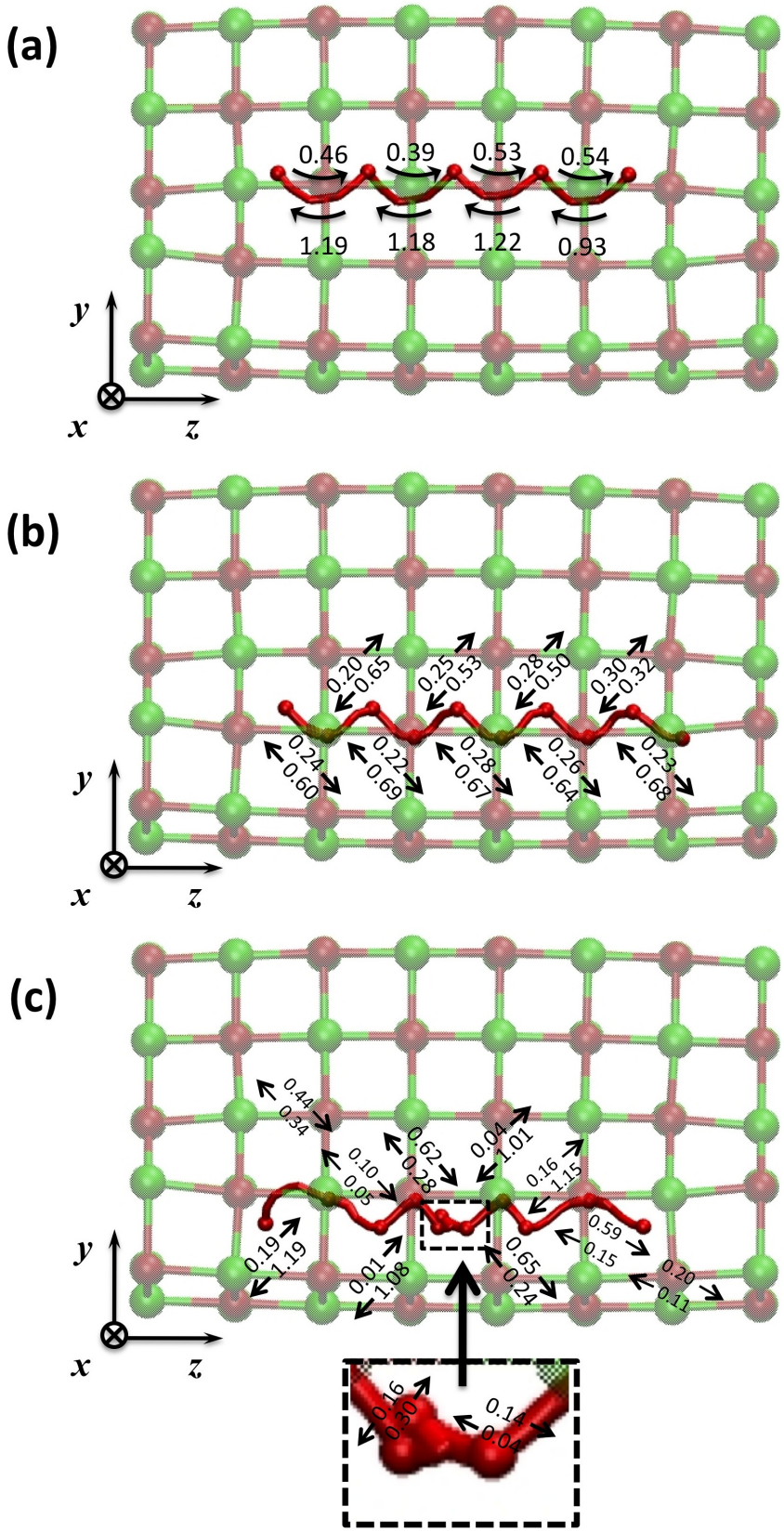

Figure 6.42: Activation energy, in units of eV, for O interstitial migration in the grain boundary film in the presence of an external electric field corresponding to 5 V.

6.4 Conclusions

A summary of the lowest defect formation energies in bulk MgO and at the tilt grain boundary are given in Table 6.5 and Table 6.6. It can be seen that the effect of the field is to lower the formation and activation energies for both vacancies and interstitials however defect migration was found to be anisotropic. Mg vacancies and O interstitials are negatively charged defects and their formation energies decrease the closer the defect is to the positively charged electrode. Conversely the formation energy of positively charged O vacancies and Mg interstitials decreases the closer the defect is to the negatively charged plate. In the application of the field fast diffusion pathways exist for vacancy migration in the z- direction perpendicular to the grain boundary plane. A fast diffusion pathway in the z- direction can also be suggested for O interstitial migration in the presence of the field. However it can be seen that for Mg interstitials the lowest activation energy determined in the presence of the field is higher than that in bulk MgO. Therefore bulk transport will be more favourable for Mg interstitials.

		Mg Vacancy			O Vacancy			Schottky Defect	
		Formation		Migration	Formation		Migration	Formation	
		E_f [eV]	E_{f_rel} [eV]	E_a [eV]	E_f [eV]	E_{f_rel} [eV]	E_a [eV]	$E_{Schottky}$ [eV]	$E_{Schottky\_rel}$ [eV]
Bulk	No Field	25.69	-	2.03	26.42	-	2.05	11.16	-
	With Field	24.77	-	1.66	25.51	-	1.69	9.34	-
Grain Boundary	No Field	25.13	-0.56	0.84	25.75	-0.67	0.96	10.27	-0.89
	With Field	24.25	-0.55	0.58	25.08	-0.67	0.59	8.73	-0.61

Table 6.5: Summary of the lowest vacancy formation energies, activation energies and corresponding Schottky defect formation energies for a vacancy in the bulk-like MgO film and at the grain boundary in the absence of an external electric field and in the presence of an electric field corresponding to a potential difference of 5 V.

		Mg Interstitial			Mg Frenkel Defect		O Interstitial			O Frenkel Defect	
		Formation		Migration	Formation		Formation		Migration	Formation	
		E_f [eV]	E_{f_rel} [eV]	E_a [eV]	$E_{Frenkel}$ [eV]	$E_{Frenkel\_rel}$ [eV]	E_f [eV]	E_{f_rel} [eV]	E_a [eV]	$E_{Frenkel}$ [eV]	$E_{Frenkel\_rel}$ [eV]
Bulk	No Field	-10.41	-	0.14	15.28	-	-11.39	-	0.25	15.03	-
	With Field	-11.29	-	0.11	13.48	-	-12.25		0.22	13.26	-
Grain Boundary	No Field	-14.81	-4.38	0.18	10.32	-4.96	-15.32	-3.92	0.15	10.43	-4.6
	With Field	-16.19	-5.76	0.22	8.06	-5.42	-16.79	-5.38	0.20	8.29	-4.97

Table 6.6: Summary of the lowest interstitial formation energies, activation energies and corresponding Frenkel defect formation energies for an interstitial in the bulk-like MgO film and at the grain boundary in the absence of an external electric field and in the presence of an electric field corresponding to a potential difference of 5 V.

Chapter 7

The Effect of Temperature on Grain Boundary Properties

7.1 Introduction

MgO has a high melting temperature of 3125 K and as a result it is used in many refractory applications. MgO is also present in the lower mantle of the Earth where grain boundaries have been suggested to provide fast pathways for the transport of carbon from the metallic core of the Earth [39]. This chapter presents the results from an atomistic molecular dynamics study on the stability of two different types of MgO grain boundary as a function of temperature. Here the grain boundaries studied were the Σ17 {410}/[001] tilt grain boundary along with two of its variations - the shifted tilt grain boundary and the additional column grain boundary, and the Σ5 twist grain boundary. Properties of bulk MgO are also included for comparison. Possible structural transformations between the tilt grain boundary variations were of particular interest and the properties investigated include structure, interfacial energy and entropy. These were determined in the temperature range 300 K to 3000 K.

7.2 Methods

7.2.1 Generating the Grain Boundary Unit Cells

The standard Σ17 {410}/[001] tilt grain boundary was generated using the METADISE code as described in Chapter 4, and is shown in Figure 7.1 (a). In the diagram the grain boundary plane is

parallel to the y- axis and the structural units propagate in the z- direction. The shifted tilt grain boundary unit cell was produced by cleaving the standard tilt grain boundary unit cell along the plane of the boundary and shifting one half of the cell with respect to the other by 3.911 Å parallel to the boundary plane as in Figure 7.1 (b). To produce the additional column grain boundary the standard tilt boundary unit cell was again cleaved however this time one half of the cell was displaced by 2.106 Å (half the lattice constant of MgO) in the x- direction perpendicular to the grain boundary plane and also by 2.106 Å in the z- direction with respect to the other half of the cell such that like atoms are coincident across the boundary plane. Three columns of alternating Mg and O ions, propagating in the z- direction, were then added to the grain boundary space as shown in Figure 7.1 (c). The standard and shifted tilt grain boundary supercells comprise of 1344 ions whereas the additional column grain boundary consists of 1488 ions.

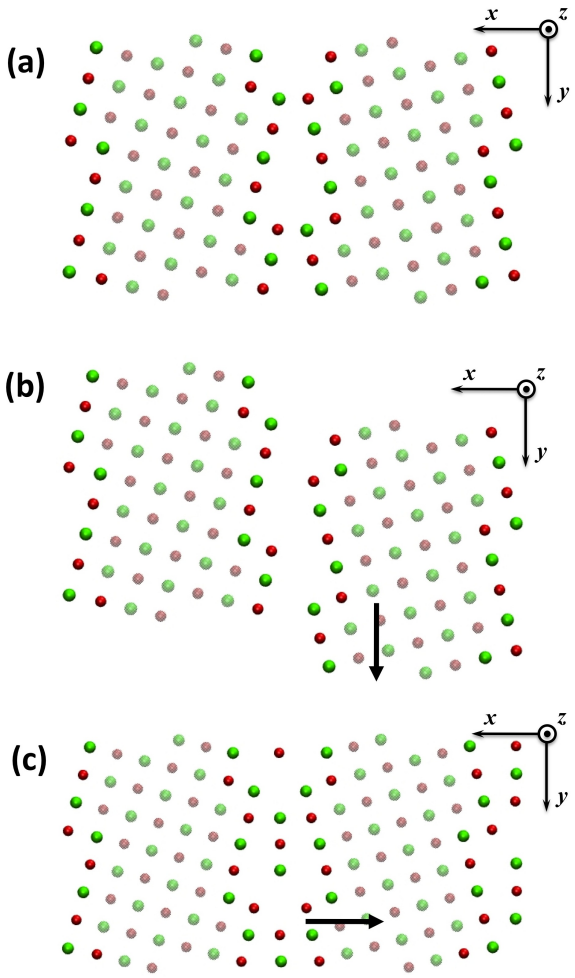

Figure 7.1: The unrelaxed tilt grain boundary variations. The (a) standard tilt grain boundary, (b) the shifted tilt grain boundary and (c) the additional column tilt grain boundary. The arrows show the directions of the half cell displacements. Solid spheres represent the ions at the grain boundary, whereas translucent spheres are used to depict the rest of the lattice.

The twist grain boundary was generated using the MIDAS code as described in Chapter4. This structure consists of a grain boundary which is parallel to the z- axis and is sandwiched between bulk-like planes of MgO. Figure 7.2 shows the grain boundary unit cell, the grain boundary plane and one of the bulk-like planes. The twist grain boundary supercell contains 1584 ions.

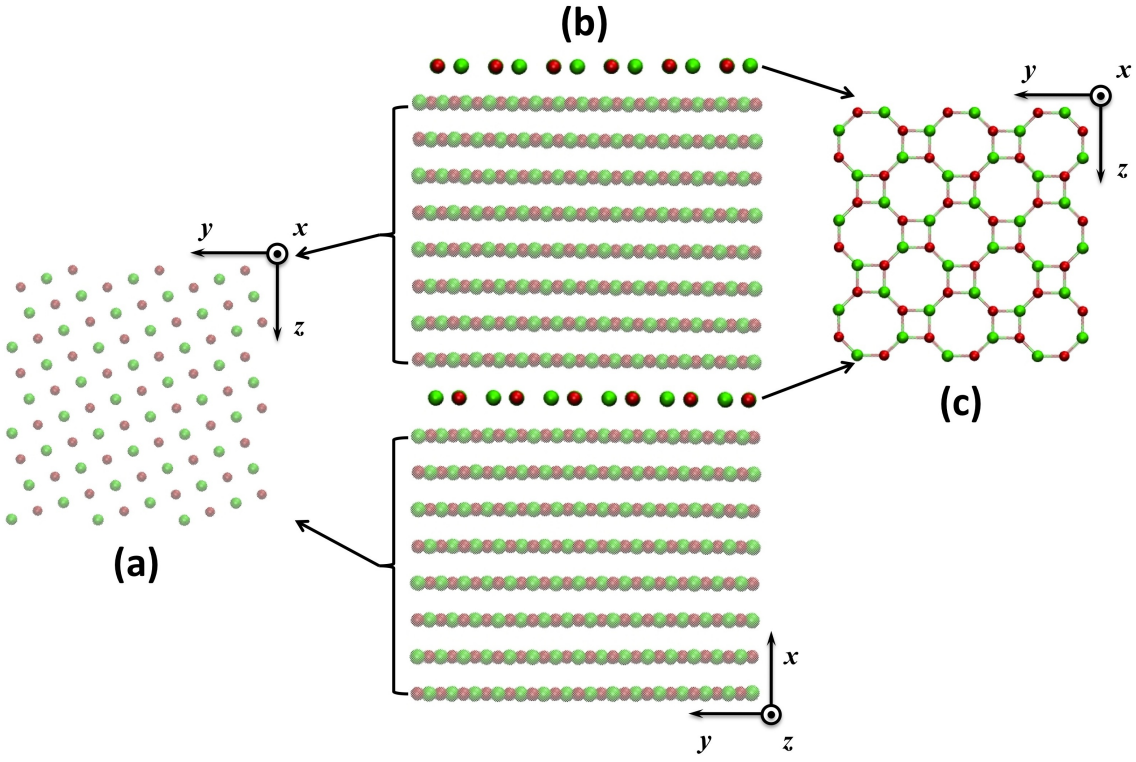

Figure 7.2: The (a) bulk-like plane, (b) the unit cell and (c) the grain boundary plane for the MgO twist grain boundary.

7.2.2 Computational Methods

In order for temperature effects to be included explicitly calculations were carried out on the periodic models using molecular dynamics simulations implemented in the DL_POLY_2 code. The interactions between ions were represented by the semi-empirical pair potential of Sangster and Stoneham [119] with a rigid ion model as opposed to the shell model. The NPT Hoover ensemble was used for bulk MgO simulations whereas the NST Hoover ensemble was used for the grain boundary simulations. For both ensembles the thermostat and barostat relaxation times were 0.1 ps and 1.0 ps respectively. A timestep equating to 0.001 ps was used and simulations were executed for 20,000 time steps with a 200 timestep equilibration period. In all simulations a pressure of 0 k atm was used. For a single simulation the force and Van der Waals cutoffs had the same value, however they differed between systems. For the bulk, the standard tilt and the

twist grain boundaries the cutoff was 8.5 Å, however for the shifted and additional column grain boundaries the cutoffs were 7.5 Å and 8.0 Å respectively. For each structure simulations were carried out in the temperature range 300 K to 3000 K at 300 K increments. These were done in series whereby the starting configuration of a simulation was taken as the final configuration from the previous lower temperature simulation. Velocities were sampled every 0.02 ps and an origin interval of 0.08 ps was used for the velocity correlation function.

7.2.3 Methods of Analysis

The interfacial energy, E_{IF}, at temperature, T, was calculated as follows:

$$E_{IF} = E_{intern\_GB} - (E_{coh\_bulk} \cdot n_{GB})$$

where E_{intern_GB} is the internal energy of the grain boundary at T, E_{coh_bulk} is the cohesive energy of bulk MgO at temperature T and n_{GB} is the number of Mg-O units in the grain boundary unit cell. The bulk cohesive energy can be determined as:

$$E_{coh\_bulk} = \frac{E_{intern\_bulk}}{n_{bulk}}$$

where E_{intern_bulk} is the internal energy of bulk MgO and n_{bulk} is the number of Mg-O units in bulk MgO.

In order to determine the entropy, S, of the system the velocity autocorrelation function, $C(t)$, was first determined from the velocities of the atoms taken from the simulation. By taking the Fourier transform of this function the phonon density of states, $g(\omega)$, can be determined which is found in the equation for S. The velocity autocorrelation function is a time dependent function which shows the underlying nature of the dynamical processes within a system. If the duration of a process consists of n equal and finite timesteps of δt then the velocity autocorrelation of atom i at time t is essentially the scalar product of its velocity at a time t and its velocity at a previous reference time, t_0. An average can be taken over all N atoms in the system and this can be repeated for subsequent timesteps to determine the normalised velocity autocorrelation function, $C(t)$, of the system:

$$C(t) = C(t = n\,\delta t) = \frac{\langle v_i(t = t_0)\, v_i(t_0 + n\,\delta t)\rangle}{\left\langle |v_i(t = t_0|^2 \right\rangle}$$

Usually the velocity autocorrelation function is determined for a finite number of timesteps before the a new reference time is taken. Thus for one process several autocorrelation functions can be produced and an average can be determined.

The phonon density of states, $g(\omega)$ can be produced by taking the Fourier transform of $C(t)$. The result is a function of phonon frequency revealing the underlying frequencies of the atomic vibrations. The Fourier transform of the autocorrelation function is as follows:

$$g(\omega) = \hat{C}(\omega) = \int_{-\infty}^{+\infty} C(t)\ \exp(-i\omega t)\, dt$$

Using Eulers formula:

$$\begin{aligned}\exp(-i\omega t) =& \cos(-\omega t) + i\ \sin(-\omega t) \\ =& cos(\omega t) - i\, sin(\omega t)\end{aligned}$$

the real part of the Fourier transform can be re-written as:

$$\hat{C}(\omega) = 2\int_{0}^{t_{max}} C(t)\ \cos(\omega t)\, dt$$

since $C(t)$ is an even function. The function can be divided into $2n$ equal intervals and therefore the total time elapsed by the simulation, t_{max}, is as follows:

$$t_{max} = 2n\, \delta t$$

If

$$\theta = \omega\, \delta t$$

then using the method of Filon [155, 156] the Fourier transform can be written as

$$\hat{C}(\omega) = 2\, \delta t\, [\alpha C(t_{max})\, sin(\omega t_{max}) + \beta C_e + \gamma C_o]$$

where

$$\alpha = \left(\frac{1}{\theta^3}\right)\left(\theta^2 + \theta\sin\theta\cos\theta - 2\sin^2\theta\right),$$
$$\beta = \left(\frac{2}{\theta^3}\right)\left(\theta\left(1+\cos^2\theta\right) - 2\sin\theta\cos\theta\right),$$
$$\gamma = \left(\frac{4}{\theta^3}\right)\left(\sin\theta - \theta\cos\theta\right),$$

C_e is the sum of the even terms of $C(t)\cos(\omega t)$ less one half of the first and last terms, and C_o is the sum of all the odd terms.

The phonon density of states, $g(\omega)$, can then be used to determine the phonon entropy, S, of the system using the following equation [157]:

$$S = 3Nk\int_0^\infty \left[\frac{x}{\exp(x)-1} - \ln\left(1-\exp(-x)\right)\right] g(\omega)\, d\omega$$

here,

$$N = nN_A$$

where n is the number of atoms in a formula unit and N_A is Avogadro's number and

$$x = \frac{h\upsilon}{kT}$$

where h is Planck's constant, k is the Boltzmann constant and T is temperature.

7.3 Results and Discussion

7.3.1 Structure

By observing the structure of the grain boundary unit cells after a simulation it was found that the standard tilt, additional column tilt and twist grain boundaries maintain their structure in the temperature range investigated. The structure of the grain boundaries at 300 K and 3000 K are shown in Figure 7.3. The shifted tilt grain boundary relaxes into the additional column grain boundary from 300 K and upholds this structure with increasing temperature up to 3000 K. The structures for the shifted tilt grain boundary at 300 K and 3000 K are shown in Figure 7.4.

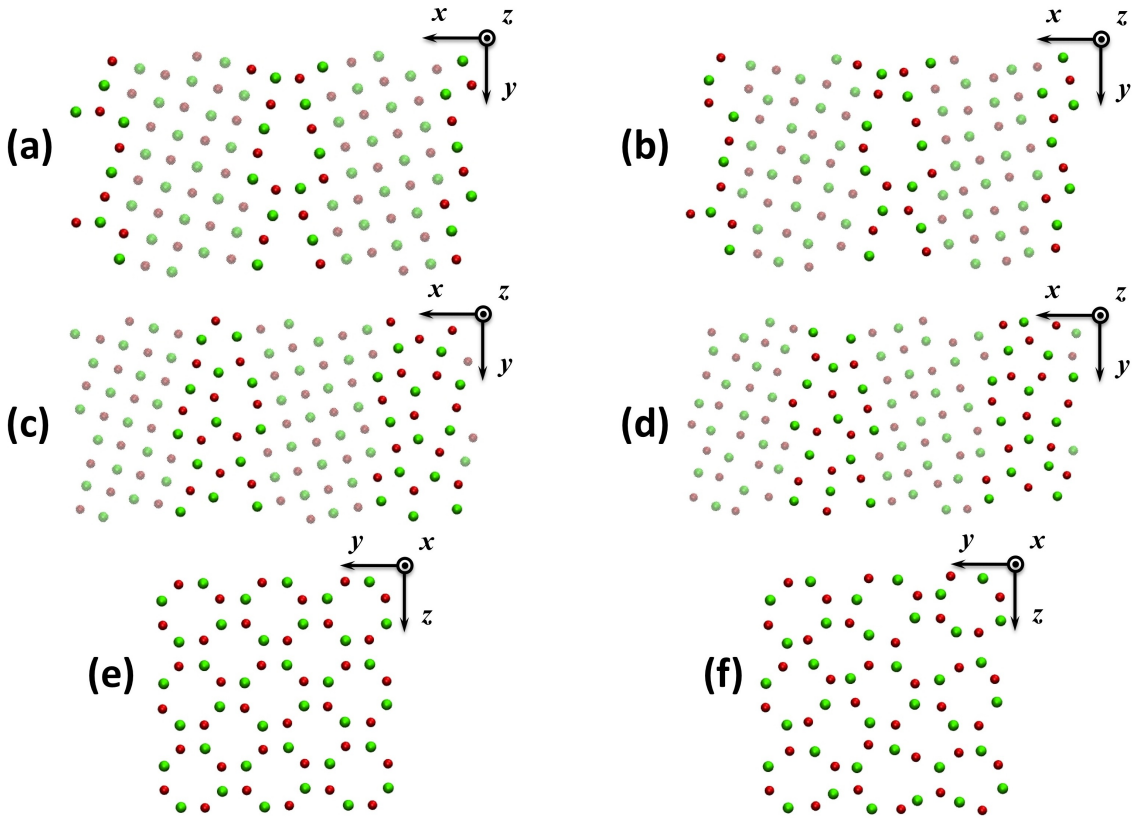

Figure 7.3: The standard tilt grain boundary at (a) 300 K and (b) 3000 K, the additional column tilt grain boundary at (c) 300 K and (d) 3000 K, and the twist grain boundary at (e) 300 K and (f) 3000 K.

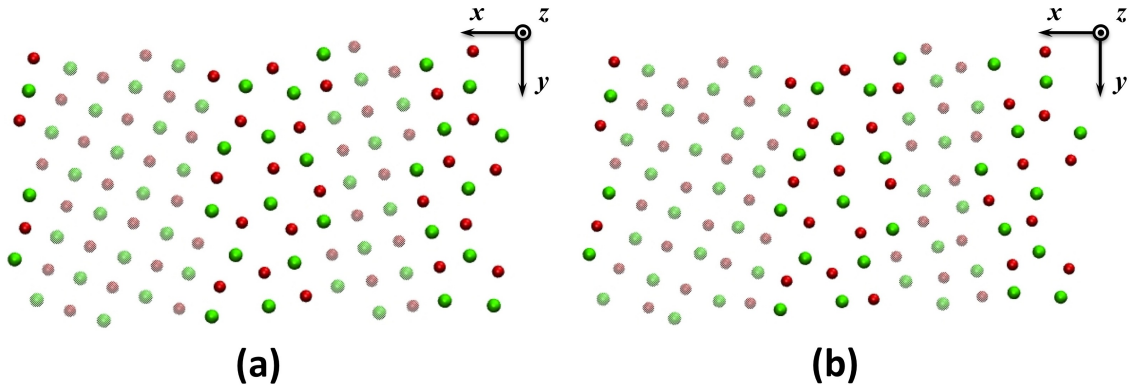

Figure 7.4: The shifted tilt grain boundary after simulations at (a) 300 K and (c) 3000 K.

7.3.2 Interfacial Energy

The graphs of interfacial energy as a function of temperature are shown in Figure 7.5. It can be seen that the standard tilt and the twist grain boundary are significantly more stable in comparison to the shifted tilt and additional column tilt grain boundaries. The shifted and additional column

tilt grain boundaries are very similar and undergo the same trends with increasing temperature which supports the finding that the shifted tilt structure relaxes to the additional column structure at low temperature. This additional column tilt grain boundary has a higher interfacial energy than the standard tilt and the twist grain boundaries because it is essentially the standard tilt grain boundary with a regular set of interstitials in the grain boundary space.

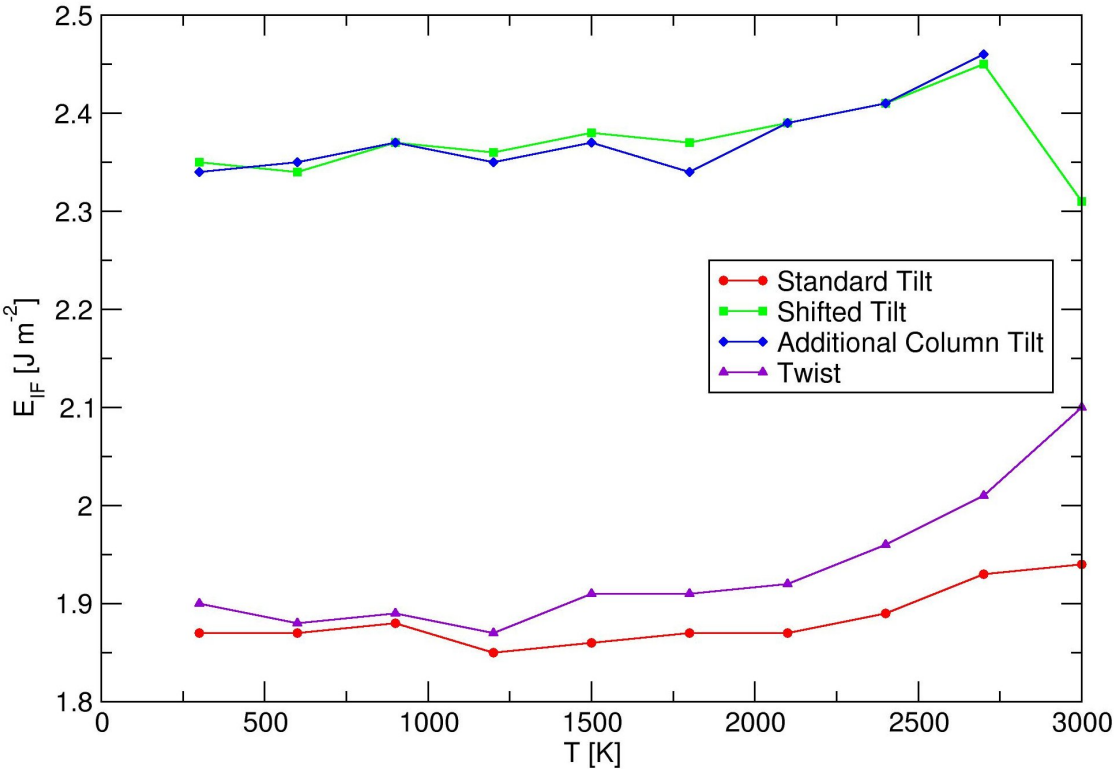

Figure 7.5: Interfacial energy as a function of temperature.

7.3.3 Phonon Entropy

The velocity autocorrelation function for bulk MgO is shown in Figure 7.6. From the graph it can be seen that the autocorellation function is sinusoidal-like with the amplitudes of oscillation decaying rapidly over time. This results in a damped harmonic function which represents a system of closely packed atoms with strong forces. The function suggests that the atoms locate themselves in positions where there is a balance between attractive and repulsive forces hence the harmonic oscillation. As the time elapsed between t and t_0 increases the velocity of an atom deviates greatly with respect to its reference velocity and there is a decorrelation which causes the damping in the velocity autocorrelation function.

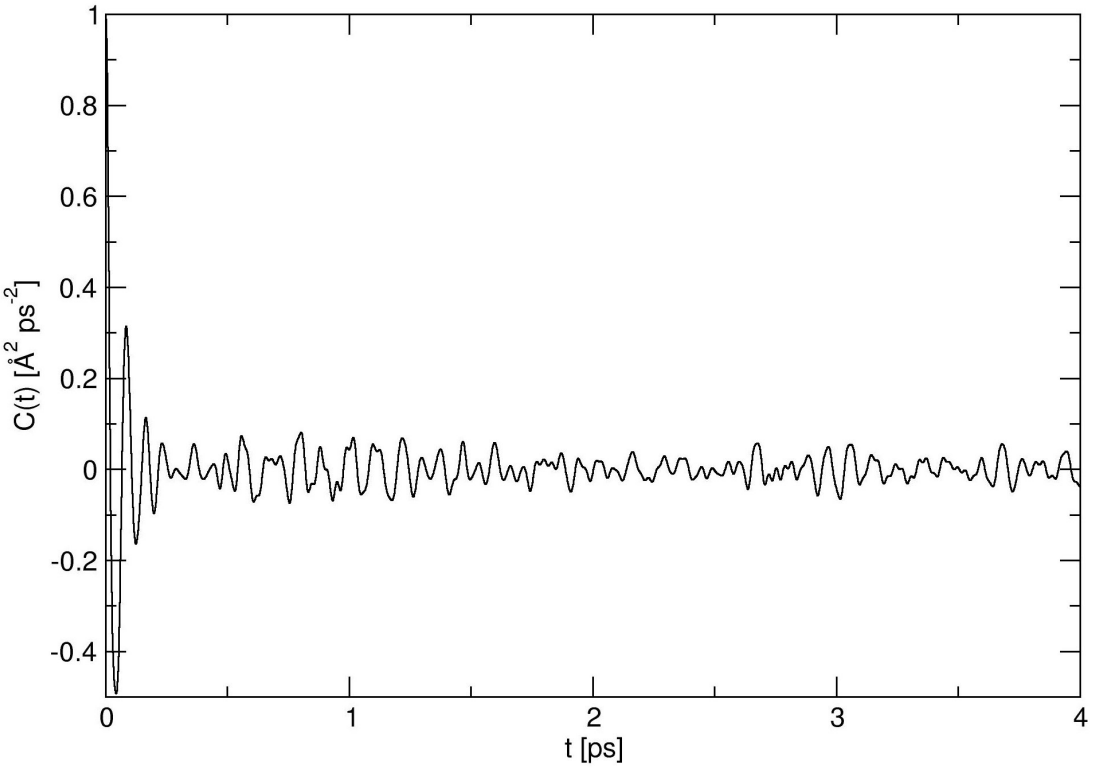

Figure 7.6: The velocity autocorrelation function of bulk MgO.

The density of states was determined from the Fourier transform of the velocity autocorrelation function. In order to produce density of states comparable to experiment multiple simulations are required in order to build the statistics over which an average can be taken. Therefore the phonon density of states was compared to that produced using a facility included in the GULP code as shown in Figure 7.7. In this method the Sangster and Stoneham pair potential was also used along with the rigid ion model in order to make a direct comparison. It can be seen that the main features of the graphs correspond although the GULP method abruptly cuts off the main peak. Further investigations using the GULP method with different pair potentials as well as the shell model indicate that the cut of the peak is due to the method. A further comparison was made to phonon density of states produced using *ab-initio* calculations [158] which is shown in Figure 7.8. It can be seen that the results from the Fourier transform of the autocorrelation function contain more noise in comparison. Again this is due to lack of statistics, the size of the supercell which affects the permitted vibrational modes, as well as the exclusion of the shells in the rigid ion model. However the main peaks correspond.

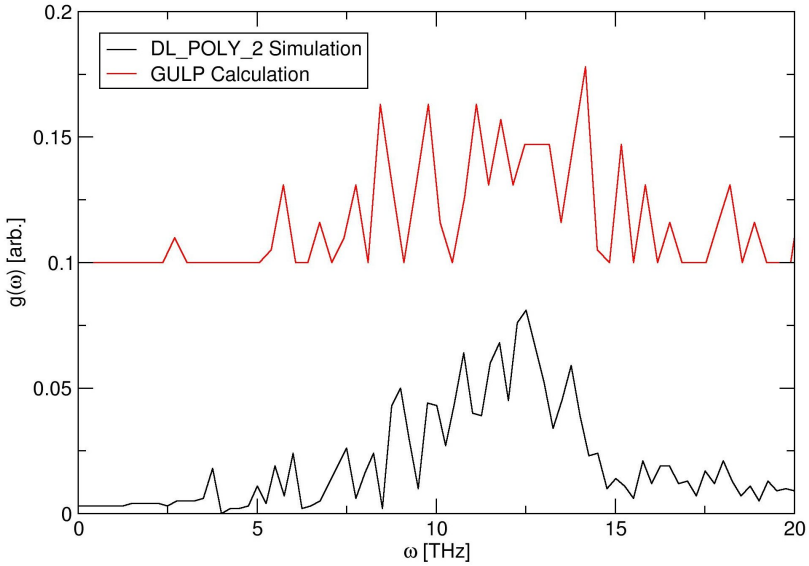

Figure 7.7: The phonon density of states produced using molecular dynamics and static simulations.

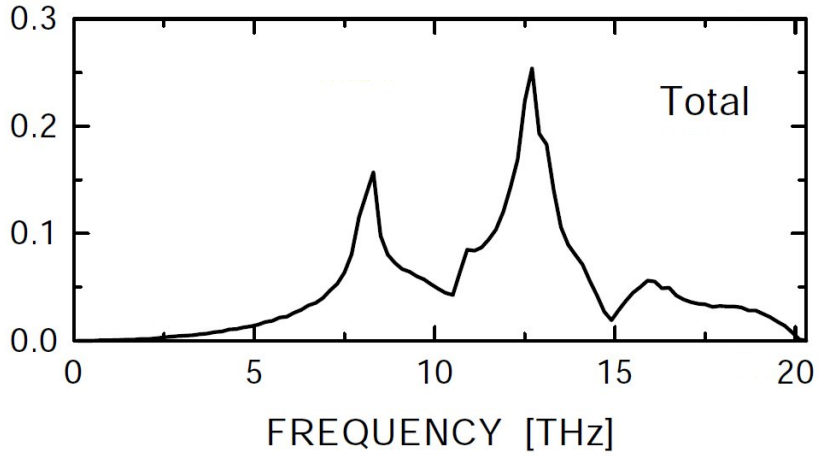

Figure 7.8: The phonon density of states for bulk MgO determined using *ab-initio* methods [158].

Graphs of phonon entropy as a function of temperature are shown in Figure 7.9. Also included are published phonon entropy results determined analytically using some empirical values [159]. As expected the graph shows that the grain boundaries become more disordered as temperature increases. Qualitatively the results compare well to the analytical values. The shift in entropy from the analytical results is due to the simulation cell size, the rigid ion model and the reduced statistics. In order to elucidate more clearly the variations in the entropy of the grain boundary structures the relative entropy was determined as the difference in the grain boundary entropy to that of the bulk entropy at the corresponding temperature. This is shown in Figure 7.10.

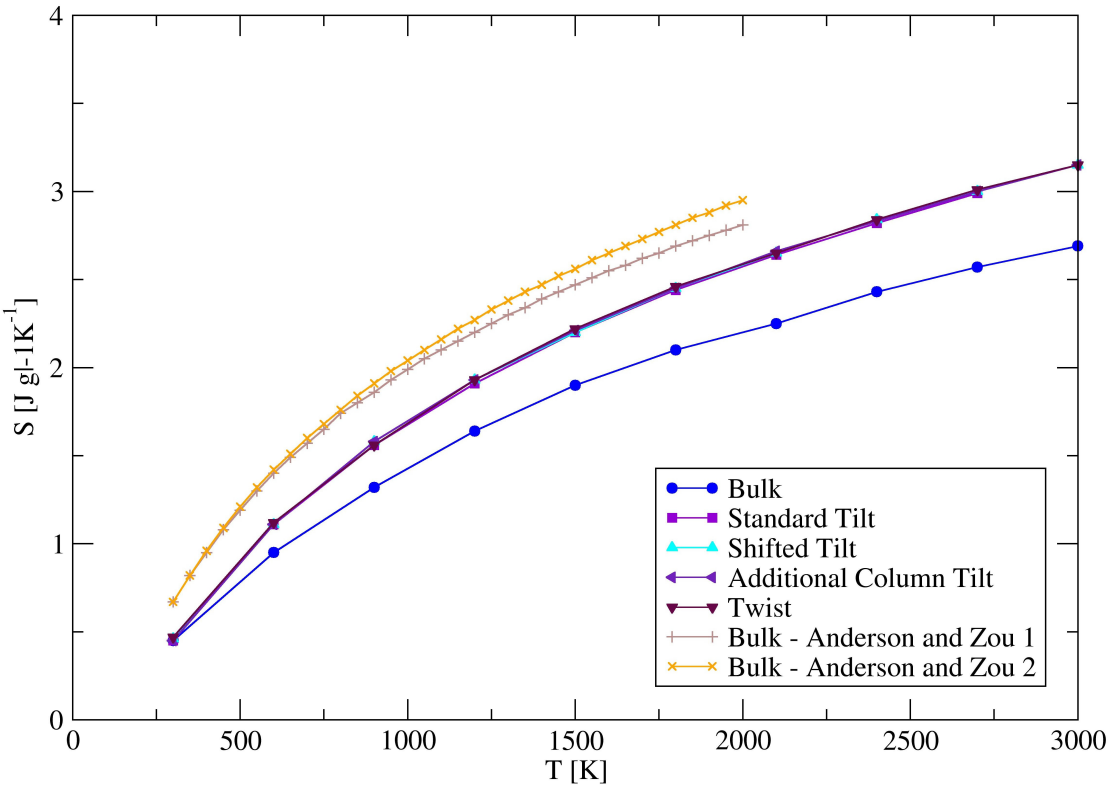

Figure 7.9: Phonon entropy as a function of temperature.

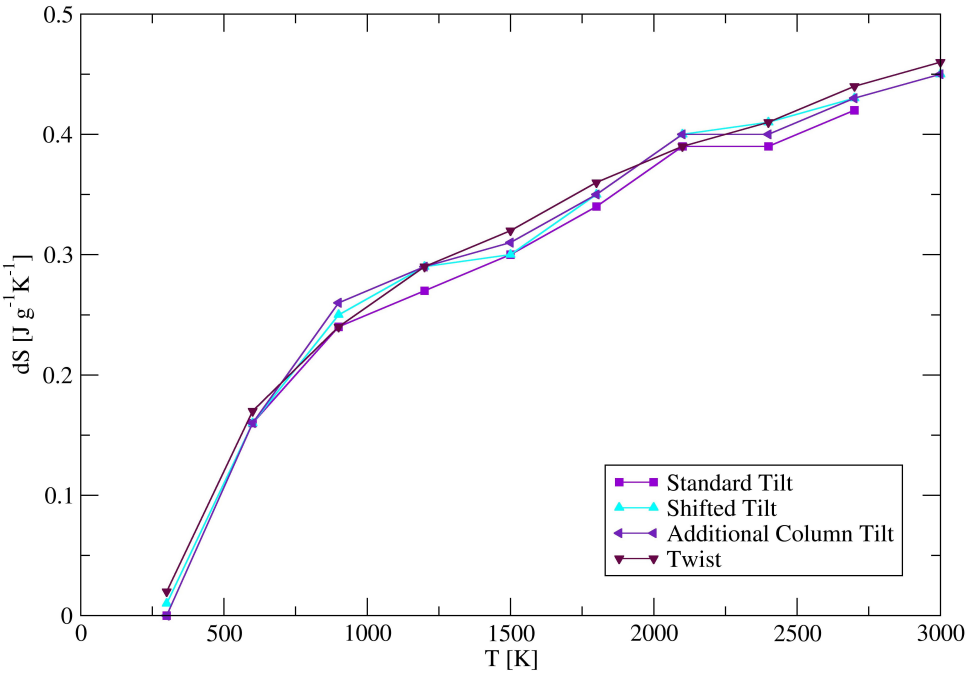

Figure 7.10: Relative phonon entropy as a function of temperature. The entropies of the grain boundaries are relative to that of bulk MgO at the corresponding temperature.

It can be seen that the standard tilt grain boundary has the lowest entropy in the temperature range investigated. Whereas the twist grain boundary has the highest entropy at all temperatures with the exception of 900 K and 2100 K where the additional column tilt grain boundary has the highest entropy.

7.4 Conclusions

The results show that the shifted tilt grain boundary is not a stable configuration and that this structure rapidly transforms into the additional column tilt grain boundary at 300 K. Out of the three remaining grain boundary structures studied the standard tilt grain boundary was found to have the lowest interfacial energy in the temperature range 300 K to 3000 K. This grain boundary structure was also found to have the lowest entropy. This means that less spontaneous heat is transferred from the environment to the system and more work is therefore used to create this structure. It can be seen that in the same temperature range the twist grain boundary generally has the highest entropy and will therefore require less work during formation. This suggests that temperature is significant to the formation of grain boundaries in thermal processes such as sintering, with the formation of twist grain boundaries being more favourable.

Chapter 8

Oxygen Vacancies in Amorphous Silica - An Embedded Cluster Study

8.1 Introduction

Amorphous silica (a-SiO_2) is a type of a glass ceramic with a vast array of technological applications. In addition to the examples given in Chapter 2 a-SiO_2 also has applications in erasable programmable read only memory chips, photolithography, optical fibres and telescopes, as well as being used as a bulb in halogen lamps and as a refractory material in the production of steel. As mentioned in Chapter 2 a-SiO_2 is widely used in the microelectronics industry as a dielectric in metal-oxide-semiconductor (MOS) devices, however the reliability and performance of these devices is affected by issues such as 1/f noise, negative bias temperature instability and leakage currents. These phenomena are thought to involve the capture and emission of charge carriers by oxygen vacancy defects in the gate dielectric close to its interface with silicon. Over the past few decades molecular models have been proposed for oxygen vacancies in various charge states which have been incorporated into models predicting the underlying mechanisms behind some of the key MOS reliability issues. These phenomena and models have been discussed in more detail in Chapter 3 Section 3.3. Electron paramagnetic resonance has been used to study paramagnetic defects in irradiated a-SiO_2. Some of the detected signals have been attributed to the positively charged oxygen vacancy with various local structures. These defects have become known as E'_n centres and in amorphous silica the subscript, n, corresponds to a greek letter (e.g. δ, γ, α, $\varkappa$) distinguishing the different local structures, some of which are shown in Figure 8.1. In models pre-

dicting the mechanisms behind 1/f noise and negative bias temperature instability these positively charged oxygen vacancies are usually the product of charge trapping by a neutral oxygen precursor. However the neutral oxygen vacancy has also been suggested as a precursor for the negatively charged oxygen vacancy [101]. Unlike the positively charged defects these neutral vacancies have not been studied extensively experimentally as they are not paramagnetic and cannot be detected using electron paramagnetic resonance. They have however been suggested to exhibit bistability like that of positively charged oxygen vacancies.

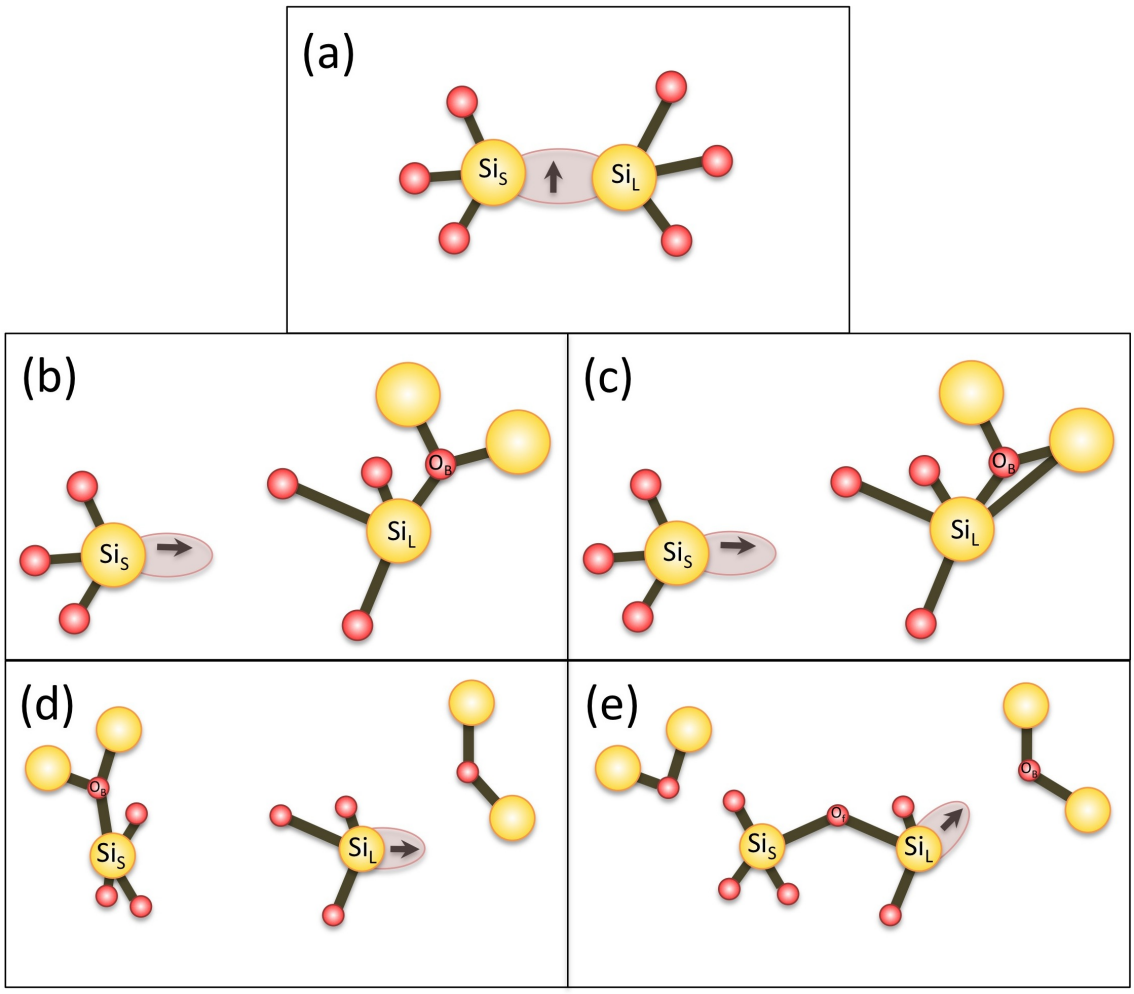

Figure 8.1: The local structure of some positively charged E' oxygen vacancy centres. The (a) E'$_\delta$ dimer, (b) E'$_{\gamma 4}$ four fold puckered, (c) E'$_{\gamma 5}$ five fold puckered, and two types of back projected configurations (d) E'$_\alpha$ and (e) E'$_\varkappa$.

In this study the first principles embedded cluster technique was used to investigate oxygen vacancies in amorphous silica in puckered and back projected configurations. Criteria for predicting puckered sites in an amorphous silica network [77, 85] was utilised in order to study the properties of neutral and positively charged oxygen vacancies in four clusters formed from a continuous

random network SiO_2 supercell. Four neutral oxygen vacancy clusters were also investigated using previously studied positively charged back projected configurations [88] as precursors. These positively charged defects were found to be stable with high barriers for conversion to the puckered E'$_\gamma$ centre which has led to the suggestion that upon electron capture their neutral successors may be more stable than other neutral vacancy configurations. Again these four clusters were formed from the same amorphous supercell as those of the puckered configuration clusters. Properties such as geometry, charge, formation energy, highest occupied molecular orbital, one electron energy levels, g-factor and the isotropic hyperfine constant have been determined in order to discuss the feasibility of the involvement of the defects in MOS device reliability issues.

8.2 Methods

8.2.1 Generation of the Amorphous Structure

Molecular dynamics simulation was used to generate an a-SiO_2 model [82,85,160] with the DL_POLY [151] code. The $-\frac{1}{r^6}$ dispersion term of the Buckingham potential, where r is interatomic distance, causes the potential to diverge at small interatomic distances which introduces artificial attraction between atoms in close proximity. This effect can be removed by using the BKS potential of Van Beest et al [113],

$$V(r) = \begin{cases} V_{BKS}(r) = A\exp(-\alpha r) - \frac{C}{r^6} & , \quad r \geq r_0 \\ V_d(r) = B\exp(-\beta r) & , \quad r \leq r_0 \end{cases}$$

r_0 is the value at which the deviation of $V(r)$ from $V_{BKS}(r)$ is minimised, whereby

$$V_{BKS}(r_0) = V_d(r_0)$$

and

$$\frac{d\,V_{BKS}(r_0)}{d\,r_0} = \frac{d\,V_d(r_0)}{d\,r_0}$$

The parameters B and β are derived from these conditions. The values of r_0, B and β are shown in Table 8.1.

Parameter	Interaction	
	Si-O	O-O
r_0 [Å]	1.18	1.9
B [eV]	505.05	313.96
β [Å^{-1}]	3.53	2.35

Table 8.1: The parameters of V_d from the BKS potential.

A 3 × 3 × 3 supercell of an initial 24 atom β-crystobalite unit cell was generated. In order to produce an amorphous structure the isothermic-isobaric (NPT) ensemble was used and the supercell was subjected to the following procedure:

- melting to a temperature of 7000 K at a rate of 5×10^{13} K s^{-1}
- equilibration at 7000 K for 100 ps
- quenching to 0 K at a cooling rate of 8×10^{12} K s^{-1}
- further relaxation using static calculations

This produced a 648 atom continuous network, free of defects and dangling bonds, in which all silicon atoms are coordinated to four oxygen atoms and each oxygen atom is coordinated to two silicon atoms. The structure has a density of 2.37 g cm^{-3} which is slightly higher than the general density of a-SiO_2 which is reported as 2.2 g cm^{-3} [161]. This difference occurs due to the properties of the BKS potential and the dynamic volume permitted by the NPT ensemble. The distributions of the Si-O nearest neighbour distance and of the Si-O-Si angles were found to be in good agreement with published values [36, 85].

8.2.2 Obtaining Puckered Configurations

The EPR signal, E'$_1$, in α-quartz has been attributed to an asymmetrically relaxed positively charged oxygen vacancy which is said to be in the puckered configuration. Here the long bonded Si atom, Si_L, neighbouring the oxygen vacancy, O_V, relaxes through the plane formed by its three oxygen neighbours and forms a bond with a back oxygen, O_B. However the short bonded silicon, Si_S, does not exhibit puckering as there is no back oxygen atom available for it to bond with. It was suggested that this configuration also exists for positively charged oxygen vacancies in amorphous silica, however due the random network not all oxygen sites have a local geometry that will enable puckering to occur. Lu et al [77] used density functional theory to correlate the local geometry of oxygen sites in non-defective amorphous supercells with the puckered configuration of the positively

charged oxygen vacancy. This produced criteria for predicting the oxygen sites within the network likely to exhibit four-fold or five-fold puckering (see Figure 3.5), upon hosting an oxygen vacancy. The parameters for these criteria are shown in Figure 8.2, which take into account the Si_L- O_B distance, r, and the angle, α as well as the distance between the long-bonded silica and its nearest neighbours.

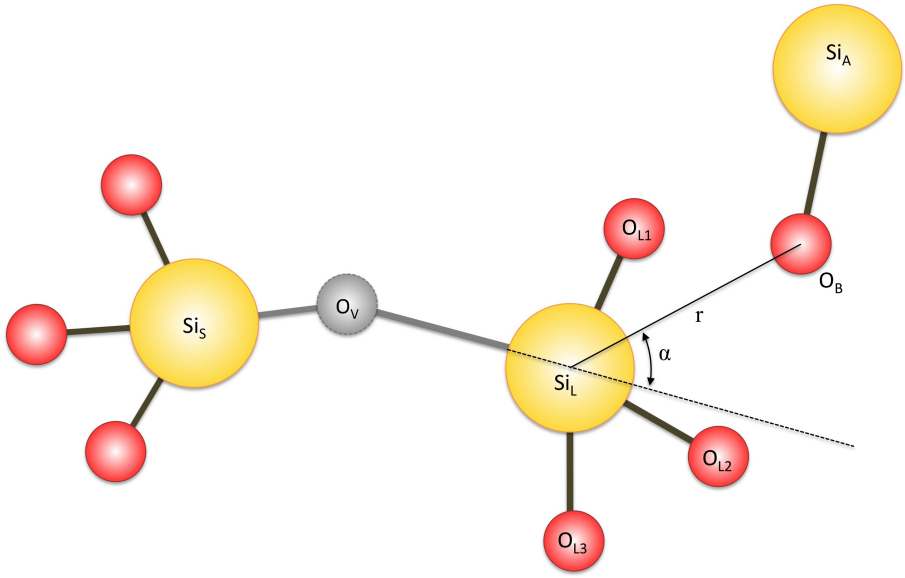

Figure 8.2: Parameters in the criteria by Lu et al [77] for predicting sites that will undergo puckering.

The criteria suggest that in order for four-fold puckering to occur the following should be satisfied:

$$3.2\,\mathring{A} < r < 3.8\,\mathring{A}$$

$$\alpha < 30^{\circ}$$

$$Si_L - O_1,\ S_L - O_2,\ Si_L - O_3 > 3.8\,\mathring{A}$$

whereas for five-fold puckering to occur the criteria are as follows:

$$2.5\,\mathring{A} < r < 3.2\,\mathring{A}$$

$$\alpha < 15^{\circ}$$

Using these criteria Lu et al [77] predicted that upon hosting an oxygen vacancy 80% of sites from the initial amorphous structure will form dimer configurations, 12% will exhibit four-fold puckering and the remaining 8% will undergo five-fold puckering.

Mukhopadhyay et al [82] also studied the local geometry of oxygen sites in amorphous silica and proposed alternative criteria for predicting puckered configuration sites using the embedded cluster method. In these criteria it was first assumed that the puckering Si_L atom will relax through the plane of its three oxygen neighbours to the point P as shown in Figure 8.3 (a). By scrutinising the oxygen sites in the locality of this point the existence of a back oxygen atom, O_B, that is part of a Si_A-O_B-Si_B unit pointing towards P can be determined. It was suggested that oxygen sites satisfying this condition will pucker if the P-O_B distance is less than that of Si_A-O_B and Si_B-O_B .

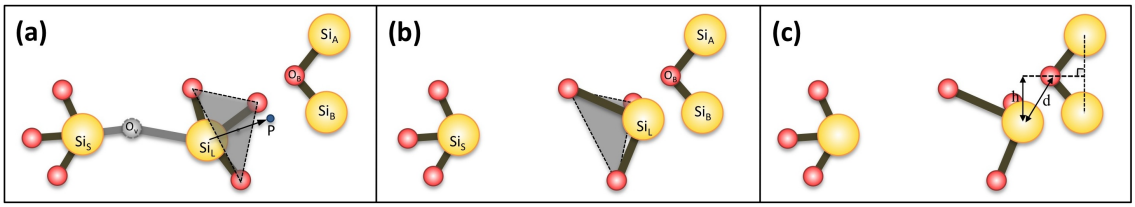

Figure 8.3: The criteria of Mukhopadhyay et al [85] for predicting sites in amorphous silica that are likely to undergo puckering upon hosting a positively charged oxygen vacancy.

Using the criteria of Lu et al [77] and Mukhopadhyay et al [82] a Fortran 90 program was written to analyse the amorphous supercell in order to determine oxygen vacancy sites common to both sets of criteria that are likely to undergo puckering when a positively charged vacancy is present. The procedure shown in Figure 8.4 was used to obtain the bistable neutral and positively charged oxygen vacancy states. In this procedure the defect states are described using the V_y^x notation whereby V indicates that the defect in the cluster is a vacancy, x indicates the charge of the vacancy and y is equal to a or b depending on whether the state occurs before or after a perturbation. The procedure is initialised by adding a neutral oxygen vacancy to the cluster by removing an O^0 atom forming the V_a^0 vacancy state. By removing an electron from the cluster the positively charged V_a^{+1} state is produced. The defect can then be perturbed by moving Si_L to point P. Upon relaxation the V_b^{+1} state is formed. By adding an electron back to the system the V_b^0 vacancy is formed. Here the positively charged V_a^{+1} and V_b^{+1} states correspond to one of the positively charged E' centres.

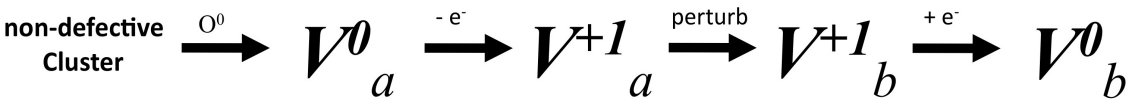

Figure 8.4: Procedure for obtaining puckered configurations.

8.2.3 Obtaining Back Projected Configurations

In the study by Kimmel et al [88] back projected configurations were obtained using the procedure shown in Figure 8.5. Here a neutral oxygen vacancy is added to the non-defective cluster forming the V_a^0 vacancy. By removing an electron the V_a^{+1} vacancy is produced. The defect is strongly perturbed by the removal of an additional electron forming a doubly positively charged V^{+2} vacancy. The V_b^{+1} vacancy is produced by adding an electron to the cluster. In this study an additional electron is added to the system in order to investigate the V_b^0 state as depicted by the boxed section of the procedure.

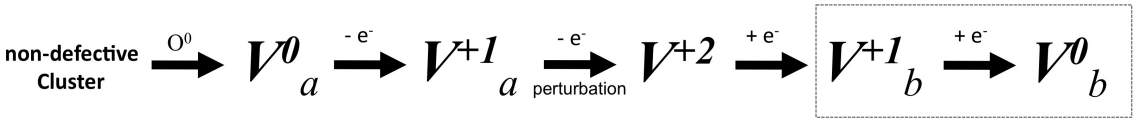

Figure 8.5: The procedure for obtaining back projected configurations.

8.2.4 Computational Methods and Methods of Analysis

The properties of the vacancies were determined using the GUESS embedded cluster method program [110] which includes a cluster builder to produce a hybrid quantum mechanical and classical cluster around a specific site from the generated amorphous supercell. The cluster builder ensures that the quantum mechanical and classical components of the cluster are interfaced by pseudo silicon atoms. The quantum mechanical components of the system were described using the modified Beck-Lee-Yang-Par [111,112] , B3LYP-x, hybrid functional due to its efficiency and ability to determine energy band gaps with good agreement to experimental results [162], in contrast to the LDA and GGA functionals which underestimate this property. In the B3LYP-x functional the Hartree Fock exact exchange, x, is equal to 32.5%. This method is described in more detail in Chapter 4. The molecular orbitals were modelled using the 6-31G split valence basis set. Here the core basis functions are composed of six primitive Gaussians whereas two basis functions are used to represent each valence orbital. The first is composed of a linear combination of three primitive Gaussians and the second basis function is contains a single primitive Gaussian.

The geometry of the clusters was analysed in terms of the distance between the two Si atoms neighbouring the vacancy site, A, and also by the distance between the long bonded, Si_L atom and the proposed back oxygen atom O_B, B. These distances along with some displacements were determined relative to their analogues in the non-defective cluster. These distances are shown in Figure 8.6.

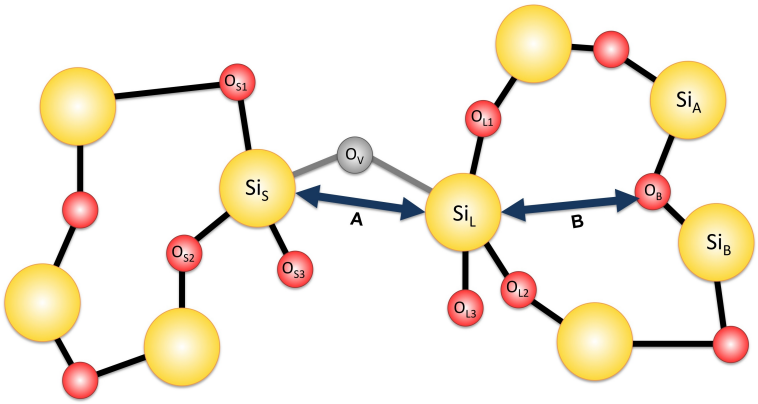

Figure 8.6: The Si_S-Si_L distance and the Si_L-O_B distance.

The charges were determined using Bader charge analysis [163, 164] which is a method used to partition the charge density of the system such that a finite charge is associated with a each atom. In this method 2D zero flux surfaces are determined perpendicular to which the charge density is at a minimum. This enables 3D regions of charge density to be associated with a particular atom as shown in Figure 8.7. A single atom can therefore be assigned a total charge and the relative charge can be determined with respect to the charge of the corresponding atom in the non-defective cluster.

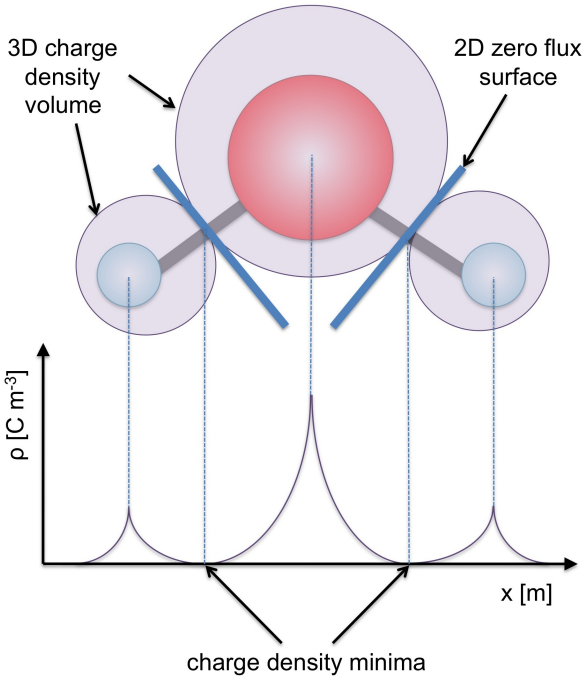

Figure 8.7: Charge partitioning using the Bader method.

The vacancy formation energy, E_{vac}, was determined as the difference between the energy of the

defective cluster, E_{def}, and the energy of the non-defective perfect cluster, E_{perf}, corrected with respect to the energy of an oxygen atom corresponding to the charge of the vacancy, E_O, as follows:

$$E_{vac} = E_{def} - E_{perf} + E_O$$

For neutral vacancies, E_O is the energy of a lone oxygen atom in the triplet state, whereas for positively charged vacancies E_O is taken as the energy of a negatively charged oxygen atom in the doublet state.

The positively charged vacancies are paramagnetic defects and contain an unpaired electron that is sensitive to local magnetic fields. Electron paramagnetic (EPR) data such as the Landé g factor and isotropic hyperfine constants can therefore determined for these clusters. EPR involves the interaction between electromagnetic radiation and the magnetic moments of the electron. The basic principle behind this technique involves the application of a magnetic field, B, to a paramagnetic system. As a result the unpaired electron will align itself in one of two states, either parallel or antiparallel to the applied field. The parallel state and antiparallel states have energies $E_\alpha = +\frac{1}{2} g_e \beta_e B$ and $E_\beta = -\frac{1}{2} g_e \beta_e B$ respectively, where g_e is the free electron g tensor and β_e is the Bohr magneton. Figure 8.8 depicts the alignment for the most simple paramagnetic system, a single electron. Here the energy splitting between the two states is:

$$\triangle E = h\nu = g_e \beta_e B \tag{8.1}$$

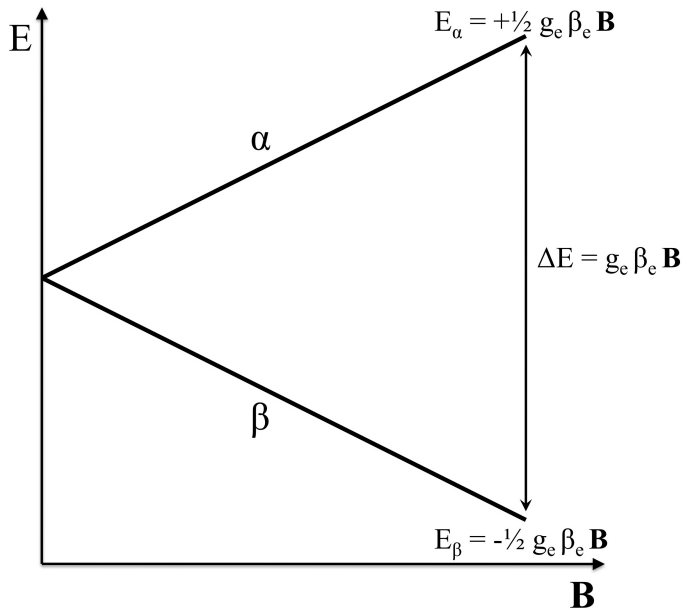

Figure 8.8: Energy splitting of an unpaired electron in response to an applied magnetic field.

An electron in the lower energy state can make a transition to the higher energy state if it acquires an energy of $\triangle E$ which results in resonance. This is generally achieved using radio frequency electromagnetic radiation to excite the electron enabling an absorption spectrum to be produced. Since the electron responds to both the local and applied magnetic field, B_{loc} and B_{app} respectively, the effective magnetic field, B_{eff}, can be determined as follows:

$$B_{eff} = B_{app} + B_{loc} = B_{app}(1 - \theta) \tag{8.2}$$

where θ is a constant containing the effects of the local field. Substituting Equation 8.2 into Equation 8.1 produces the following:

$$h\nu = g_e \, \beta_B \, B_{app}(1 - \theta)$$

where the effective g-factor, g, is:

$$g = g_e(1 - \theta)$$

If g is not equal to g_e this indicates a gain or loss in the angular momentum of the electron which occurs via spin orbit coupling. This provides information on the nature of the orbital containing the electron and it has found that systems with similar local geometry have a similar g-tensors.

Hyperfine splitting occurs due to the interaction between the spin of an electron and a magnetic nucleus, and is characterised by the hyperfine coupling constant A. The isotropic hyperfine coupling constant for a magnetic nucleus, A_{iso}, is:

$$A_{iso}(N) = \frac{8\pi}{3} \left(\frac{g}{g_e} \right) g_N \beta_N \rho_s(r_N)$$

where g is the g-factor of the unpaired electron interacting with the nucleus, g_e is the g-factor of a free electron, g_N is the nuclear g-factor, β_N is the nuclear magneton and $\rho_s(r_N)$ is the electronic spin density at the location of the nucleus, r_N. The hyperfine coupling constant provides an indication of the degree in which the electron interacts with neighbouring nuclei.

8.3 Results and Discussion

8.3.1 Vacancies Associated with the Puckered Configuration

8.3.1.1 Non-defective Clusters

Upon relaxation of the four non-defective clusters the Si_S-Si_Ldistances were found to be in the range 3.20-3.32 Å, which is an increase of 0.2-0.3 Å with respect to the corresponding distances from the unrelaxed supercell. The Si_L-O_B distances for the clusters were found to be in the range 3.1-3.4 Å, and the bandgaps were determined as 7.9-8.3 Å which is slightly smaller than the published value of the bandgap of approximately 9 eV [165, 166]. This suggests that the electrons in the clusters are more prone to delocalisation.

8.3.1.2 Neutral Vacancy Clusters

Highest Occupied Molecular Orbital

The highest occupied molecular orbital (HOMO) is shown for the neutral vacancies in States *a* and *b* in Figure 8.9 and Figure 8.10 respectively. It can be seen that for both states the HOMO of Cluster A is in the dimer configuration. However the HOMOs of the other three clusters have a dimer configuration in State *a* and a puckered configuration in State *b*.

Geometry

The relative Si_S-Si_L and Si_L-O_B distances are shown in Table 8.2 relative to those in the non-defective clusters. It can be seen that in State *a* the Si_S-Si_L distance decreases suggesting that the atoms relax towards each other in order to occupy some of the space made available by the vacancy. As a result the Si_L-O_B distances are greater than those in the non-defective cluster. These State *a* vacancies have dimer configurations. In State *b* Cluster B, Cluster C and Cluster D have Si_S-Si_L distances that are greater than those of the non-defective clusters with shorter Si_L-O_B distances. These State *b* vacancies have puckered configurations. Cluster A in State *b* has a Si_S-Si_L distance similar to its analogue in State *a*, this reflects the dimer configuration that was observed for the HOMO of this defect.

The relative displacements of the atoms local to the defect are given in Table 8.3. It can be seen that the most significant displacements occur for Si_L and Si_S which neighbour the vacancy site and that the lattice relaxation decreases with distance from the vacancy site.

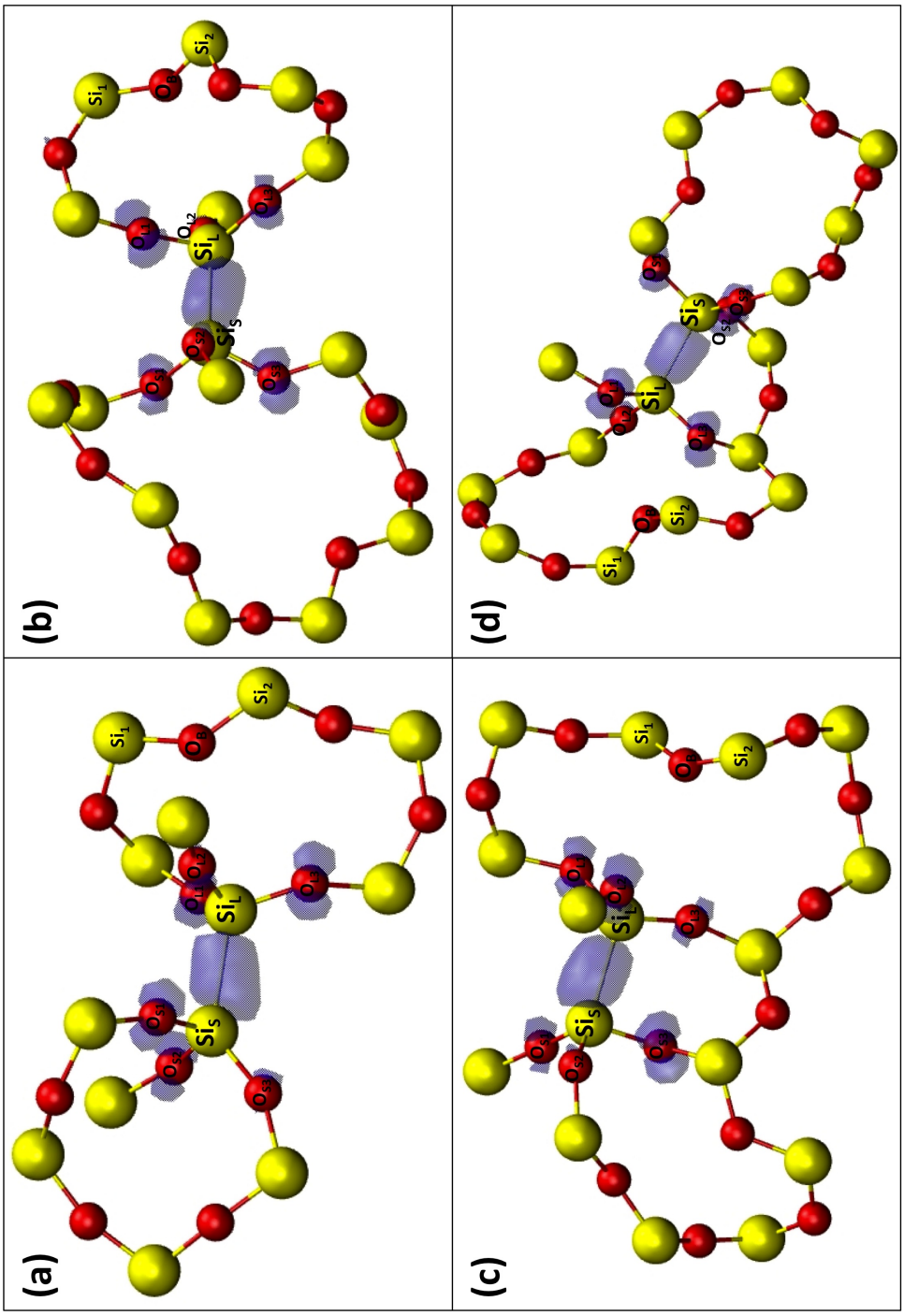

Figure 8.9: The highest occupied molecular orbitals for neutral oxygen vacancy clusters (a) A, (b) B, (c) C and (d) D in State *a*.

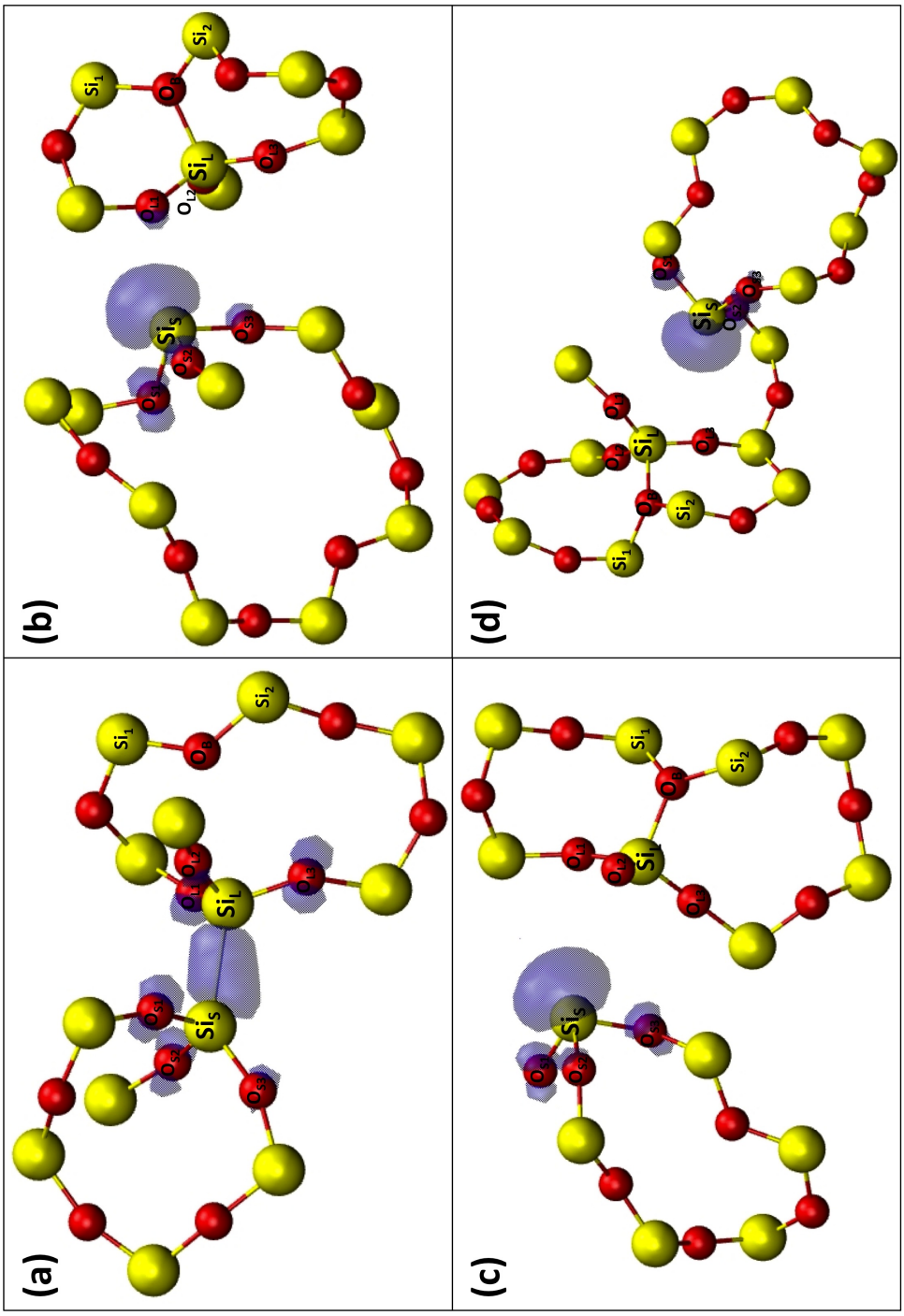

Figure 8.10: The highest occupied molecular orbitals for neutral oxygen vacancy clusters (a) A, (b) B, (c) C and (d) D in State *b*.

Cluster	Relative Si_S-Si_L [Å]		Relative Si_L-O_B[Å]	
	V_a^0	V_b^0	V_a^0	V_b^0
A	-0.72	-0.69	0.39	0.10
B	-0.84	0.77	0.34	-1.56
C	-0.77	-3.21	0.57	3.09
D	-0.80	0.59	0.40	-1.27

Table 8.2: The relative Si_S-Si_L and Si_L-O_B distances of the neutral vacancy clusters in States a and b.

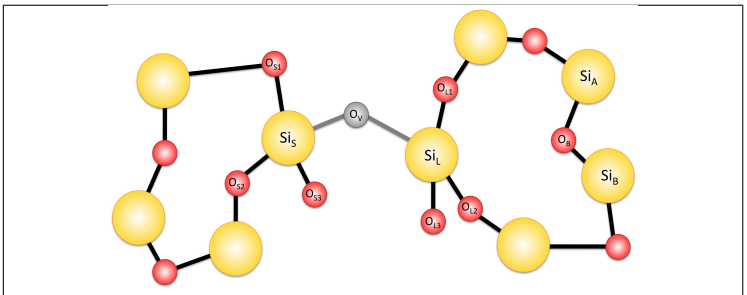

Atom	Displacement [Å]							
	Cluster A		Cluster B		Cluster C		Cluster D	
	V_a^0	V_b^0	V_a^0	V_b^0	V_a^0	V_b^0	V_a^0	V_b^0
Si_S	0.31	0.41	0.49	1.00	0.28	0.49	0.36	0.45
Si_L	0.42	0.33	0.36	1.28	0.50	0.92	0.46	0.99
O_{S1}	0.27	0.26	0.43	1.52	0.14	0.21	0.26	0.09
O_{S2}	0.26	0.35	0.36	0.08	0.18	0.21	0.24	0.22
O_{S3}	0.14	0.32	0.38	0.24	0.23	0.43	0.33	0.19
O_{L1}	0.26	0.23	0.26	0.79	0.26	0.23	0.25	0.27
O_{L2}	0.51	0.17	0.31	0.51	0.37	0.17	0.32	0.85
O_{L3}	0.21	0.39	0.28	0.32	0.44	0.24	0.47	0.19
O_B	0.09	0.16	0.08	0.38	0.09	0.35	0.09	0.36
Si_1	0.05	0.07	0.03	0.12	0.06	0.07	0.02	0.10
Si_2	0.03	0.08	0.03	0.09	0.03	0.05	0.03	0.08

Table 8.3: The displacements of atoms close to the neutral vacancy site in State a and State b. These values are given with respect to the analogous atoms in the non-defective clusters. A schematic of the atoms local to the defect is also included for clarity.

Formation Energy

The vacancy formation energies for the neutral clusters are shown in Table 8.4. In general can be seen that the vacancies in State a, which correspond to dimer configurations, are the most energetically stable. Whereas the puckered vacancy configurations in State b are metastable. Cluster A is the exception as both State a and State b have similar formation energies. This is reflective of the HOMO for both states which is in a dimer configuration.

Cluster	Formation Energy [eV]	
	V_a^0	V_b^0
A	9.81	9.63
B	9.39	11.67
C	9.37	10.30
D	9.79	10.44

Table 8.4: Vacancy formation energies for neutral vacancies in State a and State b.

Bader Charge

Relative Bader charges for the clusters in States a and b are given in Table 8.5, determined with respect to the charges in the non-defective cluster. It can be seen that the main effect of the vacancy is the redistribution of the charge at the two Si atoms, Si_L and Si_S, neighbouring the vacancy site. The charge on the Si_L and Si_S atoms in the dimer configurations is close to 1 e which suggests that each atom has an electron localised on it. However for the puckered configurations the short bonded Si_S atom has a the highest Bader charge whereas that of the Si_L atom is close to zero. This suggests two electrons are localised on Si_S which supports the puckered configuration of the HOMO. The exception is Cluster B in State a. Although the HOMO indicates that this cluster has a dimer configuration Bader analysis associates most of the charge to atom $Si_S$and the charge of Si_L is close to zero. The α and β HOMO-1 are however localised on Si_S which accounts for the high Bader charge on this atom.

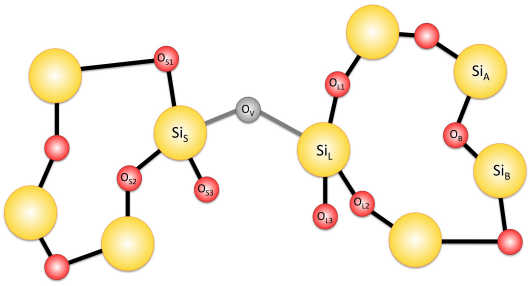

Atom	Relative Bader Charge [e]							
	Cluster A		Cluster B		Cluster C		Cluster D	
	V_a^0	V_b^0	V_a^0	V_b^0	V_a^0	V_b^0	V_a^0	V_b^0
Si_S	0.99	0.99	1.79	1.55	0.99	1.67	0.83	1.56
Si_L	0.82	0.80	0.01	-0.01	0.62	0.02	0.94	0.01
O_{S1}	-0.02	0.01	0.07	0.08	0.08	0.00	0.08	0.04
O_{S2}	0.11	2.13	-0.10	0.25	0.23	0.09	0.59	0.03
O_{S3}	0.03	0.02	0.02	0.08	0.02	0.00	0.03	0.72
O_{L1}	0.10	0.45	0.22	-0.03	0.01	0.02	-0.02	0.08
O_{L2}	0.04	0.04	-0.06	-0.02	0.07	0.05	0.02	-0.02
O_{L3}	0.07	0.08	0.03	0.02	0.09	0.05	0.09	0.07
O_B	0.01	-0.05	-0.04	0.07	-0.06	0.13	-0.09	-0.03
Si_1	-0.01	-0.02	0.01	-0.01	0.01	-0.01	-0.01	0.01
Si_2	0.00	0.01	0.00	-0.01	-0.16	0.00	0.00	-0.03

Table 8.5: The relative Bader charges of atoms close to the vacancy site in the neutral clusters. A schematic of the atoms local to the defect is also included for clarity.

8.3.1.3 Positively Charged Vacancies

Highest Occupied Molecular Orbital

The highest occupied molecular orbitals for positively charged clusters in State a and State b are shown in Figure 8.11 and Figure 8.12 respectively. It can be seen that in State a Cluster A and Cluster C have puckered configurations, whereas the vacancy in Cluster D has a distorted dimer configuration. The vacancy in Cluster B has a configuration similar to that of the back projected V_κ^{+1} configuration shown in Figure 3.10 (b) of Chapter 3. It differs in that the long bonded Si_L atom does not pucker and that the spin density is orientated towards the vacancy as opposed to towards atom O_B as is the case for the V_κ^{+1}. This configuration can therefore be described as being forward projected. From Figure 8.11 it can also be seen that in State b the vacancy in all four clusters is in the puckered configuration.

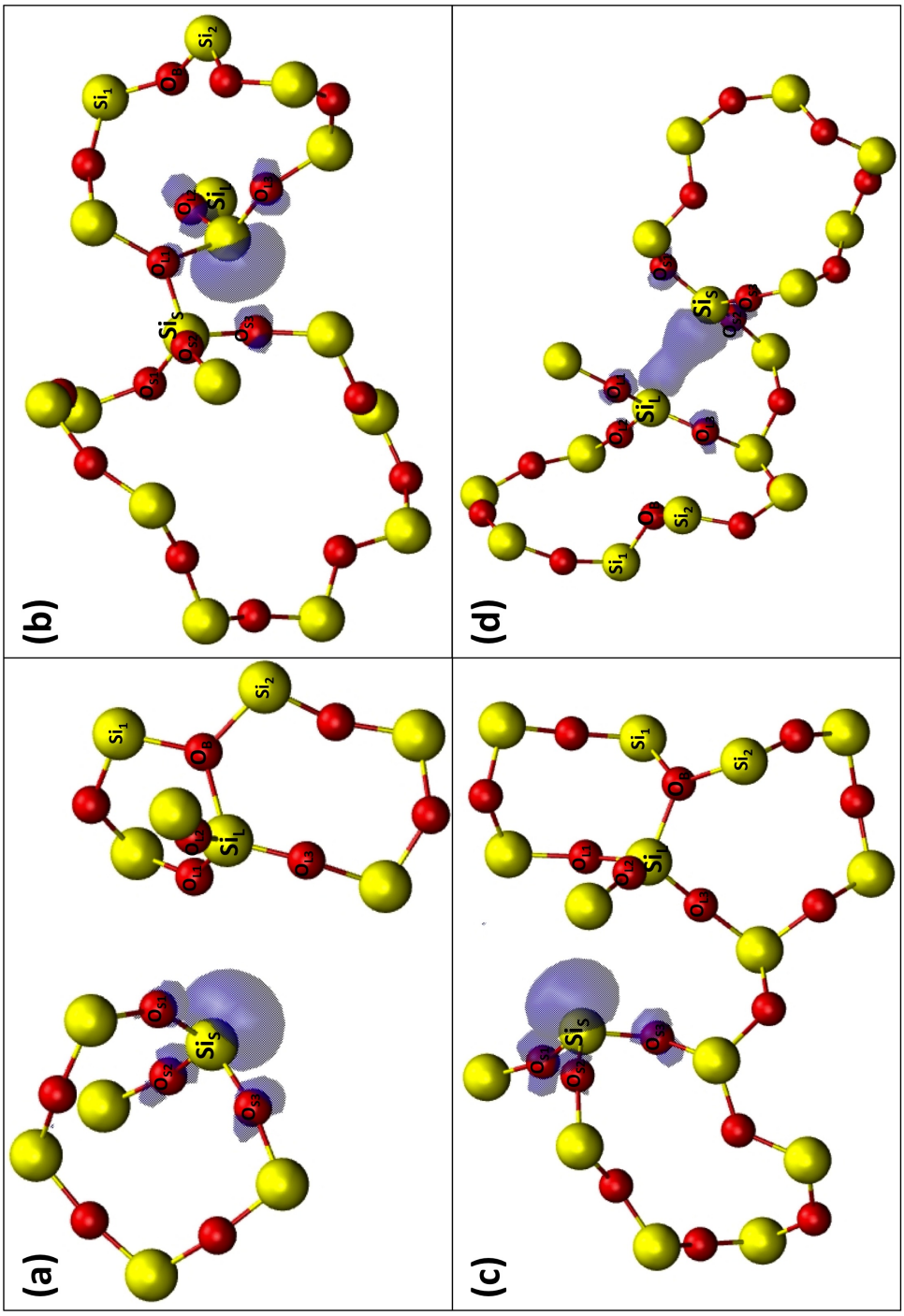

Figure 8.11: The highest occupied molecular orbitals for positively charged oxygen vacancy clusters (a) A, (b) B, (c) C and (d) D in State *a*.

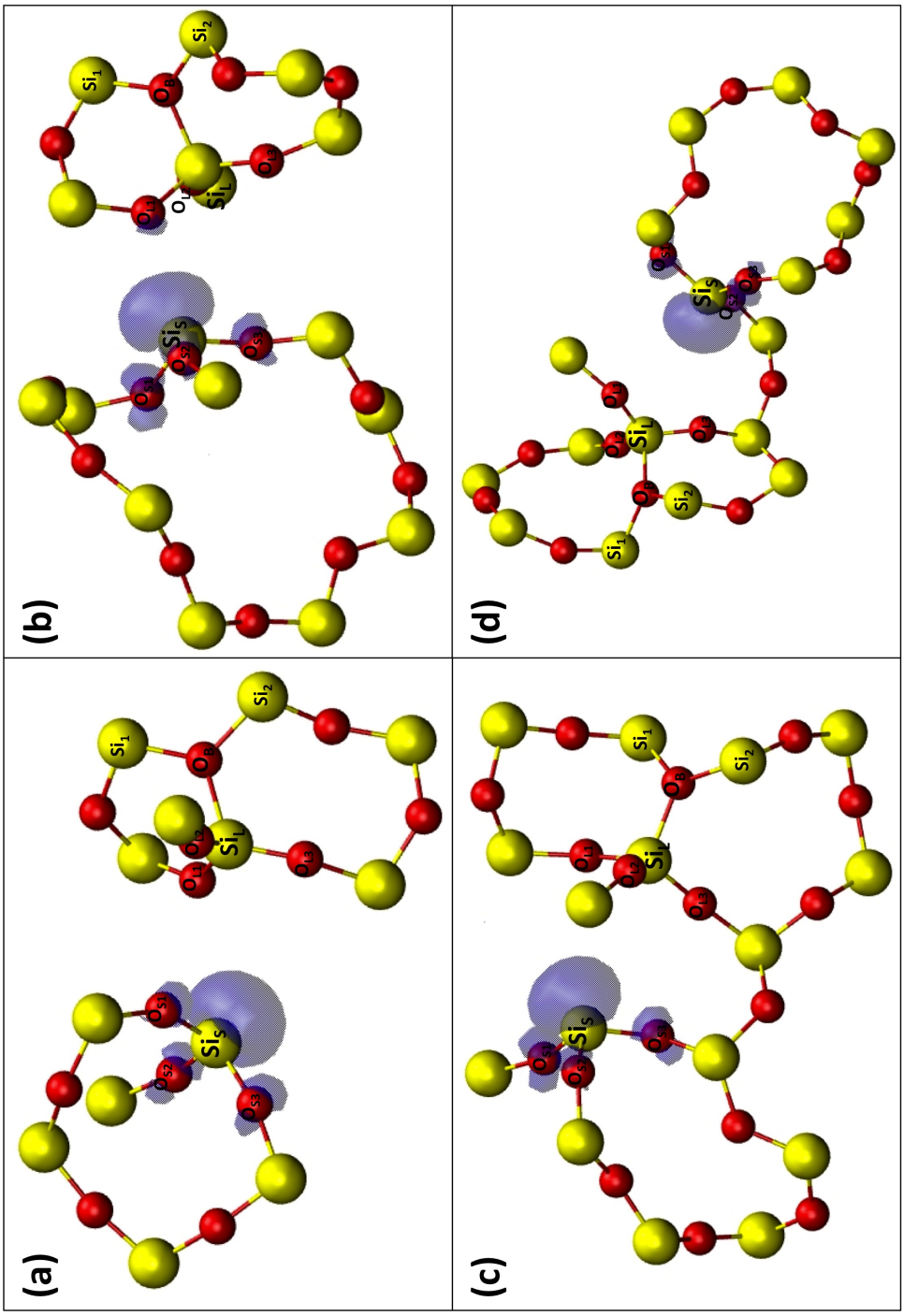

Figure 8.12: The highest occupied molecular orbitals for positively charged oxygen vacancy clusters (a) A, (b) B, (c) C and (d) D in State *b*.

Geometry

Like the puckered configuration of the neutral clusters, all positively charged puckered configurations have a larger Si_S-Si_L distance and a smaller Si_L-O_B distance in comparison to the perfect clusters. These relative distances can be seen in Table 8.6, which were determined with respect to the corresponding distances in the non-defective clusters. Also, like its neutral counterpart the positively charged dimer configuration has a smaller Si_S-Si_Ldistance and larger Si_L-O_B distance compared to those of the perfect clusters, reflecting the shorter distance required in order for the unpaired electron to be associated with both Si_S and Si_L. The vacancy in Cluster B in State *a* was found to have a smaller Si_S-Si_L distance and a larger Si_L-O_B distance compared to that of the perfect cluster. This occurs due to the relaxation and subsequent bonding of Si_S to one of the O atoms coordinated to Si_L.

Cluster	Relative Si_S-Si_L [Å]		Relative Si_L-O_B[Å]	
	V_a^{+1}	V_b^{+1}	V_a^{+1}	V_b^{+1}
A	0.90	0.96	-1.19	-1.19
B	-0.30	0.82	0.39	-1.58
C	0.82	0.82	-1.24	-1.23
D	-0.06	0.94	0.07	-1.28

Table 8.6: The relative Si_S-Si_L and Si_L-O_B distances of the positively charged vacancy clusters in States *a* and *b*.

The displacement relative to the non-defective cluster was determined for the atoms local to the vacancy. These displacements are given in Table 8.7. It can be seen that for the puckered configurations atom Si_L has the largest displacement and that the displacement of O_B is also significant.

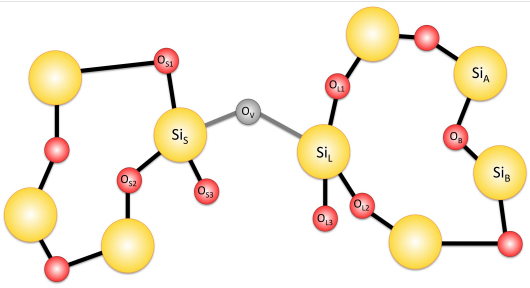

Atom	Displacement [Å]							
	Cluster A		Cluster B		Cluster C		Cluster D	
	V_a^{+1}	V_b^{+1}	V_a^{+1}	V_b^{+1}	V_a^{+1}	V_b^{+1}	V_a^{+1}	V_b^{+1}
Si_S	0.12	0.15	0.77	0.63	0.23	0.22	0.18	0.17
Si_L	0.96	0.99	0.58	1.20	0.94	0.93	0.21	1.03
O_{S1}	0.31	0.28	1.46	1.11	0.40	0.37	0.36	0.14
O_{S2}	0.10	0.05	0.33	0.06	0.06	0.06	0.14	0.18
O_{S3}	0.16	0.16	0.30	0.20	0.05	0.05	0.18	0.14
O_{L1}	0.11	0.09	0.37	0.74	0.20	0.19	0.48	0.20
O_{L2}	0.36	0.36	0.14	0.38	0.14	0.13	0.16	0.74
O_{L3}	0.16	0.09	1.14	0.31	0.12	0.12	0.64	0.21
O_B	0.27	0.26	0.28	0.45	0.31	0.31	0.21	0.33
Si_1	0.04	0.04	0.11	0.16	0.04	0.04	0.06	0.09
Si_2	0.07	0.10	0.27	0.13	0.06	0.06	0.12	0.02

Table 8.7: The displacements of atoms close to the positively charged vacancy site in State a and State b. These values are given with respect to the analogous atoms in the non-defective clusters. A schematic of the atoms local to the defect is also included for clarity.

Bader Charge

The relative Bader charges for atoms in the positively charged cluster are given in Table 8.8. It can be seen that in State a the unpaired electron of the puckered configurations is associated with Si_S. For the forward projected configuration of Cluster B in State a the unpaired electron is localised on Si_L. For the dimer-like configuration the unpaired electron is associated with both Si_S and Si_L.

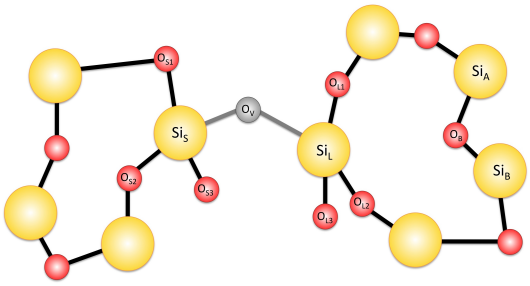

Atom	Relative Bader Charge [e]							
	Cluster A		Cluster B		Cluster C		Cluster D	
	V_a^{+1}	V_b^{+1}	V_a^{+1}	V_b^{+1}	V_a^{+1}	V_b^{+1}	V_a^{+1}	V_b^{+1}
Si_S	0.77	0.79	-0.02	0.81	0.29	0.84	0.35	0.72
Si_L	-0.01	0.00	0.85	-0.01	0.09	-0.02	0.22	0.00
O_{S1}	0.03	0.06	0.05	0.17	0.35	0.11	0.17	0.16
O_{S2}	0.00	0.06	-0.07	-0.03	0.14	0.10	0.09	0.36
O_{S3}	0.05	-0.03	0.03	0.03	0.05	0.05	0.14	-0.18
O_{L1}	0.04	0.00	0.01	-0.02	0.09	-0.02	0.16	0.00
O_{L2}	0.02	0.01	0.00	0.20	0.09	0.02	0.00	-0.01
O_{L3}	0.01	0.03	0.10	-0.03	0.15	0.10	0.06	0.04
O_B	0.17	0.12	-0.04	0.03	0.00	0.12	-0.13	-0.01
Si_1	0.01	-0.01	0.00	-0.02	0.00	-0.02	0.01	0.02
Si_2	-0.01	-0.02	-0.02	0.00	-0.01	-0.14	-0.01	-0.02

Table 8.8: The relative Bader charges of atoms close to the vacancy site in the neutral clusters. A schematic of the atoms local to the defect is also included for clarity.

Formation Energy

The formation energies of the positively charged vacancy clusters are given in Table 8.9. It can be seen that with the exception of Cluster D the vacancy in State a is stable whereas the State b vacancies are metastable. For Cluster D the distorted dimer HOMO of State a is metastable in comparison to the stable puckered HOMO of State b.

Cluster	Formation Energy [eV]	
	V_a^{+1}	V_b^{+1}
A	34.51	34.74
B	34.21	34.53
C	30.29	31.15
D	35.22	33.69

Table 8.9: Vacancy formation energies for neutral vacancies in State a and State b.

Density of States

g-Factor and Hyperfine Coupling Constant

The g-tensor components for the positively charged oxygen vacancy clusters are given in Table 8.10. Previously published experimental and theoretical results report that a common characteristic of E' centres is that one of the principle values of the g-tensor is $g_1 = 2.0018$. With the exception of the V_a^{+1} state of Cluster B the E' centres investigated in this study all have a principle g-tensor value in the range 2.0016-2.0018 which is good agreement with the published values. The the g_2 and g_3 values for the distorted dimer configuration of the E' centre in Cluster D are not greater in magnitude than the g_1 value as reported by the published values, however this is due to the asymmetric nature of the HOMO. In the V_a^{+1} state of Cluster B the vacancy has a forward projected dangling bond configuration whereby both Si atoms neighbouring the vacancy are orientated towards the vacancy space and the spin density of the unpaired electron is directed towards the vacancy. The Si_L atom remains three-coordinated however Si_S forms an additional bond with one of the oxygen atoms neighbouring Si_L, making it four coordinated. For this vacancy two of the principle g-tensor values are equal, $g_1 = g_3 = 2.0010$, whereas the remaining principle g-tensor value is half this amount.

Cluster	State	g-Tensor Components		
		g_1	g_2	g_3
A	V_a^{+1} (E'$_\gamma$)	2.0017	2.0005	2.0004
	V_b^{+1} (E'$_\gamma$)	2.0017	2.0005	2.0005
B	V_a^{+1}	2.0010	2.0005	2.0010
	V_b^{+1} (E'$_\gamma$)	2.0016	2.0008	2.0003
C	V_a^{+1} (E'$_\gamma$)	2.0018	2.0009	2.0006
	V_b^{+1} (E'$_\gamma$)	2.0018	2.0009	2.0006
D	V_a^{+1} (E'$_\delta$)	2.0017	2.0015	2.0009
	V_b^{+1} (E'$_\gamma$)	2.0016	2.0010	2.0008
Experiment	$E_\delta^{'}$ [167]	2.0018	2.0021	2.0021
	$E_\gamma^{'}$ [167]	2.0018	2.0006	2.0003
Computation	$E_\delta^{'}$ [168]	2.0018	2.0043	2.0034
	$E_\gamma^{'}$ [168]	2.0018	2.0008	2.0001

Table 8.10: Diagonal g-tensor components for the positively charged oxygen vacancy for the clusters in States a and b.

The hyperfine constants for atoms local to the vacancy are given in Table 8.11. It can be seen that the unpaired electron interacts most strongly with the nucleus of the two Si atoms neighbouring the vacancy. In the case of the back projected configurations where the unpaired electron density is localised on Si_S the hyperfine constant ranges from 43.27 mT - 46.51 mT which is in good

agreement with the published results of 43.1 mT and 48.9 mT which were also obtained using the embedded cluster method [79]. The distorted dimer configuration observed for Cluster D in state V_a^{+1} has hyperfine constants of 8.47 mT and 18.00 mT for Si_L and Si_S respectively. This compares reasonably well to the published values for the regular dimer for which a hyperfine constant of 10.0 mT was reported for each of these Si atoms, and in both cases the sum of the constants is around 20 mT which reflects the distortion of the dimer. The hyperfine constant of Si_L for Cluster B in the V_a^{+1} state is 56.87 mT which is high in comparison to that of the other Si atoms. It compares most closely to the hyperfine constant of 52 mT reported for the E'_χ configuration. In fact these two configurations share a feature in that the two Si atoms neighbouring the vacancy site are bonded to a common oxygen atom whereby one Si atom remains three-coordinated and the other Si atom becomes four-coordinated. This high hyperfine constant suggests that the spin density of the unpaired electron is strongly localised on the three coordinated Si atom.

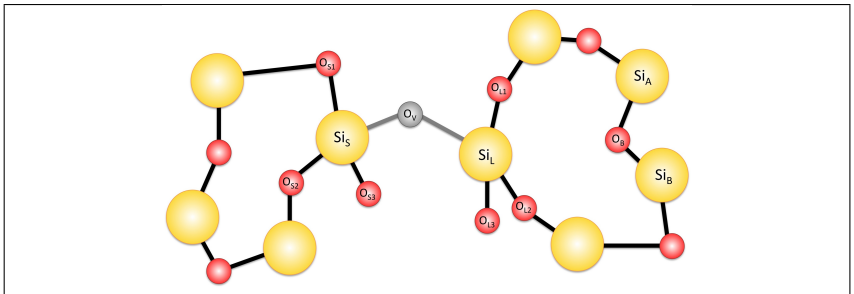

Atom	Hyperfine Constant [mT]							
	Cluster A		Cluster B		Cluster C		Cluster D	
	V_a^{+1}	V_b^{+1}	V_a^{+1}	V_b^{+1}	V_a^{+1}	V_b^{+1}	V_a^{+1}	V_b^{+1}
Si_S	46.24	46.51	0.01	46.47	43.56	43.27	18.00	43.94
O_{S1}	4.31	4.23	2.29	2.50	2.73	2.67	3.34	3.20
O_{S2}	3.67	3.56	0.04	2.04	3.40	3.24	1.56	3.00
O_{S3}	3.40	3.41	0.08	4.02	2.46	2.47	1.97	2.53
Si_L	0.00	0.00	56.87	0.37	0.02	0.02	8.47	0.01
O_{L1}	0.15	0.13	2.16	0.04	0.01	0.02	2.01	0.19
O_{L2}	0.02	0.02	1.92	0.00	0.07	0.07	0.70	0.01
O_{L3}	0.09	0.06	2.56	2.14	0.02	0.02	1.98	0.14
O_B	0.00	0.00	0.01	0.11	0.00	0.00	0.03	0.01

Table 8.11: The hyperfine constants for atoms close to the positively charged oxygen vacancy for clusters A, B, C and D in States *a* and *b*. A schematic of the atoms local to the defect is also included for clarity.

8.3.2 Neutral Back Projected Configurations

Highest Occupied Molecular Orbital

Following on from the study by Kimmel et al [88] of positively charged oxygen vacancies in the back projected configuration, the same clusters were investigated in their neutral state. Following the procedure given in Figure 8.5 the neutral vacancy in State b, V_b^0, was generated by adding an electron to the positively charged oxygen vacancy precursor in State b, V_b^{+1}. Of the four positively charged precursors Cluster E and Cluster G were found to have α back projected configurations, whereas Cluster F and Cluster H were in the κ configuration. The neutral oxygen vacancy in State b was also produced by adding a neutral oxygen vacancy to the non-defective clusters.

The highest occupied molecular orbitals are shown for these neutral clusters in Figure 8.13 and Figure 8.14. It can be seen that in State a all clusters contain the dimer configuration. In State b Cluster E has an α back projected configuration whereas Cluster F and Cluster G both have κ back projected configurations. These three clusters have the same configuration as their positively charged precursors. In the positively charged precursor of cluster H the long bonded silicon atom, Si_L, and the short bonded silicon, Si_S, are both coordinated to the oxygen atom O_{L1}such that Si_L is three coordinated and Si_S is coordinated to four oxygen atoms. The addition of the electron causes Si_L to relax towards a back oxygen atom, O_B, causing the Si_L- O_{L1} bond to break. This results in a four coordinated Si_S atom and a two coordinated Si_L.

Geometry

The distance between the two Si atoms neighbouring the vacancy is given in Table 8.12. It can be seen that for each of the dimer configurations in the V_a^0 state Si_S-Si_L is shorter than that of the corresponding non-defective cluster. The configurations of state V_b^0 are all dangling bond configurations and as a result Si_S-Si_L are longer than their non-defective analogues.

Cluster	Relative Si_S-Si_L [Å]	
	V_a^0	V_b^0
E	-0.80	1.40
F	-0.50	0.39
G	-0.54	2.04
H	-0.67	0.67

Table 8.12: The relative Si_S-Si_L distances of the neutral vacancy clusters in States a and b.

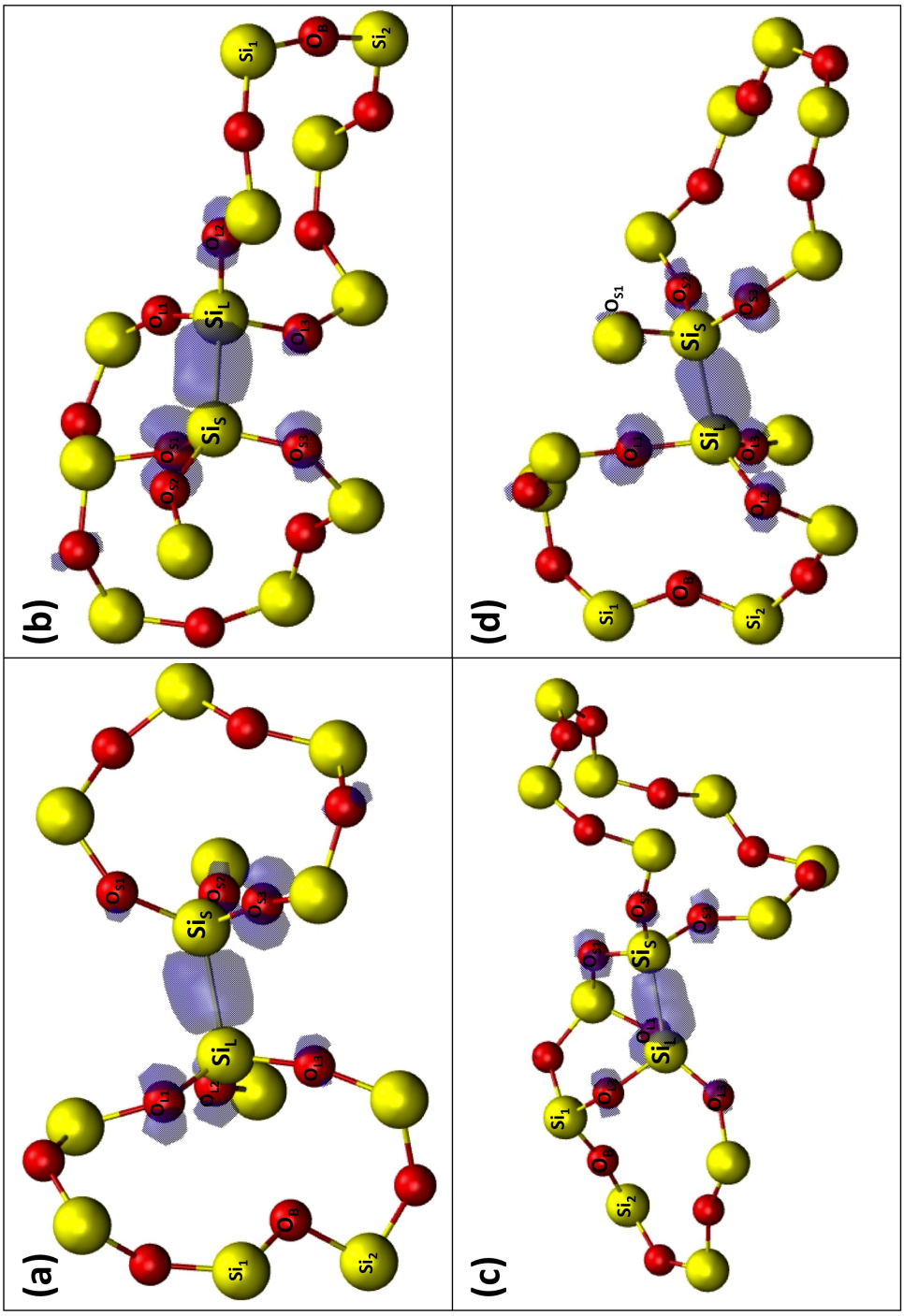

Figure 8.13: The highest occupied molecular orbitals for neutral oxygen vacancy clusters (a) E, (b) F, (c) G and (d) H in State *a*.

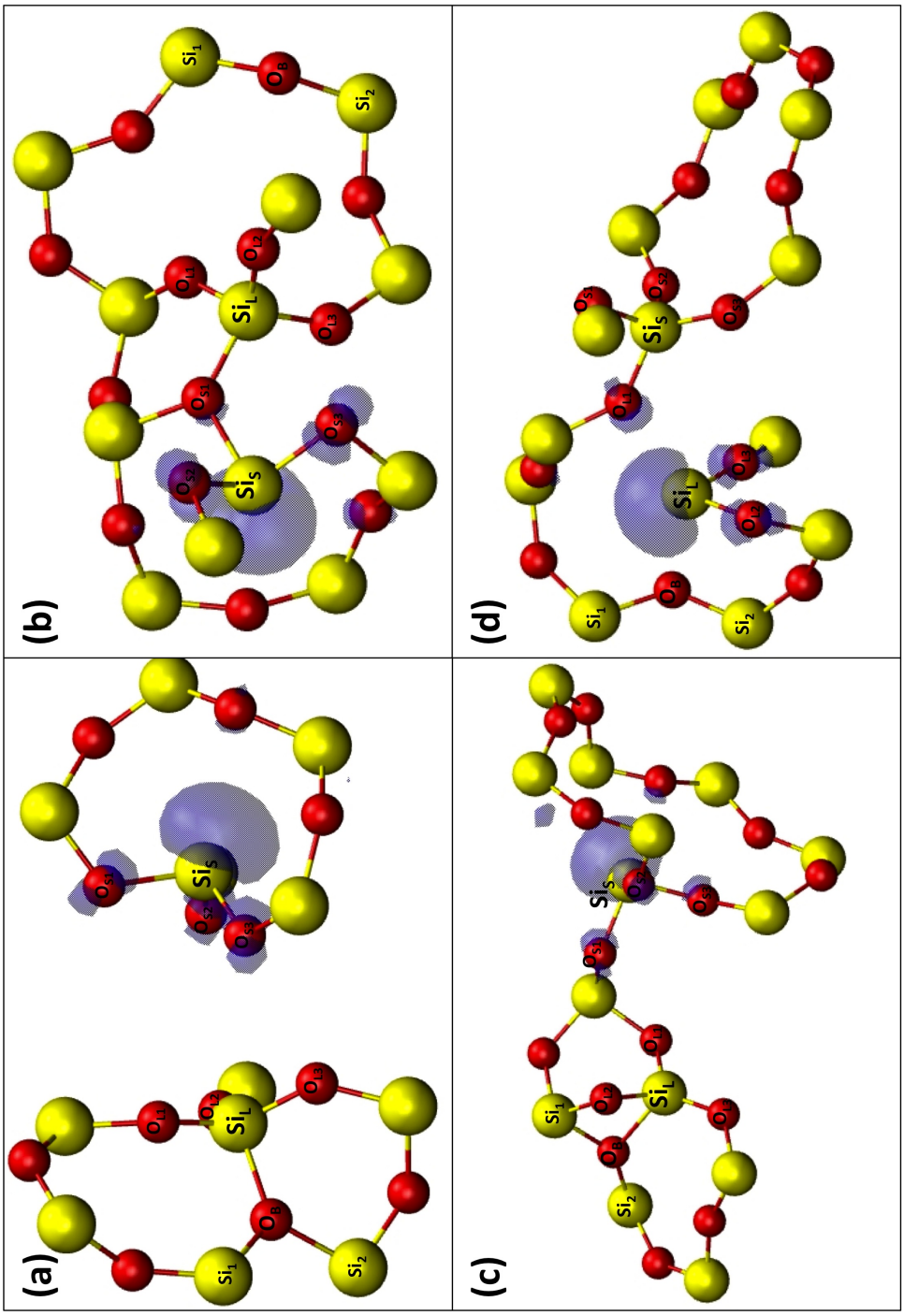

Figure 8.14: The highest occupied molecular orbitals for neutral oxygen vacancy clusters (a) E, (b) F, (c) G and (d) H in State *b*.

Formation Energy

The formation energies are given in Table 8.13. It can be seen that the dimer configurations are metastable for the neutral oxygen vacancy, whereas the dangling bond configurations of state V_b^0 are stable.

Cluster	Formation Energy [eV]	
	V_a^0	V_b^0
E	8.65	12.11
F	9.49	12.17
G	9.82	12.67
H	9.24	9.77

Table 8.13: Vacancy formation energies for neutral vacancies in State a and State b.

Bader Charge

The relative charges for the neutral vacancy clusters are given in Table 8.14. It can be seen that in State a roughly two electrons are shared by Si_S and Si_L. The exception is Cluster F in State a in which the Bader charges suggest that most of the charge is associated with atom Si_S, with a significant amount of charge also localised on atoms O_{S3} and O_B. For Cluster E, Cluster F and Custer G in State b Bader charge analysis suggests that a pair of electrons is associated with atom Si_S. Whereas for Cluster H most of the charge is associated with atom Si_L, however a significant amount of the charge is also localised on the oxygen atoms to which it is coordinated along with atom O_{L1}.

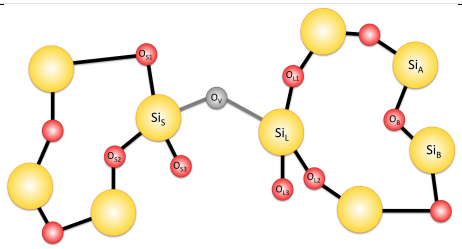

Atom	Relative Bader Charge [e]							
	Cluster E		Cluster F		Cluster G		Cluster H	
	V_a^0	V_b^0	V_a^0	V_b^0	V_a^0	V_b^0	V_a^0	V_b^0
Si_S	1.21	1.72	1.85	-0.01	1.10	0.01	1.00	0.00
Si_L	0.61	0.01	0.03	1.7	0.85	0.63	0.83	1.79
O_{S1}	-0.10	-0.14	0.01	0.03	-0.06	-0.03	0.04	0.17
O_{S2}	0.04	0.03	0.02	0.01	-0.03	-0.05	0.06	0.22
O_{S3}	-0.01	0.06	0.41	-0.04	-0.02	0.01	0.07	0.04
O_{L1}	-0.06	-0.10	-0.03	0.06	-0.01	0.02	0.03	0.70
O_{L2}	-0.02	0.04	-0.02	0.09	0.08	0.06	0.02	0.04
O_{L3}	0.04	0.01	0.03	0.04	0.03	-0.02	-0.03	0.14
O_B	0.01	0.16	0.61	-0.03	0.01	0.07	-0.02	0.00
Si_1	0.02	-0.01	0.00	-0.01	0.03	-0.01	0.00	0.00
Si_2	0.01	-0.01	-0.01	0.02	0.00	0.04	0.00	0.01

Table 8.14: The relative Bader charges of atoms close to the vacancy site in the neutral clusters. A schematic of the atoms local to the defect is also included for clarity.

8.4 Conclusions

The oxygen vacancy configurations and corresponding formation energies is summarised in Table 8.15. The results show that of the eight clusters investigated in this study the most stable formation for neutral oxygen vacancies is the dimer configuration. It can also be seen that contrary to the suggestion of Kimmel et al [88], the capture of an electron by positively charged oxygen vacancies in the back projected configuration results in neutral back projected configurations that are less stable than the puckered configurations described by Lu et al [77] and Fleetwood et al [66].

(a)

	V_a^0		V_b^0	
	Configuration	Formation Energy [eV]	Configuration	Formation Energy [eV]
A	dimer	9.81	dimer	9.63
B	dimer	9.39	puckered	11.66
C	dimer	9.37	puckered	10.30
D	dimer	9.79	puckered	10.44

(b)

	V_a^{+1}		V_b^{+1}	
	Configuration	Formation Energy [eV]	Configuration	Formation Energy [eV]
A	puckered	34.51	puckered	34.74
B	forward-projected dangling bond	34.21	puckered	34.53
C	puckered	34.05	puckered	34.18
D	distorted dimer	35.22	puckered	33.69

Table 8.15: A summary of the configurations and corresponding formation energies for (a) the neutral vacancy states and (b) the positively charged vacancy states associated with puckered configurations.

	V_a^0		V_b^0	
	Configuration	Formation Energy [eV]	Configuration	Formation Energy [eV]
E	dimer	8.65	back-projected α	12.63
F	dimer	9.49	back-projected $\varkappa$	12.17
G	dimer	9.82	back-projected $\varkappa$	12.67
H	dimer	9.24	dangling bond	9.77

Table 8.16: A summary of the configurations and corresponding formation energies for the neutral vacancy states associated with back projected configurations.

During this study an unusual positively charged oxygen vacancy in a forward projected dangling bond configuration was observed. This occurred on a site predicted to host the puckered configuration. In this configuration both Si atoms neighbouring the vacancy are directed towards the vacancy site. Both of these Si atoms are coordinated to a common oxygen atom such that one Si is three-coordinated and the other is four-coordinated. The spin density of the unpaired electron is localised on the three-coordinated Si atom and is also directed towards the vacancy. The hyperfine constant of this atom was found to be 56.87 mT which is high in comparison to that in other E' configurations, however it compares most closely to the hyperfine constant of the equivalent Si atom in the E'$_\varkappa$ configuration, which was found to be 52 mT. These two configurations share a common feature in that the two Si atoms neighbouring the vacancy are bonded to a common oxygen atom and the unpaired electron is localised on the three-coordinated Si atom. The high hyperfine constant suggests that the electron is strongly bound to this Si atom.

From the results the one electron energy levels were determined for the neutral and positively charged clusters associated with the puckered configuration, as well as for the neutral clusters associated with the back projected configuration. These are shown in Figure 8.15, Figure 8.16 and Figure 8.17 respectively. A value of 4.60 eV was used for the Si-SiO_2 valence band alignment [169].

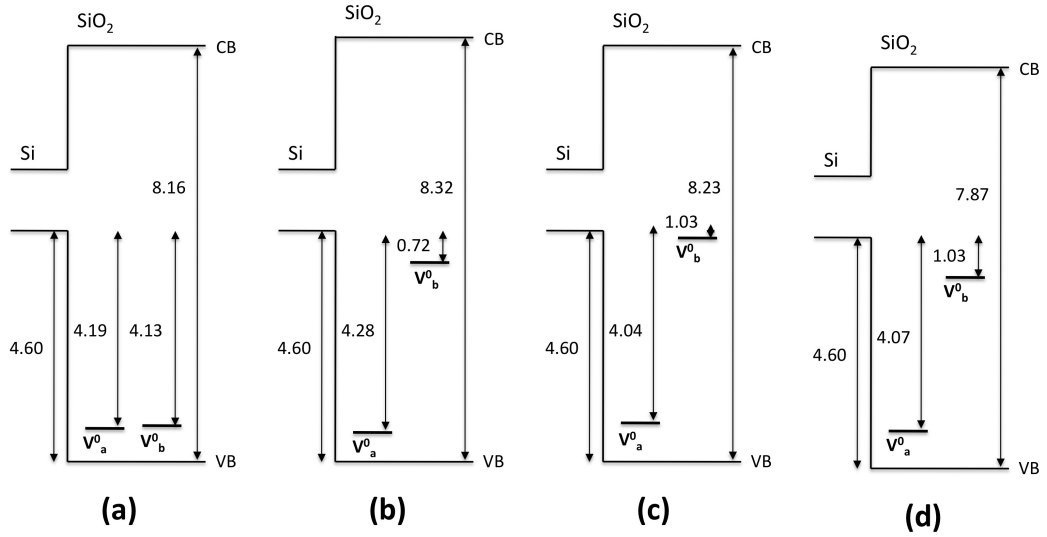

Figure 8.15: The one electron levels, in units of eV, for neutral clusters associated with the puckered configuration in States a and b.

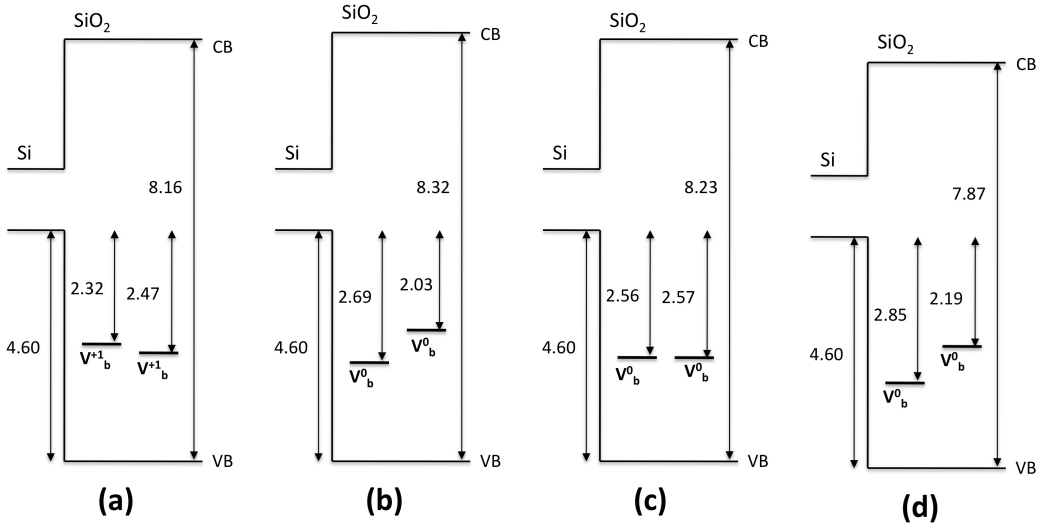

Figure 8.16: The one electron levels, in units of eV, for positively charged clusters associated with the puckered configuration in States a and b.

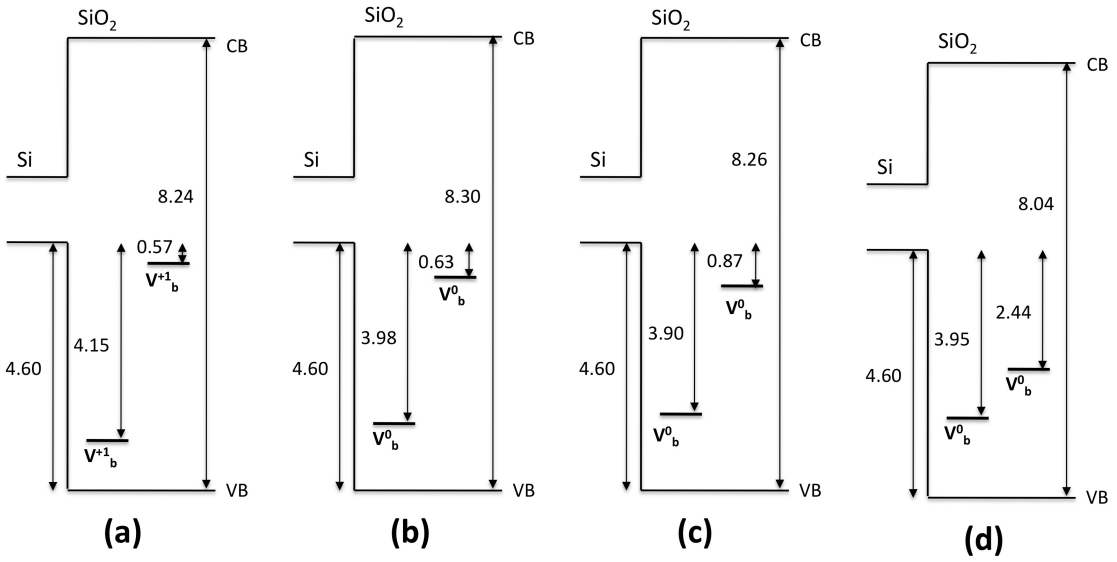

Figure 8.17: The one electron levels, in units of eV, for neutral clusters associated with the back projected configuration in States a and b.

These diagrams can be combined and further summarised by the one electron energy levels in Figure 8.18 (a). It can be seen that all energy levels for the neutral and positively charged vacancies investigated lie below the Si valence band and that the one electron energy levels of the back projected and puckered configurations are higher that those of their puckered precursors. This is in disagreement with previous computational work [170,171] using semi-empirical cluster calculations in which it was suggested that the one electron energy levels to be located within the Si bandgap. The electron levels of published results shown in Figure 8.18 (b) and have been used to form the basis of the two stage model for negative bias temperature instability [67]. In this model it is expected that the neutral oxygen vacancy precursor is below the Si valence band and that the defect states are within the Si band gap. This model also regards defect states below the Si valence band to be electrically neutral and non contributory to the threshold voltage shift [67]. Therefore from this work it can be suggested that it is not feasible to describe the the mechanism behind the recoverable component of the NBTI model as the capture and emission of a hole by a neutral oxygen vacancy if the positively charged successor has a puckered configuration. However a statistical average over a wider range of oxygen vacancies is required in order to confirm this.

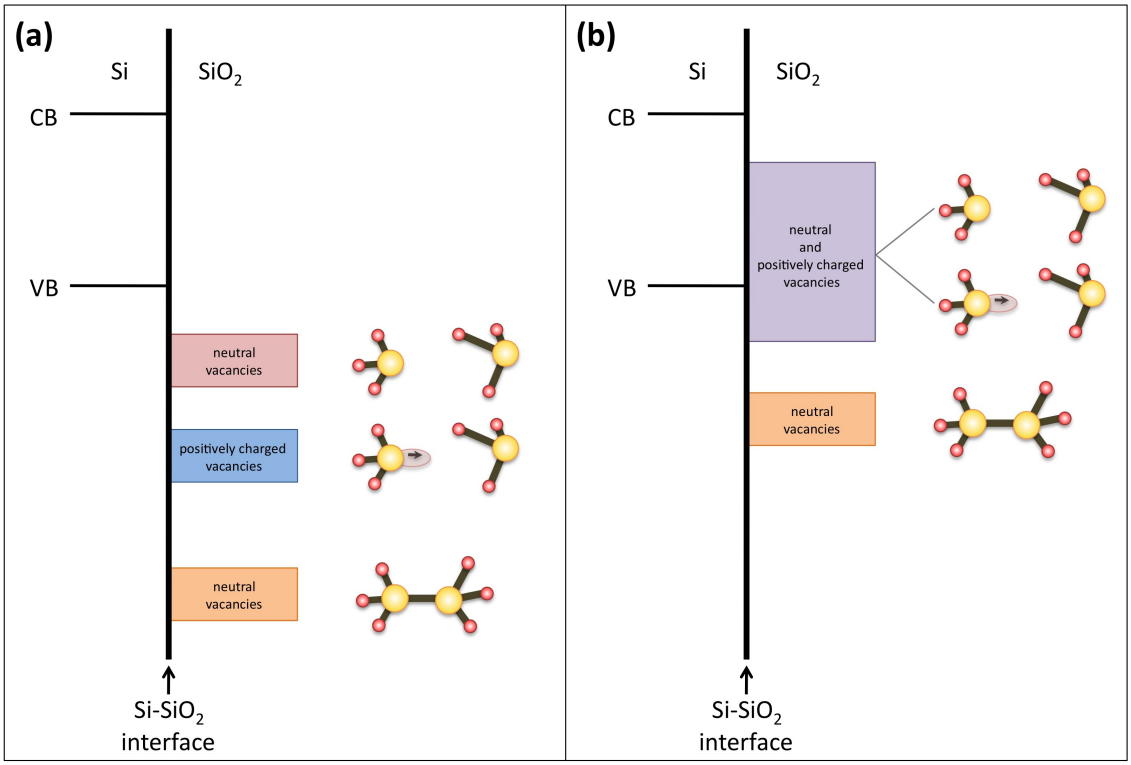

Figure 8.18: One electron energy level diagrams (a) of the defects investigated in this study and (b) for the negative bias temperature instability model proposed by Grasser et al.

Chapter 9

Overall Conclusions and Final Remarks

Fast diffusion pathways were found to occur for vacancies in the symmetric tilt grain boundary and also in the twist grain boundary. For the tilt grain boundary this involves vacancy sites at the close-packed region of the boundary. Whereas for the twist grain boundary fast diffusion can be suggested to occur in a zig-zag path between sites at the grain boundary plane and sites at adjacent bulk-like planes. No fast diffusion pathways were found to exist for interstitials at these grain boundaries although low activation energies were found for interstitials at the sparse-packed region of the tilt grain boundary where the energy landscape is flat. The possibility of lower interstitial activation energies at the tilt grain boundary via an interstitialcy mechanism can therefore be explored in future work. This will possibly involve migration between the most energetically favourable interstitial sites at the centre of the grain boundary structural unit and nearest neighbour lattice sites.

Upon application of an electric field an anisotropic lowering of the defect formation energies was observed. For Mg vacancies and O interstitials the formation energy decreased with decreasing distance to the positively charged electrode. On the contrary, for O vacancies and Mg interstitials decreasing formation energies were observed with decreasing distance to the negatively charged electrode. For Mg interstitials it was found that despite the application of the field the lowest activation energy observed is larger than that in bulk MgO, therefore no fast diffusion pathway can be suggested. Fast diffusion pathways can however occur for vacancy and O interstitial migration and it was found that O interstitial migration is more favourable than O vacancy migration. It

can be suggested that an increase in the applied electric field will further reduce defect activation energies with the limit being the threshold voltage of MgO.

Of the four types of grain boundary investigated in this work it was found that the twist grain boundary has the highest entropy in the temperature range 300 - 3000 K. This suggests that upon the formation of this grain boundary more random energy is obtained by the system from the surrounding environment. Therefore less work is required to form the grain boundary structure. The twist grain boundaries is likely be more common in MgO compared to the occurrence of other grain boundaries.

From the investigation into oxygen vacancies in amorphous SiO_2 clusters it can be suggested that the recoverable component of the two stage model for negative bias temperature instability cannot be described as capture and emission of a hole by a neutral oxygen vacancy if the positively charged successor has a puckered configuration. This is because the positively charged oxygen vacancies studied were found to have one electron energy levels below the Si valence band and are electrically neutral. Therefore they cannot contribute to the threshold voltage shifts. The one electron energy levels should be determined for a wide range of oxygen vacancies with varying topologies in order to confirm this.

Bibliography

[1] C. B. Cater and M. G. Norton. *Ceramic Materials: Science and Engineering*. Springer, New York, USA, 2007.

[2] I. Milas, B. Hinnemann, and E. A. Carter. Diffusion of Al, O, Pt, Hf, and Y atoms on α-Al_2O_3(0001): implications for the role of alloying elements in thermal barrier coatings. *J. Mater. Chem.*, 21:1447–1456, 2011.

[3] K. E. Sickafus, L. Minervini, R. W. Grimes, J. A. Valdez, M. Ishimaru, F. Li, K. J. McClellan, and T. Hartmann. Radiation tolerance of complex oxides. *Science*, 289(5480):748–751, 2000.

[4] B. P. Uberuaga, R. Smith, A. R. Cleave, F. Montalenti, G. Henkelman, R. W. Grimes, A. F. Voter, and K. E. Sickafus. Structure and mobility of defects formed from collision cascades in MgO. *Phys. Rev. Lett.*, 92:115505, 2004.

[5] X. Bai, A. F. Voter, R. G. Hoagland, M. Nastasi, and B. P. Uberuaga. Efficient annealing of radiation damage near grain boundaries via interstitial emission. 327(5973):1631–1634, 2010.

[6] H. Chen, B. Raghothamachar, W. Vetter, M. Dudley, Y. Wang, and B. J. Skromme. Effects of different defect types on the performance of devices fabricated on a 4H-SiC homoepitaxial layer. 2006.

[7] *Introduction to Ceramics*. Wiley, 1976.

[8] M. W. Barsoum. *Fundamentals of Ceramics*. Institute of Physics Publishing, 2003.

[9] F.L. Riley. Structural ceramics: Fundamentals and case studies.

[10] R. J. Brook, editor. *Concise Encyclopedia of Advanced Ceramic Materials*. Pergamon Press, 1991.

[11] C. Ronchi and M. Sheindlin. Melting point of MgO. *Journal of Applied Physics*, 90(7):3325–3331, 2001.

[12] D. M. Roessler and W. C. Walker. Electronic spectrum and ultraviolet optical properties of crystalline mgo. *Phys. Rev.*, 159:733–738, Jul 1967.

[13] A. S. Rao and R. J. Kearney. Logarithmic derivative reflectance spectra of bao and sro. *physica status solidi (b)*, 95(1):243–250, 1979.

[14] O. G. Palanna. *Engineering Chemistry*. Tate McGraw Hill Education Private Limited, 2009.

[15] J. L. Krumhansl, H. W. Papenguth, P-.C. Zhang, J. W. Kelly, H. L. Anderson, and J. O. E. Hardesty. Behaviour of MgO as a CO_2 scavenger at the Waste Isolation Pilot Plant (WIPP), carlsbad, new mexico. *MRS Proceedings*, 608:155, 1999.

[16] T. Jüstel and H. Nikol. Optimization of luminescent materials for plasma display panels. *Advanced Materials*, 12(7):527–530, 2000.

[17] J. P. Boeuf. Plasma display panels: physics, recent developments and key issues. *Journal of Physics D: Applied Physics*, 36(6):R53, 2003.

[18] A. V. Narliker, editor. *Studies of High Temperature Superconductors: Advances in Research and Applications*, volume 35. 2001.

[19] H. W. Kim, M. H. Kong, and J.-H. Yang. Catalyst-free growth of magnesium oxide whiskers and their characteristics. *Acta Physica Polonica A*, 113.

[20] Morgan Technical Ceramics. Morgan technical ceramics - Magnesium Oxide, January 2012. `http://www.morgantechnicalceramics.com/products-materials/advanced-ceramics/magnesium-oxide/`.

[21] MaterialScientist. A-quartz, December 2011. `http://en.wikipedia.org/wiki/File:A-quartz.png`.

[22] MaterialScientist. B-quartz, December 2011. `http://en.wikipedia.org/wiki/File:B-quartz.png`.

[23] MaterialScientist. A-tridymite, December 2011. `http://en.wikipedia.org/wiki/File:A-tridymite.png`.

[24] MaterialScientist. B-tridymite, December 2011. `http://en.wikipedia.org/wiki/File:B-tridymite.png`.

[25] MaterialScientist. A-cristobalite, December 2011. `http://en.wikipedia.org/wiki/File:A-cristobalite.png`.

[26] MaterialScientist. B-cristobalite, December 2011. `http://en.wikipedia.org/wiki/File:B-cristobalite.png`.

[27] MaterialScientist. Faujasite structure, December 2011. `http://en.wikipedia.org/wiki/File:Faujasite-structure.svg`.

[28] MaterialScientist. Melanophlogite structure, December 2011. `http://en.wikipedia.org/wiki/File:MelanophlogiteStucture.png`.

[29] MaterialScientist. Keatite, December 2011. `http://en.wikipedia.org/wiki/File:Keatite.png`.

[30] MaterialScientist. Mognite, December 2011. `http://en.wikipedia.org/wiki/File:Moganite.png`.

[31] MaterialScientist. Coesite, December 2011. `http://en.wikipedia.org/wiki/File:Coesite.png`.

[32] MaterialScientist. Stishovite, December 2011. `http://en.wikipedia.org/wiki/File:Stishovite.png`.

[33] MaterialScientist. Sis2typesilica, December 2011. `http://en.wikipedia.org/wiki/File:SiS2typeSilica.png`.

[34] MaterialScientist. Seifertite, December 2011. `http://en.wikipedia.org/wiki/File:SeifertiteStructure.png`.

[35] Hui Xie, Zhi-Cheng Wang, and Jun-Xin Fang. Study of material dispersion in amorphous silica optical fibers. *physica status solidi (a)*, 96(2):483–487, 1986.

[36] G. Pacchioni, L. Skuja, and D. L. Griscom, editors. *Defects in SiO_2 and Related Dielectrics: Science and Technology*. Kluwer Academic, Dordecht, 2000. NATO Science Series, Series II: Mathematical and Physical Chemistry.

[37] A. Panchula P. M. Rice B. Hughes M. Samant S. Yang S. P. Parkin, C. Kaiser. Giant tunnelling magnetoresistance at room temperature with MgO (100) tunnel barriers. *Nature Materials*, 3(12):862.

[38] T. J. Vink, A. R. Balkenende, R. G. F. A. Verbeek, H. A. M. van Hal, and S. T. de Zwart. Materials with a high secondary-electron yield for use in plasma displays. 80(12):2216–2218, 2002.

[39] L. A. Hayden and E. B. Watson. Grain boundary mobility of carbon in earth's mantle: A possible carbon flux from the core. *Proceedings of the National Academy of Sciences*, 105(25):8537–8541, 2008.

[40] Hei Wong, B. Sen, V. Filip, and M.C. Poon. Material properties of interfacial silicate layer and its influence on the electrical characteristics of MOS devices using hafnia as the gate dielectric. *Thin Solid Films*, 504(1-2):192 – 196, 2006.

[41] C. R. M. Grovenor. Grain boundaries in semiconductors. *Journal of Physics C: Solid State Physics*, 18(21):4079, 1985.

[42] T. Kizuka, M. Iijima, and N. Tanaka. Atomic process of electron irradiation induced grain boundary migration in a MgO tilt boundary. *Philosophical Magazine A*, 77(2):413–422, 1998.

[43] K. L. Merkle and D. J. Smith. Atomic structure of symmetric tilt grain boundaries in NiO. *Phys. Rev. Lett.*, 59:2887–2890, Dec 1987.

[44] P. Chaudhari and J.W. Matthews. Coincidence twist boundaries between crystalline smoke particles. 42(8):3063–3066, 1971.

[45] H. Mykura, P. S. Bansal, and M. H. Lewis. Coincidence site lattice relations for MgO-CdO interfaces. *Philosophical Magazine A*, 42(2):225–233, 1980.

[46] C. P. Sun and R. W. Balluffi. Secondary grain boundary dislocations in [001] twist boundaries in MgO I. intrinsic structures. *Philosophical Magazine A*, 46(1):49–62, 1982.

[47] Y. Yan, M. F. Chisholm, G. Duscher, A. Maiti, S. J. Pennycook, and S. T. Pantelides. Impurity induced structural transformation of a MgO grain boundary. *Phys. Rev. Lett.*, 81:3675–3678, 1998.

[48] P. Wynblatt, G. S. Rohrer, and F. Papillon. Grain boundary segregation in oxide ceramics. *Journal of the European Ceramic Society*, 23(15):2841 – 2848, 2003.

[49] Y. M. Chiang, A. F. Henriksen, W. D. Kingery, and D. Finello. Characterization of grain boundary segregation in MgO. *Journal of the American Ceramic Society*, 64(7):385–389, 1981.

[50] J. W. Osenbach and V. S. Stubican. Grain boundary diffusion of ^{51}Cr in MgO and Cr doped MgO. *Journal of the American Ceramic Society*, 66(3):191–195, 1983.

[51] B. J. Wuensch and T. Vasilos. Grain-boundary diffusion in MgO. *Journal of the American Ceramic Society*, 47(2):63–68, 1964.

[52] N. Mizutani, A. J. Garratt-Reed, and W. D. Kingery. Grain boundary segregation of iron, chromium an scandium in polycrystalline magnesium oxide. *Ceramics International*, 9(1):31 – 32, 1983.

[53] D. J. Harris, G. W. Watson, and S. C. Parker. Atomistic simulation studies on the effect of pressure on diffusion at the MgO 410/[001] tilt grain boundary. *Phys. Rev. B*, 64:134101, 2001.

[54] C. M. Osburn and R. W. Vest. Electrical properties of single crystals, bicrystals, and polycrystals of MgO. *Journal of the American Ceramic Society*, 54(9):428–435, 1971.

[55] A. Atkinson and R. I. Taylor. The diffusion of ^{63}Ni along grain boundaries in nickel oxide. *Philosophical Magazine A*, 43(4):979–998, 1981.

[56] A. Atkinson, A. E. Hughes, and A. Hammou. The self-diffusion of Ni in undoped and Al-doped NiO single crystals. *Philosophical Magazine A*, 43(5):1071–1091, 1981.

[57] D. M. Duffy. Grain boundaries in ionic crystals. *Journal of Physics C: Solid State Physics*, 19(23):4393, 1986.

[58] D. J. Harris, G. W. Watson, and S. C. Parker. Vacancy migration at the 410/[001] symmetric tilt grain boundary of MgO: An atomistic simulation study. *Phys. Rev. B*, 56:11477–11484, 1997.

[59] G. V. Lewis and C. R. A. Catlow. Potential models for ionic oxides. *Journal of Physics C: Solid State Physics*, 18(6):1149, 1985.

[60] K. P. McKenna and A. L. Shluger. First-principles calculations of defects near a grain boundary in MgO. *Phys. Rev. B*, 79:224116, Jun 2009.

[61] D. Wolf and R Benedek. Grain boundary phenomena in electronic ceramics. *Adv. Ceram*, 1:107, 1981.

[62] D. Wolf. On the stability of (001) CSL twist boundaries in MgO: A theoretical study. *J. Phys. Colloques*, 43:C6–45–C6–63, 1982.

[63] D. M. Duffy and P. W. Tasker. A general structure for coincidence twist grain boundaries in rock salt structured oxides. *Journal of the American Ceramic Society*, 67(9):C–176–C–177, 1984.

[64] D. M. Duffy and P. W. Tasker. Properties of grain boundaries in rock salt structured oxides. *Advances in Ceramics*, 10:275, 1984.

[65] J. H. Harding and C. Noguera. Empirical and *italic* ab initio local-density approximation studies of an MgO(100) twist grain boundary. *Philosophical Magazine Letters*, 77(6):315–320, 1998.

[66] D. M. Fleetwood, H. D. Xiong, Z.-Y. Lu, C. J. Nicklaw, J. A. Felix, R. D. Schrimpf, and S. T. Pantelides. Unified model of hole trapping, 1/f noise, and thermally stimulated current in MOS devices. *Nuclear Science, IEEE Transactions on*, 49(6):2674 – 2683, 2002.

[67] T. Grasser, B. Kaczer, W. Goes, Th. Aichinger, Ph. Hehenberger, and M. Nelhiebel. A two-stage model for negative bias temperature instability. *Reliability physics*, pages 33–44, 2009.

[68] P. M. Lenahan and J. J. Mele. E′ centers and leakage currents in the gate oxides of metal oxide silicon devices. *Papers from the 27th conference on the physics and chemistry of semiconductor interfaces*, 18(4):2169–2173, 2000.

[69] R. A. Weeks. Paramagnetic resonance of lattice defects in irradiated quartz. *Journal of Applied Physics*, 27(11):1376–1381, 1956.

[70] R. A. Weeks and C. M. Nelson. Trapped electrons in irradiated quartz and silica: II, electron spin resonance. *Journal of the American Ceramic Society*, 43(8):399–404, 1960.

[71] R. H. Silsbee. Electron spin resonance in neutron-irradiated quartz. *Journal of Applied Physics*, 32(8):1459–1462, 1961.

[72] F. J. Feigl, W. B. Fowler, and K. L. Yip. Oxygen vacancy model for the $e\prime_1$ center in SiO_2. *Solid State Communications*, 14(3):225 – 229, 1974.

[73] Kwok Leung Yip and W. Beall Fowler. Electronic structure of E_1' centers in SiO_2. *Phys. Rev. B*, 11:2327–2338, Mar 1975.

[74] J. K. Rudra and W. B. Fowler. Oxygen vacancy and the $E_1^{'}$ center in crystalline SiO_2. *Phys. Rev. B*, 35:8223–8230, 1987.

[75] M. Boero, A. Pasquarello, J. Sarnthein, and R. Car. Structure and hyperfine parameters of E_1' centers in α-quartz and in vitreous SiO_2. *Phys. Rev. Lett.*, 78:887–890, Feb 1997.

[76] C. J. Nicklaw, Z.-Y. Lu, D. M. Fleetwood, R. D. Schrimpf, and S. T. Pantelides. The structure, properties, and dynamics of oxygen vacancies in amorphous SiO_2. *Nuclear Science, IEEE Transactions on*, 49(6):2667 – 2673, 2002.

[77] Z.-Y. Lu, C. J. Nicklaw, D. M. Fleetwood, R. D. Schrimpf, and S. T. Pantelides. Structure, properties, and dynamics of oxygen vacancies in amorphous SiO_2. *Phys. Rev. Lett.*, 89:285505, 2002.

[78] A. H. Edwards, P. V. Sushko, A. L. Shluger, and V. B. Sulimov. Embedding techniques for irradiation-induced defects in crystalline SiO_2. *Nuclear Science, IEEE Transactions on*, 49(3):1383 – 1388, jun 2002.

[79] A. S. Mysovsky V. B. Sulimov A. Taga A. L. Shluger P. V. Sushko, S. Mukhopadhyay. Structure and properties of defects in amorphous silica: new insights from embedded cluster calculations. *J. Phys.: Condens. Matter*, 17:S2115, 2005.

[80] V. B. Sulimov, P. V. Sushko, A. H. Edwards, A. L. Shluger, and A. M. Stoneham. Asymmetry and long-range character of lattice deformation by neutral oxygen vacancy in α-quartz. *Phys. Rev. B*, 66:024108, Jul 2002.

[81] A. S. Mysovsky, P. V. Sushko, S. Mukhopadhyay, A. H. Edwards, and A. L. Shluger. Calibration of embedded-cluster method for defect studies in amorphous silica. *Phys. Rev. B*, 69:085202, 2004.

[82] S. Mukhopadhyay, P. V. Sushko, A. H. Edwards, and A. L. Shluger. Calculation of relative concentrations of e′ centres in amorphous silica. *Journal of Non-Crystalline Solids*, 345-346(0):703 – 709, 2004. <ce:title>Physics of Non-Crystalline Solids 10</ce:title>.

[83] D. L. Griscom and M. Cook. ^{29}Si superhyperfine interactions of the E′ center: a potential probe of range-II order in silica glass. *Journal of Non-Crystalline Solids*, 182(1-2):119 – 134, 1995.

[84] G. Pacchioni, F. Frigoli, D. Ricci, and J. A. Weil. Theoretical description of hole localization in a quartz Al center: The importance of exact electron exchange. *Phys. Rev. B*, 63:054102, 2000.

[85] S. Mukhopadhyay, P. V. Sushko, A. M. Stoneham, and A. L. Shluger. Modeling of the structure and properties of oxygen vacancies in amorphous silica. *Phys. Rev. B*, 70:195203, Nov 2004.

[86] David L. and Griscom. Characterization of three E′-center variants in X- and β-irradiated high purity a-SiO_2. *Nuclear Instruments and Methods in Physics Research Section B: Beam Interactions with Materials and Atoms*, 1(2-3):481 – 488, 1984.

[87] G. Buscarino, S. Agnello, and F. M. Gelardi. ^{29}Si hyperfine structure of the E_α' center in amorphous silicon dioxide. *Phys. Rev. Lett.*, 97:135502, Sep 2006.

[88] A. Kimmel, P. Sushko, A. Shluger, and G. Bersuker. Positive and negative oxygen vacancies in amorphous silica. *ECS Transactions*, 19(2):3–17, 2009.

[89] A. J. Lelis and T. R. Oldham. Time dependence of switching oxide traps. *IEEE Transactions on Nuclear Science*, 41(6), 1994.

[90] P. M. Lenahan and P. V. Dressendorfer. Hole traps and trivalent silicon centers in metal/oxide/silicon devices. *Journal of Applied Physics*, 55(10):3495–3499, 1984.

[91] A. J. Lelis, H. E. Boesch, T. R. Oldham, and F. B. McLean. Reversibility of trapped hole annealing. *IEEE Transactions on Nuclear Science*, 35(6):1186, 1988.

[92] A. J. Lelis, T. R. Oldham, H. E. Boesch, and F. B McLean. The nature of the trapped hole annealing process. *IEEE Transactions on Nuclear Science*, 36(6):1808, 1989.

[93] J. R. Schwank, P. S. Winokur, P. J. McWhorter, F. W. Sexton, P. V. Dressendorfer, and D. C. Turpin. Physical mechanisms contributing to device "rebound". *IEEE Transactions on Nuclear Science*, 31(6):1434 –1438, dec. 1984.

[94] V. Lakshmanna and A. S. Vengurlekar. Logarithmic detrapping response for holes injected into SiO_2 and the influence of thermal activation and electric fields. *Journal of Applied Physics*, 63(9):4548–4554, 1988.

[95] A. Reisman, C. K. Williams, and J. R. Maldonado. Generation and annealing of defects in silicon dioxide. *Journal of Applied Physics*, 62(3):868–874, 1987.

[96] J. M. Aitken, D. R. Young, and K. Pan. Electron trapping in electron-beam irradiated SiO_2. *Journal of Applied Physics*, 49(6):3386–3391, 1978.

[97] J.M. and Aitken. Radiation-induced trapping centers in thin silicon dioxide films. *Journal of Non-Crystalline Solids*, 40(1-3):31 – 47, 1980.

[98] M. Walters and A. Reisman. The distribution of radiation-induced charged defects and neutral electron traps in SiO_2, and the threshold voltage shift dependence on oxide thickness. *Journal of Applied Physics*, 67(6):2992–3002, 1990.

[99] M. Walters and A. Reisman. Defect centroid, partial distribution, and areal density in process-induced radiation-damaged igfets with gate insulators grown at 1000 and 800 °C. *Journal of Electronic Materials*, 19:711–720, 1990. 10.1007/BF02655239.

[100] M. Walters and A. Reisman. The effects of "normal" annealing cycles during igfet fabrication on initial and radiation-induced gate insulator defects. *Journal of The Electrochemical Society*, 136(12):3791–3794, 1989.

[101] M. Walters and A. Reisman. Radiation-induced neutral electron trap generation in electrically biased insulated gate field effect transistor gate insulators. *Journal of The Electrochemical Society*, 138(9):2756–2762, 1991.

[102] B. G. Dick and A. W. Overhauser. Theory of the dielectric constants of alkali halide crystals. *Phys. Rev.*, 112:90–103, Oct 1958.

[103] Max Born and Joseph E. Mayer. Zur gittertheorie der ionenkristalle. *Zeitschrift für Physik A Hadrons and Nuclei*, 75:1–18, 1932. 10.1007/BF01340511.

[104] J. D. Gale. *General Utility Lattice Program Version 3.4.*

[105] N. F. Mott and M. J. Littleton. Conduction in polar crystals. i. electrolytic conduction in solid salts. *Trans. Faraday Soc.*, 34:485–499, 1938.

[106] Graeme Henkelman and Hannes Jonsson. Improved tangent estimate in the nudged elastic band method for finding minimum energy paths and saddle points. *The Journal of Chemical Physics*, 113(22):9978–9985, 2000.

[107] Daniel Sheppard, Rye Terrell, and Graeme Henkelman. Optimization methods for finding minimum energy paths. *The Journal of Chemical Physics*, 128(13):134106, 2008.

[108] Shuichi Nose. A unified formulation of the constant temperature molecular dynamics methods. *The Journal of Chemical Physics*, 81(1):511–519, 1984.

[109] William G. Hoover. Canonical dynamics: Equilibrium phase-space distributions. *Phys. Rev. A*, 31:1695–1697, Mar 1985.

[110] Peter V. Sushko, Alexander L. Shluger, and C.Richard A. Catlow. Relative energies of surface and defect states: ab initio calculations for the MgO (001) surface. *Surface Science*, 450(3):153 – 170, 2000.

[111] Axel D. Becke. Density-functional thermochemistry. iii. the role of exact exchange. *The Journal of Chemical Physics*, 98(7):5648–5652, 1993.

[112] Chengteh Lee, Weitao Yang, and Robert G. Parr. Development of the colle-salvetti correlation-energy formula into a functional of the electron density. *Phys. Rev. B*, 37:785–789, Jan 1988.

[113] B. W. H. van Beest, G. J. Kramer, and R. A. van Santen. Force fields for silicas and aluminophosphates based on *ab initio* calculations. *Phys. Rev. Lett.*, 64:1955–1958, Apr 1990.

[114] P. S. Baram and S. C. Parker. Atomistic simulation of hydroxide ions in inorganic solids. *Philosophical Magazine Part B*, 73(1):49–58, 1996.

[115] D. J. Binks. *Computational Modelling of Zinc Oxide and Related Oxide Ceramics.* PhD thesis, University of Surrey, 1994.

[116] T. S. Bush, J. D. Gale, C. R. A. Catlow, and P. D. Battle. Self-consistent interatomic potentials for the simulation of binary and ternary oxides. *J. Mater. Chem.*, 4:831–837, 1994.

[117] C. R. A. Catlow, C. M. Freeman, M. S. Islam, R. A. Jackson, M. Leslie, and S. M. Tomlinson. Interatomic potentials for oxides. *Philosophical Magazine A*, 58(1):123–141, 1988.

[118] R. A. Jackson and C. R. A. Catlow. Computer simulation studies of zeolite structure. *Molecular Simulation*, 1(4):207–224, 1988.

[119] M. J. L. Sangster and A. M. Stoneham. Calculations of off-centre displacements of divalent substitutional ions in CaO, SrO and BaO from model potentials. *Philosophical Magazine Part B*, 43(4):597–608, 1981.

[120] Maureen I. McCarthy and Nicholas M. Harrison. *italic*Ab initio determination of the bulk properties of MgO. *Phys. Rev. B*, 49:8574–8582, Apr 1994.

[121] K. J. Chang and Marvin L. Cohen. High-pressure behavior of MgO: Structural and electronic properties. *Phys. Rev. B*, 30:4774–4781, Oct 1984.

[122] M. J. L. Sangster and D. K. Rowell. Calculation of defect energies and volumes in some oxides. *Philosophical Magazine A*, 44(3):613–624, 1981.

[123] B. B. Karki, L. Sixtrude, S. L. Clark, M. C. Warren, G. J. Ackland, and J. Crain. Structure and elascicity of MgO at high pressure. *American Mineralogist*, 82:51–60, 1997.

[124] A. Vijay and T.S. Verma. Analysis of temperature dependence of elastic constants and bulk modulus for ionic solids. *Physica B: Condensed Matter*, 291(3-4):373 – 378, 2000.

[125] C. R. A. Catlow, I. D. Faux, and M. J. Norgett. Shell and breathing shell model calculations for defect formation energies and volumes in magnesium oxide. *Journal of Physics C: Solid State Physics*, 9(3):419, 1976.

[126] J. H. Harding and A. H. Harker. Calculations of interionic potentials in oxides. *Philosophical Magazine Part B*, 51(2):119–125, 1985.

[127] M. J. Gillan, I. Manassidis, and A. De Vita. The ab-initio energetics of oxides. *Philosophical Magazine Part B*, 69(5):879–888, 1994.

[128] J. Woltersdorf, A.S. Nepijko, and E. Pippel. Dependence of lattice parameters of small particles on the size of the nuclei. *Surface Science*, 106(1-3):64 – 69, 1981.

[129] G. V. Samsonov. *The Oxide Handbook*. Plenum Press, 1981.

[130] D.-H. Chung. Elastic moduli of single crystal and polycrystalline MgO. *Philosophical Magazine*, 8(89):833–841, 1963.

[131] O. L. Anderson and P. Andreatch. Pressure derivatives of elastic constants of single-crystal MgO at 23° and -195.8°C. *Journal of the American Ceramic Society*, 49(8):404–409, 1966.

[132] B. J. Wuensch, W. C. Steele, and T. Vasilos. Cation self-diffusion in single-crystal mgo. *The Journal of Chemical Physics*, 58(12):5258–5266, 1973.

[133] Y. Oishi and W. D. Kingery. Oxygen diffusion in periclase crystals. *The Journal of Chemical Physics*, 33(3):905–906, 1960.

[134] M J L Sangster, G Peckham, and D H Saunderson. Lattice dynamics of magnesium oxide. *Journal of Physics C: Solid State Physics*, 3(5):1026, 1970.

[135] G. Leibfried and W. Ludwig. Theory of anharmonic effects in crystals. volume 12 of *Solid State Physics*, pages 275 – 444. Academic Press, 1961.

[136] O. L. Anderson and D. G. Isaak. Elastic constants of mantle minerals at high temperature. In T. J. Ahrens, editor, *Mineral Physics and Crystallography: A Handbook of Physical Constants*, volume 2, pages 64–97. AGU, 1995.

[137] B. C. Harding and D. M. Price. Cation self-diffusion in MgO up to 2350 °C. *Philosophical Magazine*, 26(1):253–260, 1972.

[138] Shin ichi Shirasaki, Hiroshi Yamamura, Masaaki Hama, and Hidehisa Hashimoto. Oxygen diffusion in Li-doped polycrystalline MgO. *Japanese Journal of Applied Physics*, 12(10):1654–1655, 1973.

[139] W. H. Gourdin and W. D. Kingery. The defect structure of MgO containing trivalent cation solutes: shell model calculations. *Journal of Materials Science*, 14:2053–2073, 1979. 10.1007/BF00688410.

[140] C. Susse. Measurement of the elastic constants of LiF and MgO as a function of temperature and pressure. 54, 1961.

[141] D. R. Sempolinski and W. D. Kingery. Ionic conductivity and magnesium vacancy mobility in magnesium oxide. *Journal of the American Ceramic Society*, 63(11-12):664–669, 1980.

[142] S. Shirasaki and M. Hama. Oxygen-diffusion characteristics of loosely-sintered polycrystalline MgO. *Chemical Physics Letters*, 20(4):361 – 365, 1973.

[143] D. H. Chung. PhD thesis, Pennsylvania State Universisity, 1966.

[144] Yuki Satoh, Chiken Kinoshita, and Kiyomichi Nakai. Kinetic study of defect clusters in the MgO-Al_2O_3 system under electron- and/or ion-irradiation. *Journal of Nuclear Materials*, 179-181, Part 1(0):399 – 402, 1991.

[145] I. Jackson and H. Niesler. The elasticity of periclase to 3 GPa and some physical implications. In S. Akimoto and M. H. Manghani, editors, *High Pressure research in geophysics*, pages 93–133. Center for academic publications, Tokyo, 1982.

[146] C. Kinoshita. Characteristics of microstructural evolution of radiation damage in ceramics under fusion environment. *Journal of Nuclear Materials*, 179-181, Part 1(0):53 – 59, 1991.

[147] Donald G. Isaak, Orson L. Anderson, and Takayasu Goto. Measured elastic moduli of single-crystal MgO up to 1800 K. *Physics and Chemistry of Minerals*, 16:704–713, 1989. 10.1007/BF00223321.

[148] G Peckham. The phonon dispersion relation for magnesium oxide. *Proceedings of the Physical Society*, 90(3):657, 1967.

[149] G. W. Watson, E. T. Kelsey, N. H. de Leeuw, D. J. Harris, and S. C. Parker. Atomistic simulation of dislocations, surfaces and interfaces in MgO. *J. Chem. Soc., Faraday Trans.*, 92:433–438, 1996.

[150] P. W. Tasker. A guide to midas. Harwell report r9130, Harwell Laboratory, Didcot, Oxfordshire, UK, 1978.

[151] W. Smith, C.W. Yong, and P.M. Rodger. DL_POLY: Application to molecular simulation. *Molecular Simulation*, 28(5):385–471, 2002.

[152] D.M.Duffy and P.W. Tasker. Theoretical studies of diffusion processes down coincident tilt boundaries in nio. *Philosophical Magazine A*, 54(6):759, 1986.

[153] B. P. Uberuaga, R. Smith, A. R. Cleave, G. Henkelman, R. W. Grimes, A. F. Voter, and K. E. Sickafus. Dynamical simulations of radiation damage and defect mobility in MgO. *Phys. Rev. B*, 71:104102, Mar 2005.

[154] T. Brudevoll, E. A. Kotomin, and N. E. Christensen. Interstitial-oxygen-atom diffusion in MgO. *Phys. Rev. B*, 53:7731–7735, Mar 1996.

[155] M. P. Allen and D. J. Tildesley. *Computer Simulation of Liquids*. Oxford University Press, 1987.

[156] L. N. G. Filon. On a quadrature formula for trigonometric integrals. *Proceedings of the Royal Society of Edinburgh*, A49.

[157] A. Chopelas. Thermal expansion, heat capacity, and entropy of MgO at mantle pressures. *Physics and Chemistry of Minerals*, 17:142–148, 1990. 10.1007/BF00199665.

[158] K. Parlinski, J. Lazewski, and Y. Kawazoe. Ab initio studies of phonons in MgO by the direct method including LO mode. *Journal of Physics and Chemistry of Solids*, 61(1):87 – 90, 2000.

[159] Orson L. Anderson and Keshan Zou. Formulation of the thermodynamic functions for mantle minerals: MgO as an example. *Physics and Chemistry of Minerals*, 16:642–648, 1989. 10.1007/BF00223312.

[160] Katharina Vollmayr, Walter Kob, and Kurt Binder. Cooling-rate effects in amorphous silica: A computer-simulation study. *Phys. Rev. B*, 54:15808–15827, Dec 1996.

[161] A. Navrotsky. Energetics of metastable forms of amorphous silica. *Diffusion and Defect Data*, 53-54:61–66, 1987.

[162] Zhao-ying Chen and Jin-long Yang. The b3lyp hybrid density functional study on solids. *Frontiers of Physics in China*, 1:339–343, 2006. 10.1007/s11467-006-0026-8.

[163] Graeme Henkelman, Andri Arnaldsson, and Hannes Jónsson. A fast and robust algorithm for bader decomposition of charge density. *Computational Materials Science*, 36(3):354 – 360, 2006.

[164] W Tang, E Sanville, and G Henkelman. A grid-based bader analysis algorithm without lattice bias. *Journal of Physics: Condensed Matter*, 21(8):084204, 2009.

[165] R. B. Laughlin. Optical absorption edge of sio_2. *Phys. Rev. B*, 22:3021–3029, Sep 1980.

[166] L. Jiang and H.L. Tsai. Energy transport and material removal in wide bandgap materials by a femtosecond laser pulse. *International Journal of Heat and Mass Transfer*, 48(3-4):487 – 499, 2005.

[167] D. L. Griscom and E. J. Friebele. Fundamental radiation-induced defect centers in synthetic fused silicas: Atomic chlorine, delocalized e' centers, and a triplet state. *Phys. Rev. B*, 34:7524–7533, Dec 1986.

[168] Sanghamitra Mukhopadhyay, Peter V Sushko, Vladimir A Mashkov, and Alexander L Shluger. Spectroscopic features of dimer and dangling bond e ' centres in amorphous silica. *Journal of Physics: Condensed Matter*, 17(8):1311, 2005.

[169] J. G. Mihaychuk, N. Shamir, and H. M. van Driel. Multiphoton photoemission and electric-field-induced optical second-harmonic generation as probes of charge transfer across the Si/SiO_2 interface. *Phys. Rev. B*, 59:2164–2173, Jan 1999.

[170] Edward H. Poindexter and William L. Warren. Paramagnetic point defects in amorphous thin films of SiO_2 and Si_3N_4: Updates and additions. *Journal of The Electrochemical Society*, 142(7):2508–2516, 1995.

[171] Kenneth C. Snyder and W. Beall Fowler. Oxygen vacancy in α-quartz: A possible bi- and metastable defect. *Phys. Rev. B*, 48:13238–13243, Nov 1993.

[172] J. D. Gale and A. L. Rohl. The general utility lattice program (GULP). *Molecular Simulation*, 29(5):291–341, 2003.

[173] M. J. Frisch, G. W. Trucks, H. B. Schlegel, G. E. Scuseria, M. A. Robb, J. R. Cheeseman, V. G. Zakrzewski, J. A. Montgomery Jr., R. E. Stratmann, J. C. Burant, S. Dapprich, J. M. Millam, A. D. Daniels, K. N. Kudin, M. C. Strain, O. Farkas, J. Tomasi, V. Barone, M. Cossi, R. Cammi, B. Mennucci, C. Pomelli, C. Adamo, S. Clifford, J. Ochterski, G. A. Petersson, P. Y. Ayala, Q. Cui, K. Morokuma, P. Salvador, J. J. Dannenberg, D. K. Malick, A. D. Rabuck, K. Raghavachari, J. B. Foresman, J. Cioslowski, J. V. Ortiz, A. G. Baboul, B. B. Stefanov, G. Liu, A. Liashenko, P. Piskorz, I. Komaromi, R. Gomperts, R. L. Martin, D. J. Fox, T. Keith, M. A. Al-Laham, C. Y. Peng, A. Nanayakkara, M. Challacombe, P. M. W. Gill, B. Johnson, W. Chen, M. W. Wong, J. L. Andres, C. Gonzalez, M. Head-Gordon, E. S. Replogle, and J. A. Pople. Gaussian 98. Gaussian, Inc., Pittsburgh, PA.

[174] Ciprian Iliescu, Jianmin Miao, and Francis E.H. Taya. Optimization of an amorphous silicon mask pecvd process for deep wet etching of pyrex glass. *Surface and Coatings Technology*, 192:43–47, 2005.

[175] Linards Skuja. Optically active oxygen-deficiency-related centers in amorphous silicon dioxide. *Journal of Non-Crystalline Solids*, 239(1-3):16 – 48, 1998.

[176] M. J. Verkerk, B. J. Middelhuis, and A. J. Burggraaf. Effect of grain boundaries on the conductivity of high-purity ZrO_2 Y_2O_3 ceramics. *Solid State Ionics*, 6(2):159 – 170, 1982.

[177] Lionel Canioni Arnaud Brocas Arnaud Zoubir, Martin Richardson and Laurent Sarger. Optical properties of infrared femtosecond laser-modified fused silica and application to waveguide fabrication. *J. Opt. Soc. Am. B*, 22:2138–2143, 2005.